IntechOpen

Nanowires

New Insights

Edited by Khan Maaz

NANOWIRES - NEW INSIGHTS

Edited by **Khan Maaz**

Nanowires - New Insights
http://dx.doi.org/10.5772/65179
Edited by Khan Maaz

Contributors

Simas Rackauskas, Nadia Barbero, Guido Viscardi, Claudia Barolo, Hao Zhu, Marcos Vincius Puydinger Dos Santos, Fanny Béron, Kleber Roberto Pirota, José Alexandre Diniz, Stanislav Moshkalev, Ozgur Ergul, Soumen Dhara, Shengmao Zhang, Ningning Zeng, Shuguang Fan, Jingyi Ma, Yujuan Zhang, Pingyu Zhang, Zhijun Zhang, Paruğ İzzet Duru, Caner Değer, Vahap Eldem, Salah Obayya, Mohamed Hameed, Mohamed Hussein, Pavel Geydt, Mikhail Dunaevskiy, Erkki Lähderanta, Rosaria A. Puglisi, Maxim Shkunov, Grigorios Rigas, Marios Constantinou

© The Editor(s) and the Author(s) 2017
The moral rights of the and the author(s) have been asserted.
All rights to the book as a whole are reserved by INTECH. The book as a whole (compilation) cannot be reproduced, distributed or used for commercial or non-commercial purposes without INTECH's written permission.
Enquiries concerning the use of the book should be directed to INTECH rights and permissions department (permissions@intechopen.com).
Violations are liable to prosecution under the governing Copyright Law.

Individual chapters of this publication are distributed under the terms of the Creative Commons Attribution 3.0 Unported License which permits commercial use, distribution and reproduction of the individual chapters, provided the original author(s) and source publication are appropriately acknowledged. If so indicated, certain images may not be included under the Creative Commons license. In such cases users will need to obtain permission from the license holder to reproduce the material. More details and guidelines concerning content reuse and adaptation can be foundat http://www.intechopen.com/copyright-policy.html.

Notice

Statements and opinions expressed in the chapters are these of the individual contributors and not necessarily those of the editors or publisher. No responsibility is accepted for the accuracy of information contained in the published chapters. The publisher assumes no responsibility for any damage or injury to persons or property arising out of the use of any materials, instructions, methods or ideas contained in the book.

First published in Croatia, 2017 by INTECH d.o.o.
eBook (PDF) Published by IN TECH d.o.o.
Place and year of publication of eBook (PDF): Rijeka, 2019. IntechOpen is the global imprint of IN TECH d.o.o.
Printed in Croatia

Legal deposit, Croatia: National and University Library in Zagreb

Additional hard and PDF copies can be obtained from orders@intechopen.com

Nanowires - New Insights
Edited by Khan Maaz
p. cm.
Print ISBN 978-953-51-3283-7
Online ISBN 978-953-51-3284-4
eBook (PDF) ISBN 978-953-51-4762-6

Meet the editor

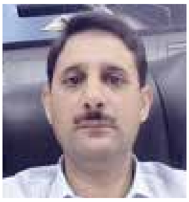

Dr. Maaz Khan is working as a senior researcher in the Pakistan Institute of Nuclear Science and Technology (PINSTECH), Pakistan. He has done his PhD from Quaid-i-Azam University, Islamabad, and postdoctorates from South Korea and China. His research interests include fabrication of nanomaterials and their structural, magnetic, optical, and electrical characterizations. He has authored more than 70 articles in peer-reviewed journals. He is the author and editor of many books. Dr. Maaz is working as the editor in chief of *Journal of Materials, Processing and Design* and executive editor of *International Journal of Nano Studies & Technology*. Besides, he is among the editorial board member and reviewer of many journals.

Contents

Preface

This book describes understanding about the nanowires, their fabrication, characterization, and applications in the recent technology. The book is organized into eleven chapters in total, which include fabrication of various metallic and oxide nanowires using different chemical and electrochemical techniques and their physical characterizations. Some very important applications of the nanowires such as for dye-sensitized and plasmonic nanowire solar cells, field-effect transistors, DNA, power transmission, and photovoltaic applications are discussed and presented in this book. The writing of each chapter is generally clear and precise, and numerous illustrations provide an easier understanding of the phenomena described in the book. This book addresses not only researchers in specialized field but also PhD students, postdoctorate fellows, and experienced technical professionals.

All the contributors of the book are active researchers in their fields, and therefore, this book provides up-to-date information about the nanowires and their applications. The content of the book provides the fundamental preparation needed for further study of advanced topics in nanowires. At the end of each chapter, proper references have been included that can lead the readers to the best sources in the literature and help them to go into more details about the nanowires.

I am grateful to all the authors who are experts in their fields for helping me complete this project and also to the entire InTech's publishing team for making this project possible. I am very thankful to the Publishing Process Manager Ms. Mirena Calmic for her cooperative attitude during the entire reviewing and publishing processes. I hope that this book will provide an opportunity to the readers to strengthen their knowledge and research capabilities in the field of materials science and nanotechnology with their specializations in one-dimensional nanostructures.

Maaz Khan
Physics Division, PINSTECH,
Islambad, Pakistan

Chapter 1

Synthesis and Application of Copper Nanowires and Silver Nanosheet-Coated Copper Nanowires as Nanofillers in Several Polymers

Ningning Zeng, Shuguang Fan, Jingyi Ma,
Yujuan Zhang, Shengmao Zhang, Pingyu Zhang and
Zhijun Zhang

Additional information is available at the end of the chapter

http://dx.doi.org/10.5772/67782

Abstract

A large amount of copper (Cu) nanowires was synthesized through the reduction of $Cu(OH)_2$ by hydrazine in an aqueous solution containing NaOH and ethylenediamine. Besides, Cu nanowires coated by silver nanosheet (denoted as Cu@Ag nanowires) were prepared with a facile transmetalation reaction method. In the meantime, the as-prepared Cu and Cu@Ag nanowires were used as the nanofillers of polyvinyl chloride (PVC), ultra-high molecular weight polyethylene (UHMWPE) and epoxy resin (EP), and their effects on the thermal properties and mechanical properties as well as friction and wear behavior of the polymer-matrix composites nanocomposites were examined. Results indicate that the as-prepared Cu@Ag nanowires consist of Cu nanowires core and Ag nanosheet shell. The Ag nanosheet shell can well inhibit the oxidation of the Cu nanowires core, thereby providing the as-prepared Cu@Ag nanowires with good thermal stability even at an elevated temperature of 230°C. As compared with Cu nanowires, Cu@Ag nanowires could effectively increase the thermal stability of the PVC matrix composites. Moreover, due to the special morphology and microstructure, the as-prepared Cu@Ag nanowires can effectively improve the mechanical properties and wear resistance of PVC, UHMWPE, and EP.

Keywords: Cu nanowires, Cu@Ag nanowires, nanocomposite, mechanical properties, tribological properties

1. Introduction

Copper nanowires could have promising applications in electronics [1–6], optoelectronics [7], solar cells [8–10], photonics, magnetics, genetic engineering, chemical sensors, and lubrication [11, 12], due to their unique characteristics such as high electrical conductivity and thermal conductivity as well as high aspect ratio and tribological properties. Particularly, copper nanowires often can effectively improve the mechanical properties, thermal properties, and wear resistance of polymers such as polystyrene [13, 14] and polyamide 6 [15, 16].

A variety of methods such as solution-phase method and complex-surfactant-assisted hydrothermal reduction approach are currently available for the synthesis of Cu nanowires [17–35]. Here the solution-phase method uses hydrazine (N_2H_4) to reduce Cu^{2+} ions in the highly basic aqueous solution of copper nitrate ($Cu(NO_3)_2$) at 25–100°C in the presence of ethylenediamine (EDA, $C_2H_8N_2$) as the surface-capping agent [32, 33]. The resultant Cu nanowires have a length of >40 μm and a diameter in the range of 60–160 nm, where a high concentration of NaOH (pH = 13–14) is required to prevent copper ions from forming copper hydroxide precipitates. The so-called complex-surfactant-assisted hydrothermal reduction approach can achieve facile synthesis of metal copper nanowires with an average diameter of 85 nm and a length of several tens of micrometers [34], where the copper nanowires are formed through the reduction of CuII−glycerol complex ($Cu(C_3H_6O_3)$) by phosphite (HPO_3^{2-}) at 120°C in the presence of surfactant sodium dodecyl benzenesulfonate (SDBS).

The synthesis and application of Cu nanowires, however, are still challenging because Cu nanowires are liable to spontaneous oxidation in air. Therefore, it is imperative to adopt carbon materials [36–39], polymers [40], and metals [10, 41–45] as the sources to introduce nonoxidizable shells on the surface of Cu nanowires, thereby preventing them from oxidation.

Among various surface-capped Cu nanowires, the metal-capped ones are of special interest, because they can be well prevented from oxidation while basic characteristics of metals are retained. We are particularly interested in Ag as a potential surface-capping shell of Cu nanowires. This is because, with thermal conductivity and electrical conductivity similar to that of Cu, Ag exhibits excellent oxidation resistance [46–51]. A couple of Ag-capped Cu nanowires have been reported elsewhere, mainly involving Cu nanowires-Ag nanowires synthesized in solution phase by the heterogeneous nucleation and growth of Ag nanocrystals on presynthesized Cu nanowires [50] and Cu@Ag nanowires with rough surface obtained by the transmetalation reaction at the room temperature [51]. The Cu nanowire cores of these Ag-capped Cu nanowires indeed can be well prevented from oxidation. However, the Ag shell of Cu@Ag nanowires consists of Ag nanoparticles, which is unfavorable for achieving full contact between the nanofillers and polymer matrix.

Therefore, in the present research, we prepare Ag nanosheets on Cu nanowires, hoping to achieve a large contact area between the nanofillers and polymer matrix, thereby acquiring improved mechanical properties and wear resistance. This article reports the preparation of Cu@Ag nanowires as well as the evaluation of their oxidation resistance. Besides, it also deals with the effect of Cu@Ag nanowires on the mechanical properties, thermal properties, and wear resistance of polyvinyl chloride (PVC), ultrahigh molecular weight polyethylene (UHMWPE), and epoxy resin (EP).

2. Preparation and characterization of Cu nanowires

Cu nanowires were prepared through the reduction of $Cu(OH)_2$ by hydrazine in an aqueous solution containing NaOH and ethylenediamine (EDA), with which the approach developed by Zeng et al. was modified to scale up the reaction by 3900 times (yield of Cu nanowires from 0.006 g to 23.5 g of) for potential large-scale production [30]. Briefly, NaOH (18 L, 7 M), $Cu(OH)_2$ (0.36 mol), EDA (135 mL), and hydrazine (18 mL, 35 wt.%) were added to a 20 L reactor and heated at 80°C for 30 min to achieve the reduction of Cu^{2+} to metallic copper at a rate of 100% (**Figure 1**). The as-prepared Cu nanowire cake is present on the top of the solution, possibly due to the entrapping of nitrogen bubbles among the nanowires ($2Cu^{2+} + N_2H_4 + 4OH^- \rightarrow 2Cu + N_2 + 4H_2O$). **Figure 1a** shows the scanning electron microscopic (SEM) images of the as-prepared Cu nanowires. They are straight and have a diameter of 150–200 nm and a length of about 10 μm. **Figure 1b** shows the X-ray diffraction (XRD) pattern of the Cu nanowires. The peaks at $2\theta = 43.3$, 50.4, 74.1, and 89.9° correspond to the (1 1 1), (2 0 0), (2 2 0), and (3 1 1) crystal planes of cubic Cu (PDF No. 89-2838), which indicates that the copper nanowires exhibit face-centered cubic (fcc) structure. No XRD signals of other species are detected, which indicate that the as-prepared Cu nanowires are highly pure. However, when the as-prepared Cu nanowires are placed in air for 24 h, three XRD peaks emerge at $2\theta = 36.4$, 42.3 and 52.5° (**Figure 1c**), and they correspond to the (1 1 1), (2 0 0), and (2 1 1) crystal planes of Cu_2O (PDF No. 78-2076). This means that the as-prepared Cu nanowires are easily oxidized in air environment.

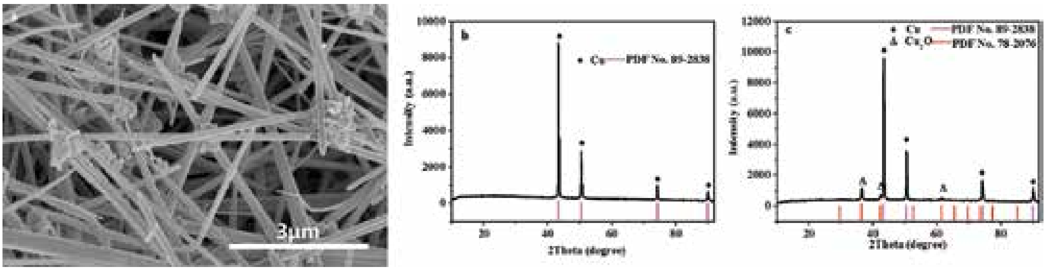

Figure 1. (a) SEM image of as-prepared Cu nanowires in mother liquor and XRD patterns, (b) as-prepared Cu nanowires, and (c) Cu nanowires after being stored in air for 24 h.

3. Preparation and characterization of Cu@Ag nanowires

The formation of Cu@Ag nanowires by the transmetalation reaction should be closely related to the different reduction potentials of Cu and Ag. First, 1.5 mmol $AgNO_3$ was dispersed in distilled water. Into the $AgNO_3$ solution was dropwise added the ammonium hydroxide (NH_4OH, 28–30%, BDH) aqueous solution under vigorous stirring until the yellow precipitate disappeared and the solution became clear. The as-obtained Ag-amine reagent solution was then directly added into 50 mL of Cu nanowires dispersion (with 0.5 g of Cu nanowires) under vigorous magnetic stirring at 40°C. After 2 h of reaction, the as-obtained product was washed with deionized water and collected by centrifugation, followed by redispersion in deionized water. During the synthesis progress, the Cu atoms on the surface of Cu nanowires quickly react with Ag^+ ions to release Cu^{2+}. Simultaneously, Ag^+ ions are reduced into Ag atoms and deposited on the surface of the Cu nanowires, during which the color of Cu nanowires dispersion turns grey along with the appearance of metallic Ag. Therefore, the morphology and microstructure of the as-prepared Cu@Ag nanowires should be highly dependent on the reaction conditions. Through comprehensive analysis, the optimal reaction condition is that temperature is 40°C; Cu/Ag molar ratio is 5:1; Cu dispersion concentration is 1% and silver ammonia reagent dropping speed is poured directly.

Figure 2 shows the SEM and TEM images as well as XRD pattern and EDS line map of the Cu@Ag nanowires prepared under the optimal reaction condition. It can be seen that the as-prepared Cu@Ag nanowires have a diameter of about 250 nm and a length of about 10 μm (**Figure 2a**). Besides, the major XRD peaks of the as-prepared Cu@Ag nanowires can be indexed to metallic Ag (PDF No. 87-0717) and Cu (PDF No. 89-2838) with fcc structure (**Figure 2b**). The

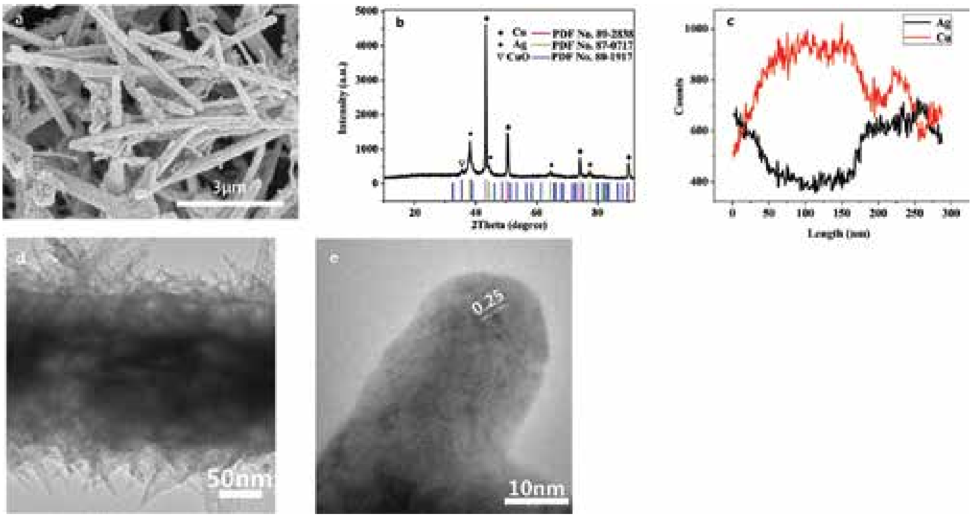

Figure 2. Characterization of Cu@Ag nanowires prepared under the optimal reaction condition: (a) SEM image, (b) XRD pattern, (c) EDS line map, (d) TEM image, and (e) HRTEM image.

small peak at $2\theta = 35.5°$ can be indexed to CuO (PDF No. 80-1917), which is possibly due to the oxidation of original Cu nanowires before coating with Ag nanosheets. In terms of the element line distribution, the copper element has a maximum value at the center part whereas the Ag shows a complementary profile with two maxima on both sides (**Figure 2c**). This indicates that the as-prepared Cu@Ag nanowires have a core-shell structure composed of Cu core and Ag shell. Such a core-shell structure of the as-prepared Cu@Ag nanowires is also supported by corresponding TEM image shown in **Figure 2d**. Namely, there is a layer of Ag nanosheets on Cu nanowires. Moreover, the high-resolution TEM (HRTEM) image of Cu@Ag nanowires indicates that the Ag crystal exhibits a fringe lattice spacing of 0.25 nm (**Figure 2e**), and it corresponds to the (200) plane of the Ag crystal.

The thermal stability of Cu@Ag nanowires with different treatments was measured by XRD. **Figure 3a** shows the XRD pattern of Cu@Ag nanowires prepared under the optimal condition after 2 month of storage in ambient condition. All the characteristic peaks remain unchanged after 2 month of storage in air, which indicates that the Ag shell layer can well inhibit the oxidation of the Cu nanowires core. **Figure 3b** shows the XRD patterns of the same product after being sintered at different temperatures. It can be seen that the XRD patterns have no change before 200°C contrasted with the XRD of as-prepared samples, while after being sintered at 300°C, a distinct peak of Cu_2O emerges and the major peaks of metallic Cu and Ag still remain, which indicates the Ag coating can protect Cu nanowires core from oxidation at high temperature. This means that the Cu@Ag nanowires show better thermal stability than Cu nanowires.

In order to further determine oxidation resistance of Cu@Ag nanowires, TG analysis was conducted in air flow. **Figure 4** shows the TG curves of the as-prepared Cu nanowires and Cu@Ag nanowires in air. The TG curves show Cu nanowires undergo a weight-gain around 100°C attributed to the oxidation thereat, while the Cu@Ag nanowires began to add the weight at around 230°C indicating that Cu@Ag nanowires have the higher oxidation resistance temperature, which also demonstrates that Cu@Ag nanowires exhibit much better thermal stability than Cu nanowires.

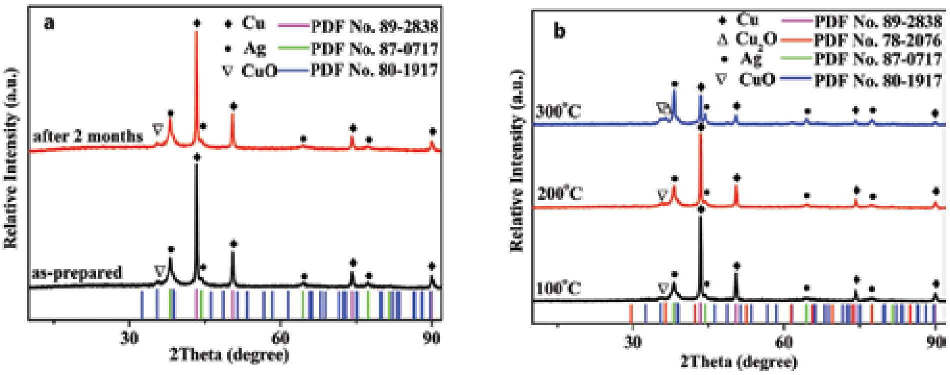

Figure 3. XRD paterns of Cu@Ag nanowires prepared under the optimal reaction condition: (a)after storage for different times in air, (b) after being sintered at different temperatures.

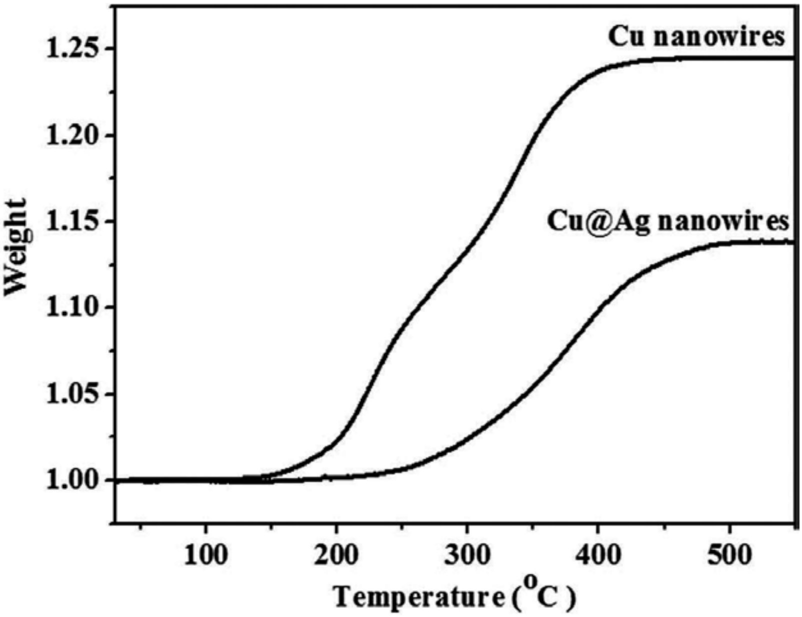

Figure 4. TG curves of Cu nanowires and Cu@Ag nanowires in air at a heating rate of 10°C/min.

4. Cu/Cu@Ag nanowires-PVC nanocomposites

The component and dosage for the preparation of Cu/Cu@Ag nanowires-PVC composites materials are listed in **Table 1**. The raw materials were mixed with mechanical stirring for 20 min, then melt blended by a laboratory two roll mill with a rotate speed of 50 rpm under 100°C for 10 min. The milled sheets were compressed by a press machine at 175°C and 20 MPa for 5 min. The samples for performance test were cut from the final sheets.

Nano-filler mass fraction (%)	Component (g)					
	PVC	Octadecanoic acid	Lead stearate	Calcium stearate	Dioctyl phthalate	Cu/Cu@Ag nanowires
0	160	1.28	0.64	0.64	32	0
0.1	160	1.28	0.64	0.64	32	0.195
0.5	160	1.28	0.64	0.64	32	0.978
1.0	160	1.28	0.64	0.64	32	1.97
3.0	160	1.28	0.64	0.64	32	6.02

Table 1. The component and dosage for the preparation of Cu nanowires- and Cu@Ag nanowires-PVC composites.

4.1. Thermal properties of Cu/Cu@Ag nanowires-PVC nanocomposites

Thermal properties of the composites were studied by differential scanning calorimetry (DSC). DSC curves were obtained by heating at 10°C/min rate under N_2 at a flow rate of 100 mL/min in the range of 20–120°C by using NETZSCH DSC 204HP instrument (Bavarian, Germany). The heated sample was cooled to 20°C and reheated for the second time using the same heating program.

An exemplary DSC heating curve for Cu nanowires-PVC nanocomposites is presented in **Figure 5**, with the indication of the procedure of glass transitions temperatures (Tg) determination as a central point value of the tangent line to the DSC curve, at the inflection point where the characteristic augment of the base line, related to the increase of the specific heat, was used for the determination of the glass transition. For all samples, the run of the DSC curve at the domain of the glass transition was similar.

The Tg of the Cu@Ag nanowires-PVC nanocomposites is presented in **Figure 6**. It can be seen that, as compared with Cu nanowires, the introduction of Cu@Ag nanowires results in a larger increase in the Tg value. Besides, the Tg of the Cu@Ag nanowires-PVC nanocomposites tends to rise with the increase of Cu@Ag nanowire content. This is because, with the increase of the Cu@Ag nanowire content, more Cu@Ag nanowires act as physical cross-linkers to be intertwined with macromolecular chains, thereby reducing the chain segmental mobility of PVC and increasing the Tg. However, when the content of Cu@Ag nanowires

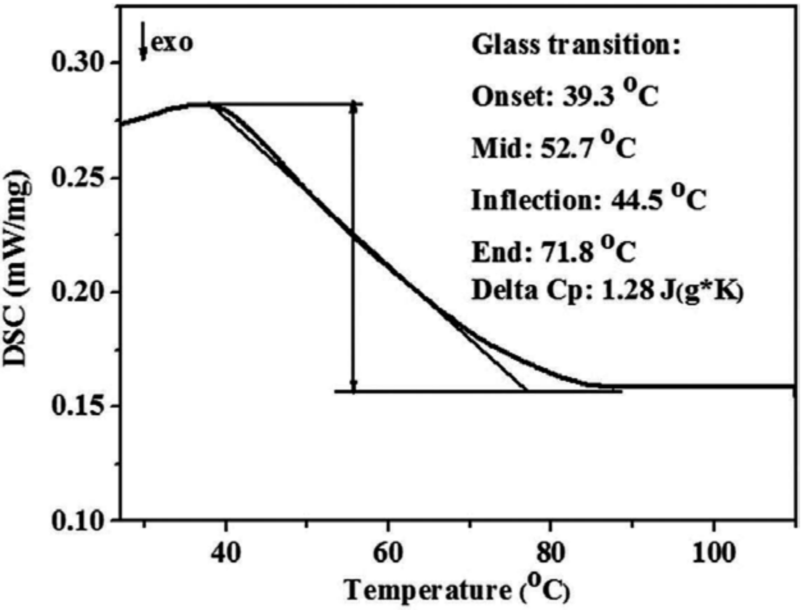

Figure 5. An exemplary DSC trace for Cu nanowires-PVC composite (Cu nanowires contain: 1 wt.%) at the domain of the glass transition.

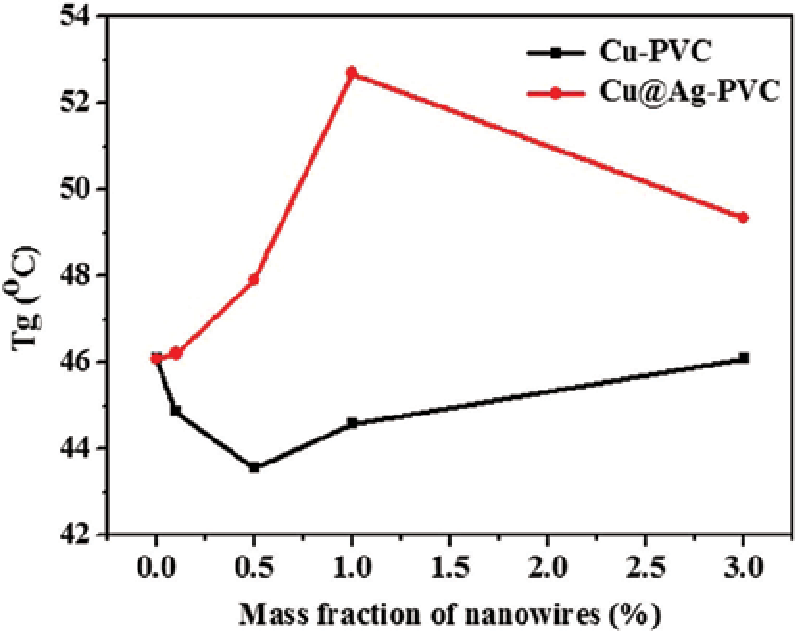

Figure 6. The glass transition temperature (Tg) of Cu/Cu@Ag nanowires-PVC nanocomposites with various mass fractions of the nanofillers.

is too high, the Tg values of the PVC-matrix nanocomposites declines to some extent. The reason lies in that a too high content of Cu@Ag nanowires would tend to agglomerate in the polymer matrix and weaken the interaction with the macromolecular chains, thereby limiting the movements of the macromolecular chains and reducing the Tg value of the PVC-matrix nanocomposites. Moreover, the presence of Cu@Ag nanowires in PVC matrix contributes to increasing the elasticity especially in the glass transition region, which corresponds to enhanced thermal stability of the PVC-matrix nanocomposites.

4.2. Mechanical properties of Cu/Cu@Ag nanowires-PVC nanocomposites

Mean values of five factors on mechanical properties were analyzed in this work. The tensile strength and elongation at break of these samples are shown in **Figure 7**. From **Figure 7**, it can be seen that the elongation at break of composite materials all increase to varying degrees by addition of the nanowires. And the effect of Cu@Ag nanowires is much larger than the Cu nanowires. Meanwhile, the tensile strength keeps no change on the whole.

4.3. Tribology properties of Cu/Cu@Ag nanowires-PVC nanocomposites

Figure 8 shows the friction coefficient and wear rate of Cu/Cu@Ag nanowires-PVC nanocomposites (load: 20 N; route: 5 mm; frequency: 2 Hz; time: 5 min; room temperature). The friction coefficient of Cu/Cu@Ag nanowires PVC nanocomposites has little change with

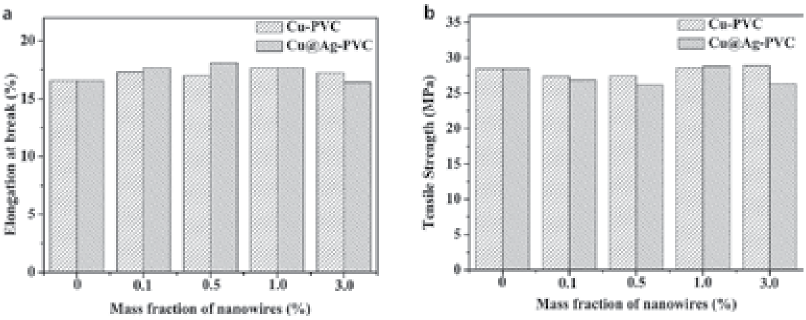

Figure 7. The elongation at break (a) and tensile strength and (b) Cu/Cu@Ag nanowires-PVC nanocomposites with different nanowires contents.

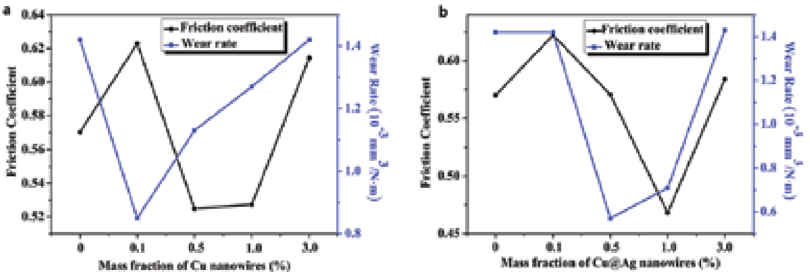

Figure 8. The friction and wear behavior (friction coefficient and wear rate) of PVC nanocomposites with different contents of (a) Cu nanowires and (b) Cu@Ag nanowires.

increasing amount of copper nanowire, while the wear rate changes greatly therewith. Namely, pure PVC (without Cu nanowires) has a larger wear rate as much as 1.42 × 10^{-3} mm^3/N m, while PVC composite containing 0.5 wt.% Cu@Ag nanowires has an obviously reduced wear rate of 0.57 × 10^{-3} mm^3/N m (reduced by nearly 60%). It can be clearly seen that lower or higher concentrations of fillers in the matrix are less effective in reducing the friction coefficient and wear rate. It can be inferred that, at a too low concentration, the nanofillers can hardly play its role on the friction-reducing and wear resistance in the friction process, thereby leading to relatively not very good friction property. When the additive concentration is too high, the nanofiller would tend to agglomerate and form a large number of weak interfaces in the matrix, which makes the nanofillers easily fall off from the matrix in the friction process causing a higher abrasive wear [52], thus resulting in relatively poor friction property. Therefore, it is suggested to keep the concentration of the nanofillers in polymer matrix as 0.5 wt.% Cu@Ag nanowires in order to effectively reduce the friction coefficient and wear rate. Moreover, the wear rate of Cu nanowires-PVC nanocomposites tends to decline with the increasing content of the Cu nanowires, and the minimum wear rate (0.85 × 10^{-3} mm^3/N m) is obtained at a Cu nanowires content of 0.1 wt.%.

5. Cu/Cu@Ag nanowires-UHMWPE nanocomposites

The component and dosage for the preparation of Cu@Ag nanowires-UHMWPE composites are listed in **Table 2**. The nanowires and UHMWPE raw material were mixed with ball milling for 1 h. The mixture was heated to 200°C and pressed under 20 MPa for 10–20 min, followed by cooling to room temperature in the mold to afford the Cu@Ag nanowires-UHMWPE nanocomposites. All the samples for performance test were cut from the final sheets.

5.1. Crystallization and melting behavior of Cu/Cu@Ag nanowires-UHMWPE nanocomposites

The crystallization and melting behavior of Cu/Cu@Ag nanowires-UHMWPE nanocomposites were studied by differential scanning calorimetry (DSC). DSC curves in the range of 20–200°C were measured with a NETZSCH DSC 204HP instrument (Bavarian, Germany) at a heating rate of 10°C/min under N_2 atmosphere (flow rate: 100 mL/min). **Figure 9** shows the crystallization and melting temperature of Cu/Cu@Ag nanowires-UHMWPE nanocomposites. It is seen from **Figure 9a** that Cu nanowires have a strong influence on the crystallization and melting temperature of UHMWPE matrix. When the content of Cu nanowires is 0.1 wt.%, the crystallization temperature of nanocomposite rises from 118.10 to 118.32°C, which could be because that the heterogeneous nucleation in the presence of copper nanowire served as nucleating agent contributes to improving the crystallinity of UHMWPE matrix. With the increasing of nanowires content, the crystallization temperature significantly decreases, which indicates that Cu nanowires hinder the orientation of PA6 crystals and restrict the movement of the molecular chains of UHMWPE. When the nanowires content is further increased, the effect of Cu nanowires on the crystallization and melting behaviors tends to decline, possibly due to the aggregation of the nanofillers in the polymer matrix. When the Cu nanowires content reaches 3 wt.%, however, the crystallization temperature decreases again, probably because that the interaction between excess nanowires and molecular chains of UHMWPE is enhanced to restrict the movement of the molecular chains. Correspondingly, a change in melting temperature occurs with the increasing of nanowires content.

Interestingly, the Cu@Ag nanowires have opposite effects on the crystallization and the melting temperature as compared with Cu nanowires, which could be because the Cu@Ag nanowires

Component	**Mass fraction (%)**						
	0	**0.1**	**0.3**	**0.5**	**0.8**	**1.0**	**3.0**
UHMWPE (g)	120	120	120	120	120	120	120
Cu/Cu@Ag nanowires (g)	0	0.120	0.361	0.603	0.968	1.21	3.71

Table 2. The component and dosage for the preparation of Cu/Cu@Ag nanowires-UHMWPE composites.

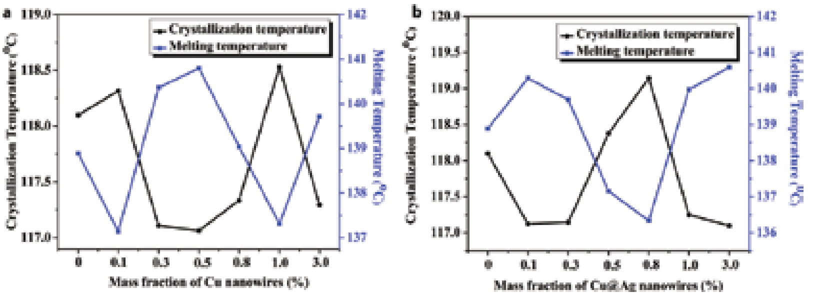

Figure 9. The crystallization and melting temperature of Cu/Cu@Ag nanowires-UHMWPE nanocomposites with different nanowires contents.

with unique morphology and microstructure exhibit significantly increased contact area with the UHMWPE matrix.

5.2. Mechanical properties of Cu/Cu@Ag nanowires-UHMWPE nanocomposites

The effect of Cu/Cu@Ag nanowires on the mechanical properties of UHMWPE is shown in **Figure 10**. We find that the elongation at break of composite materials gradually increases with increasing dosage of Cu/Cu@Ag nanowires; and in particular, the UHMWPE-based nanocomposites with 0.8 wt.% of Cu nanowires or with 0.3 wt.% of Cu@Ag nanowires possesses the maximum values of elongation at break (168 and 190%, respectively), larger than that of unfilled UHMWPE by 78.5 and 101.9% (**Figure 10a**). Besides, the elongation rate at break of the UHMWPE-based nanocomposites tends to decline with further increase of nanowires content, possibly due to the aggregation of the nanowires thereat. Moreover, the elongation rate at break of Cu@Ag nanowires-UHMWPE is higher than that of Cu nanowires-UHMWPE, which could be closely related to the special morphology and microstructure of the Cu@Ag nanowires. Furthermore, the UHMWPE-based nanocomposites change slightly with increasing dosage of Cu/Cu@Ag nanowires. The UHMWPE-based nanocomposites with 0.3 wt.% of Cu nanowires or with 0.5 wt.% of Cu@Ag nanowires possess the maximum values of tensile

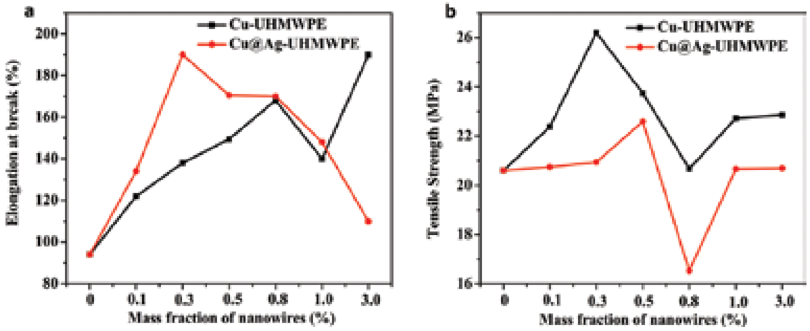

Figure 10. The mechanical properties of Cu/Cu@Ag nanowires-UHMWPE nanocomposites with different nanowires contents.

strength of 26.2 and 22.6 MPa, respectively, showing an increase by 27.1 and 9.7% in comparison with pure UHMWPE (20.6 MPa; **Figure 10b**).

5.3. Tribology properties of Cu/Cu@Ag nanowires-UHMWPE nanocomposites

Figure 11 shows the friction coefficient and wear rate of Cu/Cu@Ag nanowires-UHMWPE nanocomposites (load: 250 N; route: 5 mm; frequency: 2Hz; time: 5 min; room temperature). For Cu nanowires-UHMWPE nanocomposites (**Figure 11a**), the friction coefficient and wear rate of Cu nanowires-UHMWPE nanocomposites gradually decrease with increasing dosage of Cu nanowires; and the friction coefficient is rather large when the Cu nanowires content is below 0.3 wt.%. This may be because that when the content of Cu nanowires is too low to play its role on the friction-reducing and wear resistance in the friction process, thereby leading to relatively not very good friction property. Cu@Ag nanowires-UHMWPE nanocomposites show similar variation tendency as Cu nanowires-UHMWPE nanocomposites (**Figure 11b**) except the one with 3 wt.% of Cu@Ag nanowires is somewhat different.

6. Cu/Cu@Ag nanowires-EP nanocomposites

The Cu/Cu@Ag nanowires-EP (epoxy resin) nanocomposites were prepared by mixing the raw materials with high-speed mixers (1500 rpm, 3 min) in association with curing in the mold under ambient conditions. The content of each component is shown in **Table 3**.

6.1. The electrical conductivity Cu/Cu@Ag nanowires-EP nanocomposites

In general, the electrical conductivity of silver and copper is similar. The special structure of Cu@Ag nanowires makes it feasible to significantly improve the electrical conductivity of Cu nanowires by incorporating Ag shell because of their better oxidation resistance and more conductive network in the polymer matrix nanocomposites. We measured the electrical resistivity of EP-matrix composites filled with Cu and Cu@Ag nanowires using a Hall effect

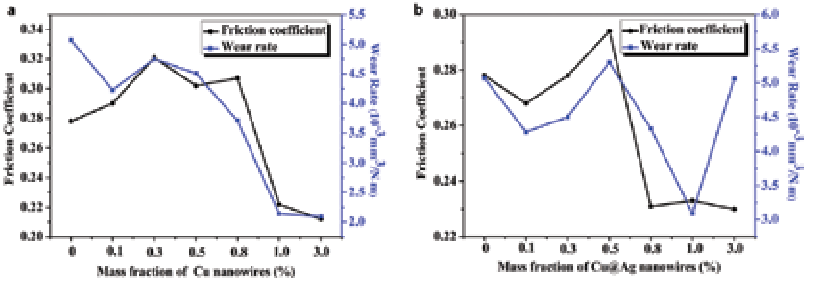

Figure 11. The friction and wear behavior (friction coefficient and wear rate) of UHMWPE nanocomposites with different contents of (a) Cu nanowires and (b) Cu@Ag nanowires.

Component	**Mass fraction (%)**						
	0	**0.1**	**0.3**	**0.5**	**0.8**	**1.0**	**3.0**
EP (g)	60	60	60	60	60	60	60
Curing agent (g)	15	15	15	15	15	15	15
Cu/Cu@Ag nanowires (g)	0	0.075	0.226	0.377	0.606	0.758	2.320

Table 3. The component and dosage for the preparation of Cu nanowires- and Cu@Ag nanowires-EP composites.

measurement system. The electrical resistivity of pure EP is about 10^{14} Ω cm, while the introduction of Cu/Cu@Ag nanowires results in greatly reduced electrical resistivity (**Figure 12**). Namely, the electrical resistivity decreases obviously with increasing content of Cu or Cu@Ag nanowires, and the EP-matrix nanocomposites filled with Cu@Ag nanowires exhibit lower electrical resistivity than the counterparts filled with Cu nanowires. For example, the resistivity of the EP composite containing 3 wt.% Cu nanowires is about 1.49×10^5 Ω cm, and it does not satisfy the conductive requirement for electrostatic conductive materials (10^4 Ω cm). The resistivity of Cu@Ag nanowires-EP composite (filler mass fraction: 3 wt.%) is reduced to 2.11×10^4 Ω cm, and it satisfies the conductive requirement for electrostatic conductive materials.

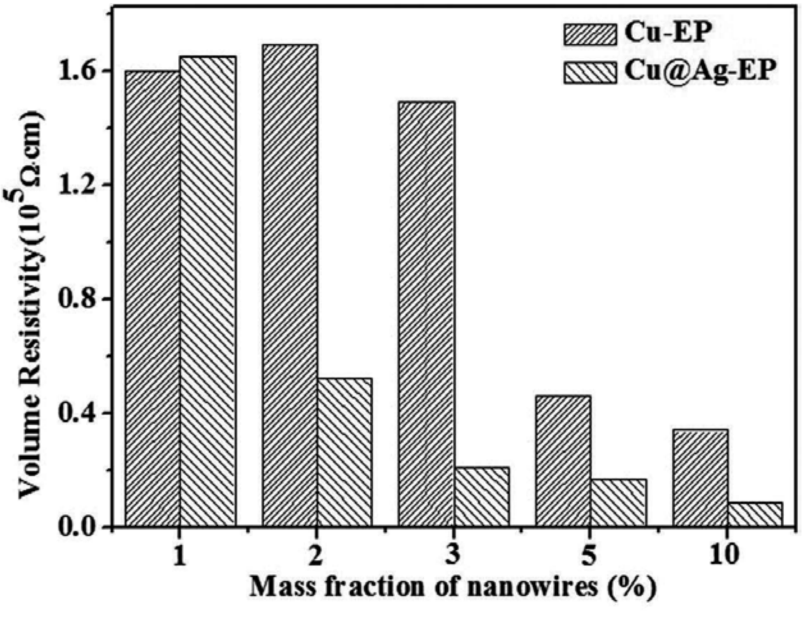

Figure 12. The electrical resistivity of Cu/Cu@Ag nanowires-EP nanocomposites with different nanowires contents.

In other words, encapsulating Cu nanowires with Ag nanosheets makes it feasible for the copper nanowires to be applied as potential electrostatic conductive filler, thereby broadening their application scope.

6.2. Mechanical properties of Cu/Cu@Ag nanowires-EP nanocomposites

The tensile strength and the elongation at break of pure EP and its nanocomposites filled with Cu nanowires or Cu@Ag nanowires are shown in **Figure 13**. Both the tensile strength and elongation at break increase after the introduction of Cu nanowires and Cu@Ag nanowires. Particularly, the EP-matrix nanocomposite with 0.8 wt.% of Cu nanowires exhibits the maximum tensile strength of 74.2 MPa, while the one with 1 wt.% of Cu@Ag nanowires exhibits the maximum tensile strength of 67.5 MPa. In addition, compared with the change of the elongation at break values, the tensile strength has little change with the increase of nanowires content. When the content of the nanowires is too high, the tensile strength and elongation at break are relatively low, which could be due to the aggregation of the nanowires in EP matrix at a high content.

6.3. Tribology properties of Cu/Cu@Ag nanowires-EP nanocomposites

Figure 14 shows the variation in the friction coefficient and wear rate of Cu/Cu@Ag nanowires-EP composites with the content of the nanofillers (load: 20 N; amplitude: 5 mm; frequency: 2Hz; time: 30 min; room temperature). Unfilled EP has a friction coefficient and wear rate of 0.646 and 4.82 × 10^{-3} mm^3/N m. Namely, the EP-matrix nanocomposites with less than 0.5 wt.% of Cu nanowires have reduced friction coefficient and wear rate than neat EP; and in particular, the EP-matrix composite with 0.1% of Cu nanowires exhibits the best friction coefficient and wear rate (0.555, 1.42 × 10^{-3} mm^3/N m; a reduction by 14.1 and 70.5% as compared with that of neat EP). However, the increase in the content of the Cu nanowires above 0.5 wt.% results in increased friction coefficient and wear rate, due to aggregation of the nanofillers thereat. Similar variation tendency is also observed for Cu@Ag nanowires-EP nanocomposites.

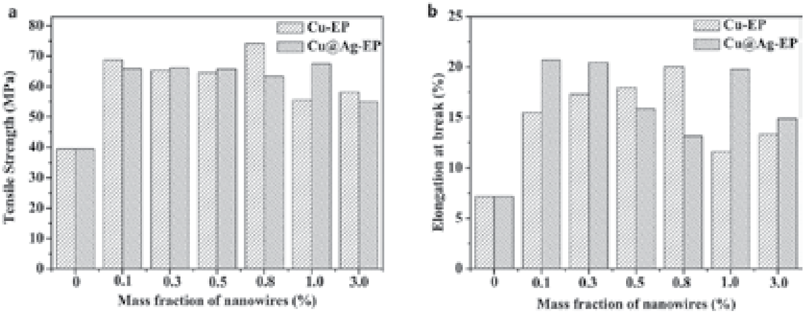

Figure 13. The mechanical properties of Cu/Cu@Ag nanowires-EP nanocomposites with different nanowires content.

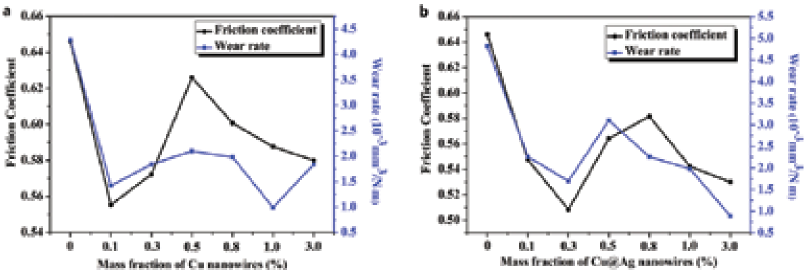

Figure 14. The friction and wear behavior (friction coefficient and wear rate) of EP-matrix nanocomposites with different contents of (a) Cu nanowires and (b) Cu@Ag nanowires.

7. Conclusion

A large amount of Cu nanowires is prepared by a solution-reduction approach, while Cu@Ag nanowires are prepared by a simple and efficient transmetalation reaction method. The morphology and microstructure of the as-prepared Cu@Ag nanowires can be well manipulated by properly adjusting the reaction condition. Resultant Cu@Ag nanowires consist of Cu nanocores and uniformly distributed Ag nanosheet shell, and they exhibit improved thermal stability and electrical conductivity as compared with Cu nanowires, due to the incorporation of the Ag shell. Besides, the as-prepared Cu@Ag nanowires can better improve the mechanical properties and wear resistance than the Cu nanowires.

Acknowledgements

We acknowledge the financial support provided by National Natural Science Foundation of China (Grant no. 51275154, 51405132, 21671053), the Plan for Young Scientific Innovation Talent of Henan Province (Grant no. 154100510018) and Natural Science Foundation of Henan Province (14A150006).

Author details

Ningning Zeng[1], Shuguang Fan[1], Jingyi Ma[1], Yujuan Zhang[1], Shengmao Zhang[1,2]*, Pingyu Zhang[1] and Zhijun Zhang[1]

*Address all correspondence to: zsm@henu.edu.cn

1 Engineering Research Center for Nanomaterials, Henan University, Kaifeng, P. R. China

2 Collaborative Innovation Center of Nano Functional Materials and Applications of Henan Province, Henan University, Kaifeng, P. R. China

References

[1] Hsu P, Wu H, Carney T J. Passivation coating on electrospun copper nanofibers for stable transparent electrodes. ACS Nano. 2012;**6**(6):5150-5156. DOI: 10.1021/nn300844g

[2] Kumar Ravi D V, Woo K, Moon J. Promising wet chemical strategies to synthesize Cu nanowires for emerging electronic applications. Nanoscale. 2015;**7**(41):17195-17210. DOI: 10.1039/c5nr05138j

[3] Yin Z, Lee C, Cho S. Facile synthesis of oxidation-resistant copper nanowires toward solution-processable, flexible, foldable, and free-standing electrodes. Small. 2014;**10**(24):5047-5052. DOI: 10.1002/smll.201401276

[4] He C, Liu G, Zhang W X. Tuning the structures and electron transport properties of ultrathin Cu nanowires by size and bending stress using DFT and DFTB methods. RSC Advances. 2015;**29**(5):22463-22470. DOI: 10.1039/C4RA15051A

[5] Nam V, Lee D. Copper nanowires and their applications for flexible, transparent conducting films: a review. Nanomaterials. 2016;**6**(3):47. DOI:10.3390/nano6030047

[6] Jung S M, Preston D J, Jung H Y. Porous Cu nanowire aerosponges from one-step assembly and their applications in heat dissipation. Advanced Materials. 2016;**28**(7):1413-1419. DOI: 10.1002/adma.201504774

[7] Im H G, Jung S H, Jin J. Flexible transparent conducting hybrid film using a surface-embedded copper nanowire network: a highly oxidation-resistant copper nanowire electrode for flexible optoelectronics. ACS Nano. 2014;**8**(10):10973-10979. DOI: 10.1021/nn504883m

[8] Zhao Y, Zhang Y, Li Y. Rapid and large-scale synthesis of Cu nanowires via a continuous flow solvothermal process and its application in dye-sensitized solar cells (DSSCs). RSC Advances. 2012;**2**(30):11544-11551. DOI: 10.1039/c2ra21224b

[9] Liang J, Bi H, Wan D. Novel Cu nanowires/graphene as the back contact for CdTe solar cells. Advanced Functional Materials. 2012;**22**(6):1267-1271. DOI: 10.1002/adfm.201102809

[10] Stewart I E, Rathmell A R, Yan L. Solution-processed copper–nickel nanowire anodes for organic solar cells. Nanoscale. 2014; **6**(11):5980-5988. DOI: 10.1039/c4nr01024h

[11] Stortini A M, Moretto L M, Mardegan A. Arrays of copper nanowire electrodes: preparation, characterization and application as nitrate sensor. Sensors and Actuators B: Chemical. 2015;**207, Part A**:186-192. DOI: 10.1016/j.snb.2014.09.109

[12] Huang J, Dong Z, Li Y. High performance non-enzymatic glucose biosensor based on copper nanowires–carbon nanotubes hybrid for intracellular glucose study. Sensors and Actuators B: Chemical. 2013;**182**:618-624. DOI: 10.1016/j.snb.2013.03.065

[13] Lin B, Gelves G A, Haber J A. Electrical, morphological and rheological study of melt-mixed polystyrene/copper nanowire nanocomposites. Macromolecular Materials and Engineering. 2008; **293**(7):631-640. DOI: 10.1002/mame.200800045

[14] Gelves G A, Sundararaj U, Haber J A. Electrostatically dissipative polystyrene nanocomposites containing copper nanowires. Macromolecular Rapid Communications. 2005;**26**(25): 1677-1681. DOI: 10.1002/marc.200500490

[15] Xu Q, Li X, Zhang S. Preparation and characterization of copper nanowire/polyamide 6 nanocomposites and its properties. Journal of Macromolecular Science, Part A. 2014;**51**(7):598-603. DOI: 10.1 080/10601325. 2014.916182

[16] Xu Q, Li X, Zhang S. Copper nanowire/PA6 composites prepared by in situ polymerization and its properties. Journal of Polymer Research. 2013;**20**(10):1-6. DOI: 10.1007/s10965-013-0257-7

[17] Cui F, Yu Y, Dou L. Synthesis of ultrathin copper nanowires using tris(trimethylsilyl) silane for high-performance and low-haze transparent conductors. Nano Letters. 2015;**15**(11): 7610-7615. DOI: 10.1021/acs.nanolett.5b03422

[18] Gelves G A, Murakami Z T M, Krantz M J. Multigram synthesis of copper nanowires using ac electrodeposition into porous aluminium oxide templates. Journal of Materials Chemistry. 2006;**16**(30):3075-3083. DOI: 10.1039/b603442j

[19] Inguanta R, Piazza S, Sunseri C. Influence of the electrical parameters on the fabrication of copper nanowires into anodic alumina templates. Applied Surface Science. 2009;**255**(21):8816-8823. DOI: 10.1016/j.apsusc.2009.06.062

[20] Gerein N J, Haber J A. Effect of ac electrodeposition conditions on the growth of high aspect ratio copper nanowires in porous aluminum oxide templates. The Journal of Physical Chemistry B. 2005;**109**(37):17372-17385. DOI: 10.1021/jp051320d

[21] Pate J, Zamora F, Watson S M D. Solution-based DNA-templating of sub-10 nm conductive copper nanowires. Journal of Materials Chemistry C. 2014;**2**(43):9265-9273. DOI: 10.1039/C4TC01632G

[22] Monson C F, Woolley A T. DNA-templated construction of copper nanowires. Nano Letters. 2003; **3**(3):359-363. DOI: 10.1021/nl034016+

[23] Zhang X, Cui Z. Synthesis of Cu nanowires via solventhermal reduction in reverse microemulsion system. Journal of Physics: Conference Series. 2009;**152**(1):012022. DOI: 10.1088/1742 6596/152/1/012022

[24] Shi Y, Li H, Chen L. Obtaining ultra-long copper nanowires via a hydrothermal process. Science and Technology of Advanced Materials. 2005;**6**(7):761-765. DOI: 10.1016/j.stam.2005.06.008

[25] Xu S, Sun X, Ye H. Selective synthesis of copper nanoplates and nanowires via a surfactant-assisted hydrothermal process. Materials Chemistry and Physics. 2010;**120**(1):1-5. DOI: 10.1016/j.matchemphys.2009.10.049

[26] Liu Y, Zhang M, Wang F. Facile microwave-assisted synthesis of uniform single-crystal copper nanowires with excellent electrical conductivity. RSC Advances. 2012;**2**(30):11235-11237. DOI: 10.1039/C2RA21578K

[27] Jiang Z, Tian Y, Ding S. Synthesis and characterization of ultra-long and pencil-like copper nanowires with a penta-twinned structure by hydrothermal method. Materials Letters. 2014;**136**:310-313. DOI: 10.1016/j.matlet.2014.08.033

[28] Ye E, Zhang S, Liu S. Disproportionation for growing copper nanowires and their controlled self-assembly facilitated by ligand exchange. Chemistry – A European Journal. 2011;**17**(11):3074-3077. DOI: 10.1002/chem.201002987

[29] Yang H, He S, Tuan H. Self-seeded growth of five-fold twinned copper nanowires: mechanistic study, characterization, and SERS applications. Langmuir. 2014;**30**(2):602-610. DOI: 10.1021/la4036198

[30] Wang W, Li G, Zhang Z. A facile templateless, surfactantless hydrothermal route to ultralong copper submicron wires. Journal of Crystal Growth. 2007;**299**(1):158-164. DOI: 10.1016/j.jcrysgro.2006.11.221

[31] Zhang X, Zhang D, Ni X. One-step preparation of copper nanorods with rectangular cross sections. Solid State Communications. 2006;**139**(8):412-414. DOI: 10.1016/j.ssc.2006.06.042

[32] Chang Y, Lye M L, Zeng H C. Large-scale synthesis of high-quality ultralong copper nanowires. Langmuir. 2005;**21**(9):3746-3748. DOI: 10.1021/la050220w

[33] Rathmell A R, Bergin S M, Hua Y L. The growth mechanism of copper nanowires and their properties in flexible, transparent conducting films. Advanced Materials. 2010;**22**(32):3558-3563. DOI: 10.1002/adma.201000775

[34] Liu Z, Yang Y, Liang J. Synthesis of copper nanowires via a complex-surfactant-assisted hydrothermal reduction process. The Journal of Physical Chemistry B. 2003;**107**(46):12658-12661. DOI: 10.1021/jp036023s

[35] Ye S, Stewart I E, Chen Z. How copper nanowires grow and how to control their properties. Accounts of Chemical Research. 2016;**49**(3):442-451. DOI: 10.1021/acs.accounts.5b00506

[36] Dou L, Cui F, Yu Y. Solution-processed copper/reduced-graphene-oxide core/shell nanowire transparent conductors. ACS Nano. 2016;**10**(2):2600-2606. DOI: 10.1021/acsnano.5b07651

[37] Mehta R, Chugh S, Chen Z. Enhanced electrical and thermal conduction in graphene-encapsulated copper nanowires. Nano Letters. 2015;**15**(3):2024-2030. DOI: 10.1021/nl504889t

[38] Zhao Y, Zhang Y, Li Y. A flexible chemical vapor deposition method to synthesize copper@carbon core–shell structured nanowires and the study of their structural electrical properties. New Journal of Chemistry. 2012;**36**(5):1161-1169. DOI: 10.1039/c2nj21026f

[39] Zhao Y, Wang J, Zhang Y. The investigation of a hydro-thermal method to fabricate Cu@C coaxial nanowires and their special electronic transport and heat conduction properties. New Journal of Chemistry. 2012;**36**(5):1255-1264. DOI: 10.1039/c2nj40036g

[40] Liu Y, Liu Z, Lu N. Facile synthesis of polypyrrole coated copper nanowires: a new concept to engineered core-shell structures. Chemical Communications. 2012;**48**(20):2621-2623. DOI: 10.1039/c2cc16961d

[41] Liu Z, Elbert D, Chien C. FIB/TEM characterization of the composition and structure of core/shell Cu−Ni nanowires. Nano Letters. 2008;**8**(8):2166-2170. DOI: 10.1021/nl080492u

[42] Alia S M, Yan Y. Palladium coated copper nanowires as a hydrogen oxidation electrocatalyst in base. Journal of the Electrochemical Society. 2015;**162**(8):F849-F853. DOI: 10.1149/2.0211508jes

[43] Alia S M, Jensen K, Contreras C. Platinum coated copper nanowires and platinum nanotubes as oxygen reduction electrocatalysts. ACS Catalysis. 2013;**3**(3):358-362. DOI: 10.1021/cs300664g

[44] Zhang S, Zeng H C. Solution-based epitaxial growth of magnetically responsive Cu@Ni nanowires. Chemistry of Materials. 2010;**22**(4):1282-1284. DOI: 10.1021/cm903105f

[45] Luo X, Gelves G A, Sundararaj U. Silver-coated copper nanowires with improved anti-oxidation property as conductive fillers in low-density polyethylene. The Canadian Journal of Chemical Engineering. 2013;**91**(4):630-637. DOI: 10.1002/cjce.21701

[46] Wei Y, Chen S, Lin Y. Cu–Ag core–shell nanowires for electronic skin with a petal molded microstructure. Journal of Materials Chemistry C. 2015;**3**(37):9594-9602. DOI: 10.1039/c5tc01723h

[47] Wang X, Wang R, Shi L. Synthesis of metal/bimetal nanowires and their applications as flexible transparent electrodes. Small. 2015;**11**(36):4737-4744. DOI: 10.1002/smll.201501314

[48] Stewart I E, Ye S, Chen Z. Synthesis of Cu–Ag, Cu–Au, and Cu–Pt Core–Shell nanowires and their use in transparent conducting films. Chemistry of Materials. 2015;**27**(22):7788-7794. DOI: 10.1021/acs.chemmater.5b03709

[49] Easow J S, Selvaraju T. Unzipped catalytic activity of copper in realizing bimetallic Ag@Cu nanowires as a better amperometric H_2O_2 sensor. Electrochimica Acta. 2013;**112**: 648-654. DOI: 10.1016/j.electacta.2013.09.033

[50] Han M, Liu S, Zhang L, et al. Synthesis of octopus-tentacle-like Cu nanowire-Ag nanocrystals heterostructures and their enhanced electrocatalytic performance for oxygen reduction reaction. ACS Applied Materials & Interfaces. 2012;**4**(12):6654-6660. DOI: 10.1021/am301814y

[51] Zhao J, Zhang D, Zhang X. Preparation and characterization of copper/silver bimetallic nanowires with core-shell structure. Surface and Interface Analysis. 2015;**47**(4):529-534. DOI: 10.1002/sia.5743

[52] Wetzel B, Haupert F, Zhang M. Epoxy nanocomposites with high mechanical and tribological performance. Composites Science and Technology. 2003;**63**(14):2055-2067. DOI: 10.1016/S0266-3538(03)00115-5

Chapter 2

Second Harmonic Generation in ZnO Nanowires

Soumen Dhara and Stephen A. Lynch

Additional information is available at the end of the chapter

http://dx.doi.org/10.5772/intechopen.68150

Abstract

Second harmonic generation (SHG) is one of the most researched nonlinear material properties and finds applications in many fields ranging from laser projection to cancer detection to future optical switches for molecular devices. Studying SHG in ZnO nanostructures started few years ago and there is a long way to go to compete with the existing nonlinear crystals. Information gathered over the past few years in research on SHG of ZnO nanowires (NWs) is summarized in this chapter. Recent advancement in the growth techniques for various types of ZnO NWs used for SHG studies is also discussed. We present an extensive analysis and discussion on some key parameters that directly modify the efficiency of SHG in ZnO NWs. The key parameters considered for discussion are aspect ratio of NWs, doping, and external strain. At the end, current standing on the reported values of nonlinear coefficients and future outlook are presented.

Keywords: second harmonic generation, sum frequency generation, ZnO, symmetry deviation

1. Introduction

ZnO is a unique material with application prospects in areas ranging from medical to optoelectronic industry to astronomical radiation detection [1–5]. ZnO is a II–VI group wide-band gap semiconductor and is highly transparent in the visible region. In the hexagonal wurtzite phase of ZnO, each Zn ion is surrounded by a tetrahedron of four O ions and vice versa. This tetrahedral coordination results in a noncentrosymmetric crystal structure, which makes it a promising candidate to observe second harmonic generation (SHG) in ambient conditions. SHG is a second-order nonlinear coherent process in which two lower energy photons are up-converted to a single photon with frequency exactly twice the incident frequency. This interesting property of nonlinear materials has several important applications in various fields, e.g., probing the electronic and magnetic structure of crystals, cancer cell diagnostics, switches in molecular-scale memory devices, and many more [6–10]. It is a very sensitive all-optical and noninvasive technique that is compatible with bulk or surface detection under various circumstances.

Among the huge variety of ZnO nanostructures, nanorods and nanowires (NWs) have undoubtedly been the focus of most studies since their geometries allow the preparation of arrays of well-controlled uniformity and use as building blocks of many nanoscale devices. As well as for ZnO thinfilms, SHG from ZnO NWs grown by different methods has been widely investigated. Studying SHG in ZnO NWs started few years ago and lot of information/knowledge has been gathered over the years by the nanoscale research community. Previous studies reported efficient generation of SHG signal from various types of ZnO nanostructures, including NWs [11–20]. Therefore, with improvement in the fabrication technique for large area ZnO NWs, it can be widely used as one of the best SHG materials. It has been discovered that the magnitude of SHG is strongly influenced by crystal orientation, aspect ratio, crystal symmetry modification, and so on. Therefore, by controlling such parameters one can tune the SHG of ZnO NWs. However, effective implementation of the knowledge gathered over the past years to ZnO to get the best SHG performance is yet to be achieved. Strategies for raising the optical nonlinearities of materials are an active research theme with rich and broad implications/applications. Keeping this in mind, some previous studies attempted to improve the second-order nonlinearity of ZnO and developed some efficient methodologies. Very high values of susceptibility tensorial component of 22–30 pm/V were achieved by changing the crystallographic orientation or decorating the surface with metal nanoparticles followed by bicolor coherent treatment or doping-induced crystal symmetry deviation [20–23]. Recently, development of ZnO-based SHG microscopy has been successfully demonstrated [24, 25].

Presently there is no review article dedicated to SHG of ZnO NWs with extensive analysis of SHG parameters and up-to-date advancement in this field. In this chapter, we present an extensive review of recent advances in SHG from ZnO NWs including our own results. Following this brief introduction, crystal structure of ZnO and theoretical background of SHG from ZnO and nonvanishing second-order nonlinear tensorial components are presented in Section 2. Section 3 describes the methodology adopted to measure SHG and an extensive analysis of the associated susceptibility tensor components. Recent advancement in the growth techniques for various types of ZnO NWs used for SHG studies and their SHG characteristics is discussed in the next section. The effects of aspect ratio of NWs, doping, and external strain on SHG magnitude are extensively addressed in subsections. At the end, a summary of the current standing on the reported values of nonlinear coefficients and future outlook are presented.

2. Second harmonic generation

SHG is one of the most studied material properties since its discovery in the 1960s by Franken et al. [26]. It is also known as the sum frequency generation because of the frequency doubling effect. When a strong primary radiation beam (frequency ω) is fed into the NLO crystal, along with the transmitted primary beam an additional light beam (frequency 2ω) appears from the crystal with frequency twice that of the primary beam. In other words, wavelength of the SHG signal is exactly half of the wavelength of the incident primary beam. **Figure 1** depicts the schematic illustration of nonlinear optical process SHG. Most often, the polarization field is considered to be linearly related to the incident electric field

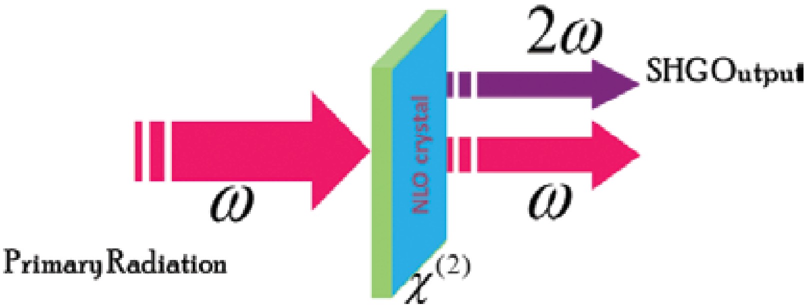

Figure 1. Schematic diagram of SHG in NLO crystal.

$$\vec{P} = \epsilon_0 \chi \vec{E} \tag{1}$$

where the electrical susceptibility, χ is a second-rank tensor. While this consideration tends to be sufficient when relating incident fields at low field strengths, it is a simplified approximation. In reality, the polarization field is more complicated than the linear relation given above. If the variation is small under strong electric field, comparable to interatomic electric fields, the polarization can be exactly expressed with the help of Taylor series

$$P_i = \epsilon_0 (\chi_{ij}^{(1)} E_j + \chi_{ijk}^{(2)} E_j E_k + \chi_{ijkl}^{(3)} E_j E_k E_l + \ldots) \tag{2}$$

where terms are summed over repeated indices. The first coefficient $\chi_{ij}^{(1)}$ is the linear electric susceptibility component. The $\chi_{ijk}^{(2)}$ and $\chi_{ijkl}^{(3)}$ are second-order and third-order nonlinear susceptibilities responsible for SHG and third harmonic generation phenomenon. The second-order susceptibility tensor is also expressed in terms of nonlinear optical coefficients, $d_{ijk} = \frac{1}{2}\chi_{ijk}^{(2)}$. SHG arises only when the particular material has nonzero second-order susceptibility tensor, $\chi_{ijk}^{(2)}(-2\omega, \ \omega, \ \omega)$. The nonzero components exist only in the noncentrosymmetric crystal structure of the particular material. Furthermore, nanometer-sized centrosymmetric materials (nanostructures) also show weak SHG due to the breaking of space inversion symmetry at the boundary [27, 28].

The crystal structures shared by ZnO are wurtzite, zinc blende, and rocksalt; however, in ambient condition, only the wurtzite phase is thermodynamically stable. The wurtzite structure has a hexagonal unit cell with two lattice parameters, *a* and *c*, in a ratio of *c*/*a* = 1.633 and belongs to the space group of C6*v*4 or *P*63*mc*. The hexagonal lattice of ZnO is characterized by two interconnecting sub-lattices of Zn^{2+} and O^{2-}, such that each Zn ion is surrounded by a tetrahedron of O ions, and vice versa, which is shown in **Figure 2**. The tetrahedral coordination in ZnO results in noncentral symmetric structure. Another important characteristic of ZnO is the polar surfaces. The most common polar surface is the basal plane. The oppositely charged ions produce positively charged Zn-(0001) and negatively charged O-$(000\bar{1})$ polar surfaces, resulting in a normal dipole moment and spontaneous polarization along the *c*-axis. The (001) polar face along the *c*-axis is the primary growth orientation of ZnO.

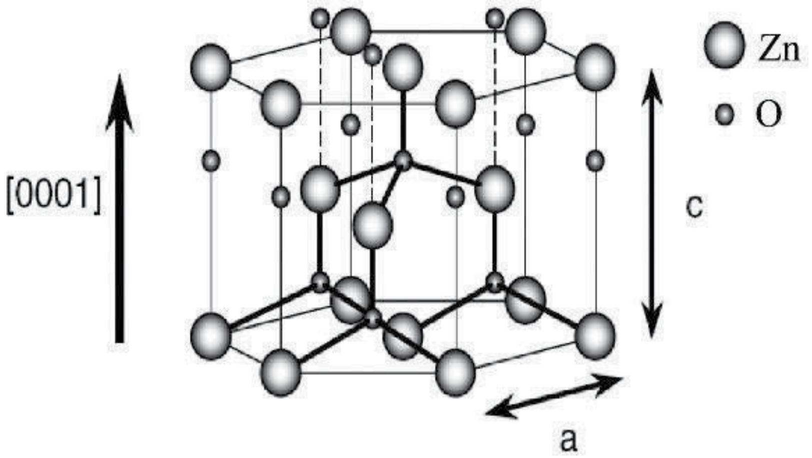

Figure 2. The wurtzite crystal structure model of ZnO having lattice constants *a* in the basal plane and *c* in the basal direction.

As a consequence of noncentrosymmetric crystal structure, ZnO possess nonvanishing second-order susceptibility tensor. The *c*-axis-grown vertically aligned ZnO NWs present five nonvanishing second-order susceptibility tensor elements, which are governed by point group symmetry of wurtzite crystal structure. The values of these second-order tensors or nonlinear optical coefficients are represented in pm/V. Five nonvanishing susceptibility tensorial components are $\chi_{15}^{(2)}$, $\chi_{24}^{(2)}$, $\chi_{31}^{(2)}$, $\chi_{32}^{(2)}$ and $\chi_{33}^{(2)}$ or equivalent in nonlinear optical coefficients d_{15}, d_{24}, d_{31}, d_{32}, and d_{33}. The point group symmetry *P*63*mc* of ZnO further reduces the nonvanishing terms to three components, d_{15} ($d_{15} = d_{24}$), d_{31} ($d_{31} = d_{32}$), and d_{33}. In ideal wurtzite structure, Kleinman's symmetry rule can be applied in a condition where the SHG wavelength is far from the absorption resonance. Within this approximation, $d_{15} = d_{31}$ is allowed and the number of independent d_{ij} terms further reduces to two.

3. Measurement technique and methodology

Since its introduction, several experimental techniques have been developed to calculate the magnitude of nonvanishing macroscopic nonlinear coefficients. Out of several techniques, the Maker fringes technique [29] is widely used to determine the magnitude of second-order susceptibility tensor elements. In brief, an SHG signal transmitted through the nonlinear crystal was measured as a function of angle of incidence of the fundamental beam with respect to the sample plane. This method is based on analysis of variation of SHG magnitude by incidence angle of the fundamental beam and crystal thickness. A schematic block diagram of the standard Maker fringes-based SHG measurement setup is shown in **Figure 3**. To generate SHG signal, we used an 800 nm, mode-locked femtosecond pulse light source from Ti:sapphire laser as a primary radiation. The polarization state of the fundamental beam and SHG signal are selected by using a polarizer ($\lambda/2$ plate) before the sample and an analyzer after the sample. The laser beam is tightly focused on the sample using suitable mirrors and lens assembly. The

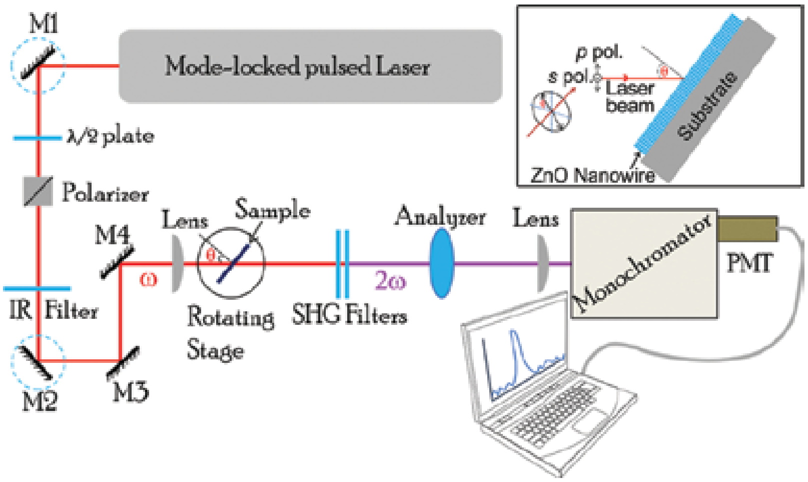

Figure 3. Schematic block diagram of SHG measurement setup according to the Maker fringes technique. Inset shows the ZnO nanowire film with the incident laser beam. θ and ϕ represent the incident angle and polarization angle of the laser beam, respectively.

variation of angle of incidence (θ) is achieved by placing the sample on a rotating stage. The generated SHG signal is analyzed using a monochromator and a highly sensitive detector. The angular dependence of SHG signal is measured either in P-in/P-out (*p-p*) or in S-in/P-out (*s-p*) polarization configuration.

The original Maker fringes methodology was based on the assumption of 100% transparency of the material in the SHG wavelength region. It is perfectly applicable only to a 100% transparent crystal. However, none of the real crystals are perfectly transparent up to that level. The original Maker fringes methodology failed to correctly estimate magnitude of the second-order d_{ij} values and large errors occur for absorbing materials. To take into account the absorption effect of the crystal in fundamental (ω) and SHG (2ω) wavelength regions, Herman and Hayden [30] presented a modified version of Maker fringes equation. According to Herman et al., the intensity of the second harmonic signal of Maker fringes, when the sample has significant absorption in the SHG wavelength region, is given by

$$
\begin{aligned}
&\mathrm{P}_{2\omega}^{x-p}(\theta,\lambda) = \frac{128\pi^3}{\mathrm{cA}}\frac{[\mathrm{t}_{\mathrm{af}}^{\omega}]^4[\mathrm{t}_{\mathrm{fs}}^{2\omega}]^2[\mathrm{t}_{\mathrm{sa}}^{2\omega}]^2}{\mathrm{n}_2^2\mathrm{c}_2^2}\left(\frac{2\pi\mathrm{L}}{\lambda}\right)^2 \mathrm{d}_{\mathrm{eff}}^2\,\mathrm{P}_{\omega}^2 \times \exp[-2(\delta_1+\delta_2)]\frac{\sin^2\psi+\sinh^2\chi}{\psi^2+\chi^2}\\
&\psi = \left(\frac{2\pi L}{\lambda}\right)(n_1c_1 - n_2c_2)\\
&\delta_1 = \left(\frac{2\pi L}{\lambda}\right)\left(\frac{n_1\kappa_1}{c_1}\right), \delta_2 = \left(\frac{2\pi L}{\lambda}\right)\left(\frac{n_2\kappa_2}{c_2}\right), \chi = \delta_1 - \delta_2\\
&[\mathrm{t}_{\mathrm{af}}^{\omega}] = \begin{cases} \dfrac{2cos\theta}{c_1 + n_1cos\theta}, & x = p\\ \dfrac{2cos\theta}{n_1c_1 + cos\theta}, & x = s \end{cases}, [\mathrm{t}_{\mathrm{fs}}^{2\omega}] = \frac{2n_2c_2}{n_{2s}c_2 + n_2c_{2s}}, [\mathrm{t}_{\mathrm{sa}}^{2\omega}] = \frac{2n_{2s}c_{2s}}{n_{2s}cos\theta + c_{2s}}
\end{aligned}
\tag{3}
$$

where $[\mathrm{t}_{\mathrm{ij}}^{\mathrm{k}}]$ are the Fresnel transmission coefficients of fundamental (ω) and SHG (2ω) wavelength regions at different interfaces; *af*—air to film, *fs*—film to substrate and *sa*—

substrate to air. c and A are velocity of light and the area of the laser beam spot; P_ω and $P_{2\omega}$ are the power of the incident beam and the SHG output; L is the thickness of the film. Remaining terms in Eq. (3) arise from the absorption of ZnO and phase mismatch parameter (Ψ). The complex refractive index is $n_m = n_m(1+ ik_m)$ and $c_m = (1-(1/n_m)^2 \sin^2\theta)^{1/2}$. Subscripts 1, 2 are the fundamental beam and second harmonics, respectively. Finally, the term d_{eff} represents effective optical nonlinear coefficient, arising from the second-order nonlinear optical tensor. The general expression for d_{eff} is a bit complicated, being dependent on the polarization states of both first and second harmonic electric fields, respectively, and, of course, on the angle of incidence of the fundamental beam. Considering the ZnO group symmetry and Kleinman's symmetry approximation, the final expressions for d_{eff} for p and s polarization configurations are,

$$d_{eff} = \begin{cases} 2d_{31}c_1c_2 sin\theta/n_1 + d_{31}c_1^2 sin\theta/n_2 \; + \; d_{33}sin^3\theta/n_1^2 n_2, & x = p \\ \dfrac{d_{31}sin\theta}{n_2}, & x = s \end{cases} \tag{4}$$

Therefore, at a monochromated fundamental beam of fixed wavelength (λ), the intensity of the SHG in Eq. (3) can be simplified as a function of θ only. After fitting Eq. (3) into the measured SHG profile as a function of angle of incidence, one can estimate the associated d_{eff} value. In s-p configuration, d_{eff} depends only on d_{31}. By fitting the SHG signal data, one can obtain the value of the coefficient d_{31} which can be introduced into data fitting in the p-p configuration to calculate d_{33}. In another way, the d_{eff} value can be more accurately estimated by considering Eq. (3) as a function of wavelength (λ) only [14, 20]. This method minimizes error due to the Gaussian profile broadening of the fundamental beam with finite full width at half maximum (FWHM). At a fixed incident angle (θ), Eq. (3) can be adapted in the given form

$$\mathrm{P}_{2\omega}^{p-p}(\lambda) = [\mathrm{P}_{2\omega(\lambda)}^{p-p}]'\mathrm{P}_{\omega(\lambda)}^2 \left(\frac{2\pi \mathrm{L}}{\lambda}\right)^2 \mathrm{d}_{\mathrm{eff}}^2 \tag{5}$$

where $P_{\omega(\lambda)}$ is the relative power of the primary beam at a particular wavelength, λ.

Alternative to Maker fringes experimental configuration, the reflective second harmonic generation (RSHG) scheme involves the measurement of the SHG signal in reflection mode, at a fixed incidence angle and as a function of the azimuthal angle, which is the angle between the incidence plane and the x-axis on the sample surface. In brief, the sample is rotated along its surface normal, *i.e.*, along the z-axis, while the reflected SHG signal is systematically measured. The RSHG signals originating from the symmetry of ZnO crystal as a function of the azimuthal angle ϕ are given by

$$\mathrm{P}_{2\omega}^{x-p} = \begin{cases} d_{15}\mathrm{E}_0^2\hat{x} + \dfrac{1}{2}(\, d_{31} + d_{33})\mathrm{E}_0^2\hat{z}, & x = p \\ d_{31}\mathrm{E}_0^2\hat{z}, & x = s \end{cases} \tag{6}$$

The RSHG is independent of azimuthal angle, if the direction of ZnO (0002) is along the z-axis. However, a tilt of the ZnO (0002) direction may cause a variation of the resulting SHG on the azimuthal polar plot.

4. Second harmonic generation in ZnO nanowires

As a consequence of noncentrosymmetric structure, ZnO is expected to possess nonzero second-order optical nonlinearity parameters and hence room temperature SHG is expected. SHG from ZnO nanostructures including NWs has been experimentally demonstrated by several groups. Many efforts have been made to quantitatively estimate the second-order nonlinear coefficients of single ZnO NWs or ZnO NW arrays. A theoretical study on the estimation of SHG intensity from ZnO nanostructures was done by Attaccalite et al. [31]. The modified Maker fringes equation was employed by considering the dense NW arrays as a NW film. All the important experimental results on SHG of ZnO NWs are summarized in **Table 1**.

Chan et al. [13] show room temperature SHG from ZnO NWs with angular dependence exactly similar to thinfilms. Vertically aligned ZnO NWs were grown on the ZnO-seeded glass substrate by low temperature aqueous chemical solution method, which is shown in **Figure 4 (a)**. Following the reaction at 90°C, glass substrates were rinsed with de-ionized water to remove the residual salt on the surface, and then dried at 100°C. The average length of the ZnO NWs ranged from 50 to 700 nm. A Q-switched Nd:YAG laser was used as fundamental incident beam (λ = 1064 nm, 8 ns) at 10 Hz frequency. SHG signal from samples was detected by a photo-multiplier tube and then further processed with a signal-integrating oscilloscope. The variation of SHG intensity with the angle of incidence depicts periodic profile and obeys the Maker fringes methodology (**Figure 4(b)**). The second-order coefficients d_{31} and d_{33} were estimated after fitting to the experimental angular variation of SHG data by Maker fringes Eq. (3) and were found to be $d_{31} = 1.28$ and $d_{33} = -15.7$ pm/V.

The nonlinear second-order coefficients, d_{ij} can also be estimated precisely in another way by fitting the experimental SHG data with Maker fringes Eq. (5) [14, 20, 32]. The SHG signal was measured at fixed incidence angle, where SHG is maximum as a function of wavelength within the range of Gaussian beam profile. Broadband frequency-doubling properties of *c*-axis-oriented ZnO NW arrays grown by low-temperature chemical bath deposition method on glass substrate were investigated by Das et al. [14]. The measured spectral profile of SHG was found to be in good agreement with theoretical simulations. The generated SHG signals were analyzed using a spectrometer at pumping wavelength of 806 nm (Ti:sapphire laser oscillator at pulse durations ~13 fs and spectral FWHM ~100 nm) and pump intensity of 5.5×10^{10} W/cm^2. The maximum effective nonlinearity was found to be $d_{\text{eff}} = 15$ pm/V, which is about 7.5 times higher than that of a type-I beta-barium borate (BBO) crystal. Changes in the growth parameters in the chemical bath deposition also result in an improvement in the SHG intensity [41].

Our group used similar theoretical fitting method to retrieve the d_{eff} by measuring SHG signal as a function of wavelength. We prepared dense and *c*-axis-oriented ZnO NWs onto quartz substrate by modified aqueous chemical method as shown in **Figure 5(a)** [20]. Highly crystalline ZnO NWs with diameters of 70–100 nm and length of few microns were grown perpendicular to the substrate. The SHG signal was measured by passing a linearly polarized femtosecond pulse beam (at 800 nm) from a mode-locked Ti:sapphire laser through the sample and analyzing in a spectrometer with a spectral resolution of 0.2 nm. At an incident angle (θ) of 0° *i.e.*, when the incident beam is perpendicular to the substrate plane, the magnitude of

Growth technique	**Substrate**	**Laser source**	**Aspect ratio**	d_{ij} **(pm/V)**	**Reference**
Sonication and dispersion	Sapphire	fs Laser @800 nm	–	$d_{31} = 1.36$ $d_{33} = -14.3$	Wang et al. [33]
Chemical vapor deposition	Sapphire	fs Laser @800 nm	–	$\chi_{eff}^{(2)} = 5.5$	Johnson et al. [34]
Aqueous solution method	Glass	ns Laser @1064 nm	5.7 10.8	$d_{31} = 0.14$ $d_{33} = 7.8$ $d_{31} = 2.88$ $d_{33} = 18.0$	Chan et al. [13]
Low temperature chemical bath method	Glass	fs Laser @806 nm	23.2 14.7 10.7	$d_{\text{eff}} = 15.0$ $d_{\text{eff}} = 2.0$ $d_{\text{eff}} = 3.2$	Das et al. [14]
Aqueous solution method	–	fs Laser @810 nm	–	$d_{31} = -3.0$ $d_{33} = 0.56$ $d_{33} = 0.86$	Green et al. [35]
Chemical bath deposition	Glass	fs Laser @800 nm	8	$d_{31} = -31.4$ $d_{33} = 2.56$	Das et al. [36]
Hydrothermal method	ITO coated glass	fs Laser @1034 nm	6.0 13.2	$d_{31} = 0.29$ $d_{33} = -1.38$ $d_{31} = 0.99$ $d_{33} = -9.53$	Zhou et al. [37]
Chemical vapor deposition	Si	fs Laser @800 nm	–	$d_{15} = 10.2$	Liu et al. [38]
Modified aqueous chemical method, Europium doping	Quartz	fs Laser @800 nm	–	$d_{\text{eff}} = 12.57$ $d_{\text{eff}} = 19.09$ after 1% doping	Dhara et al. [20]
Aqueous solution method	Glass	fs Laser @1044 nm	10.0	$d_{33}/d_{31} = 1.11$	Liu et al. [39]
Hydrothermal synthesis, Co doping	Glass	fs Laser @1044 nm	15.5	$d_{31}/d_{31(\text{undoped})} = 1.17$ $d_{33}/d_{33(\text{undoped})} = 2.34$	Liu et al. [40]

Table 1. Summary of SHG results of ZnO NWs.

SHG is almost zero. Then SHG increases with the changes in the tilting axis of the substrate and shows a maximum at an incident angle of –55°, as expected. The polarization dependence of SHG shows a periodic variation (periodicity π for P-in/P-out and π/2 for S-in/P-out) with changes in the degree of polarization of the incident beam. The incident laser power dependence on the SHG intensity increases with the increase in incident laser power and shows very good linearity with power dependence factor of ~1.91 ± 0.02, very close to the reported value (2.02 ± 0.10) for the bulk ZnO crystal [18]. Therefore, the SHG output closely follows the ideal square law dependence on the incident laser power. **Figure 5(b)** shows measured SHG spectral profile of the as prepared ZnO NWs in P-in/P-out polarization configuration at an angle of incidence (θ) of 50°. The estimated second-order nonlinear coefficient (d_{eff}) was found to be 12.57 ± 0.04 pm/V, which is larger than the reported results from ZnO thinfilms [12, 42, 43].

The microscopic SHG mapping of a single ZnO NW was measured for the first time by near-field scanning optical microscopy (NSOM) [34]. For NSOM studies, ZnO NWs were removed

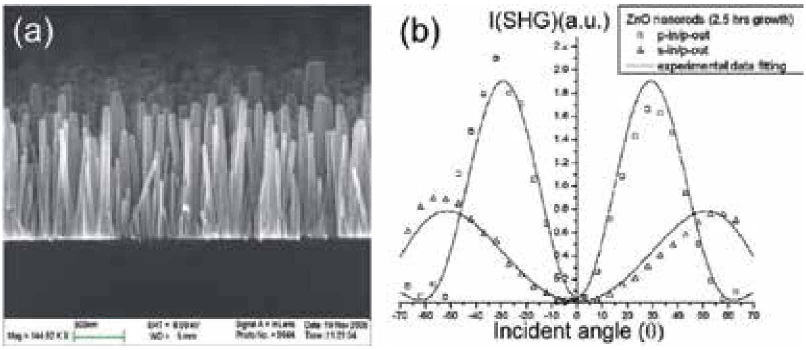

Figure 4. (a) Side-view SEM image of the ZnO nanorods/nanowires grown by aqueous chemical solution method. SHG vs. incident angle (θ) of ZnO nanorods in s-in/p-out and p-in/p-out configurations and their experimental data fittings according to the Maker fringes method. Reproduced with permission from Chan et al. [13] © Springer-Verlag 2006.

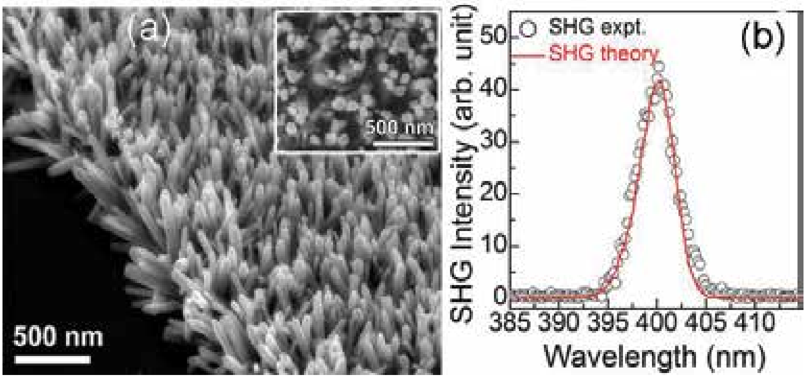

Figure 5. (a) FESEM image (tilted view) of the chemically grown vertically aligned undoped ZnO NWs. Inset shows the top view image of the same ZnO NWs. (b) Spectrum of the measured SHG signal (circle) of the ZnO NWs and theoretical fit (red line). Reproduced with permission from Dhara et al. [20] © IOP Publishing Ltd 2014.

from the substrate by sonication and dispersed onto a flat sapphire substrate for NSOM studies. Near-field SHG wave was collected using a scanning fiber probe at an oblique angle (θ, angle between the surface normal and the fundamental beam k-vector) of 55°. A large nonlinear SHG response with asymmetric variation across the diameter of the NW was presented (**Figure 6**). Furthermore, a strong polarization dependence was evidenced by the SHG images, which is ascribed to the asymmetry of the nonlinear susceptibility. The NW shows relatively efficient SHG with a larger $\chi_{eff}^{(2)} = 5.5$ pm/V than a BBO crystal, $\chi_{eff}^{(2)} \approx 2.0$ pm/V, a commonly used frequency doubling crystal. However, the estimated highest coefficient ($\chi_{33}^{(2)}$) is considerably lower than the reported bulk value (14.3 pm/V) [33]. One of the possible reasons for lower value is that the number of ZnO molecules probed for a single NW is less than those probed on a solid disk.

Studying SHG sometimes allows us to use a contactless surface as investigation tool to identify structural defects. Similar to thinfilms, if twin defects are present in the NWs, it can be experimentally investigated using SHG mapping to the individual rods [44]. The ZnO rods were grown on fused quartz by the aqueous solution method. The rods (length of several microns and diameter of 100–250 nm) were grown horizontally to the substrate where the polar axes of rods are parallel to the surface of fused quartz, as shown in **Figure 7(a)** and **(b)**. The SHG signal was generated using a mode-locked femtosecond pulse Ti:sapphire laser at approximately 810 nm. The transmitted SHG signals were measured under normal incidence with the polarization direction along the rod's axis. The far-field scattering patterns of the

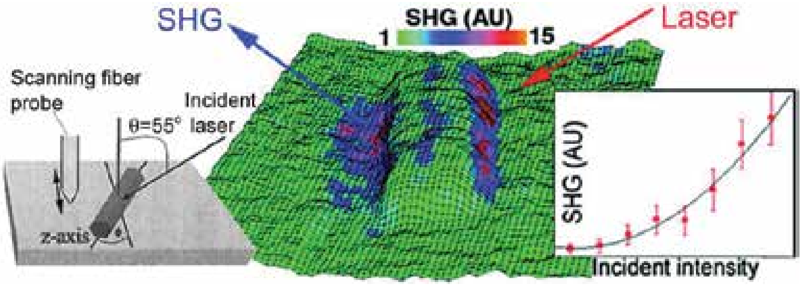

Figure 6. Near-field SHG image of single ZnO NW measured by NSOM. Insets show the illustration of the sample/beam geometry and incident laser power dependence of the SHG signal. Reproduced with permission from Johnson et al. [34] © American Chemical Society 2002.

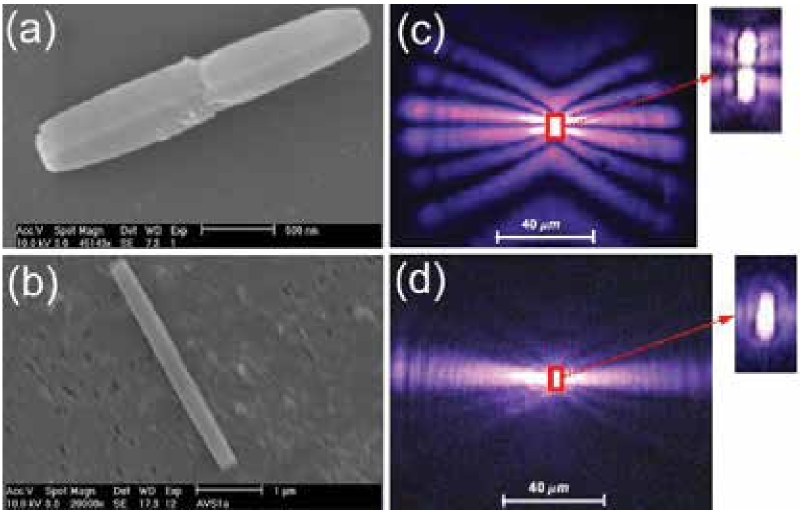

Figure 7. SEM images of two typical ZnO nanowires. (a) ZnO nanowire with twinning boundary structure and (b) ZnO nanowire without the twinning structure. SHG images and scattering patterns for single, (c) twinned ZnO nanowire of length 3.8 μm and (d) twin-free ZnO nanowire of length 1.5 μm. The insets show the enlarged view of above SHG images. Reproduced with permission from Liu et al. [44] ©The American Physical Society 2008.

transmitted SHG waves from single twinned rod were compared to the pattern arising from a twin-free ZnO rod to see if it is possible to differentiate between twinned and twin-free ZnO rods. **Figure 7(c)** and **(d)** shows typical SHG image for a single rod with twinned and twin-free structure, respectively. The images exhibit strong far-field scattering fringes resulting from the interferences of the SHG waves originating from different locations along the axis of the rod. Interestingly, a clear striking difference in the SHG fringes pattern was observed between SHG mapping images of twinned and twin-free rods. In particular, the zero-angle fringes highlight the different features of the two kinds of rods; a bright spot of SHG with a small dark gap for the twinned rod and very wide bright spot with no dark gap for the twin-free rods. A dark (bright) fringe at the 0° scattering angle was ascribed to destructive (constructive) interference of the SHG waves originating from each halve of the twinned (twin-free) rods. A small dark gap with low SHG efficiency (dark fringe) was observed only in the twinned rod, which indicates the existence of twin defects. Furthermore, use of polarization-dependent SHG microscopy to efficiently detect the lattice distortion in single-bent ZnO NWs has been demonstrated [25].

From SHG studies, it is found that SHG signal from bulk ZnO or even ZnO nanostructures is not so strong for application purpose. The reported value of an effective second-order tensorial component varies from 2 to 15 pm/V. However, it could be improved further by proper control of its crystal structure and disturbing crystal symmetry. Many studies have shown dependence of nonlinear parameters on various factors (internal or external to ZnO NWs) and also demonstrated several methods to improve the SHG further. Effects of some of the important parameters on the SHG are discussed in the following subsections. Recent advancement suggests that it is possible, in principle, for the researchers to identify the crystalline orientation, symmetry deviation, and polarities in more complicated ZnO nanostructures by the SHG patterns.

4.1. Wavelength dependence

When SHG was measured near the resonance region of ZnO, in most of the studies SHG signal was detected along with two-photon photoluminescence (2PL). Considering the different nonlinear mechanisms of both the process, final output intensities strongly depend on both pumping wavelength and light intensity. Competition between SHG and 2PL was observed and explained in several works [45–48]. Measuring emitted light as a function of fundamental beam wavelength is a useful way to distinguish the different contributions of SHG and 2PL to the emission spectrum. SHG wavelength changes according to the change in fundamental beam wavelength, while the wavelength of 2PL is fixed by the ZnO band gap energy. The competition between SHG and 2PL as a function of pump wavelength was described by Pedersen et al. [45] in randomly oriented ZnO NWs (**Figure 8(a)**). The monochromator was scanned over a broad region around SHG wavelength for a wide spectral range from 710 to 1000 nm. The contour plot that depicts the structure with highest intensity is the SHG signal at half the pump wavelength, while the weaker horizontal structure is multi-photon excited luminescence from the ZnO band gap. When the 2PL appears at shorter wavelengths than SHG (below the SHG line), it is presumably multiple-photon luminescence while the much stronger two-photon process is seen above the SHG line. The normalized $d_{\mathrm{eff},}$ retrieved from

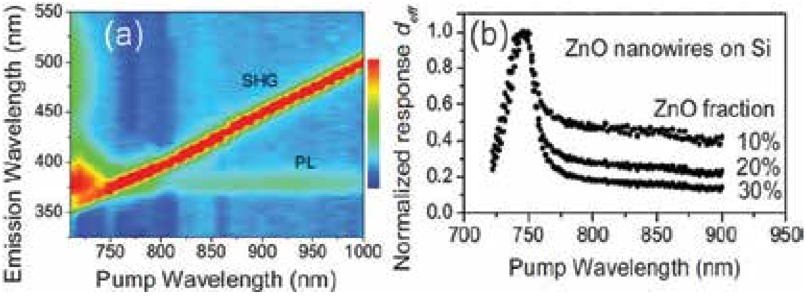

Figure 8. (a) Contour plot showing light emission intensity as a function of pump emission wavelength from ZnO nanowires. Structures due to SHG and multi-photon photoluminescence are marked. (b) Normalized effective nonlinear response of ZnO nanowires as a function of the pump wavelength. Reproduced with permission from Pedersen et al. [45] © WILEY-VCH Verlag GmbH & Co. KGaA 2008.

SHG profile in **Figure 8(a)** shows a strong wavelength-dependent behavior. At a pumping wavelength below two times of the band gap, d_{eff} gradually increases and reaches a maximum close to 760 nm and then varies slowly at higher pumping wavelength.

4.2. Dependence on aspect ratio

It is observed that the second-order nonlinear optical coefficients are strongly modified by dimensions of the NWs and aspect ratio. Chan et al. [13] and later Das et al. [14] demonstrated that changing of the aspect ratio of the ZnO nanorods could lead to a stronger SHG signal. ZnO NWs with different dimensions were grown by chemical method for different growth times, having diameter 10 to 62 nm and length 57 to 667 nm, respectively. Influence of aspect ratio on d_{31} and d_{33} is shown in **Figure 9** with aspect ratios ranging from 5.7 to 10.8. Interestingly, both the nonlinear second-order coefficients, d_{31} and d_{33}, were found to increase with increasing aspect ratio. The observed enhancement of d_{ij} is closely related to local field effects associated to the elongated nanorod structure. As we know, only d_{31} is excited when pumping beam is polarized along the rod's diameter. On the other hand, d_{33} being excited along the rod's longitudinal axis, the local field effect enhancement is predominantly connected to the rod's length. Similar effect on enhancement of d_{eff} was presented by Das et al. [14] for ZnO NWs with different length and diameters. Three different samples were grown with diameters 56, 59, and 95 nm and lengths 1300, 870, and 1020 nm, respectively. Calculated d_{eff} values are found to be 15.0, 2.0, and 3.2 pm/V, which is in correlation with the nanorod's length only. Later, a relationship between nanorod's diameter/length (aspect ratio) and corresponding $\chi^{(2)}$ values was established based on Lorentz local field, both theoretically and experimentally by Zhou et al. [37]. Theoretically, Lorentz local field-induced spectral red shift and the consequent dielectric constant modification were used to elucidate the size effect. The maximal value of $\chi_{31}^{(2)}$ of NW is the same as its bulk nonlinear susceptibility, while the maximum of $\chi_{33}^{(2)}$ of NW is significantly larger than its bulk counterpart. Therefore, the local field enhancement effect is more dominant along the longitudinal axis of NWs.

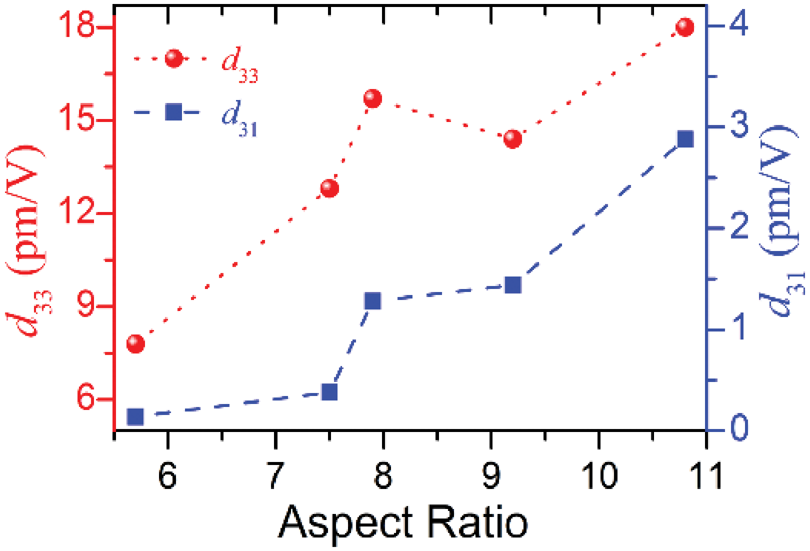

Figure 9. Dependences of d_{31} and d_{33} with the aspect ratio of ZnO nanowires.

4.3. The effect of doping

In order to improve the magnitude of the SHG in ZnO NWs, our group developed a technique to modify the crystal site symmetry of the ZnO crystal through rare earth element (Eu) doping [20]. We were able to improve the SHG about four times higher than the undoped ZnO NWs. That was the first ever report that used crystal symmetry modification technique to improve SHG. In the first step, Eu-doped ZnO (Eu:ZnO) NWs were grown vertically on the ZnO-seeded quartz substrate by a modified low temperature aqueous chemical method, using europium nitrate doping precursor. To facilitate the incorporation of larger Eu ions than the Zn ions into the ZnO lattice, a modification was done in the standard aqueous chemical method [49–52]. Eu doping was performed in a controlled way and a set of samples were prepared for different concentrations of Eu ranging from 0.5 to 5.0 at.%. Incorporation of Eu inside the ZnO lattice causes modification in the crystal site symmetry by disturbing the internal lattice arrangement. Extensive structural analysis using XRD data and high-resolution lattice images reveals expansion of lattice spacing and existence of several lattice distortions, as shown in the inset in **Figure 10**. Due to the larger ionic radius of Eu ions and the charge imbalance, incorporation of Eu completely disturbed the inside lattice arrangement. It is expected that the existence of a "self-purification process" [53] may further disturb the lattice arrangement. As a result, the formation of several lattice distortions in the Eu:ZnO NWs and hence degradation of structural quality and modification of site symmetry around the doped ions are expected.

The SHG intensity is found to increase after Eu doping. A nonmonotonic enhancement in the SHG is observed with increase in europium concentration. Maximum SHG was obtained from the 1 at.% Eu:ZnO NWs with an enhancement factor of 4.5. The effective second-order

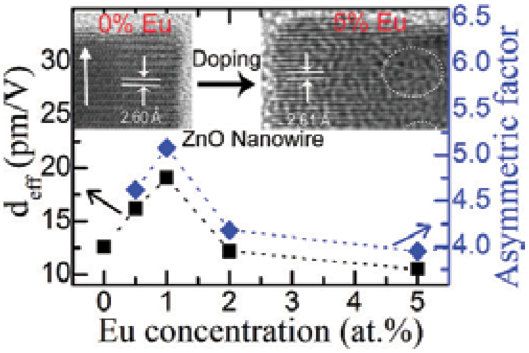

Figure 10. Plot of the d_{eff} and asymmetric factor (calculated from the PL intensity ratio) as a function of the Eu doping concentration for the Eu-doped ZnO nanowires. Inset shows high-resolution lattice image of the above undoped and 5 at.% Eu-doped ZnO NWs with growth orientation along <0001>. Formation of several lattice distortions in the Eu-doped ZnO nanowires is marked by dotted circles. Reproduced with permission from Dhara et al. [20] © IOP Publishing Ltd 2014.

nonlinear coefficient (d_{eff}) estimated from modified Maker fringes method is shown in **Figure 10** as a function of europium doping level. The highest d_{eff} (19.09 ± 0.11 pm/V) is obtained for the 1 at.% doped Eu:ZnO NWs, which is comparable to the value obtained by previous efforts to enhance the second-order susceptibility of ZnO thinfilms. Previous attempts to improve the second-order nonlinearity by changing the crystallographic orientation led to highest susceptibility ~30 pm/V [21] and decorating the surface with metal nanoparticles followed by bicolor coherent treatment led to the highest obtained susceptibility ~22.5 pm/V [54]. In comparison, our technique uses a simple process, whereas previous efforts were quite complicated from a technological point of view. Observed nonmonotonic enhancement was explained on the basis of Eu doping-induced symmetry deviation. The deviation in the crystal site symmetry (defined as the asymmetric factor) was estimated by employing photoluminescence (PL) spectroscopy and further supported by the microstructural characterizations. A strong correlation (linear dependence) is found between d_{eff} values and the magnitude of the asymmetric factor, which reveals that deviation in the local site symmetry around the Eu^{3+} ions in the Eu:ZnO crystal is the origin of the observed large second-order nonlinearity. Therefore, Eu doping on the ZnO NWs significantly influences the centrosymmetricity of the ZnO crystal, which results in an enhancement of the d_{eff} and hence SHG. This study opens up an avenue to improve the SHG of ZnO nanostructures through modification of local symmetry by incorporation of rare earth ions.

The effect of cobalt or thulium doping in ZnO NWs on the SHG characteristic was studied by other research group [40, 55]. Liu et al. [40] performed an SHG study after doping ZnO nanorods with cobalt. SHG was used to investigate bulk and surface structure quality of ZnO nanorods by measuring net dipole contribution for a different level of Co doping. Co-doped ZnO nanorods, $Zn_{1-x}Co_xO$ [$0 \leq x \leq 0.40$, x is the weight (wt.) % of Co in the growth solution], were fabricated by hydrothermal synthesis on seeded glass substrate. The SHG experiment was performed by varying incident angles in transmission mode (P-in/P-out configuration) with a femtosecond laser (1044 nm) light source. Ratios of d_{33} of Co-doped ZnO nanorods to the undoped ones are 2.34, 1.06, and 0.59 for Co concentration of 1, 15, and 35 wt.%, respectively. Similar analysis found d_{31} to be 1.17, 0.83, and 1.48 for Co concentration of 1, 15, and 35 wt.%, respectively. Dilute Co concentration (1 wt.%) leads to larger d_{33} coefficient with maximum enhancement that leads to enhancement in the bulk crystal quality of ZnO nanorods.

4.4. External strain dependence

As we know, second harmonic generation depends on the nonzero second-order susceptibility tensor, which indeed depends on the crystal symmetry of that material. Now the question arises, can we modify the SHG in ZnO by applying external strain? To verify this, our group investigated external strain (tensile and compressive) dependent SHG in ZnO NWs after bending the NWs by applying external force [56]. In the first step, ZnO NWs were transferred from substrate and dispersed into a PMMA solution. The solution mixture was spin coated on a thin steel substrate (thickness 0.5 mm) to prepare a thin layer (~200 nm) of PMMA with horizontally aligned ZnO NWs within it. The PMMA thinfilm was heated at ~60°C to remove residuals and get a continuous film. External force was applied at the center of the substrate (opposite side of the film) to bend it along the radius of curvature of the substrate. The bending of substrate led to bending of the attached ZnO NWs and it experienced a strain on the surface, as shown in the inset of **Figure 11**. The PMMA matrix was used to hold the ZnO NWs during bending of the substrate. Applied strain at the center of the substrate along the direction of the applied force was estimated according to the strain equation developed earlier [57, 58].

We measured RSHG at an angle of incidence of 45° using a *p* polarized fundamental femtosecond pulse light tightly focused at the center of the substrate. The RSHG signal in both the stretched side and compressed side of the ZnO NWs were measured with increasing strain and then with decreasing strain (**Figure 11**). Stretched side of the NWs experienced tensile strain whereas compressed side experienced compressive strain. With increasing tensile strain, the SHG intensity first increases up to a certain amount of tensile strain and then decreases to the initial value with further strain. The magnitude of SHG trace during release of tensile strain showed reproducible strain-dependent characteristic. Maximum enhancement was obtained

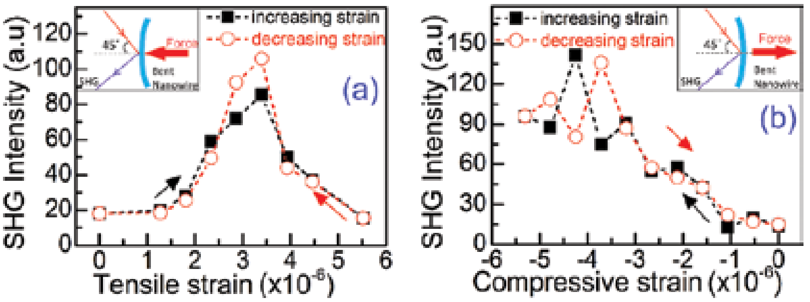

Figure 11. External strain-dependent RSHG intensity of bent ZnO NWs plotted as a function of (a) tensile strain and (b) compressive strain. SHG was measured by applying strain (black arrow, increasing strain) and then releasing strain (red arrow, decreasing strain). Insets show the measurement geometry of the bent ZnO NWs with external applied force (solid arrow).

about 400% at a tensile strain of 3.39×10^{-6}. On the other hand, SHG intensity gradually increases with increase in compressive strain. Reproducible SHG characteristic during release of compressive strain was also observed. At a compressive strain of 3.39×10^{-6}, obtained enhancement was about 430%. Therefore, SHG intensity in ZnO NWs could be enhanced and tuned through incorporation of external strain, either tensile or compressive.

5. Conclusion and future outlook

In this chapter, an up-to-date summary of important studies and results by several research groups worldwide on the SHG of ZnO NWs/nanorods is demonstrated. We present an extensive analysis and discussion on some key parameters that directly modify the efficiency of SHG in ZnO NWs. The key parameters considered for discussion are aspect ratio of NWs, doping, and external strain. Sample growth techniques, SHG measurement parameters, and extracted values of the nonlinear second-order coefficients from all the important studies are tabulated in **Table 1**. Most SHG studies are conducted on ZnO NWs with *c*-axis orientation (perpendicular to substrate) since their geometries allow to prepare *c*-axis–oriented vertically aligned structure, while only few studies deal with NWs with *c*-axis parallel to substrate. A significant advancement has been made in the improvement of nonlinearity of ZnO NWs, hence SHG intensity. Modified ZnO NWs now can compete with the existing standard nonlinear crystals. However, its needs further optimization and tailoring to get the maximum second-order nonlinearity. Fabrication of nonlinear optical devices using SHG characteristic of the ZnO NWs is certainly one of the future research directions.

Author details

Soumen Dhara[1]* and Stephen A. Lynch[2]

*Address all correspondence to: soumen5484@yahoo.co.in

1 Department of Condensed Matter Physics and Materials Sciences, S. N. Bose National Centre for Basic Sciences, Salt Lake, Kolkata, India

2 School of Physics and Astronomy, University of Cardiff, Cardiff, United Kingdom

References

[1] Kumar N, Dorfman A, Hahm J. Ultrasensitive DNA sequence detection using nanoscale ZnO sensor arrays. Nanotechnology. 2006;**17**:2875–2881

[2] Cui Y, Wei Q, Park H, Lieber CM. Nanowire nanosensors for highly sensitive and selective detection of biological and chemical species. Science. 2001;**293**:1289–1292

[3] Bano N, Zaman S, Zainelabdin A, Hussain S, Hussain I, Nur O, et al. ZnO-organic hybrid white light emitting diodes grown on flexible plastic using low temperature aqueous chemical method. Journal of Applied Physics. 2010;**108**:043103

[4] Fu X-W, Liao Z-M, Zhou Y-B, Wu H-C, Bie Y-Q, Xu J, et al. Graphene/ZnO nanowire/graphene vertical structure based fast-response ultraviolet photodetector. Applied Physics Letters. 2012;**100**:223114

[5] Johnson JC, Yan H, Schaller RD, Haber LH, Saykally RJ, Yang P. Single nanowire laser. The Journal of Physical Chemistry B. 2001;**105**:11387–11390

[6] Fiebig M, Pavlov VV, Pisarev RV. Second-harmonic generation as a tool for studying electronic and magnetic structures of crystals: Review. Journal of the Optical Society of America B. 2005;**22**:96−118

[7] Eisenthal KB. Second harmonic spectroscopy of aqueous nano- and microparticle interfaces. Chemical Review. 2006;**106**:1462–1477

[8] Campagnola P. Second harmonic generation imaging microscopy: Applications to diseases diagnostics. Analytical Chemistry. 2011;**83**:3224–3231

[9] Chen X, Nadiarynkh O, Plotnikov S, Campagnola PJ. Second harmonic generation microscopy for quantitative analysis of collagen fibrillar structure. Nature Protocols. 2012;**7**:654–669

[10] Castet F, Rodriguez V, Pozzo J-L, Ducasse L, Plaquet A, Champagne B. Design and characterization of molecular nonlinear optical switches. Accounts of Chemical Research. 2013;**46**:2656–2665

[11] Cao H, Wu JY, Ong HC, Dai JY, Chang RPH. Second harmonic generation in laser ablated zinc oxide thin films. Applied Physics Letters. 1998;**73**:572

[12] Griebner U, Kaindl RA, Elsaesser T, Seeber W. Frequency doubling and autocorrelation studies of 20-fs pulses using polycrystalline zinc oxide thin films. Applied Physics B. 1998;**67**:757–760

[13] Chan SW, Barille R, Nunzi JM, Tam KH, Leung YH, Chan WK, et al. Second harmonic generation in zinc oxide nanorods. Applied Physics B. 2006;**84**:351–355

[14] Das SK, Bock M, O'Neill C, Grunwald R, Lee KM, Lee HW, et al. Efficient second harmonic generation in ZnO nanorod arrays with broadband ultrashort pulses. Applied Physics Letters. 2008;**93**:181112

[15] Lo K-Y, Lo S-C, Yu C-F, Tite T, Huang J-Y, Huang Y-J, et al. Optical second harmonic generation from the twin boundary of ZnO thin films grown on silicon. Applied Physics Letters. 2008;**92**:091909

[16] Huang Y-J, Lo K-Y, Liu C-W, Liu C-C, Chu S-Y. Characterization of the quality of ZnO thin films using reflective second harmonic generation. Applied Physics Letters. 2009;**95**:091904

[17] Shi SL, Xu SJ, Xu Z-X, Roy VAL, Che C-M. Broadband second harmonic generation from ZnO nano-tetrapod. Chemical Physics Letters. 2011;**506**:226–229.

[18] Zheng CC, Xu SJ, Ning JQ, Zhang SF, Wang JY, Che CM, et al. Inner surface enhanced femtosecond second harmonic generation in thin ZnO crystal tubes. Journal of Applied Physics. 2011;**109**:013528

[19] Lu X, Zhou H, Salamo GJ, Tian ZR, Xiao M. Generation of exciton-polaritons in ZnO microcrystallines using second-harmonic generation. New Journal of Physics. 2012;**14**:073017

[20] Dhara S, Imakita K, Mizuhata M, Fuji M. Europium doping induced symmetry deviation and its impact on the second harmonic generation of doped ZnO nanowires. Nanotechnology. 2014;**25**:225202.

[21] Kityk IV, Ebothe J, Elchichou A, Addou M, Bougrine A, Sahraoui B. Linear electro-optics effect in ZnO–F film–glass interface. Physica Status Solidi B. 2002;**234**:553–562.

[22] Hyun JK, Kang T, Baek H, Oh H, Kim D-S, Yi G-C. Enhanced second harmonic generation by coupling to exciton ensembles in Ag-coated ZnO nanorods. ACS Photonics. 2015;**2**:1314−1319.

[23] Yang M, Shen S, Wang X, Yu B, Huang S, Xu D, et al. Plasmon-enhanced second-harmonic generation from hybrid ZnO-covered silver-bowl array. Journal of Physics: Condensed Matter. 2016;**28**:214003.

[24] Ren M-L, Agarwal R, Liu W, Agarwal R. Crystallographic characterization of II−VI semiconducting nanostructures via optical second harmonic generation. Nano Letters. 2015;**15**:7341−7346.

[25] Han X, Wang K, Long H, Hu H, Chen J, Wang B, et al. Highly sensitive detection of the lattice distortion in single bent ZnO nanowires by second-harmonic generation microscopy. ACS Photonics. 2016;**3**:1308−1314.

[26] Franken PA, Hill AE, Peters CW, Weinreich G. Generation of optical harmonics. Physical Review Letters. 1961;**7**:118.

[27] Rumpel A, Manschwetus B, Lilienkamp G, Schmidt H, Daum W. Polarity of space charge fields in second-harmonic generation spectra of Si(100)/SiO_2 interfaces. Physical Review B. 2006;**74**:081303.

[28] Jun B, White YV, Schrimpf RD, Fleetwood DM, Brunier F, Bresson N, et al. Characterization of multiple Si/SiO_2 interfaces in silicon-on-insulator materials via second-harmonic generation. Applied Physics Letters. 2004;**85**:3095–3097.

[29] Maker PD, Terhune RW, Nisenhoff M, Savage CM. Effects of dispersion and focusing on the production of optical harmonics. Physical Review Letters. 1962;**8**:21–22.

[30] Herman WN, Hayden LM. Maker fringes revisited: Second-harmonic generation from birefringent or absorbing materials. Journal of the Optical Society of America B. 1995;**12**:416–427.

[31] Attaccalite C, Nguer A, Cannuccia E, Gruning M. Strong second harmonic generation in SiC, ZnO, GaN two-dimensional hexagonal crystals from first-principles many-body calculations. Physical Chemistry Chemical Physics. 2015;**17**:9533–9540.

[32] Dhara S, Imakita K, Mizuhata M, Fujii M. Eu-doping induced improvement on the second harmonic generation of ZnO Nanowires. In: Jagadish C, editor. Materials Research Society Symposium Proceedings; 2014. pp. 95–100; DOI: 10.1557/opl.2014.367

[33] Wang G, Wong GL, Ketterson JB. Redetermination of second-order susceptibility of zinc oxide single crystals. Applied Optics. 2001;**40**:5436

[34] Johnson JC, Yan H, Schaller RD, Petersen PB, Yang P, Saykally RJ. Near-field imaging of nonlinear optical mixing in single ZnO nanowires. Nano Letters. 2002;**2**:279–283

[35] Geren K, Liu SW, Zhou HJ, Zhang Y, Tian R, Xiao M. Second-order susceptibilities of ZnO nanorods from forward second-harmonic scattering. Journal of Applied Physics. 2009;**105**:063531.

[36] Das M, Rana S, Sen P. Second harmonic generation in ZnO nanorods. The Journal of Nonlinear Optical Physics & Materials. 2010;**19**:445–458.

[37] Zhou G-Y, Hsu K-J, Su T-Y, Huang N-H, Chen Y-F, Chu S-W. Effect of Lorentz local field for optical second order nonlinear susceptibility in ZnO nanorod. Journal of Applied Physics. 2012;**111**:103112.

[38] Liu W, Wang K, Long H, Chu S, Wang B, Lu P. Near-resonant second-order nonlinear susceptibility in c-axis oriented ZnO nanorods. Applied Physics Letters. 2014;**105**:071906.

[39] Liu C-W, Chang S-J, Huang C-HHR-J, Lin Y-S, Su M-C, Wang P-H, et al. Probing surface structure quality of ZnO nanorods by second harmonic generation. IEEE Photonics Technology Letters. 2014;**26**:789–792.

[40] Liu C-W, Chang S-J, Brahma S, Hsiao C-H, Chang FM, Wang PH, et al. Enhancement in the structure quality of ZnO nanorods by diluted Co dopants: Analyses via optical second harmonic generation. Journal of Applied Physics. 2015;**117**:084315.

[41] Panda R, Bhattacharya S, Samal R, Singh A, Sahoo PK, Datta PK, et al. Second harmonic generation of femtosecond pulses using ZnO nanorods grown by chemical bath deposition with drop casted seed layer. Journal of Nonlinear Optical Physics & Materials. 2016;**25**:1650029.

[42] Kulyk B, Essaidi Z, Kapustianyk V, Turko B, Rudyk V, Partyka M, et al. Second and third order nonlinear optical properties of nanostructured ZnO thin films deposited on α-BBO and $LiNbO_3$. Optics Communications. 2008;**281**:6107–6111.

[43] Narayanan V, Thareja RK. Harmonic generation in ZnO nanocrystalline laser deposited thin films. Optics Communications. 2006;**260**:170–174.

[44] Liu SW, Zhou HJ, Ricca A, Tian R, Xiao M. Far-field second-harmonic fingerprint of twinning in single ZnO rods. Physical Review B. 2008;**77**:113311.

[45] Pedersen K, Fisker C, Pedersen TG. Second-harmonic generation from ZnO nanowires. Physica Status Solidi C. 2008;**5**:2671–2674.

[46] Prasanth R, Vugt LKV, Vanmaekelbergh DAM, Gerritsen HC. Resonance enhancement of optical second harmonic generation in a ZnO nanowire. Applied Physics Letters. 2006;**88**:181501.

[47] Zhang CF, Dong ZW, You GJ, Zhu RY, Qian SX, Deng H, et al. Femtosecond pulse excited two-photon photoluminescence and second harmonic generation in ZnO nanowires. Applied Physics Letters. 2006;**89**:042117.

[48] Das SK, Biswas M, Byrne D, Bock M, McGlynn E, Breusing M, et al. Multiphoton-absorption induced ultraviolet luminescence of ZnO nanorods using low-energy femtosecond pulses. Journal of Applied Physics. 2010;**108**:043107.

[49] Greene LE, Law M, Goldberger J, Kim F, Johnson JC, Zhang Y, et al. Low-temperature wafer-scale production of ZnO nanowire arrays. Angewandte Chemie International Edition. 2003;**42**:3031–3034.

[50] Xu S, Wang ZL. One-dimensional ZnO nanostructures: Solution growth and functional properties. Nano Research. 2011;**4**:1013–1098.

[51] Tak Y, Yong K. Controlled growth of well-aligned ZnO nanorod array using a novel solution method. The Journal of Physical Chemistry B. 2005;**109**:19263–19269.

[52] Dhara S, Giri PK. Ti nanoparticles decorated chemically grown ZnO nanowires: Photocurrent and photoluminescence properties. Journal of Experimental Nanoscience. 2013;**8**: 332–340.

[53] Gustavo MD, James RC. Self-purification in semiconductor nanocrystals. Physical Review Letters. 2006;**96**:226802.

[54] Ozga K, Kawaharamura T, Umar AA, Oyama M, Nouneh K, Slezak A, et al. Second order optical effects in Au nanoparticle-deposited ZnO nanocrystallite films. Nanotechnology. 2008;**19**:185709.

[55] Aloufy A, Ebothé J, Dumelié N, Chaki I, Abd-Lefdil M, AlZayed NS, et al. Optically stimulated optical effects in the ZnO:Tm nanorods. Physica E. 2015;**73**:96–99.

[56] Dhara S, Imakita K, Mizuhata M, Fuji M. External strain dependent anomalous second harmonic generation in ZnO nanowires film. (unpublish work).

[57] Liarokapis E, Papadimitriou D, Rumberg J, Richter W. Raman and RAS measurements of uniaxially strained thin semiconductor layer. Physica Status Solidi B. 1999;**211**:309–316.

[58] Zhao J-H, Chen Q-D, Chen Z-G, Jia G, Su W, Jiang Y, et al. Enhancement of second-harmonic generation from silicon stripes under external cylindrical strain. Optics Letters. 2009;**34**:3340–3342.

Chapter 3

Electrical Manipulation of a Single Nanowire by Dielectrophoresis

Marcos Vinicius Puydinger dos Santos, Fanny Béron,
Kleber Roberto Pirota, José Alexandre Diniz and
Stanislav Moshkalev

Additional information is available at the end of the chapter

http://dx.doi.org/10.5772/67386

Abstract

Nanowires (NWs), due to their unique highly anisotropic characteristics, hold a great promise to be used in wide technological fields, such as building blocks for data storage and memory, advanced scanning probes, and biotechnological applications. In addition, given the high sensitivity to their environment, NWs can be used as sensor for a number of applications. The fabrication and electrical characterization of NW-based devices can be achieved after proper placing of NWs between electrodes, which represents one of the major challenges in this field. The dielectrophoresis (DEP) method can be used to trap electrically neutral NWs by the application of an alternating electric field between a pair of electrodes. Here, we present a systematic study of DEP parameters as well as electrodes geometry for NW deposition. This method presents a suitable protocol for deposition in a useful and coherent fashion of post-growth electrodeposited NWs and further electrical characterization. This can be used for investigation of the fundamental transport properties of individual NWs and fabrication of NW-based devices, such as sensors and field-effect transistors.

Keywords: nanowire, dielectrophoresis, electrically-induced manipulation, electrical characterization

1. Introduction

Nanowires (NWs) represent adequate elements for electronic devices that require ultra-low power consumption, given their low current levels and high sensitivity they usually exhibit [1–5]. Their one-dimensional geometry, as well as unique possibilities for engineering of magnetic, electric and optic properties, make them to be promising nanostructures for a variety of applications, including chemical and biological sensors [6, 7], field-effect transistors [8], advanced scanning probes and magnetic sensors [9], light-emitting diodes [10], lasers [11] and photodetectors [12, 13]. Furthermore, NWs can be synthesized through a number of techniques, such as metal-organic epitaxy [14], focused-ion-beam (FIB) [8], focused-electron-beam-induced deposition (FEBID) [15], electron beam lithography [5] and electrodeposition [16, 17], yielding to unique attributes, such as particular crystallographic properties, geometry and axial/coaxial heterostructures [18].

However, despite significant advances that have been made in NWs synthesis and devices characterization, post-growth manipulation and placement of single NWs in a coherent and useful fashion remains one of the major challenges to fabricate and study the electrical transport properties of NW-based devices [19–21], especially the ones made of a single NW. So far, numerous techniques have been proposed to realize NW-based devices from already existing NWs assembly, such as atomic force microscopy nanomanipulation [22], Langmuir-Blodgett films [23], fluidic-directed assembly [24], dry-transfer printing [25], although with relatively low NW yield for precise positioning of functional system [18].

Alternatively, NWs suspended in a dielectric electrolytic solution can be manipulated through electric fields [1, 5, 26–31]. When an electrically neutral NW is subjected to a non-uniform electric field, the electric charges redistribution within the NW as well as in the solid-liquid interface builds up an electric dipole moment [32]. Thus, as the Coulomb forces on either sides of the dipole can differ in direction and intensity, a net force is exerted on the NW, which is known as the dielectrophoretic force [19, 27–32]. The force direction depends on the relative polarizabilities of the electrolyte and of the NW, inducing the latter move towards or against the region of higher electric field intensity. Such motion of nanoparticles is termed as dielectrophoresis (DEP) [19, 20, 26–32]. DEP has a tremendous advantage over the aforementioned techniques, as it relies on the possibility of working with NWs of a wide range of conductivities as well as arbitrary substrates including those that require low-temperature processing such as flexible substrates [18]. Since DEP directly depends on the dielectric properties of the particles and diluting medium, as well as the nanoparticles geometry, it allows high process selectivity [18, 32]. Moreover, large electrode arrays can be properly defined by lithography such that DEP can take place concomitantly in a large number of electrodes, leading to high throughput.

However, to fully realize these capabilities, DEP must be carefully controlled to ensure that wires are precisely placed at desired locations. Therefore, it is necessary to determine the relevant parameters that affect DEP experiment and how to control them. In this work, nickel nanowires (NiNWs) with length of around 4 μm and 35 nm of diameter, obtained by electrodeposition into pores of anodized alumina membrane and further dispersed in a dimethylformamide (DMF) electrolytic solution, were manipulated by DEP in order to make electrical contact between a pair of electrodes. Electrodes geometry and DEP electrical parameters were varied to evaluate the NiNW deposition efficiency by this technique. The materials for NW and diluting medium presented in this work were arbitrarily chosen to provide a proof-of-concept for the reader, though a selection of several NW materials and diluting medium is provided as well. In addition, COMSOL simulation supports experimental results on NWs deposition.

2. Dielectrophoresis

2.1. DEP theory

The electric force induced by non-uniform electric fields on polarizable and anisotropic nanoparticles can be used to properly align and trap individual liquid-suspended nanoparticles at predefined locations of a substrate. This force, termed as the DEP force, uses AC electric fields to selectively move neutral nanoparticles (e.g. NiNWs) dispersed in a dielectric diluting medium (e.g. DMF) (**Figure 1a**) [26, 32]. It relies on the polarizability differences between the NW and the DMF. The electrodes shape yields to a non-uniform electric field, which is proportional to the applied voltage. It creates a net force on the NW that exceeds the viscous force between the NW and the fluid, inducing a preferential NW movement towards the electrodes gap (**Figure 1b**). Although the discussion presented in this work considers only NW as example of particles, the analysis also applies to other anisotropic particles such as nanotubes, nanorods or sheets.

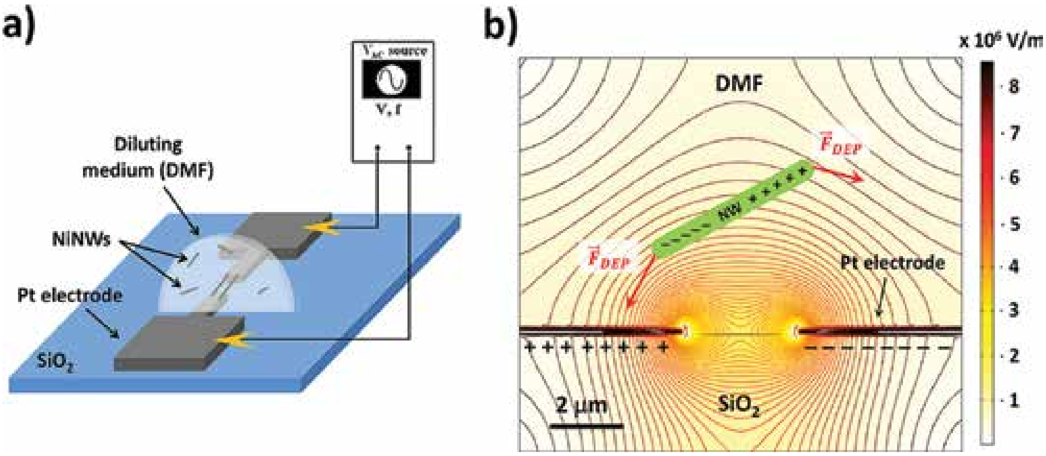

Figure 1. (a) Schematic of the DEP experiment. Adapted with permission from [33]. Copyright 2015 by American Vacuum Society. (b) DEP mechanism, in which the electric-field gradient induces attraction forces on the nanowire towards the gap between electrodes.

This force can be expressed by [5, 30, 33]

$$F_{\mathrm{DEP}} = \frac{1}{8}\pi\,\varphi^2 L\,\varepsilon_{\mathrm{DMF}}\,Re\{K\}\;\nabla\left|E\right|^2 \tag{1}$$

where φ and L represent, respectively, the NW diameter and length, *Re{}* is the real term and $K(\omega)$ the Clausius-Mossoti factor—or the so-called complex polarization factor—expressed as function of electrical permittivities of NiNW and DMF (respectively, $\varepsilon_{\mathrm{NiNW}}$ and $\varepsilon_{\mathrm{DMF}} = 36.7\,\varepsilon_0$, where ε_0 is the electrical permittivity of vacuum) [5]:

$$K(\omega) = \frac{\varepsilon^*_{\mathrm{NiNW}}(\omega) - \varepsilon^*_{\mathrm{DMF}}(\omega)}{\varepsilon^*_{\mathrm{NiNW}}(\omega) + 2\,\varepsilon^*_{\mathrm{DMF}}(\omega)}. \tag{2}$$

The imaginary component of the complex permittivity, ε^*, depends on the conductivity, σ, and the applied field angular frequency, ω:

$$\varepsilon^*(\omega) = \varepsilon - j\frac{\sigma}{\omega}. \tag{3}$$

Thus, the real-term frequency-dependent factor of the DEP force is given by

$$Re\{\mathrm{K}\} = \frac{\omega^2\left(\varepsilon_{\mathrm{DMF}}\,\varepsilon_{\mathrm{NiNW}} - \varepsilon_{\mathrm{DMF}}^2\right) + \left(\sigma_{\mathrm{DMF}}\,\sigma_{\mathrm{NiNW}} - \sigma_{\mathrm{DMF}}^2\right)}{\varepsilon_{\mathrm{DMF}}^2\,\omega^2 + \sigma_{\mathrm{DMF}}^2}. \tag{4}$$

The complex polarization factor's dependence on the permittivity introduces a relationship between the dielectrophoretic force and the frequency of the applied field. Eqs. (5) and (6) present the high- and low-frequency limits, respectively:

$$\omega \to \infty \ : Re\{\mathrm{K}\} = \frac{\varepsilon_{\mathrm{NiNW}} - \varepsilon_{\mathrm{DMF}}}{\varepsilon_{\mathrm{DMF}}} \tag{5}$$

$$\omega \to 0 : Re\{\mathrm{K}\} = \frac{\sigma_{\mathrm{NiNW}} - \sigma_{\mathrm{DMF}}}{\sigma_{\mathrm{DMF}}}. \tag{6}$$

At the high-frequency limit, the DEP force is determined by the relative permittivity of the NW and the DMF, while at low frequencies the force will be a function of their relative conductivities. Within this frequency range, the transition between those two regimes is evidenced by plotting the DEP force against frequency. Inserting the appropriate NW and diluting liquid electrical conductivities (respectively, $\sigma_{\mathrm{NiNW}} = 1.4 \times 10^7\ \Omega^{-1}\ \mathrm{m}^{-1}$ and $\sigma_{\mathrm{DMF}} = 2.5 \times 10^{-4}\ \Omega^{-1}\ \mathrm{m}^{-1}$) in Eq. (4), one may calculate the frequency-dependence of F_{DEP}, where a reduction of DEP force is observed for frequencies higher than 100 kHz (**Figure 2a**).

At 500 kHz and 1 MHz, the force approximately decreases by one and two orders of magnitude, respectively. However, this model does not consider fluid dynamics effects, such as

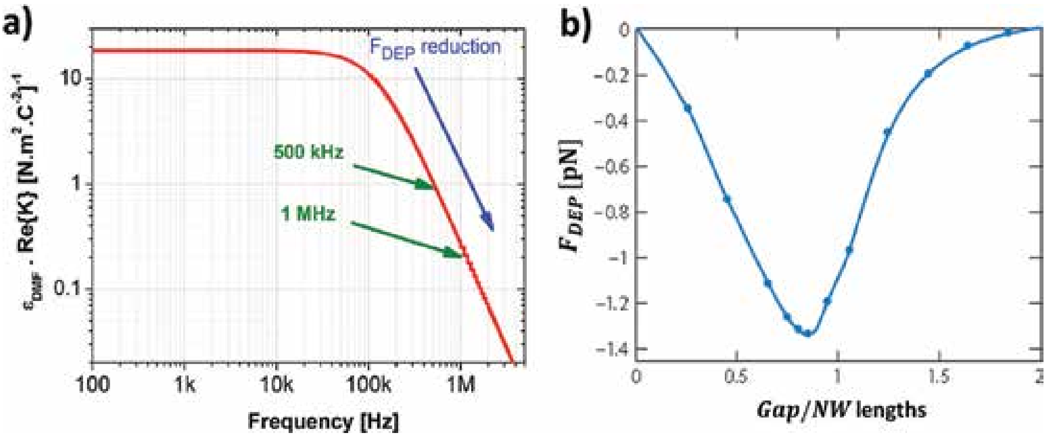

Figure 2. (a) Real part of the complex polarization factor (proportional to F_{DEP}), as function of frequency, for NiNW diluted in DMF medium, showing force reduction for frequencies above 100 kHz. Adapted with permission from [33]. Copyright 2015 by American Vacuum Society. (b) DEP force as function of the ratio between electrodes gap length and NW length, showing that the attraction force is maximized in the minimum of the force curve. Adapted with permission from [35]. Copyright 2012 by American Chemical Society.

AC electroosmosis [20]. For the electrostatics parameters of NiNW and DMF, this effect can reduce the force for frequencies above 1–10 kHz [19], as will be discussed in the next section. Other effects also act on the NW, such as viscous and frictional forces, fluid flow and NW-surface interactions [5, 34]. Therefore, the DEP force needs to overcome those effects in order to effectively perform deposition. Additionally, the DEP force will always depend on the ratio between the electrodes gap and NW lengths (**Figure 2b**), as this ratio influences the electric field lines density covering the NW and thus the applied torque [35]. The DEP force is maximized (attraction force, see in **Figure 2b**) for a ratio of around 0.8, since the electric field gradient and strength effects are the largest for this ratio [36]. For a smaller gap, the DEP force decreases because, despite that the electric field applied at the gap centre remains constant, it is reduced around the entire NW length. On the other hand, for a larger gap, the DEP force also decreases, simply because the electric field around the NW is less intense [5, 35, 36]. In this work, for NiNWs length of (4 ± 1) μm, we used a gap length of (2.5 ± 0.3) μm, yielding a ratio of (0.6 ± 0.2), which is near the maximum DEP force condition.

Furthermore, Eq. (1) exhibits a quadratic dependence of DEP force with the applied voltage, which increases the amount of deposited NWs in the gap region [5, 33]. In this work, we fixed the peak-to-peak voltage (V_{pp}) to 3 V, since it produces a reasonable DEP force without overheating and consequently damaging the NiNWs during DEP process.

Finally, although we have presented DEP analysis for NiNWs dissolved in a DMF solution, one might be interested in experiments involving NWs composed of different materials. Thus, we present **Table 1**, which provides an overview of reported parameters from the literature that optimizes DEP force.

Nanowire material	Medium	Potential (V)	Frequency (kHz)	Electrode gap (μm)	Electric field (V μm^{-1})
Au	Methanol	0.97	150	2	0.485
Au	Methanol	10	>100	2	5
Au-biotin	Methanol	0.18	1000	2	0.09
ZnO	Ethanol	5	1000	6–10	0.833–0.5
ZnO	Ethanol	5	1000	4	1.25
Ag	Ethanol	0.1	5	4	0.025
Ag or Au	H_2O or EtOH	0.2	100	30	0.00667
Rh rods	Acetone	10	Unknown	5–30	2–0.333
CNT[a]	Acetone	45	Unknown	5–30	9–1.5
p-Si	Benzyl alcohol	110	10	40	2.75
Si	IPA[b] and H_2O	0.35	0.5	2	0.175

[a] CNT, carbon nanotube.

[b] IPA, isopropanol.

Table 1. Overview of optimized parameters reported in literature for DEP alignment of different types of NW (adapted from [19]).

2.2. AC electroosmosis

Under the influence of an AC electric field, electrolytes on planar microelectrodes exhibit fluid flow tangential to the electrode surface. The Coulomb force generated from this electric field on the solution interfacial charges (**Figure 3a**) leads to fluid flow along the electrode surface away from the gap in a process termed AC electroosmosis [20, 37]. This effect is triggered by applying an alternating potential difference of the order of kHz at low voltages (around 1 V) to each pair of electrodes. It has been exploited in microfluidics to pump fluids in microcapillaries where surface forces preclude traditional pumping by pressure differentials.

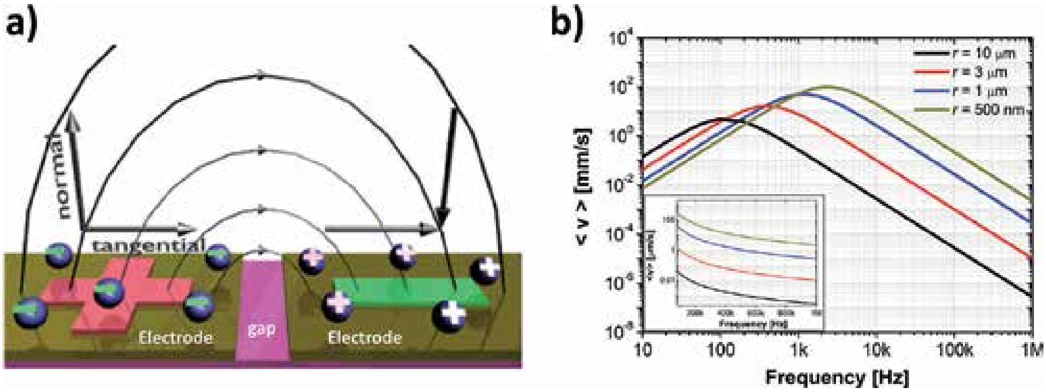

Figure 3. (a) Surface-bound interfacial charges (spheres), induced by electrodes, interact with the tangential component of electric field (curved lines), thus moving the fluid along the electrode surface away from the electrode gap. Field lines originating from the positively charged electrode and ending on the negatively charged one represent the force experienced by positive charge (negative charge experiences force in opposite direction). This force leads to fluid flow along the electrodes away from the gap. Adapted with permission from [20]. Copyright 2007 by American Chemical Society. (b) Average velocity of the fluid obtained for $V_0 = 3\ \mathrm{V_{PP}}$ for several distances from the electrodes gap centre. *Inset*: Frequency working range utilized in this work, in which the average velocity decreases about two orders of magnitude between 100 kHz and 1 MHz for any distance, *d*.

The physical mechanism responsible for driving the flow relies on non-uniformities in the AC electric fields at the gap region. They produce an electric force on the surface-bound interfacial charges, yielding a non-zero time-averaged electroosmotic slip velocity at the electrodes surface [38]. The AC electroosmotic effect can produce fluid velocities from hundreds of µm/s up to a few mm/s in some cases [20, 37]. It should be noted that this fluid flow is distinct from the one originated from electro-thermal effects, which are found at higher frequencies and higher electrolyte conductivities [38].

For symmetrical, coplanar microelectrode gaps such as those reported in this work, AC electroosmosis produces fluid flow along the electrode surface directed away from the centre of the electrode gap. The average fluid velocity near the electrode surface is given by [20, 37, 38]

$$\langle v \rangle = \frac{1}{8} \frac{\varepsilon_{\mathrm{DMF}} V_0^2 \Omega^2}{\eta d (1 + \Omega^2)^2}, \tag{7}$$

where d *is* the position along the electrodes surface with its origin at the gap centre, V_0 is the applied voltage between electrodes, η = 0.92 mPa s the electrolyte viscosity and the dimensionless frequency Ω is given by

$$\Omega = \omega d \frac{\varepsilon_{\mathrm{DMF}}}{\sigma_{\mathrm{DMF}}} \frac{\pi}{2} \kappa, \tag{8}$$

where $\kappa = (15\ \mathrm{nm})^{-1}$ is the reciprocal of electrolyte Debye length for induced double charge on the electrodes. Eq. (7) gives a bell-shaped profile for the frequency dependence of the velocity. The average velocity is small at both low and high frequencies. In the former case, most of the electric field relies in the interfacial charged layer between the electrode and the electrolyte, preventing the tangential field to extend very far into the solution. In the latter, the interfacial charged layer is thin because the charged species in the electrolyte are not fast enough to follow the rapidly changing polarities of the electrodes. On the contrary, at intermediate frequencies, the velocity can be considerably large [37]. **Figure 3b** shows average velocities of DMF for d = 500 nm, 1 μm, 3 μm and 10 μm from the electrodes gap centre, at 3 V. For these DEP conditions, the fluid velocity at the gap region will range from a few nanometres to tens of millimetres per second, depending on the frequency, which produces additional forces on the NWs and thus considerably influences NWs deposition.

3. Efficiency evaluation of DEP: a case study

In the next sections, DEP efficiency was evaluated for NiNW trapping on Pt electrodes, chosen due to the low-oxidation rate and relatively low-electrical resistivity that allows further two-wire electrical transport measurements on a single isolated NW. The DEP parameters, such as voltage and frequency, were varied in order to optimize the number of NWs that make contact between the electrodes, for which statistical evaluation was performed. The total electric field distribution over the gap area was simulated using COMSOL Multiphysics simulation tool to support experimental results.

3.1. Electrodes fabrication

Pt electrodes were defined on a SiO_2/Si structure. First, a 300 nm-thick SiO_2 layer was grown on an n^+-type Si (1 0 0) wafer (electrical resistivity of 1–10 Ω cm) by wet thermal oxidation in a conventional furnace, in order to act as a dielectric layer (**Figure 4a**). Then, photolithography was performed to define the electrodes region. An 80 nm-thick Pt layer was sputtered by a physical vapour deposition system, and lift-off process was carried out to define electrodes (**Figure 4b**). Three different electrode geometries were fabricated to evaluate the effect of electrode shape on DEP force, further denominated 1 (rectangular extremities), 2 (circular extremities) and 3 (narrow extremities) (**Figure 5**).

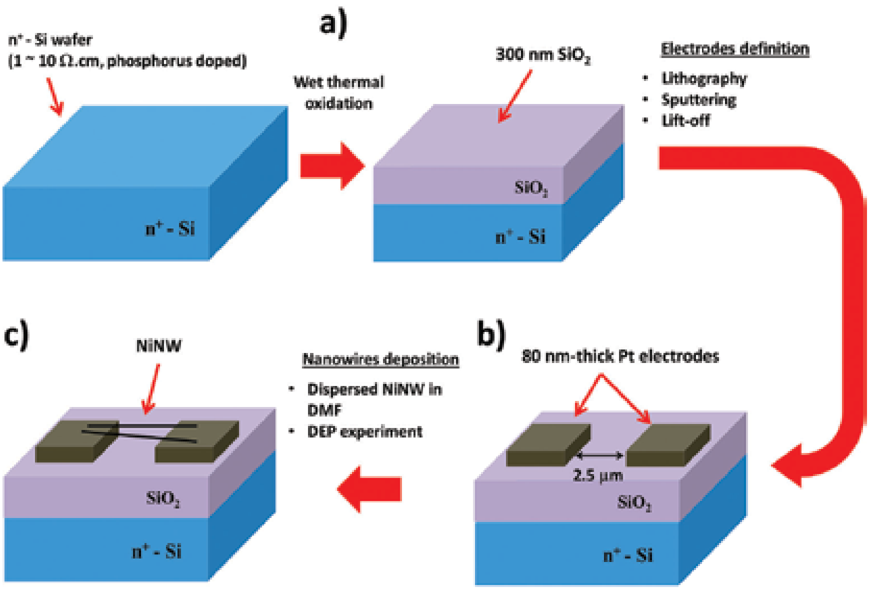

Figure 4. Schematics of experimental procedures: (a) dielectric layer formation on top of n⁺-Si wafer by thermal oxidation; (b) electrodes definition by photolithography and lift-off; (c) NiNW deposition on electrodes by DEP experiment. Adapted with permission from [33]. Copyright 2015 by American Vacuum Society.

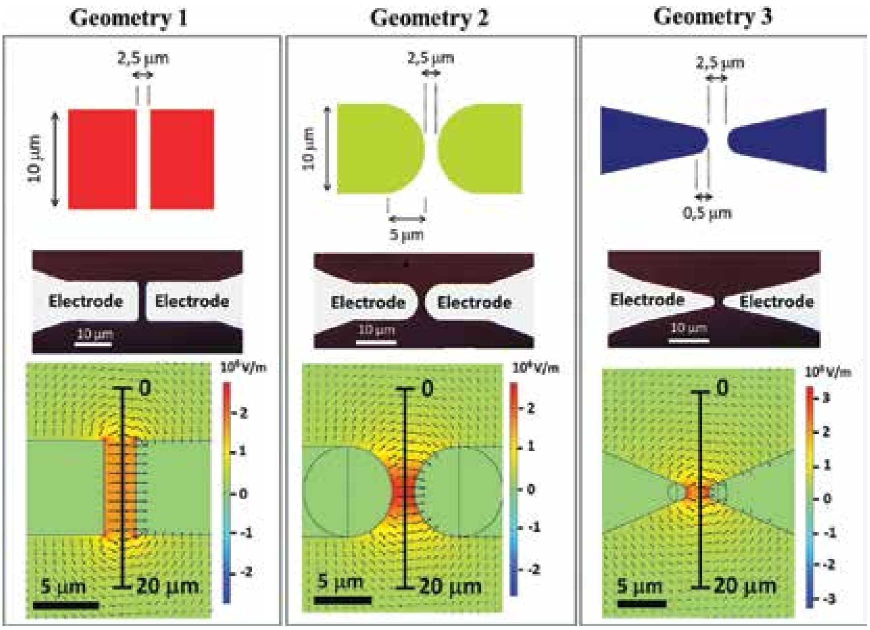

Figure 5. Schematics (top), optical microscopy (centre) and total electric field simulations, using COMSOL Multiphysics tool (below) of the three geometries tested for the Pt electrodes. The 20 μm line was taken for evaluation of the electric field profile for each geometry, as presented in **Figure 8**. Reprinted with permission from [33]. Copyright 2015 by American Vacuum Society.

3.2. NiNWs fabrication and DEP experimental procedure

NiNWs of 4 ± 1 μm-long and 35 ± 5 nm of diameter were fabricated via pulsed electrodeposition into anodized alumina membrane [16, 17]. A 1 M NaOH chemical etching solution at 24°C under agitation was employed to release the NWs from the porous alumina membrane. They were then cleaned with isopropanol and rinsed with deionized water in order to remove organic remains and further dispersed in DMF to avoid NWs clusters formation. The NiNW deposition was performed by DEP (**Figure 4c**), conducted with a HP 8116A pulse/function generator configured with 3 V_{PP} and null offset. The sinusoidal signal was generated for a frequency range between 50 kHz and 1 MHz. Before DEP process, the solution (concentration of ca. 10^8 NiNW mL^{-1}) was sonicated for 120 s at room temperature, in order to uniformly disperse the NiNWs in the DMF. Then, 1 μL solution volume was placed in the gap region and the DEP parameters were applied on each pair of electrodes during 60 s. The DMF excess was immediately rinsed with deionized water and dried with N_2. For each set of DEP parameters, the experiment was repeated ca. 100 times to ensure statistical reliability.

Visual inspection of the gap region by scanning electron microscopy (SEM) was used to evaluate the DEP efficiency for the three electrode geometries and the frequency range used (**Figure 6**). An experiment in which at least one NiNW was deposited—and made electrical contact with a pair of electrodes—was considered as success. For each geometry and frequency, we normalized the number of successes by the total number of experiments. Thus, it was possible to evaluate the efficiency percentage of NiNW deposition (**Figure 7a**) and the average number of deposited NiNW for the successful cases (**Figure 7b**), as a function of the DEP frequency and electrode geometry.

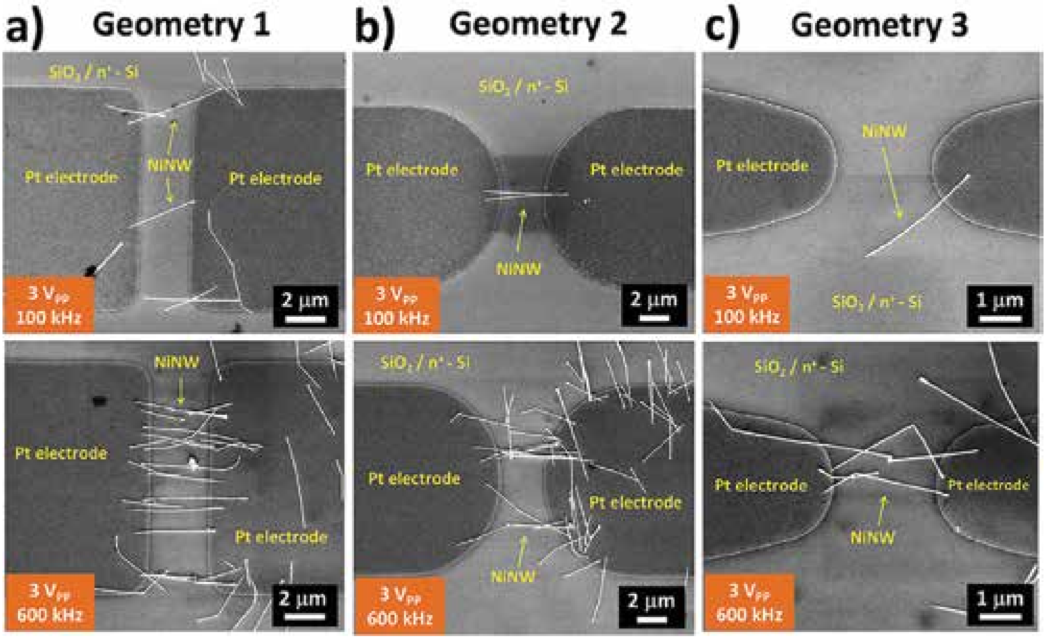

Figure 6. SEM analysis of NiNWs deposited on Pt electrodes for (a) geometry #1, (b) geometry #2 and (c) geometry #3, after DEP experiment (V_{PP} = 3 V, frequency = 100 kHz (upper row) and 600 kHz (lower row)). Reprinted with permission from [33]. Copyright 2015 by American Vacuum Society.

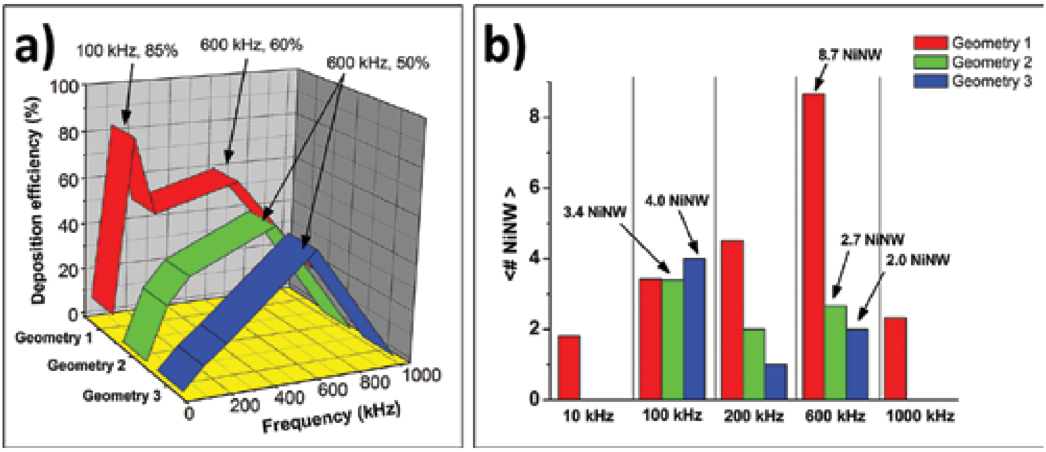

Figure 7. Charts of (a) deposition efficiency and (b) average number of deposited NiNW, obtained for DEP experiment as a function of electric field frequency, for the three electrodes geometries. Reprinted with permission from [33]. Copyright 2015 by American Vacuum Society.

First, it should be noted that DEP and AC electroosmosis might be considered as competing mechanisms for NWs deposition between electrodes. While DEP force is the main mechanism for NW trapping, AC electroosmosis, which occurs simultaneously to DEP, can induce fluid turbulence in the electrodes gap region, thus reducing the probability of success as well as the number of trapped NiNWs. Therefore, as expected from both Eq. (4) and fluid dynamics effects predictions, the DEP efficiency at 10 kHz and 1MHz was almost null, obtaining success only for geometry 1 (8% and 16%, respectively). For frequencies close to 10 kHz, the average AC electroosmosis velocity near the gap is relatively high (**Figure 3b**) and this turbulence prevents the DEP force to trap the NiNW towards the electrodes. On the other hand, for frequencies close to 1 MHz, the DEP force is about two orders of magnitude lower than the one in the range of kHz (**Figure 2a**).

Furthermore, the maximum efficiency obtained for geometry 1 was 85% at 100 kHz, while an efficiency of 60% was reached at 600 kHz. On the other hand, the DEP process was less efficient for geometries 2 and 3, both with the maximum value of 50% obtained for 600 kHz. This discrepancy may be assigned to electric field homogeneity over the electrodes gap, which is larger for geometry 1 than for geometries 2 and 3. The electrode areas are smaller in geometry 2 and 3 cases, which could create inhomogeneities and thus reduce the trapping effect in the gap region. Moreover, the maximum efficiency obtained for geometries 2 and 3 at 600 kHz still represents the frequency region that simultaneously maximizes the DEP force and minimizes the electroosmosis effect. On the other hand, for geometry 1, the larger electrode area increases the probability of success and more NiNWs are captured during DEP process. **Figure 8** presents the simulated total electric field intensity along a 20 μm transversal cross-section in the gap region, indicated in **Figure 5**. We assume that the product between the peak height, h, and its full-width half-maximum, σ, is related to the deposition efficiency. The decreasing product value for geometry 1 to 3 is in agreement with the obtained efficiency results.

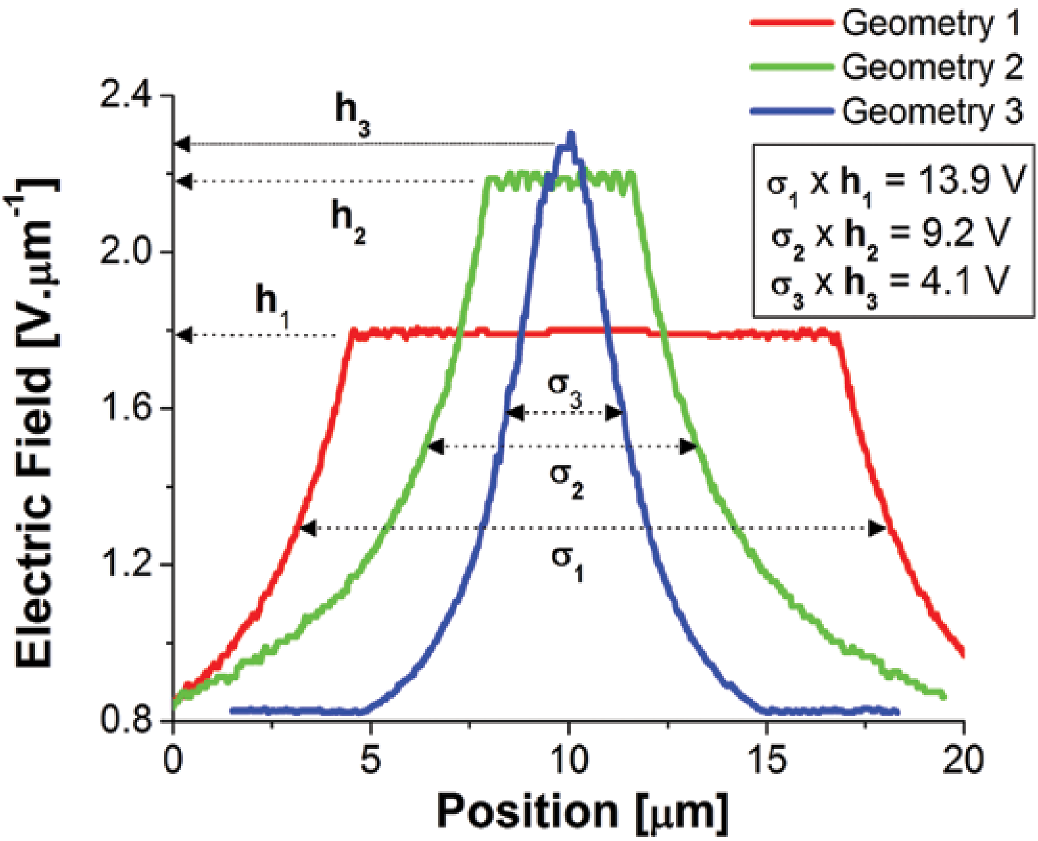

Figure 8. Total simulated electric field amplitude profile for the 20 μm transversal line shown in **Figure 4** for the three geometries, indicating the trapping efficiency to be related to the product between the peak height and its full-width half-maximum. Reprinted with permission from [33]. Copyright 2015 by American Vacuum Society.

Typically, several NiNWs were simultaneously deposited during the successful experiments, with an average number ranging from 1.0 to 8.7. Interestingly, for each investigated geometry, the maximum number of deposited NiNWs was not reached for the frequency yielding the highest efficiency. For geometry 1, only 3.4 NiNWs were deposited at 100 kHz (85% of efficiency), while a peak of 8.7 ones was attained at 600 kHz (60% of efficiency) (**Figure 7**). This result may also be attributed to the crossover between DEP and AC electroosmosis mechanisms. While the DEP force is expected to be maximized at around 100 kHz, the average fluid velocity near the gap is estimated to be close to the maximum peak value (about hundreds of micrometres/s), which limits the number of NiNWs making contact. On the contrary, at a frequency of 600 kHz, the average electroosmosis velocity reduces almost two orders of magnitude—compared to 100 kHz—yielding to less turbulence in the gap region and, therefore, a larger number of NiNWs making electrical contact between electrodes.

The situation is similar for geometries 2 and 3, but inverting the frequencies for which the efficiency and number of deposited NiNWs were maximized. The larger number of deposited NiNWs even for lower efficiency frequency may be attributed to the distortion of the electric field in the electrodes gap created by the first deposited NiNW, reducing the DEP force on the remaining NiNWs dispersed in the DMF solution and thus reducing the number of NiNWs present at higher frequencies. As shown in **Figure 9**, the electric field intensity in the gap region decreases abruptly when the first NiNW makes contact between electrodes, as the electric charges present in the metallic electrodes mainly flows through the NW. However, geometry 1 still presents a larger area, which favours more NiNWs to be present at 600 kHz, as aforementioned.

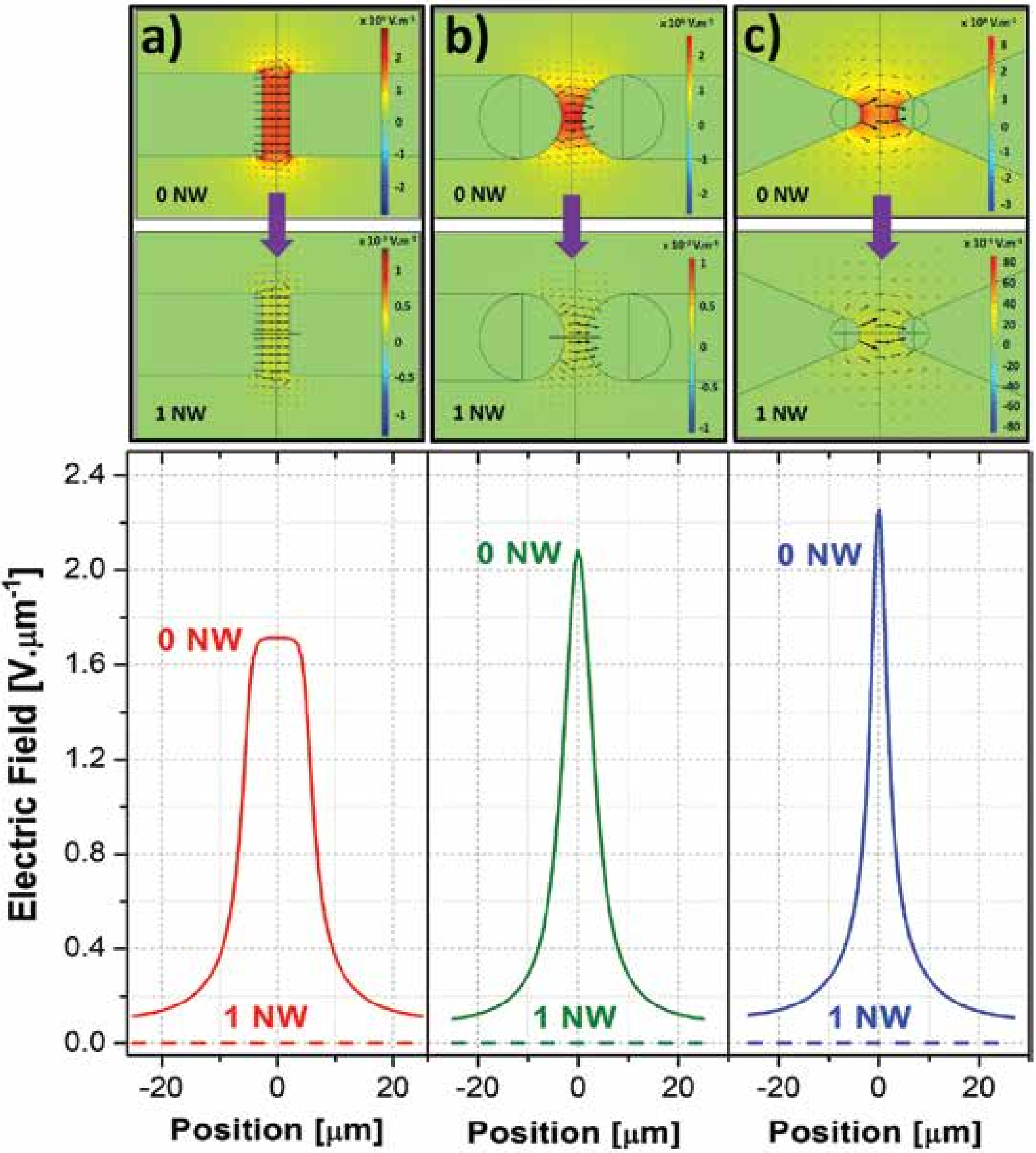

Figure 9. Total electric field simulation (using COMSOL Multiphysics) (top) and curves representing a 50 μm-long cross-section transversal line to the electrodes pair in the gap centre (bottom) for (a) geometry 1, (b) geometry 2 and (c) geometry 3. For all geometries, the total electric field substantially decreases when the first NW makes contact, reducing the probability for the second NW to make contact as well.

Globally, geometry 1 is the most efficient for DEP of NiNWs, as one can obtain efficiency up to 85% (for 3 V_{PP} and 100 kHz). However, our aim, when using DEP process, is to evaluate the transport properties of a single NiNW or only a few of them. Thus, a reasonable result is obtained when only a few NiNWs are present between electrodes. Therefore, geometries 2 and 3 reach ideal average values of NiNW (2.7 and 2.0, respectively, for 600 kHz), still with 50% of efficiency.

3.3. Electrical characterization of a single NiNW isolated by DEP

In order to evaluate the adequacy of DEP protocol for building single NW-based devices or studying fundamental properties of isolated NWs, electrical current-voltage (I-V) measurements were obtained with a Keithley 2400 source meter by applying current (without exceeding 1 nW of power to avoid damaging NiNWs due to heat dissipation) while measuring voltage with a two-wire setup. Parallel equivalent resistance as a function of the number of deposited NWs was measured and presented in a logarithm scale (**Figure 10a**). The linear fit slope of -1.0 ± 0.1 Ω NiNW^{-1} is in good agreement with the ideal case (-1 Ω NiNW^{-1}) indicating that all the NWs made proper electrical contact after DEP process. This was accomplished due to metal-like behaviour of both the electrode and the NW. It is worth to mention that the NiNW resistance is about two orders of magnitude larger than the electrodes and cables resistance as well as the contact resistance between the metallic NW and electrodes, making it possible to use a two-wire set-up for this electrical characterization. However, for processes that require DEP of semiconductor and oxide-based NWs as well as carbon-based nanostructures, post-annealing processes are usually required to make proper electrical contact and thus reduce the contact resistance [39, 40]. Alternatively, one may perform DEP of NW using four electrodes in a 4-probes measurement setup for contact resistance subtraction.

In addition, the electric resistivity of one single NiNW, ρ, was measured as a function of temperature, T, using a Physical Property Measurement System (PPMS), in the range of 2–300 K (**Figure 10b**), showing metallic behaviour, as expected. The residual resistivity value of a single NiNW is $\rho_0 = 27$ μΩ cm, which is in good agreement with the ones with similar dimensions found in literature [17, 33].

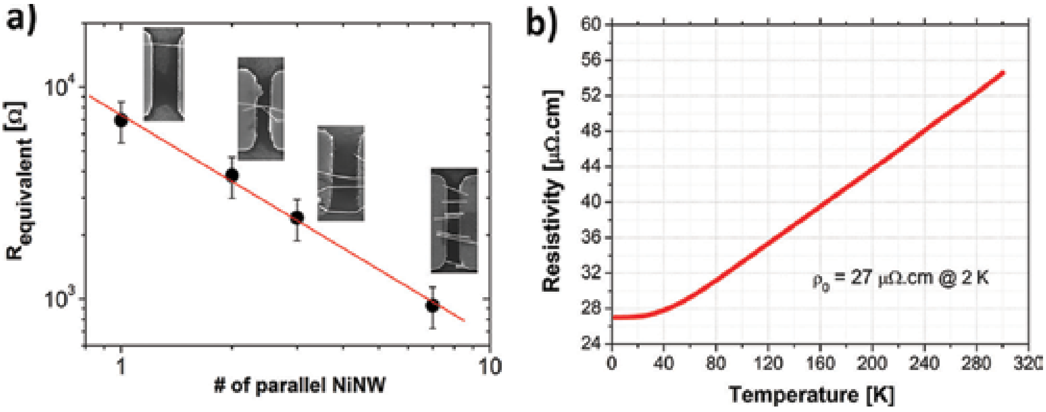

Figure 10. (a) Equivalent parallel resistance versus number of parallel-deposited NiNWs and (b) ρ x T curve of one single NiNW, showing metallic behaviour and a residual resistance of 27 μΩ cm at 2 K. Adapted with permission from [16]. Copyright 2013 by Brazilian Microelectronics Society.

4. Conclusion

This work presented DEP trapping of NiNWs between Pt electrodes defined by photolithography and lift-off. It consists of a powerful protocol for building unique and useful devices. The deposition efficiency and average number of NiNWs were evaluated as a function of the electrodes geometry and DEP frequency. Moreover, the influence of AC electroosmotic fluid flow (as a cross-over mechanism with DEP) could be observed in the mismatch between the frequencies for the largest NiNWs deposition efficiency and the largest number of deposited NiNWs. The maximum deposition efficiencies for square electrodes were 85 and 60% for 100 and 600 kHz, respectively, for averages of 3.4 and 8.7 deposited NiNWs. On the other hand, the efficiency was maximized at 600 kHz for the circular and narrow geometries, with value of 50% and averages of 2.7 and 2.0 NiNWs, respectively. This behaviour can be attributed to electric field inhomogeneities and lower trapping area over the gap present between electrodes in these geometries. For the square electrodes, since it presents a larger electrode area, it captures more NiNWs during DEP process and increases the probability of success, even with electric field intensity slightly lower than circular and narrow geometries. Adequate individual isolated NiNW electrical characterization was allowed by the successful DEP experiment of metallic NWs on the top of metallic electrodes. Additionally, post-annealing processes may be required for improving contact resistance of semiconductor and metal-oxide NWs as well as carbon-based nanostructures to metallic electrodes.

Finally, the DEP process seems to be a promising feature to evaluate fundamental properties of individual NWs as well as to build NW-based sensor devices, since they can be manipulated and isolated with relatively high efficiency. Thus, their individual electrical, thermal and/or optical output signals (in response to the environment stimulus) can be further processed. In addition, NiNWs present ferromagnetic properties, which allow their low current levels to be controlled through magnetic fields. Thus, they can be thought as an alternative for single-NW magnetic sensors as well as a promising alternative to the traditional Si-based MOSFET devices.

Author details

Marcos Vinicius Puydinger dos Santos[1,2,3]*, Fanny Béron[1], Kleber Roberto Pirota[1], José Alexandre Diniz[2] and Stanislav Moshkalev[3]

*Address all correspondence to: puyding@ifi.unicamp.br

1 Institute of Physics Gleb Wataghin, University of Campinas, Campinas-SP, Brazil

2 Faculty of Electrical Engineering and Computing, University of Campinas, Campinas-SP, Brazil

3 Center for Semiconductor Components and Nanotechnology, University of Campinas, Campinas-SP, Brazil

References

[1] Wu J, Yin B, Wu F, Myung Y, Banerjee P. Charge transport in single CuO nanowires. Applied Physics Letters. 2014;**105**(18):183506-1-183506-5. DOI: 10.1063/1.4900966

[2] Li M, Li WH, Zhang J, Alici G, Wen W. A review of microfabrication techniques and dielectrophoretic microdevices for particle manipulation and separation. Journal of Physics D: Applied Physics. 2014;**47**(6):63001-1-63001-29. DOI: 10.1088/0022-3727/47/6/063001

[3] Seo K-WW, Lee J-HH, Cho NG, Kang SJ, Kim H-KK, Na S-II, Koo H-WW, Kim T-WW. Simple brush painted Ag nanowire network on graphene sheets for flexible organic solar cells. Journal of Vacuum Science and Technology A. 2014;**32**(6):61201-1-61201-6. DOI: 10.1088/0022-3727/47/6/063001

[4] Ou MN, Yang TJ, Harutyunyan SR, Chen YY, Chen CD, Lai SJ. Electrical and thermal transport in single nickel nanowire. Applied Physics Letters. 2008;**92**(6):063101-1 –063101-3. DOI: 10.1063/1.2839572

[5] Boote JJ, Evans . Dielectrophoretic manipulation and electrical characterization of gold nanowires. Nanotechnology. 2005;**16**(9):1500-1505. DOI: 10.1088/0957-4484/16/9/015.

[6] Huang J, Wan Q. Gas sensors based on semiconducting metal oxide one-dimensional nanostructures. Sensors. 2009;**9**:9903-9924. DOI: 10.3390/s91209903

[7] Cui Y, Wei Q, Park H, Lieber . Nanowire nanosensors for highly sensitive and selective detection of biological and chemical species. Science. 2001;**293**:1289-1292. DOI: 10.1126/science.1062711.

[8] Puydinger dos Santos MV, Lima LPB, Diniz JA, Godoy Filho J. Fabrication of p-type silicon nanowires for 3D FETs using focused ion beam. Journal of Vacuum Science and Technology B. 2013;**31**(6):06FA01-1-06FA01-6. DOI: 10.1116/1.4823763

[9] De Teresa JM, Fernández-Pacheco A. Present and future applications of magnetic nanostructures grown by FEBID. Applied Physics A: Materials Science & Processing. 2014;**117**(4):1645-1658. DOI: 10.1007/s00339-014-8617-7

[10] Svensson CPT, Mårtensson T, Trägårdh J, Larsson C, Rask M, Hessman D, Samuelson L, Ohlsson J. Monolithic GaAs/InGaP nanowire light emitting diodes on silicon. Nanotechnology. 2008;**19**:305201-1-305201-6. DOI: 10.1088/0957-4484/19/30/305201

[11] Zhou H, Wissinger M, Fallert J, Hauschild R, Stelzl F, Klingshirn C, Kalt H. Ordered, uniform-sized ZnO nanolaser arrays. Applied Physics Letters. 2007;**91**:181112-1-181112-3. DOI: 10.1063/1.2805073

[12] Novotny CJ, Yu ET, Yu PKL. InP Nanowire/polymer hybrid photodiode. Nano Letters. 2008;**8**(3):775-779. DOI: 10.1063/1.2805073

[13] Soci C, Zhang A, Xiang B, Dayeh SA, Aplin DPR, Park J, Bao XY, Lo YH, Wang D. ZnO nanowire UV photodetectors with high internal gain. Nano Letters. 2007;**7**(4):1003-1009. DOI: 10.1021/nl070111x

[14] Yoshimura M, Tomioka K, Hiruma K, Hara S, Motohisa J, Fukui T. Growth and characterization of InGaAs nanowires formed on GaAs(111)B by selective-area metal organic vapor phase epitaxy. Japanese Journal of Applied Physics. 2010;**49**:04DH08-1-04DH08-5. DOI: 10.1143/JJAP.49.04DH08

[15] Puydinger dos Santos M V., Velo MF, Domingos RD, Zhang Y, Maeder X, Guerra-Nuñez C, Best JP, Béron F, Pirota KR, Moshkalev S, Diniz JA, Utke I. Annealing-based electrical tuning of cobalt–carbon deposits grown by focused-electron-beam-induced deposition. ACS Applied Materials and Interfaces. 2016;**8**:32496-32503. DOI: 10.1021/acsami.6b12192

[16] Puydinger dos Santos MV, Velo MF, Domingos RD, Bettini J, Diniz JA, Béron F, Pirota KR. Electrodeposited nickel nanowires for magnetic-field effect transistor (MagFET). Journal of Integrated Circuits and Systems. 2016;**11**(1):13-18.

[17] Leitao DC, Sousa CT, Ventura J, Amaral JS, Carpinteiro F, Pirota KR, Vazquez M, Sousa JB, Araujo JP. Characterization of electrodeposited Ni and Ni80Fe20 nanowires. Journal of Non-Crystalline Solids. 2008;**354**:5241-5243. DOI: 10.1016/j.jnoncrysol.2008.05.088

[18] Raychaudhuri S, Dayeh SA, Wang D, Yu ET. Precise semiconductor nanowire placement through dielectrophoresis. Nano Letters. 2009;**9**(6):2260-2266. DOI: 10.1021/nl900423g

[19] Maijenburg AW, Maas MG, Rodijk EJB, Ahmed W, Kooij ES, Carlen ET, Blank DHA, ten Elshof JE. Dielectrophoretic alignment of metal and metal oxide nanowires and nanotubes: A universal set of parameters for bridging prepatterned microelectrodes. Journal of Colloid and Interface Science. 2011;**335**(2):486-493. DOI: 10.1016/j.jcis.2010.12.011

[20] Gierhart BC, Howitt DG, Chen SJ, Smith RL, Collins SD. Frequency dependence of gold nanoparticle superassembly by dielectrophoresis. Langmuir. 2007;**23**(24):12450-12456. DOI: 10.1021/la701472y

[21] Vijayaraghavan A, Sciascia C, Dehm S, Lombardo A, Bonetti A, Ferrari AC, Krupke R. Dielectrophoretic assembly of high-density arrays of individual graphene devices for rapid screening. ACS Nano. 2009;**3**(7):1729-1734. DOI: 10.1021/nn900288d

[22] Decossas S, Mazen F, Baron T, Brémond G, Souifi A. Atomic force microscopy nanomanipulation of silicon nanocrystals for nanodevice fabrication. Nanotechnology. 2003;**14**:1272-1278. DOI: 10.1088/0957-4484/14/12/008

[23] Whang D, Jin S, Wu Y, Lieber CM. Large-scale hierarchical organization of nanowire arrays for integrated nanosystems. Nano Letters. 2003;**3**(9):1255-1259. DOI: 10.1021/nl0345062

[24] Huang Y, Xiangfeng D, Qingqiao W, Lieber C. Directed assembly of one-dimensional nanostructures into functional networks. Science. 2001;**291**:630-633. DOI: 10.1126/science.291.5504.630

[25] Javey A, Nam S, Friedman RS, Yan H, Lieber CM. Layer-by-layer assembly of nanowires for three-dimensional, multifunctional electronics. Nano Letters. 2007;**7**(3):773-777. DOI: 10.1021/nl063056l

[26] Pohl HA. The motion and precipitation of suspensoids in divergent electric fields. Journal of Applied Physics. 1951;**22**(7):869-871. DOI: 10.1063/1.1700065

[27] Xie C, Chen B, Ng CO, Zhou X, Wu J. Numerical study of interactive motion of dielectrophoretic particles. European Journal of Mechanics B/Fluids. 2015;**49**:208-216. DOI: 10.1016/j.euromechflu.2014.08.007

[28] Kang S. Dielectrophoretic motion of two particles with diverse sets of the electric conductivity under a uniform electric field. Computers & Fluids. 2014;**105**:231-243. DOI: 10.1016/j.compfluid.2014.09.029

[29] Schukfeh MI, Storm K, Hansen A, Thelander C, Hinze P, Beyer A, Weimann T, Samuelson L, Tornow M. Formation of nanogaps in InAs nanowires by selectively etching embedded InP segments. Nanotechnology. 2014;**25**:465306-1-465306-6. DOI: 10.1088/0957-4484/25/46/465306

[30] Hamdi FS, Français O, Dufour-Gergam E, Le Pioufle B. How medium osmolarity influences dielectrophoretically assisted on-chip electrofusion. Bioelectrochemistry. 2014;**100**:27-35. DOI: 10.1016/j.bioelechem.2014.05.004

[31] Freer EM, Grachev O, Stumbo DP, Duan X, Martin S, Stumbo DP. High-yield self-limiting single-nanowire assembly with dielectrophoresis. Nature Nanotechnology. 2010;**5**:525-530. DOI: 10.1038/nnano.2010.157

[32] Pohl HA. Dielectrophoresis: The Behavior of Neutral Matter in Non-Uniform Electric Fields. 1st ed. New York: Cambridge University Press; 1978. 579 p.

[33] Puydinger dos Santos M V., Lima LPB, Mayer RA, Béron F, Pirota KR, Diniz JA. Dielectrophoretic manipulation of individual nickel nanowires for electrical transport measurements. Journal of Vacuum Science and Technology B. 2015;**33**(3):031804-1-031804-8. DOI: 10.1116/1.4918732

[34] Dimaki M, Bøggild P. Dielectrophoresis of carbon nanotubes using microelectrodes: a numerical study. Nanotechnology. 2004;**15**:1095-1102. DOI: 10.1088/0957-4484/15/8/039

[35] Smith BD, Mayer TS, Keating CD. Deterministic assembly of functional nanostructures using nonuniform electric fields. Annual Review Physical Chemistry. 2012;**63**:241-263. DOI: 10.1146/annurev-physchem-032210-103346

[36] Liu Y, Chung JH, Liu WK, Ruoff RS. Dielectrophoretic assembly of nanowires. Journal of Physical Chemistry B. 2006;**110**(29):14098-14106. DOI: 10.1021/jp061367e

[37] Green NG, Ramos A, González A, Morgan H, Castellanos A. Fluid flow induced by nonuniform ac electric fields in electrolytes on microelectrodes. I. Experimental measurements. Physical Review E. 2000;**61**(4):4011-4018. DOI: 10.1103/PhysRevE.61.4019

[38] Ramos A, González A, Castellanos A, Green NG, Morgan H. Pumping of liquids with ac voltages applied to asymmetric pairs of microelectrodes. Physical Review E: Statistical Nonlinear Soft Matter Physics. 2003;**67**:056302-1-056302-11. DOI: 10.1103/PhysRevE.67.056302

[39] Rouxinol FP, Gelamo R V., Amici RG, Vaz AR, Moshkalev SA. Low contact resistivity and strain in suspended multilayer graphene. Applied Physics Letters. 2010;**97**:253104-1-253104-4. DOI: 10.1063/1.3528354

[40] Li M, Anderson W, Chokshi N, DeLeon RL, Tompa G. Laser annealing of laser assisted molecular beam deposited ZnO thin films with application to metal-semiconductor-metal photodetectors. Journal of Applied Physics. 2006;**100**:053106-1-053106-4. DOI: 10.1063/1.2344811

Chapter 4

ZnO Nanowires for Dye Sensitized Solar Cells

Simas Rackauskas, Nadia Barbero,
Claudia Barolo and Guido Viscardi

Additional information is available at the end of the chapter

http://dx.doi.org/10.5772/67616

Abstract

This chapter provides a broad review of the latest research activities focused on the synthesis and application of ZnO nanowires (NWs) for dye-sensitized solar cells (DSCs) and composed of three main sections. The first section briefly introduces DSC-working principles and ZnO NW application advantages and stability issues. The next section reviews ZnO NW synthesis methods, demonstrating approaches for controlled synthesis of different ZnO NW morphology and discussing how this effects the overall efficiency of the DSC. In the last section, the methods for ZnO NW interface modification with various materials are discussed, which include ZnO core-shell structures with semiconductive or protective layers, ZnO NW hybrid structures with other materials, such as nanoparticles, quantum dots and carbon nanomaterials and their benefit for charge and light transport in DSCs. The review is concluded with some perspectives and outlook on the future developments in the ZnO nanowire application for DSCs.

Keywords: Nanowires, ZnO nanowire, Synthesis, dye-sensitized solar cell, DSC, Photovoltaics, surface modification, hybrid materials

1. Introduction

World energy demand is rapidly increasing; therefore, a clean and reliable energy source is fundamental to global economy. The environmental impact of the fossil fuel use urges the need for the search of alternative energy resources. Many different renewable energy technologies were developed recently aiming for efficient solutions of clean energy supply; however, a price competitiveness is a biggest drawback. Solar energy is considered as a key solution for environmental challenge, because of its carbon neutral nature and high abundance. The conversion of solar energy to electricity is fulfilled by solar cells based on the photovoltaic effect.

Dye-sensitized solar cells (DSCs) have gained widespread attention because of the ease of fabrication, low production costs and tuneable optical properties, such as colour and transparency [1]. The most attractive properties of DSCs are their low cost and simple manufacturing processes together with their advantageous attributes such as lightweight, low toxicity and good performance in diverse light conditions [2].

ZnO attracted attention as an alternative photoelectrode material for DSCs due to multiple advantages, that is, excellent optoelectronic properties, low cost, easy synthesis, non-toxicity and others. Moreover, ZnO has the diversity of one-dimensional (1D) structures, which suggest attractive approach for photoelectrode scaffolding.

ZnO nanowire (NW) application as DSC photoelectrode shows multiple advantages, such as higher electron mobility and increased optical way because of refraction; moreover, additional functionalities such as flexible DSCs with the help of ZnO NW photoelectrode can also be obtained. The efficiency of ZnO nanowire DSCs is rapidly increasing in recent years; therefore, the interest in ZnO NW application for DSC is rapidly growing. In order to reach higher efficiency of ZnO NW DSCs, further surface modifications with an additional protective layer of TiO_2 or inert materials such as Al_2O_3 are used. Other possibilities lie in tailoring the morphology of NWs, or employing hybrid structures of ZnO nanowires with other materials.

The application of ZnO NW for DSCs is an interesting topic for nanowire community and also to researchers from diverse scientific fields, since much effort was put in this topic, numerous approaches were tried and a definite improvement was reached. Still, there is a need to direct the effort in understanding more deeply the ZnO NW interaction with other materials, processes of light and charge transfer and master the synthesis methods in order to achieve the optimal structure for application in DSCs.

This chapter will provide a comprehensive review of the state-of-the-art research activities focused on the synthesis and application of ZnO nanowires for dye-sensitized solar cells. The first section briefly overviews fundamentals of the DSC and introduces ZnO NW synthesis, divided into vapour and solution phase methods, demonstrating approaches to obtain different ZnO NW morphology. Next, the methods for ZnO NW surface modification are discussed, which include ZnO core-shell structures with semiconductive layers or protective layers and their benefit for charge and light transport in DSCs. In the last part, we will review ZnO NW hybrid structures with other materials, such as nanoparticles, quantum dots or carbon nanomaterials. The chapter will then conclude with the perspectives and the outlook on the future developments in the ZnO nanowire application for DSCs.

2. Fundamentals of dye-sensitized solar cells

The concept of a dye-sensitized solar cell was introduced in 1991, by O'Regan and Grätzel [3]. A schematic diagram showing the operation of a typical DSC is shown in **Figure 1**.

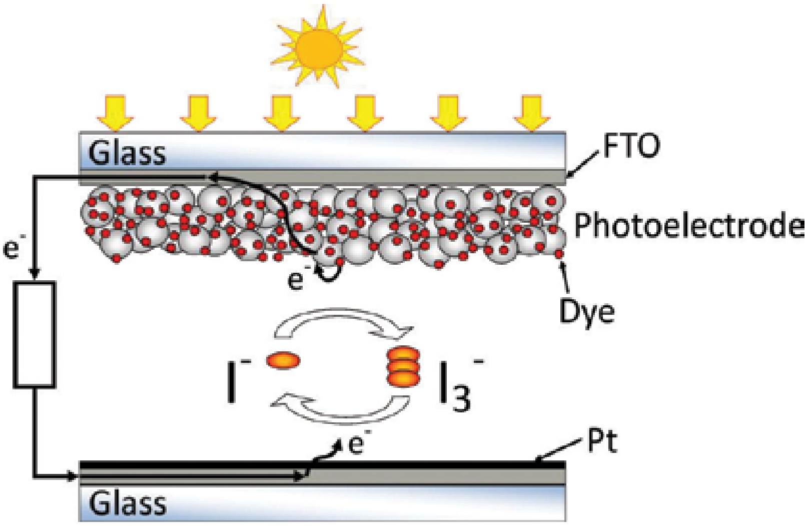

Figure 1. Schematic overview of the typical dye-sensitized solar cell (DSC).

Typical DSCs are composed of a transparent conducting oxide (such as fluorine-doped tin oxide, FTO) on glass, a nanoparticle photoelectrode covered in a monolayer of sensitizing dye, a hole-conducting electrolyte and a platinum-coated, FTO-coated glass back-contact.

Nanoparticles of TiO_2 (anatase) are mostly used as photoelectrode, although alternative wide-band-gap oxides such as ZnO and SnO_2 have also been investigated. A monolayer of the sensitizer is attached to the surface of the nanoparticle photoelectrode. Under illumination, sensitizer photo-excitation results in the injection of an electron into the conduction band of the oxide. The dye is regenerated by electron donation from the electrolyte, mostly from a redox system (iodide/triiodide couple) in an organic solvent. The regeneration of the sensitizer by iodide intercepts the recapture of the conduction band electron by the oxidized dye. The iodide is regenerated, in turn, by the reduction of triiodide at the counter-electrode, and the circuit is completed via electron migration through the external load. The voltage, which is obtained under illumination, corresponds to the difference between the Fermi level of the electron in the solid and the redox potential of the electrolyte. Overall, there are no permanent chemical transformations involved in the generation of electric power from light.

The photoelectrode serves as a support for sensitizer loading and at the same time transport media of photo-excited electrons from sensitizer to the external circuit. Hence, to ensure high dye loading, a large surface area is necessary. Moreover, a fast charge-transport rate is required to ensure high electron collection efficiency. These two properties are the defining characteristics of an ideal photoelectrode [4].

Insight into the factors limiting DSC performance is gained by comparing theoretical cell efficiencies with those of current state-of-the-art cells. The power conversion efficiency (PCE) of a solar cell is given as

$$PCE = \frac{J_{sc} V_{oc} FF}{P_{in}}, \tag{1}$$

where J_{sc} is the absolute value of the current density at short circuit, V_{oc} is the photovoltage at open circuit, *FF* is the fill factor and *P*in is the incident light power density. In principle, the maximum J_{sc} of a DSC is determined by how well the absorption window of its dye overlaps the solar spectrum. Much of the shortfall is due to the poor absorption of low-energy photons by available dyes. Thickening of the photoelectrode to increase its optical density in order to improve the absorption of red and near-infrared light is unsuccessful because the film thickness comes to exceed the electron diffusion length through the nanoparticle network.

The dynamic scale of the processes involved in light to electricity conversion (**Figure 2**) shows that the initial events of electron injection and dye regeneration leading to photoinduced charge separation occur on a femto- to nanosecond or microsecond time scale [6], while the electron transport across the photoelectrode takes place within milliseconds or even seconds [7]. However, for the efficient functioning of the DSC, the diffusion length of the electron should be greater than the thickness of the photoelectrode. Electron diffusion length L_n can be expressed through electron lifetime τ_n and electron diffusion coefficient D_n as

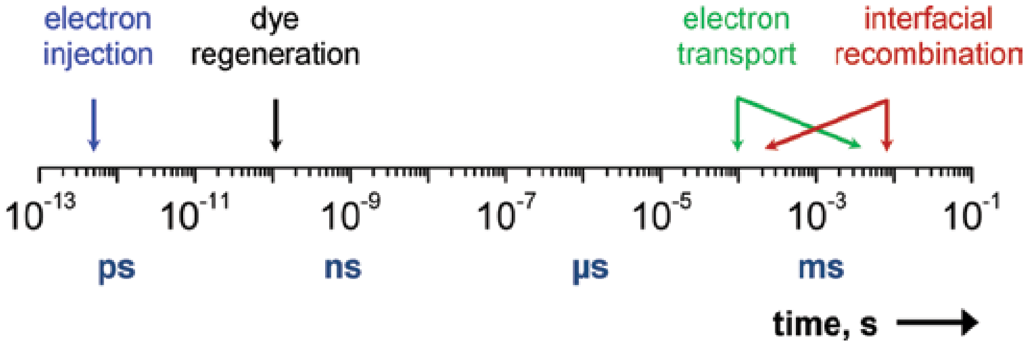

Figure 2. Dynamics competition of the processes involved in the conversion of light to electric power by typical DSCs [5].

$$L_n = \sqrt{D_n \bullet \tau_n}, \tag{2}$$

Disordered network of TiO_2 nanoparticles with numerous grain boundaries weakens electron mobility and results in slow transport and recombination of photo-excited electrons [8]. This greatly hinders the overall PCE of such devices. The mentioned problems associated with the standard architecture of the photoelectrode oblige a search for more effective nanostructured photoelectrode materials and morphologies [9–11].

3. ZnO nanowire synthesis and application in DSCs

The relatively low transport resistance of transparent high-mobility materials, such as ZnO compared to that of anatase TiO_2 nanoparticles, is one of the major advantages for the application in charge injection and collection for DSCs [12–15]. ZnO, which has an energy bandgap similar to that of the ordinarily used TiO_2 but possesses higher electron mobility, is an alternative photoelectrode material for DSCs [16]. Another advantage of ZnO is the diversity of 1D structures. Structurally, ZnO has several fast-growth directions; therefore, various morphologies can be easily obtained.

ZnO nanowires were widely considered as an alternative photoelectrode material (**Figure 3**), since they address many of the mentioned problems; however, up to date the highest power conversion efficiency of ZnO-based DSC reported [18] is still lower than TiO_2-based DSC. The main reason may be that best DSC dyes are designed for TiO_2 photoelectrode, and since ZnO is less stable especially in acid, therefore there is still no efficient dye available for ZnO anode [19, 20]. It was found that electron injection from traditional Ru-based dye to ZnO is much slower than to TiO_2 [21]. However, much research is conducted in order to find modifications for ZnO photoelectrodes and further increase the overall PCE of the DSCs.

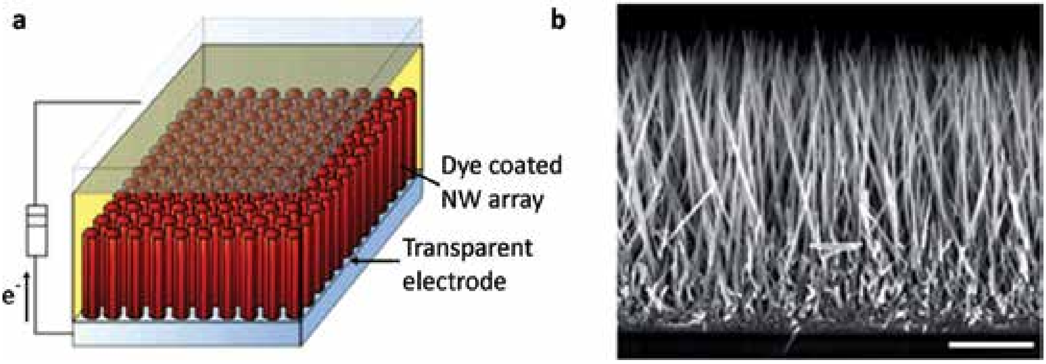

Figure 3. ZnO nanowire-based DSC: (a) a schematic of the cell; (b) SEM image of a nanowire array. Scale bar, 5 μm [17].

3.1. ZnO nanowire DSC stability

ZnO has a low chemical stability in acidic environment. After the DSC assemble, ZnO photoelectrode degrades through the carboxylic groups of the acidic dye attached to it, and thus leads to the formation of Zn^{2+}-dye agglomerates.

On the other hand, the time of dye loading is crucial for the performance of an all-ZnO-based DSC, because longer dye-loading time leads to the formation of more Zn^{2+}-dye agglomerates and shorter immersion time is insufficient for dye adsorption. For this reason, other than traditional Ru-based dyes could be used, such as porphyrin and indoline dyes [22]. Indoline dyes have been found to be a comparatively good match with ZnO because of its lower acidity and the lack of complexing agent. The CR147 dye-sensitized ZnO film is almost free from Zn^{2+}/dye agglomerations. A ZnO DSC with CR147 dye has high PCE of 6.89%, 40% higher than the cell with traditional N719 dye [23]. A metal-free organic dye D149 allows to use lower-sensitizing times, moreover a PCE of 5.14% was reported [24]. A mix of several specially engineered dyes could also be advantageous. Compared to only D149-sensitized cell, the YD2-o-C8-TBA and D149 co-sensitized ZnO DSSC with a wavelength ranging from 475–700 nm exhibited improved photon-to-current conversion efficiencies with cell PCE of 5.6% [25]. Vegetable tannin and their Fe complexes could be used for their low cost and can be obtained from renewable sources, but the efficiencies are up to 0.99% [26].

Other stability problems are associated with a liquid electrolyte used, which tends to leak in time. Device instability and the need for good device packaging have become major problems for commercial application of DSCs. This problem is common to most DSCs; liquid electrolyte could be substituted with quasi-solid-state electrolytes [27]. Metal oxide nanoparticle gelators are applied [28], ZnO nanoparticles gel [29] shows PCE of 4.17%, and the optimized DSC shows a stability of 95% on the PCE value for 150 days. The hole transport is presumably done by Grotthuss-type ion exchange mechanism.

3.2. ZnO nanowire synthesis

As it was earlier stated, competition between the transport and the recombination of photoexcited carriers is one of the main obstacles for developing higher conversion efficiency photoelectrode. To date, numerous morphologies of low-dimensional ZnO nanostructures such as nanowires, nanobelts, nanotubes and nanoflakes have been synthesized and are expected to improve the electron diffusion length in the photoelectrode.

This paragraph reviews the most important approaches of the ZnO NW synthesis with the aim of application in DSCs. In order to obtain an optimal structure for the photoelectrode of DSC, the growth of ZnO NWs should be carefully controlled. ZnO nanowires can be synthesized in a variety of methods; two main synthesis groups can be distinguished: vapour phase and solution phase synthesis.

Vapour phase ZnO NW synthesis involves temperatures typically 400–1100°C, needed to vapourize and transport the precursors. A typical reaction involves ZnO NW growth by vapour-liquid-solid mechanism (VLS) [30, 31] using catalyst particles such as Au, Pt or Ag, or by vapour solid mechanism (VS) [32] without the use of catalysts. Zn vapour is obtained by heating the mixture of ZnO and C [33] or directly from Zn powder [34]. A direct growth on Zn metallic substrate is also interesting for its simplicity [35–37]. ZnO NW growth by vapour phase synthesis typically involves a direct Zn oxidation:

$$\mathrm{Zn} + \mathrm{O}_2 \rightarrow \mathrm{ZnO} \tag{3}$$

Solution phase ZnO NW synthesis is especially interesting for its low-temperature approach and high-output possibilities. Since the typical synthesis conditions apply temperatures lower than 200°C, the variety of materials can be used as substrates. In the solution phase synthesis, the ZnO NW growth process is carried out in aqueous or organic solvents from zinc salts. Normally, aqueous solutions are used and the methods are often referred to as hydrothermal growth [38]. However, other solutions such as ethanol [39] are also used. A typical ZnO NW solution phase growth involves the following reaction:

$$\mathrm{Zn}^{2+} + 2\,\mathrm{OH}^- \rightarrow \mathrm{Zn}\,(\mathrm{OH})_2 \rightarrow \mathrm{ZnO} + \mathrm{H}_2\mathrm{O} \tag{4}$$

where hexamethylenetetramine (HMTA) [40], NH_4OH [41] or NaOH [42] may be used as the hydroxide source. High aspect ratio can be achieved by controlling the preferential growth with catalytic Au nanoparticles [43] or polymers such as polyethylenimine (PEI) [44], or polyethylene glycol (PEG) [45]. ZnO NW aspect ratio can be further improved by sequential growth [46].

Comparing the vapour and liquid phase synthesis, it is important to note that the vapour phase growth of ZnO NWs uses higher temperatures; therefore for low-melting substrates an efficient post synthesis, transferring and attachment methods should be developed, but nonetheless high crystallinity can be obtained without further annealing. On the contrary, most of the solution growth methods use low temperatures, therefore NWs can be directly grown on a variety of low-melting materials and surfaces; however, the synthesis of high aspect ratio structures with high crystallinity is demanding.

Applying the mentioned methods, ZnO NWs could be synthesized in complex forms (**Figure 4**) such as nanoforest [47], tetrapods [49, 50], hierarchical nanowires [48], coral-shaped nanostructures [51], nanocactus [24], flower-like [52] and many others [53–55] by simply controlling the crystal grow direction.

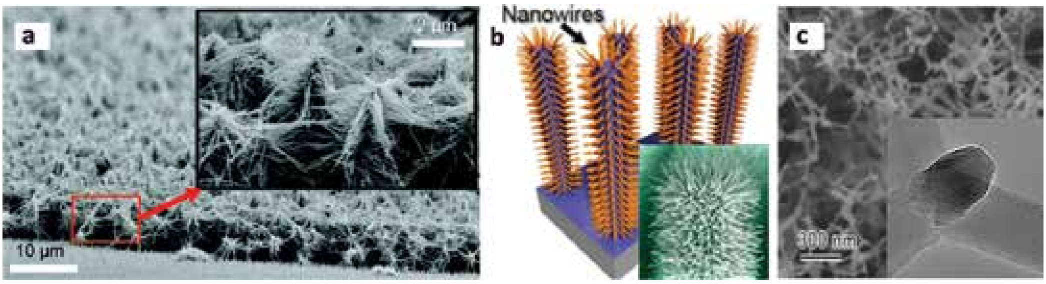

Figure 4. Complex structures of ZnO nanowires: (a) nanoforest [47]; (b) hierarchical nanowires (inset shows SEM figure) [48]; (c) tetrapods [49].

4. ZnO NW interface modifications

The advantage of fast electron transfer is often counterbalanced by faster electron recombination dynamics with the oxidized electrolyte via intrabandgap surface states which ultimately limits the PCE [15]. In order to slow down the recombination and to increase the photovoltage and photocurrent, the ZnO NW interfaces can be covered by a thin layer of various capping materials (Al_2O_3, TiO_2, ZrO_2, etc.). Alternatively, hole transfer can be modified by forming ZnO NW hybrid structures with conductive polymers, or various nanostructures such as quantum dots (QDs), nanocrystals (NCs) and carbon nanomaterials.

4.1. ZnO NW core-shell structure in DSC

The purpose of NW coating with an insulating or semiconducting oxide layer is to diminish the recombination by forming a potential barrier on NW surface, to physically separate electrons from ions and to increase the dye adsorption on the surface. Moreover, band edge can be shifted by using higher bandgap layer to increase the open-circuit voltage. In addition to acting as an effective protection layer for the chemically unstable ZnO against the acidic dye solution, the complete coverage of the NWs with a dense layer can passivate surface traps [12]. ZnO NW core-shell structures with different metal oxides can be obtained with atomic layer deposition (ALD) technique [56, 57]. The coverage of ZnO NWs with an insulating materials results in a low-efficiency DSCs [58–60]; by contrast, ZnO NW core-shell structures with semiconductors have several advantages, especially interesting is TiO_2 shell.

There are several motives why the ZnO-TiO_2 core-shell structure is attractive. TiO_2 is chemically more stable compared to ZnO in acidic dye solutions [61]. Thus, the presence of TiO_2 shell prevents ZnO surface from being dissolved and the formation of Zn^{2+}/dye agglomerates. The TiO_2 shell can also increase the injected electrons and more dye absorption, which lead to a higher light-harvesting efficiency. Moreover, the shell reduces recombination by forming a tunnelling barrier to confine the photoinjected electrons within the core, and by passivating the recombination centres on the core surface [62]. The charge transfer is significantly improved since ZnO has much higher electron mobility compared to TiO_2. DFT ab initio study of ZnO-TiO_2 core-shell structure [63] shows that TiO_2 coating induces changes in surface states and shifts the conduction and valence band edges to higher energies; therefore, an increase in open-circuit voltage and a decrease in short-circuit current are expected.

TiO_2 shell on ZnO NWs can be formed by dip coating in Ti precursors, such as tetrabutyl titanate (TBOT) [64, 65], titanium isopropoxide (TTIP) and titanium tetrachloride ($TiCl_4$). ZnO NW coated with a thin shell layer of TiO_2 (**Figure 5**) showed an increased PCE up to 6% [66]. A comparative study [67] showed that at the same conditions TBOT-treated ZnO DSC showed the best performance with the highest PCE and short-circuit current density of 4.92% and 12.49 mA/cm^2, respectively.

In order to increase the surface area of the photoelectrode and without losing the charge-transport properties, hierarchical structures could be used. A hierarchical structure of ZnO NWs could also increase the efficiency of DSCs by providing a high area for dye absorption

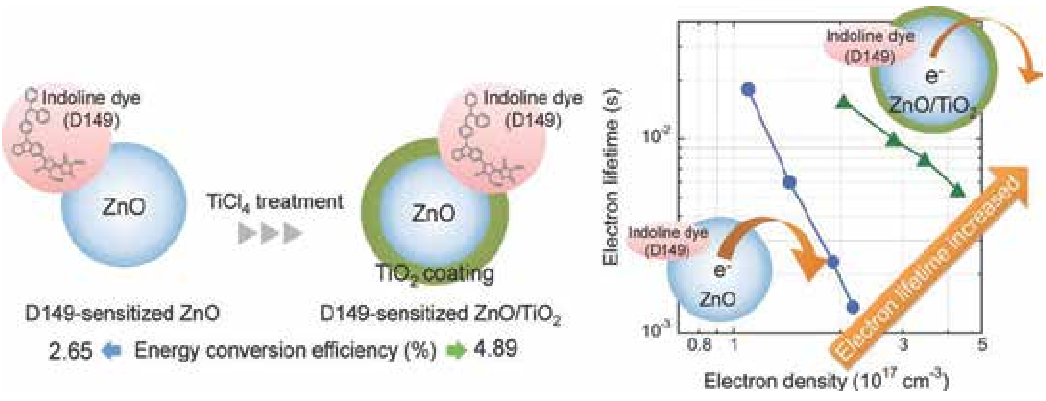

Figure 5. ZnO-TiO_2 core-shell formed by low-temperature $TiCl_4$ treatment [68].

and also effective light scattering. ZnO DSC efficiency can be doubled by decorating ZnO NW photoelectrodes with different nanoparticles of SnO_2 [69], TiO_2 [70, 71] or in situ-synthesized ZnO nanoparticles [72]. Even though the large surface area of nanoparticles empowers a high dye-loading capacity, yet the disordered network with numerous grain boundaries weakens electron mobility and results in slow transport and recombination of photo-excited electrons [8]. The application of ZnO NW with semiconductive nanoparticles has advantages of both high surface area and fast charge transport. A complex structure of hierarchical NWs improves the PCE up to five times compared to the initial NW, the reported efficiencies for nanotrees 2.63% [73], coral-shaped nanostructure gives 4.58% [51], nanocactus 5.14% [24] are encouraging.

ZnO tetrapods used with SnO_2 nanoparticles provided large roughness factors, good charge collection and tunable light-scattering properties. High PCE of 6.31% was attributed to NH_3 treatment, which was believed to create ZnO shell on SnO_2 nanoparticles [74]. A hierarchical core-shell ZnO NW with TiO_2 nanosheets resulted in an outstanding performance with a solid-state electrolyte, showing the conversion efficiencies of up to 7.46% [75].

The prepared ZnO photoelectrode can be further treated to improve the conductance and porosity parameters. Hot-press treatment of the ZnO photoelectrode was demonstrated to improve PCE of the DSC by 45% [76]. Another powerful technique, the room-temperature chemical bath deposition, was used to increase the surface area of the ZnO photoelectrode, a PCE of 5.24% was obtained [77].

4.2. ZnO NW hybrid solar-cell structures

Hybrid polymer solar cells composed of metal oxide nanostructures and polymers have attracted great interest mostly due to the good physical and chemical stability. In such solar cells, p-type donor polymers are combined with n-type acceptor ZnO nanostructures [78] among other oxides. Nanowires are one of the most attractive forms for such solar cells because they provide a direct path for charge transport, high carrier motilities and a high electron affinity necessary for charge injection from the complementary organic donor material [79]. Mostly used conducting polymer poly(3-hexylthiophene) (P3HT) composite with ZnO nanowire shows hybrid solar-cell PCE in the range of 0.2–0.5% [80–82] and can be further increased to 2% by adding dye [83]. Such low-power conversion efficiencies are associated with poor polymer infiltration and therefore low-active interfacial area between polymer and ZnO NWs. An interfacial layer of carbon nanoparticles (CNPs) can be employed to enhance the charge-transfer properties in hybrid ZnO NW solar cells. The energy-level diagram of the solar cells is shown in **Figure 6b**. The LUMO level of the CNPs (-4.00 ± 0.02 eV) is perfectly aligned with both the LUMO level of P3HT (-3.2 eV) and the conduction band edge of TiO_2 (-4.2 eV). This ensures both efficient exciton dissociation at the P3HT/CNP interface and efficient electron extraction. In such a device, ZnO-TiO_2 core-shell works as electron collector and transporter, P3HT acts as electron donor, and the CNP layer acts as electron acceptor [84].

The other possibility is to use quantum dots (QDs) for hole transfer. The use of PbS quantum dots (QDs) is promising because of the tunable, size-dependent bandgap from 0.7 to 1.3 eV [85].

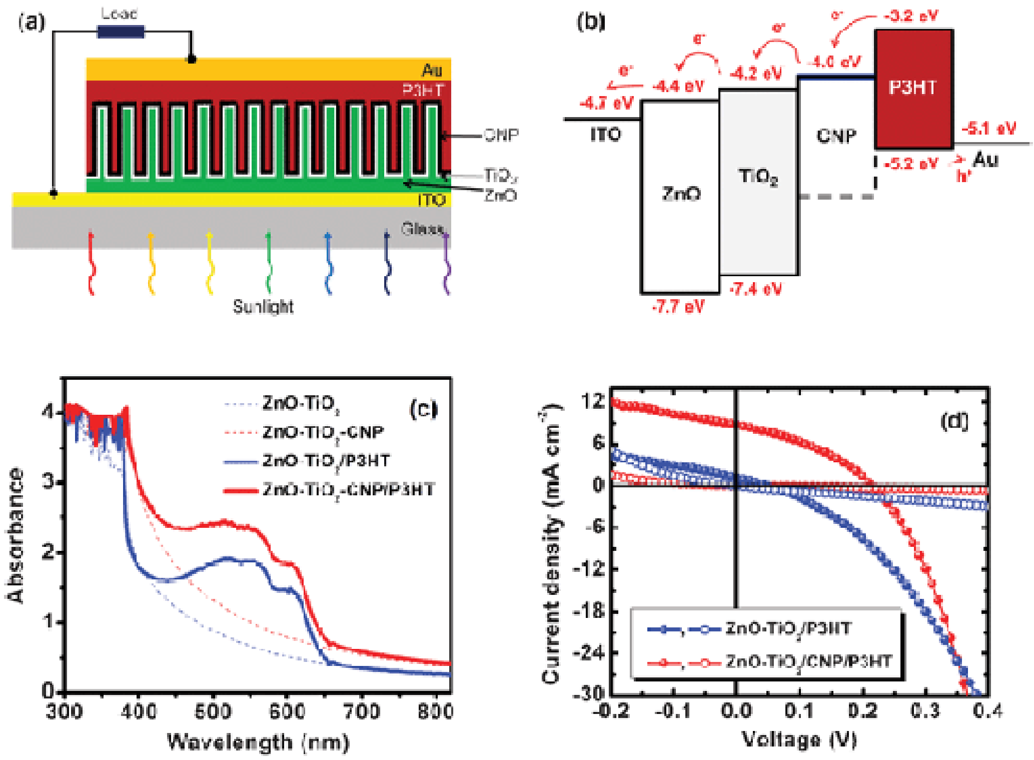

Figure 6. Hybrid solar cell with ZnO-TiO_2 core-shell, carbon nanoparticles (CNP) and conductive polymer P3HT. (a) Device structure; (b) energy-level diagram; (c) absorption spectra of the active films on ITO glass substrates; (d) J-V characteristics (empty: dark; filled: illuminated) of the solar cells with and without CNP [84].

Pairing ZnO with PbS QDs for photovoltaic applications shows high stability in ambient atmosphere. An advantage of using ZnO NWs instead of ZnO planar or nanoparticle layer is demonstrated [86]. Vertically oriented ZnO NW arrays are fully infiltrated with QDs, increasing considerably the light absorption and carrier collection. Ordered interface architecture of ZnO NW arrays can decouple absorption from collection, extending the effective depletion width throughout a thick QD film.

The ZnO NW performance was tested in both earlier mentioned hole conductor configurations: conducting polymer P3HT and PbS QDs [82]. As it is shown in **Figure 7b**, band alignment is similar; however, the PCE of 4.2% and 0.5% for QDs and P3HT, respectively, was obtained. It is worth noting that graphene was used as the conductive electrode instead of the traditional ITO, which demonstrates the flexibility of application for various substrates.

ZnO NW solar-cell absorption in the near-infrared region can be enhanced by using plasmonic nanocrystals (NCs). Ag NC enhances ZnO NW solar-cell (**Figure 8**) PCE from 4.5 to 6.0% [87].

A plasmonic NC traps a photon on the basis of localized surface plasmon resonance, and generates a strong oscillating electric field (i.e. optical near field) that is localized in the vicinity of the NC. The optical near field excites a dye molecule or semiconductor more efficiently than incident far-field light, and therefore photocurrents are enhanced.

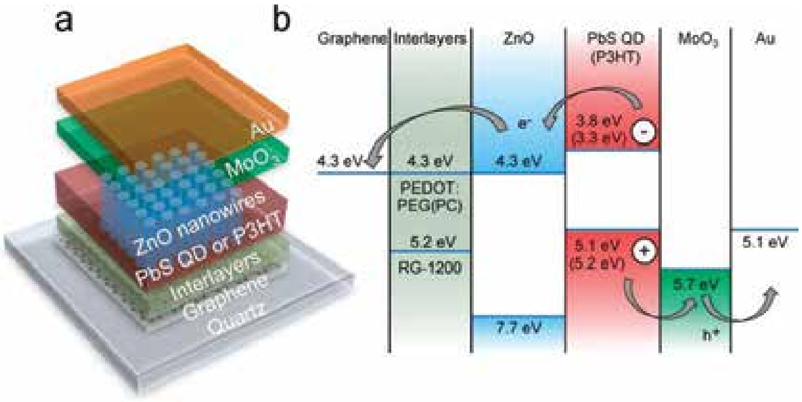

Figure 7. Hybrid ZnO NW solar cells. (a) Schematic diagram of ZnO NWs (400 nm) infiltrated and covered with PbS QDs (300 nm) or P3HT (700 nm); (b) flat-band energy-level diagram of the solar cell [82].

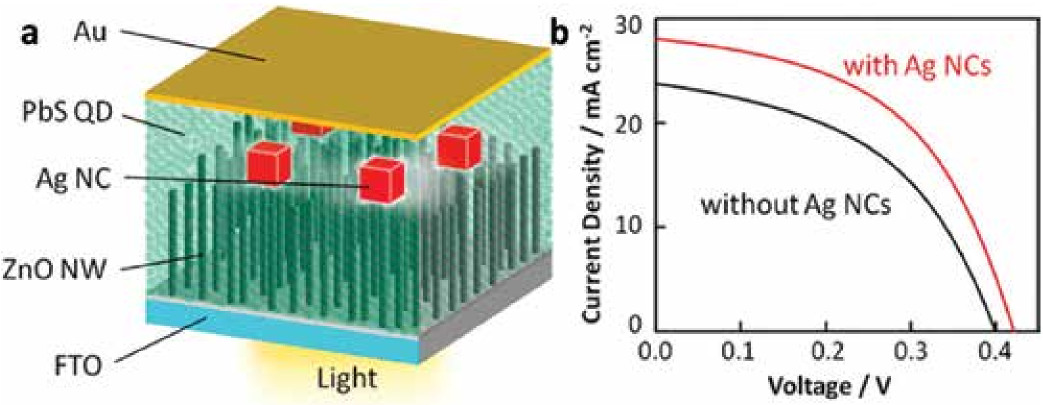

Figure 8. PbS QD/ZnO NW solar cell with embedded Ag NCs. (a) Schematic; (b) J-V characteristics without and with Ag NCs [87].

5. Conclusions

Several conclusions could be made with the proposal for the future trends:

1. First of all, since one of the main parameters for high efficiency of DSC is surface area, more attention should be paid in order to obtain ZnO NW with a structure of high surface, at the same time a virtue of high crystallinity should not be lost. Several possible methods are worth of interest: the obvious trend would be to synthesize nanowires with lower diameter, but the other ways, such as adding NP to the photoelectrode and using NW as charge delivery highway, are also interesting.
2. Non-catalytic growth methods are uncomplicated and much cheaper compared to catalytic ones. Hydrothermal methods have multiple advantages in application since they are low cost and versatile; however, it is problematic to obtain a high aspect ratio structures

with good crystallinity. Nevertheless, these methods are unbeatable for high-yield deposition. A variety of substrates can be used for hydrothermal ZnO NW growth because of the low temperatures used. By contrast, vapour phase growth of ZnO NWs uses higher temperatures, therefore for a low-melting substrates an efficient post-synthesis transferring and attachment methods should be developed; however, high crystallinity can be obtained without further annealing.

3. ZnO NW surface is decomposed in acidic environment of best-to-date dyes, therefore special dyes for ZnO should be developed or alternatively surface modification of ZnO is needed. Best-to-date results are obtained by covering the NW surface with TiO_2 or other semiconductor layer. Alternatively forming a protective layer from dielectric materials such as Al_2O_3 lowers the conductance of photoelectrode, except for an extremely thin layer.

4. Hybrid structures of ZnO NWs are primarily interesting for their high physical and chemical stability, but can also boost other properties such as charge transfer or light absorption; however, more work should be done to understand the underlying mechanisms of ZnO NW interaction with hybrid materials.

Acknowledgements

The work has received funding from the European Union's Seventh Framework programme for research and innovation under the Marie Sklodowska-Curie grant agreement No 609402 – 2020 researchers: Train to Move (T2M).

Author details

Simas Rackauskas*, Nadia Barbero, Claudia Barolo and Guido Viscardi

*Address all correspondence to: simas.rackauskas@gmail.com

Department of Chemistry, NIS Interdepartmental Centre and INSTM Reference Centre, University of Turin, Turin, Italy

References

[1] Mathew S, Yella A, Gao P, Humphry-Baker R, Curchod BFE, Ashari-Astani N, et al. Dye-sensitized solar cells with 13% efficiency achieved through the molecular engineering of porphyrin sensitizers. Nat. Chem. [Internet]. 2014 [cited 2016 Sep 16];6:242-7. Available from: http://www.nature.com/doifinder/10.1038/nchem.1861

[2] Grätzel M. The advent of mesoscopic injection solar cells. Prog. Photovoltaics Res. Appl. [Internet]. John Wiley & Sons, Ltd.; 2006 [cited 2016 Sep 16];14:429-42. Available from: http://doi.wiley.com/10.1002/pip.712

[3] O'regan B, Grätzel M. A low-cost, high-efficiency solar cell based on dye-sensitized colloidal TiO_2 films. Nature. Nature Publishing Group; 1991;353:737-40.

[4] Maçaira J, Andrade L, Mendes A. Review on nanostructured photoelectrodes for next generation dye-sensitized solar cells. Renew. Sustain. Energy Rev. 2013;27:334-49.

[5] Grätzel M. Solar energy conversion by dye-sensitized photovoltaic cells. Inorg. Chem. American Chemical Society. 2005:6841-51.

[6] Bach U, Tachibana Y, Moser J-E, Haque SA, Durrant JR, Grätzel M, et al. Charge separation in solid-state dye-sensitized heterojunction solar cells. J. Am. Chem. Soc. American Chemical Society. 1999;121:7445-6.

[7] Grätzel M. Solar energy conversion by dye-sensitized photovoltaic cells. Inorg. Chem. American Chemical Society. 2005;44:6841-51.

[8] Ye M, Wen X, Wang M, Iocozzia J, Zhang N, Lin C, et al. Recent advances in dye-sensitized solar cells: From photoanodes, sensitizers and electrolytes to counter electrodes. Mater. Today. 2015;18:155-62.

[9] Colodrero S, Forneli A, López-López C, Pellejà L, Míguez H, Palomares E. Efficient transparent thin dye solar cells based on highly porous 1D photonic crystals. Adv. Funct. Mater. [Internet]. WILEY-VCH Verlag; 2012 [cited 2016 Sep 16];22:1303-10. Available from: http://doi.wiley.com/10.1002/adfm.201102159

[10] Wang J, Lin Z. Dye-sensitized TiO_2 nanotube solar cells: Rational structural and surface engineering on TiO_2 nanotubes. Chem. - An Asian J. [Internet]. WILEY-VCH Verlag; 2012 [cited 2016 Sep 16];7:2754-62. Available from: http://doi.wiley.com/10.1002/asia.201200349

[11] Feng X, Zhu K, Frank AJ, Grimes C a, Mallouk TE. Rapid charge transport in dye-sensitized solar cells made from vertically aligned single-crystal rutile TiO_2 nanowires. Angew. Chem. Int. Ed. [Internet]. WILEY-VCH Verlag; 2012 [cited 2016 Sep 16];124:2781-4. Available from: http://doi.wiley.com/10.1002/ange.201108076

[12] Tétreault N, Arsenault É, Heiniger LP, Soheilnia N, Brillet J, Moehl T, et al. High-efficiency dye-sensitized solar cell with three-dimensional photoanode. Nano Lett. [Internet]. American Chemical Society; 2011 [cited 2016 Sep 16];11:4579-84. Available from: http://pubs.acs.org/doi/abs/10.1021/nl201792r

[13] He C, Zheng Z, Tang H, Zhao L, Lu F. Electrochemical impedance spectroscopy characterization of electron transport and recombination in ZnO nanorod dye-sensitized solar cells. J. Phys. Chem. C [Internet]. American Chemical Society; 2009 [cited 2016 Sep 16];113:10322-5. Available from: http://pubs.acs.org/doi/abs/10.1021/jp902523c

[14] Martinson ABF, Goes MS, Fabregat-Santiago F, Bisquert J, Pellin MJ, Hupp JT. Electron transport in dye-sensitized solar cells based on ZnO nanotubes: Evidence for highly efficient charge collection and exceptionally rapid dynamics. J. Phys. Chem. A [Internet]. American Chemical Society; 2009 [cited 2016 Sep 16];113:4015-21. Available from: http://pubs.acs.org/doi/abs/10.1021/jp810406q

[15] Martinson ABF, McGarrah JE, Parpia MOK, Hupp JT. Dynamics of charge transport and recombination in ZnO nanorod array dye-sensitized solar cells. Phys. Chem. Chem. Phys. [Internet]. The Royal Society of Chemistry; 2006 [cited 2016 Sep 16];8:4655-9. Available from: http://www.ncbi.nlm.nih.gov/pubmed/17047762

[16] Zhang Q, Dandeneau CS, Zhou X, Cao G. ZnO nanostructures for dye-sensitized solar cells. Adv. Mater. [Internet]. WILEY-VCH Verlag; 2009 [cited 2016 Sep 16];21: 4087-108. Available from: http://onlinelibrary.wiley.com/doi/10.1002/adma.200803827/abstract%0Ahttp://onlinelibrary.wiley.com/doi/10.1002/adma.200803827/abstract;jsessionid=28F0008F38AEB7367E640662E9AD0B66.f01t04%0Ahttp://onlinelibrary.wiley.com/store/10.1002/adma.200803827/asset/

[17] Law M, Greene LE, Johnson JC, Saykally R, Yang P. Nanowire dye-sensitized solar cells. Nat. Mater. [Internet]. Nature Publishing Group; 2005 [cited 2016 Jul 19];4:455-9. Available from: http://www.nature.com/doifinder/10.1038/nmat1387

[18] Memarian N, Concina I, Braga A, Rozati SM, Vomiero A, Sberveglieri G. Hierarchically assembled ZnO nanocrystallites for high-efficiency dye-sensitized solar cells. Angew. Chem. Int. Ed. [Internet]. WILEY-VCH Verlag; 2011 [cited 2016 Sep 16];50:12321-5. Available from: http://doi.wiley.com/10.1002/anie.201104605

[19] Anta JA, Guille E. ZnO-based dye-sensitized solar cells. J. Phys. Chem. C [Internet]. American Chemical Society; 2012 [cited 2016 Sep 16];116:11413-25. Available from: http://dx.doi.org/10.1021/jp3010025

[20] Jiang WT, Wu C Te, Sung YH, Wu JJ. Room-temperature fast construction of outperformed ZnO nanoarchitectures on nanowire-array templates for dye-sensitized solar cells. ACS Appl. Mater. Interfaces [Internet]. American Chemical Society; 2013 [cited 2016 Sep 16];5:911-7. Available from: http://pubs.acs.org/doi/abs/10.1021/am302570r

[21] Borgwardt M, Wilke M, Kampen T, Mähl S, Xiao M, Spiccia L, et al. Charge transfer dynamics at dye-sensitized ZnO and TiO_2 interfaces studied by ultrafast XUV photoelectron spectroscopy. Sci. Rep. [Internet]. Nature Publishing Group; 2016 [cited 2016 Dec 20];6:24422. Available from: http://www.nature.com/articles/srep24422

[22] Syu Y-K, Tingare Y, Yeh C-Y, Yang J-S, Wu J-J. Panchromatic engineering for efficient zinc oxide flexible dye-sensitized solar cells using porphyrin and indoline dyes. RSC Adv. [Internet]. The Royal Society of Chemistry; 2016 [cited 2016 Sep 30];6:59273-9. Available from: http://xlink.rsc.org/?DOI=C6RA09262D

[23] Lee CP, Chen PW, Li CT, Huang YJ, Li SR, Chang LY, et al. ZnO double layer film with a novel organic sensitizer as an efficient photoelectrode for dye-sensitized solar cells. J. Power Sources. 2016;325:209-19.

[24] Jiang WT, Wu C Te, Sung YH, Wu JJ. Room-temperature fast construction of outperformed ZnO nanoarchitectures on nanowire-array templates for dye-sensitized solar cells. ACS Appl. Mater. Interfaces [Internet]. American Chemical Society; 2013 [cited 2016 Sep 12];5:911-7. Available from: http://pubs.acs.org/doi/abs/10.1021/am302570r

[25] Syu Y-K, Tingare Y, Yeh C-Y, Yang J-S, Wu J-J. Panchromatic engineering for efficient zinc oxide flexible dye-sensitized solar cells using porphyrin and indoline dyes. RSC Adv. [Internet]. Royal Society of Chemistry; 2016 [cited 2016 Sep 12];6:59273-9. Available from: http://xlink.rsc.org/?DOI=C6RA09262D

[26] Çakar S, Güy N, Özacar M, Findik F. Investigation of vegetable tannins and their iron complex dyes for dye sensitized solar cell applications. Electrochim. Acta. Elsevier Ltd. 2016;209:407-22.

[27] Tao L, Huo Z, Ding Y, Li Y, Dai S, Wang L, et al. High-efficiency and stable quasi-solid-state dye-sensitized solar cell based on low molecular mass organogelator electrolyte. J. Mater. Chem. A [Internet]. The Royal Society of Chemistry; 2015 [cited 2016 Dec 20];3:2344-52. Available from: http://xlink.rsc.org/?DOI=C4TA06188H

[28] Dkhissi Y, Huang F, Cheng Y, Caruso RA. Quasi-solid-state dye-sensitized solar cells on plastic substrates. J. Phys. Chem. C [Internet]. American Chemical Society; 2014 [cited 2016 Dec 20];118:16366-74. Available from: http://pubs.acs.org/doi/abs/10.1021/jp408844q

[29] Chang WC, Sie SY, Yu WC, Lin LY, Yu YJ. Preparation of nano-composite gel electrolytes with metal oxide additives for dye-sensitized solar cells. Electrochim. Acta. 2016;212:333-42.

[30] Yang P, Yan H, Mao S, Russo R, Johnson J, Saykally R, et al. Controlled growth of ZnO nanowires and their optical properties. Adv. Funct. Mater. 2002;12:323-31.

[31] Huang MH. Room-temperature ultraviolet nanowire nanolasers. Science (80-.). [Internet]. 2001 [cited 2016 Dec 19];292:1897-9. Available from: http://www.sciencemag.org/cgi/doi/10.1126/science.1060367

[32] Pan ZW, Dai ZR, Wang ZL. Nanobelts of semiconducting oxides. Science (80-.). 2001; 291:1947-9.

[33] Zhang Z, Wang SJ, Yu T, Wu T. Controlling the growth mechanism of ZnO nanowires by selecting catalysts. J. Phys. Chem. C [Internet]. American Chemical Society; 2007 [cited 2014 May 28];111:17500-5. Available from: http://dx.doi.org/10.1021/jp075296a

[34] Sekar A, Kim SH, Umar A, Hahn YB. Catalyst-free synthesis of ZnO nanowires on Si by oxidation of Zn powders. J. Cryst. Growth. 2005;277:471-8.

[35] Rackauskas S, Nasibulin AG, Jiang H, Tian Y, Kleshch VI, Sainio J, et al. A novel method for metal oxide nanowire synthesis. Nanotechnology [Internet]. 2010;20:165603. Available from: http://stacks.iop.org/0957-4484/20/165603

[36] Kleshch VI, Rackauskas S, Nasibulin AG, Kauppinen EI, Obraztsova ED, Obraztsov AN. Field emission properties of metal oxide nanowires. J. Nanoelectron. Optoelectron. [Internet]. 2012 [cited 2016 Nov 28];7:35-40. Available from: http://openurl.ingenta.com/content/xref?genre=article&issn=1555-130X&volume=7&issue=1&spage=35

[37] Rackauskas S, Nasibulin AG, Jiang H, Tian Y, Statkute G, Shandakov SD, et al. Mechanistic investigation of ZnO nanowire growth. Appl. Phys. Lett. [Internet]. 2009 [cited 2013 Oct 3];95:183114. Available from: http://link.aip.org/link/APPLAB/v95/i18/p183114/s1&Agg=doi

[38] Nam D, Park J, Park S, Min Y, Noh Y, Lee D. High-density hydrothermal growth of zinc-oxide nanowires using printed resistive heater. Mater. Lett. 2015.

[39] Wu C, Shen L, Yu H, Huang Q, Zhang YC. Synthesis of Sn-doped ZnO nanorods and their photocatalytic properties. Mater. Res. Bull. 2011;46:1107-12.

[40] Parize R, Garnier J, Chaix-Pluchery O, Verrier C, Appert E, Consonni V. Effects of hexamethylenetetramine on the nucleation and radial growth of ZnO nanowires by chemical bath deposition. J. Phys. Chem. C [Internet]. 2016 [cited 2016 Dec 19];120:5242-50. Available from: http://pubs.acs.org/doi/abs/10.1021/acs.jpcc.6b00479

[41] Cho J, Salleh N, Blanco C, Yang S, Lee C-J, Kim Y-W, et al. Novel synthetic methodology for controlling the orientation of zinc oxide nanowires grown on silicon oxide substrates. Nanoscale [Internet]. 2014 [cited 2016 Dec 19];6:3861-7. Available from: http://www.ncbi.nlm.nih.gov/pubmed/24584438

[42] Xu S, Wang ZL. One-dimensional ZnO nanostructures: Solution growth and functional properties. Nano Res. 2011;4:1013-98.

[43] Gu C, Shanshan L, Huang J, Shi C, Liu J. Preferential growth of long ZnO nanowires and its application in gas sensor. Sens. Actuators, B Chem. 2013;177:453-9.

[44] Hu X, Shen X, Li H, Masuda Y, Ohji T, Kato K. Polyethylenimine-assisted synthesis of transparent ZnO nanowhiskers at ambient temperatures. Thin Solid Films. 2014;558:134-9.

[45] Panigrahy B, Aslam M, Misra DS, Bahadur D. Polymer-mediated shape-selective synthesis of ZnO nanostructures using a single-step aqueous approach. CrystEngComm [Internet]. Royal Society of Chemistry; 2009 [cited 2016 Dec 19];11:1920. Available from: http://xlink.rsc.org/?DOI=b904833m

[46] Caicedo N, Thomann J-S, Leturcq R, Lenoble D. Aspect ratio improvement of ZnO nanowires grown in liquid phase by using step-by-step sequential growth. CrystEngComm [Internet]. The Royal Society of Chemistry; 2016 [cited 2016 Dec 19];18:5502-11. Available from: http://xlink.rsc.org/?DOI=C6CE00904B

[47] Ko SH, Lee D, Kang HW, Nam KH, Yeo JY, Hong SJ, et al. Nanoforest of hydrothermally grown hierarchical ZnO nanowires for a high efficiency dye-sensitized solar cell. Nano Lett. [Internet]. American Chemical Society; 2011 [cited 2016 May 17];11:666-71. Available from: http://dx.doi.org/10.1021/nl1037962

[48] Bielinski AR, Kazyak E, Schlepütz CM, Jung HJ, Wood KN, Dasgupta NP. Hierarchical ZnO nanowire growth with tunable orientations on versatile substrates using atomic

layer deposition seeding. Chem. Mater. [Internet]. 2015 [cited 2016 Dec 18];27:4799-807. Available from: http://pubs.acs.org/doi/abs/10.1021/acs.chemmater.5b01624

[49] Rackauskas S, Klimova O, Jiang H, Nikitenko A, Chernenko KA, Shandakov SD, et al. A novel method for continuous synthesis of ZnO tetrapods. J. Phys. Chem. C [Internet]. American Chemical Society; 2015; Available from: http://dx.doi.org/10.1021/acs.jpcc.5b03702

[50] Rackauskas S, Mustonen K, Järvinen T, Mattila M, Klimova O, Jiang H, et al. Synthesis of ZnO tetrapods for flexible and transparent UV sensors. Nanotechnology [Internet]. 2012;23:95502. Available from: http://www.ncbi.nlm.nih.gov/pubmed/22327417

[51] Lamberti A, Gazia R, Sacco A, Bianco S, Quaglio M, Chiodoni A, et al. Coral-shaped ZnO nanostructures for dye-sensitized solar cell photoanodes. Prog. Photovoltaics Res. Appl. [Internet]. 2014 [cited 2016 Jul 18];22:189-97. Available from: http://doi.wiley.com/10.1002/pip.2251

[52] Pugliese D, Bella F, Cauda V, Lamberti A, Sacco A, Tresso E, et al. A chemometric approach for the sensitization procedure of ZnO flowerlike microstructures for dye-sensitized solar cells. ACS Appl. Mater. Interfaces [Internet]. American Chemical Society; 2013 [cited 2016 Dec 19];5:11288-95. Available from: http://pubs.acs.org/doi/abs/10.1021/am403527m

[53] Kuo S-Y, Yang J-F, Lai F-I. Improved dye-sensitized solar cell with a ZnO nanotree photoanode by hydrothermal method. Nanoscale Res. Lett. [Internet]. 2014 [cited 2016 Dec 19];9:206. Available from: http://www.pubmedcentral.nih.gov/articlerender.fcgi?artid=4022993&tool=pmcentrez&rendertype=abstract

[54] Zhang S, Chen H-S, Matras-Postolek K, Yang P. ZnO nanoflowers with single crystal structure towards enhanced gas sensing and photocatalysis. Phys. Chem. Chem. Phys. [Internet]. The Royal Society of Chemistry; 2015 [cited 2016 Dec 19];17:30300-6. Available from: http://xlink.rsc.org/?DOI=C5CP04860E

[55] Gao R, Tian J, Liang Z, Zhang Q, Wang L, Cao G. Nanorod-nanosheet hierarchically structured ZnO crystals on zinc foil as flexible photoanodes for dye-sensitized solar cells. Nanoscale [Internet]. Royal Society of Chemistry; 2013 [cited 2016 Dec 19];5:1894-901. Available from: http://dx.doi.org/10.1039/C2NR33599A%5Cnhttp://pubs.rsc.org/en/content/articlepdf/2013/nr/c2nr33599a

[56] Law M, Greene LE, Radenovic A, Kuykendall T, Liphardt J, Yang P. ZnO-Al_2O_3 and ZnO-TiO_2 core-shell nanowire dye-sensitized solar cells. J. Phys. Chem. B. American Chemical Society ; 2006;110:22652-63.

[57] Zhang Y, Lu H-L, Wang T, Ren Q-H, Chen H-Y, Zhang H, et al. Photoluminescence enhancement of ZnO nanowire arrays by atomic layer deposition of ZrO_2 layers and thermal annealing. Phys. Chem. Chem. Phys. [Internet]. The Royal Society of Chemistry; 2016 [cited 2016 Dec 19];18:16377-85. Available from: http://xlink.rsc.org/?DOI=C6CP01900E

[58] Bu IYY. Effects of post annealing temperature on formation of alumina core shell on zinc oxide nanowire: optoelectronic properties and dye sensitized solar cell applications. J. Mater. Sci. Mater. Electron. [Internet]. Springer US; 2014 [cited 2016 Dec 19];25:4458-65. Available from: http://link.springer.com/10.1007/s10854-014-2188-4

[59] Li TC, Góes MS, Fabregat-Santiago F, Bisquert J, Bueno PR, Prasittichai C, et al. Surface passivation of nanoporous TiO_2 via atomic layer deposition of ZrO_2 for solid-state dye-sensitized solar cell applications. J. Phys. Chem. C [Internet]. American Chemical Society; 2009 [cited 2016 Jul 19];113:18385-90. Available from: http://pubs.acs.org/doi/abs/10.1021/jp906573w

[60] Loh L, Dunn S. Recent progress in ZnO-based nanostructured ceramics in solar cell applications. J. Nanosci. Nanotechnol. American Scientific Publishers; 2012;12:8215-30.

[61] Greene LE, Yuhas BD, Law M, Zitoun D, Yang P. Solution-grown zinc oxide nanowires [Internet]. Inorg. Chem. 2006 [cited 2016 Jul 20]. p. 7535-43. Available from: http://pubs.acs.org/doi/abs/10.1021/ic0601900

[62] Law M, Greene LE, Radenovic A, Kuykendall T, Liphardt J, Yang P. ZnO-Al_2O_3 and ZnO-TiO_2 core-shell nanowire dye-sensitized solar cells. J. Phys. Chem. B [Internet]. American Chemical Society; 2006 [cited 2016 Jul 19];110:22652-63. Available from: http://pubs.acs.org/doi/abs/10.1021/jp0648644

[63] Pazoki M, Nafari N, Taghavinia N, O'Regan B, Gratzel M, Hagfeldt A, et al. Ab initio study of electronic effects in the ZnO/TiO_2 core/shell interface: application in dye sensitized solar cells. RSC Adv. [Internet]. The Royal Society of Chemistry; 2014 [cited 2016 Jul 19];4:301-7. Available from: http://xlink.rsc.org/?DOI=C3RA45973J

[64] Feng Y, Ji X, Duan J, Zhu J, Jiang J, Ding H, et al. Synthesis of ZnO@TiO_2 core–shell long nanowire arrays and their application on dye-sensitized solar cells. J. Solid State Chem. [Internet]. 2012 [cited 2016 Jul 19];190:303-8. Available from: http://dx.doi.org/10.1016/j.jssc.2012.02.026

[65] Ji X, Liu W, Leng Y, Wang A, Ji X, Liu W, et al. Facile synthesis of ZnO@TiO_2 core-shell nanorod thin films for dye-sensitized solar cells. J. Nanomater. [Internet]. Hindawi Publishing Corporation; 2015 [cited 2016 Jul 19];2015:1-5. Available from: http://www.hindawi.com/journals/jnm/2015/647089/

[66] Gan X, Li X, Gao X, Zhuge F, Yu W. ZnO nanowire/TiO_2 nanoparticle photoanodes prepared by the ultrasonic irradiation assisted dip-coating method. Thin Solid Films. 2010;518:4809-12.

[67] Wang D, Wang W, Ma X, Zhang C, Zhao J, Zhang X. Comparative study on the influence of TiO_2 precursors on ZnO-based dye-sensitized solar cells. Ind. Eng. Chem. Res. [Internet]. American Chemical Society; 2015 [cited 2016 Dec 20];54:12639-45. Available from: http://pubs.acs.org/doi/abs/10.1021/acs.iecr.5b03627

[68] Sakai N, Miyasaka T, Murakami TN. Efficiency enhancement of ZnO-based dye-sensitized solar cells by low-temperature $TiCl_4$ treatment and dye optimization. J. Phys.

Chem. C [Internet]. American Chemical Society; 2013 [cited 2016 Dec 6];117:10949-56. Available from: http://pubs.acs.org/doi/abs/10.1021/jp401106u

[69] Chen W, Qiu Y, Yang S. A new ZnO nanotetrapods/SnO_2 nanoparticles composite photoanode for high efficiency flexible dye-sensitized solar cells. Phys. Chem. Chem. Phys. [Internet]. The Royal Society of Chemistry; 2010 [cited 2016 Dec 18];12:9494-501. Available from: http://xlink.rsc.org/?DOI=c000584c

[70] Liu J, Wei A, Zhao Y, Lin K, Luo F. Dye-sensitized solar cells based on ZnO nanoflowers and TiO_2 nanoparticles composite photoanodes. J. Mater. Sci. Mater. Electron. [Internet]. Springer US; 2014 [cited 2016 Dec 19];25:1122-6. Available from: http://link.springer.com/10.1007/s10854-013-1698-9

[71] Yang J, Lin Y, Meng Y, Lin Y. Oriented ZnO nanotubes arrays decorated with TiO_2 nanoparticles for dye-sensitized solar cell applications. Appl. Phys. A Mater. Sci. Process. 2014;114:1195-9.

[72] Gao R, Cui Y, Liu X, Wang L, Cao G. A ZnO nanorod/nanoparticle hierarchical structure synthesized through a facile in situ method for dye-sensitized solar cells. J. Mater. Chem. A [Internet]. The Royal Society of Chemistry; 2014 [cited 2016 Dec 18];2:4765. Available from: http://www.scopus.com/inward/record.url?eid=2-s2.0-84897711028&partnerID=tZOtx3y1

[73] Ko SH, Lee D, Kang HW, Nam KH, Yeo JY, Hong SJ, et al. Nanoforest of hydrothermally grown hierarchical ZnO nanowires for a high efficiency dye-sensitized solar cell. Nano Lett. [Internet]. American Chemical Society; 2011 [cited 2016 Dec 19];11:666-71. Available from: http://pubs.acs.org/doi/abs/10.1021/nl1037962

[74] Chen W, Qiu Y, Zhong Y, Wong KS, Yang S. High-efficiency dye-sensitized solar cells based on the composite photoanodes of SnO_2 nanoparticles/ZnO nanotetrapods. J. Phys. Chem. A. American Chemical Society; 2010;114:3127-38.

[75] Miles DO, Lee CS, Cameron PJ, Mattia D, Kim JH. Hierarchical growth of TiO_2 nanosheets on anodic ZnO nanowires for high efficiency dye-sensitized solar cells. J. Power Sources. 2016;325:365-74.

[76] Haque Choudhury MS, Kishi N, Soga T. Hot-compress: A new postdeposition treatment for ZnO-based flexible dye-sensitized solar cells. Mater. Res. Bull. [Internet]. 2016 [cited 2016 Dec 18];80:135-8. Available from: https://www.scopus.com/inward/record.uri?eid=2-s2.0-84964068595&partnerID=40&md5=50ce3ec4267cd7360fa5c41dc52d7463

[77] Chang G-J, Lin S-Y, Wu J-J. Room-temperature chemical integration of ZnO nanoarchitectures on plastic substrates for flexible dye-sensitized solar cells. Nanoscale [Internet]. The Royal Society of Chemistry; 2014 [cited 2016 Dec 19];6:1329-34. Available from: http://www.ncbi.nlm.nih.gov/pubmed/24362771

[78] Oosterhout SD, Wienk MM, van Bavel SS, Thiedmann R, Koster LJA, Gilot J, et al. The effect of three-dimensional morphology on the efficiency of hybrid polymer solar cells.

Nat. Mater. [Internet]. Nature Publishing Group; 2009 [cited 2016 Dec 20];8:818-24. Available from: http://dx.doi.org/10.1038/nmat2533

[79] Briseno AL, Holcombe TW, Boukai AI, Garnett EC, Shelton SW, Fréchet JJM, et al. Oligo- and polythiophene/ZnO hybrid nanowire solar cells. Nano Lett. [Internet]. American Chemical Society; 2010 [cited 2016 Dec 20];10:334-40. Available from: http://pubs.acs.org/doi/abs/10.1021/nl9036752

[80] Ravirajan P, Peiró AM, Nazeeruddin MK, Graetzel M, Bradley DDC, Durrant JR, et al. Hybrid polymer/zinc oxide photovoltaic devices with vertically oriented ZnO nanorods and an amphiphilic molecular interface layer. J. Phys. Chem. B. American Chemical Society ; 2006;110:7635-9.

[81] Olson DC, Lee YJ, White MS, Kopidakis N, Shaheen SE, Ginley DS, et al. Effect of polymer processing on the performance of poly(3-hexylthiophene)/ZnO nanorod photovoltaic devices. J. Phys. Chem. B [Internet]. American Chemical Society ; 2007 [cited 2016 Dec 20];111:16640-5. Available from: http://pubs.acs.org/cgi-bin/doilookup/?10.1021/jp0757816

[82] Park H, Chang S, Jean J, Cheng JJ, Araujo PT, Wang M, et al. Graphene cathode-based ZnO nanowire hybrid solar cells. Nano Lett. [Internet]. American Chemical Society; 2013 [cited 2016 Dec 20];13:233-9. Available from: http://pubs.acs.org/doi/abs/10.1021/nl303920b

[83] Thitima R, Patcharee C, Takashi S, Susumu Y. Efficient electron transfers in ZnO nanorod arrays with N719 dye for hybrid solar cells. Solid. State. Electron. 2009;53:176-80.

[84] Li Y, Li S, Jin L, Murowchick JB, Peng Z. Carbon nanoparticles as an interfacial layer between TiO_2-coated ZnO nanorod arrays and conjugated polymers for high-photocurrent hybrid solar cells. RSC Adv. [Internet]. Royal Society of Chemistry; 2013 [cited 2016 Dec 20];3:16308. Available from: http://xlink.rsc.org/?DOI=c3ra42614a

[85] Moreels I, Lambert K, Smeets D, De Muynck D, Nollet T, Martins JC, et al. Size-dependent optical properties of colloidal PbS quantum dots. ACS Nano [Internet]. American Chemical Society; 2009 [cited 2016 Dec 21];3:3023-30. Available from: http://pubs.acs.org/doi/abs/10.1021/nn900863a

[86] Jean J, Chang S, Brown PR, Cheng JJ, Rekemeyer PH, Bawendi MG, et al. ZnO nanowire arrays for enhanced photocurrent in PbS quantum dot solar cells. Adv. Mater. [Internet]. WILEY-VCH Verlag; 2013 [cited 2016 Dec 20];25:2790-6. Available from: http://doi.wiley.com/10.1002/adma.201204192

[87] Kawawaki T, Wang H, Kubo T, Saito K, Nakazaki J, Segawa H, et al. Efficiency enhancement of PbS quantum Dot/ZnO nanowire bulk-heterojunction solar cells by plasmonic silver nanocubes. ACS Nano [Internet]. American Chemical Society; 2015 [cited 2016 Dec 20];9:4165-72. Available from: http://pubs.acs.org/doi/abs/10.1021/acsnano.5b00321

Chapter 5

Solution-Processable Nanowire Field-Effect Transistors

Maxim Shkunov, Grigorios Rigas and
Marios Constantinou

Additional information is available at the end of the chapter

http://dx.doi.org/10.5772/intechopen.68800

Abstract

Solution-processable single-crystalline inorganic semiconducting nanowires are excellent building blocks for printable electronics requiring high performance of semiconducting components. Excellent charge carrier mobilities of crystalline nanowires combined with solvent-based nanowire processing open up possibilities for low-cost nanowire electronics targeting a variety of applications ranging from flexible circuits to chemical and biological sensors. Nanowire field-effect transistors are key devices for most of such applications. Recent developments in controllable nanowire positioning and orientation on the substrates and electrical property selection provide the necessary technological breakthroughs enabling the fabrications of reproducible nanowire transistors. In this chapter, we discuss the nanowire assembly methods and high-spatial-resolution scanning probe microscopy techniques towards scalable fabrication of high-performance printable nanowire field-effect transistors.

Keywords: inorganic semiconducting nanowires, printed electronics, field-effect transistors, solution processability

1. Introduction

The growing interest for printed electronics using functional nanomaterials is due to a plethora of conventional and novel applications that can be generated at a fraction of the cost as compared to conventional microelectronic device fabrication involving multiple photolithographic and etching steps. These applications include flexible circuits [1], biological and chemical sensors [2–4], photovoltaic and piezo energy harvesting [5–7], low-dissipation power electronics [8], terahertz detectors [9, 10], memory storage devices [11], artificial e-skin sensors [12], flexible displays [13] and optoelectronic devices [14] including lasers [15, 16]. One-dimensional inorganic semiconductors in the form of single-crystalline nanowires

(NWs) hold most of the promise to act as a backbone for these applications. This is due to nanowires' excellent charge transport properties, the availability of both direct and indirect bandgap semiconducting materials, high aspect ratios allowing nanowires to bridge typical device electrode gaps, solution processability, chemical stability, room temperature deposition capabilities and compatibility with a variety of substrates including both rigid and flexible substrates such as plastics and paper. Separation of nanowire growth from the device assembly allows to employ low-temperature, bottom-up device fabrication approach utilising solution processing of nanowire devices. General nanowire device fabrication process flow is illustrated in **Figure 1**, where synthesised nanowires are dispersed in organic solvents for form functional inks, and then solution-based deposition is used to assemble nanowires on substrates, ideally with a good degree of nanowire orientation and positioning in respect to device electrodes. Density of nanowires after solvent-based disposition is defined by the type of the device and can vary significantly from monolayer coverage for transistor devices to very dense layers intended as energy storage electrodes in, for example, Li-ion batteries [17]. The devices are then finished by depositing the required counter-electrodes, dielectric

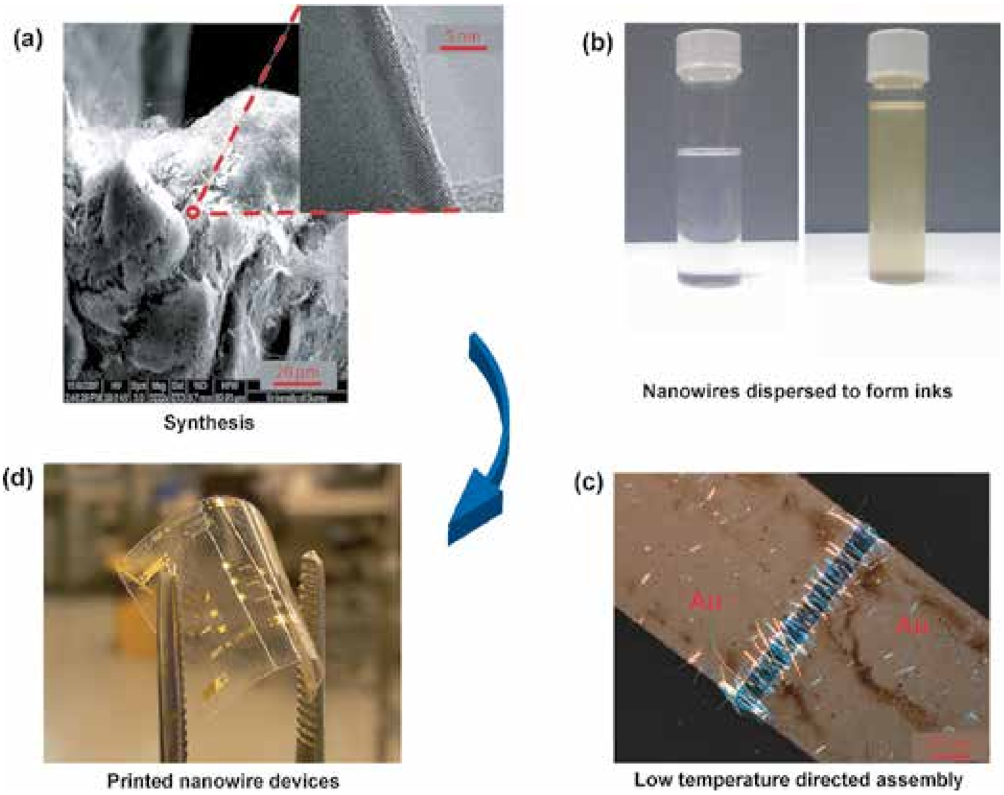

Figure 1. A concept of printable nanowire electronics on flexible substrates, where NW powder (a) is dispersed to form semiconducting nanowire inks (b), followed by aligned deposition of nanowires between device electrodes (c), and finished device can be fabricated at low-temperature process compatible with plastic substrates (d). (b) shows example of ZnO NW ink on the left and Si NW ink on the right.

layers and conducting tracks and also encapsulation layers, if devices need protection from the environment.

Reproducible positioning and alignment of nanowires with respect to device electrodes have been one of the key challenges in solution-processed nanowire electronics and has attracted a significant research effort. Advances toward nanowire assembly from liquid-based 'inks' onto device substrates are discussed in Section 3, paying attention to positioning, alignment and orientation. Recent progress toward selective nanowire deposition using dielectrophoresis is discussed in relation to separation of nanowires with different physical dimensions, such as lengths, and also selection based on the their electrical properties and types of nanowires.

Nanowire surface states play an important role in the corresponding device electrical characteristics, and large surface-to-volume ratio of nanowires opens, on one hand, enormous opportunities for surface receptor functionalisation toward chemical and biological sensors and, on the other hand, can lead to undesirable electrical hysteresis effects due to the presence of surface trap states that need to be eliminated. Further discussion of nanowire surface functionalisation and passivation methods towards stable, hysteresis-free device operation is described in Section 4.

Multiple nanowire channel devices raise particular characterisation challenges associated with both good contact formation between the nanowires and electrodes and also the need to identify nanowires which fully connect the device electrodes and those that do not participate in the conduction mechanism. Characterisation methods based on conducting scanning probe microscopy techniques are discussed in Section 5 in relation to conducting and semiconducting nanowires to probe their positioning, morphology, conductivities and other physical parameters.

2. Nanowire transistor device structures

Field-effect transistors (FETs) are key building blocks for modern electronics as they provide a variety of functions essential for analogue and digital electronics. Printable electronic fabrication approach is highly beneficial for a variety of senor transistor applications, including chemical and biological sensing and tensile and optical sensing, where extremely dense transistor integration is not required, and in many cases, sensors need to be positioned some distance apart from each other to allow, for example, transistor functionalisation with chemical or biological receptors.

Traditional microelectronic fabrication involves mainly top-down processes, such as masking; etching; stripping; ion implantation, with multiple photolithographic steps; and high-temperature annealing (often around 900°C), resulting in high amount of chemical waste required for the processing and very significant amount of energy use.

Printable electronics is based around the concept of bottom-up fabrications with additive manufacturing steps aimed at building the devices by functional inks printing and deposition techniques involving consecutive printing of conducting, semiconducting, and dielectric layers and components. These functional inks thus need to contain nanoparticles and/or material providing the necessary properties. Examples include semiconducting nanowire inks, metal nanoparticle inks and polymer dielectric inks. Printable nanowire FETs can be fabricated by various deposition techniques, with specifics related to the particular conductor, semiconductor, or dielectric materials. Metal nanoparticle ink deposition for nanowire FET electrodes, for example, can be performed by ink-jet printing [18], whereas popular gate dielectric deposition for NW FETs is by spin-coating polymer insulator materials [19]. Semiconductor nanowire transistor channel plays a defining role in the FET operation, so more attention will be devoted to the NW assembly as discussed in the next section.

FET device structures that are fully compatible with solution-based printing fabrication belong to thin-film transistor family and are represented by bottom-gate FETs and top-gate FETs. **Figure 2** is showing schematics for both types of NW FETs.

Top- and bottom-gate NW FET structures each have particular advantages: Bottom-gate structure is ideal for sensing applications, where NW channel area is fully exposed on the top to chemical or biological analytes. Additionally, bottom-gate design offers straightforward device prototyping when using commercially available oxidised silicon (Si/SiO$_2$) wafers, which can be directly used as the substrate, incorporating conducting common gate, highly doped Si and gate dielectric SiO$_2$. Such substrates are also highly amenable for ink-jet printing for electrode deposition.

Top-gate transistor architecture allows better gate control over nanowire channel due to wrap-around gate dielectric geometry, naturally occurring after the dielectric deposition. Importantly, top-gate FETs demonstrate improved environmental stability due to nanowire channel encapsulation provided by the gate dielectric together with metal gate electrode covering the channel, thus protecting nanowires from atmospheric exposure [20].

Main challenges in printable NW FET fabrication (Section 3) are due to deposition and controllable alignment of nanowires, which need to bridge the device electrodes; reproducible number of nanowires in FETs; and solvent-based deposition and alignment compatible with large-scale printing.

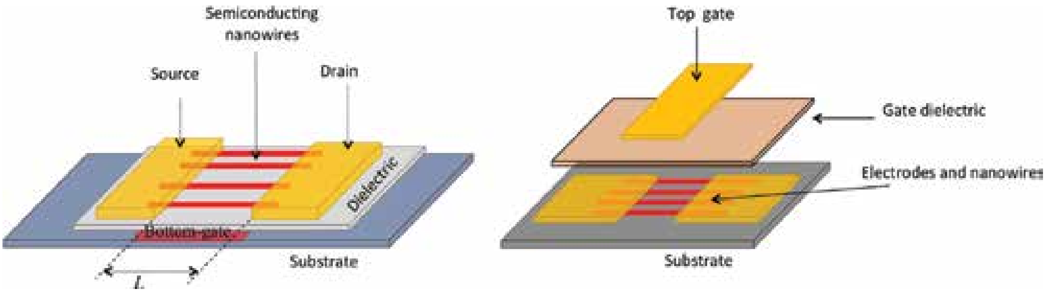

Figure 2. Schematics of bottom-gate (a) and top-gate (b) nanowire FETs.

Surface states are always present in nanomaterials due to their high surface area, and they play an important role in nanowire device performance. Thus, interface properties of nanowires need to be controlled to eliminate unwanted electrical hysteresis effects as discussed in Section 4.

3. Nanowire assembly

The bottom-up fabrication approach for nanowire transistors relies on the availability of grown nanowire materials and also on the efficient assembly methods for nanowire solvent-based deposition. The NW synthesis has been demonstrated using various methods, including supercritical fluid-liquid-solid growth (SFLS) for Si and Ge NWs [21], vapour liquid solid (VLS) growth for Si nanowires and the laser ablation for SnO_2 nanowires [22]. For the preparation of the NW formulations, the as-synthesised NWs are typically dispersed in various organic solvents using low-power sonication process for short periods of time to gently remove nanowires from the growth substrates and to promote homogeneous distribution of nanowire materials in the solvent.

Nanowire deposition and alignment on device substrates represent the next fabrication step. Several self-assembly techniques have been developed in the past for transferring the NWs onto the microelectrode structures to form the conducting channels of the FET devices. The main challenges in self-assembly are the precise alignment and positioning of the nanowires on predefined electrode areas and the purification and selection of nanowires with desired electrical properties. Most of the reported assembly techniques, apart from dielectrophoresis (DEP) provide no or very limited control of NW lateral alignment and no electrical properties selection. In this section, various NW deposition methods are discussed, and more attention is paid to the DEP process enabling electrical and morphological properties' selectivity.

3.1. Nanowire alignment techniques

A number of techniques have been developed for the alignment and deposition of NWs on the substrates, including Langmuir-Blodgett (LB), blown-bubble films (BBF), flow-directed assembly, electrostatic interactions, mechanical shear forces and electric field-assisted assembly with dielectrophoresis.

The Langmuir-Blodgett deposition is a very powerful technique for the alignment of high-density arrays of parallel nanostructures over large areas with a precise spacing between nanoparticles from μm down to nm scale. The method was first reported for barium chromate nanorods [23], with inspiration taken from centuries-old technique for timber-floating on rivers [24]. The technique has been adapted and developed to assemble a variety of nanowires from metallic silver NWs [25] to semiconducting nanowires, including silicon [26]. In the LB technique, the surfactant-wrapped NWs (e.g. 1-octadecylamine) are dispersed on the water surface of a Langmuir-Blodgett trough. Due to the impartial surfactant's solubility in water, the NWs are floating on the surface of the trough. Then, computer-controlled barriers, positioned at the edges of the LB trough, slowly compress the NWs to a higher density at the surface. The density of the monolayer, which depends on NW-to-NW stacking, is mainly limited by the amount of the suspended NWs, and their direction of alignment is dictated by the barrier orientation of the LB trough. Barrier compression causes NWs to reorient and to align parallel to the trough barrier edge, forming a highly dense monolayer. Then the NW layer can be transferred to a substrate, such as silicon wafer; however, some degree of misalignment can occur during the transfer of nanowire from the surface of the trough onto the solid substrate. This LB technique is compatible with large-area electronic fabrication; however, it is difficult to control the NW alignment yield and reproducibility of the alignment on top of the FET source-drain electrode structures [25, 26], and no lateral nanowire alignment is typically obtained.

The blown-bubble film assembly technique is able to provide uniformly aligned and controlled density of NW by utilising a bubble expansion process [27]. The surface of nanomaterials is chemically functionalised, and then, nanowires are mixed with epoxy resin. For example, Si NWs are modified using 5,6-epoxyhexyltriethoxysilane, dispersed into tetrahydrofuran and then homogenously mixed with a known mass of epoxy resin. Afterward, a bubble is expanded from the epoxy-nanomaterial viscous formulation at a controlled direction and speed, and then bubble surface is touched by a substrate to transfer the nanowires resulting in well-defined nanomaterial-incorporated thin films. The alignment of the nanomaterials is mainly attributed to the shear stress present in the epoxy fluid during the bubble expansion

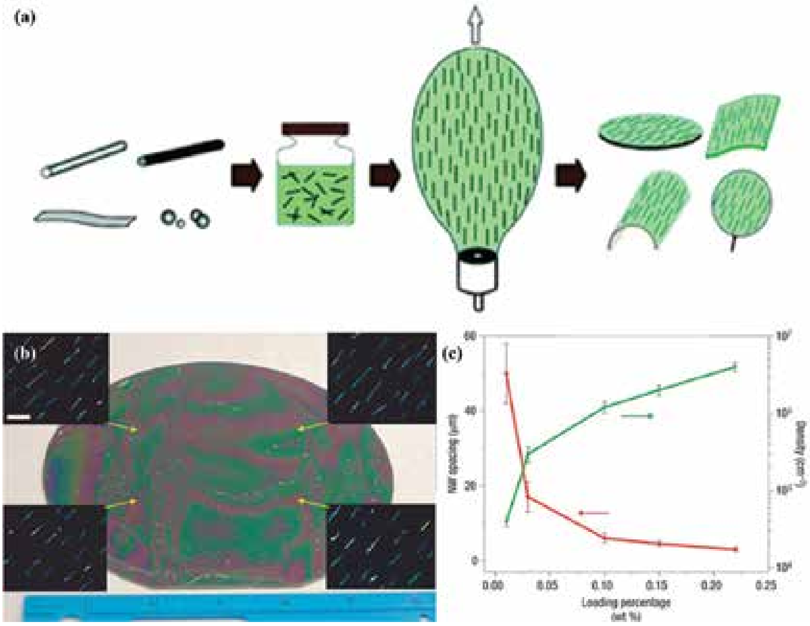

Figure 3. (a) Schematic of the BBF technique. The nanomaterials are dispersed in polymer solution, the solution is expanded as a bubble using a die, and then the uniformly aligned nanomaterials are transferred to different substrates including plastics. (b) Optical image of 6 inch Si wafer with aligned Si NWs (scale bar, 10 μm). (c) Density vs. concentration curve, indicating the density can be controlled by loading a percentage of nanomaterials [27]. © The Royal Society of Chemistry 2008.

process (**Figure 3a**). The viscosity of the homogeneous solution is the key parameter for the uniform distribution of nanomaterials in the resulting bubble films (**Figure 3b–c**). This technique provides a dense and uniform NW distribution suitable for large-area applications, and it is applicable to both rigid and flexible substrates. Although, it requires a large sample volume of NWs, the residual epoxy resin needs to be removed in order to define electrical contacts for NW FET applications, and it is difficult to control the number of the aligned NWs across the source-drain FET electrodes [27]

Highly aligned and dense nanowire packing was demonstrated by flow-directed assembly of nanowires in a microfluidic channel structure formed between poly(dimethylsiloxane) (PDMS) mould and a flat substrate (Si/SiO$_2$ modified with amine functionality). Assembled arrays of NWs, formed by passing the suspended NWs through the microfluidic channels, were aligned along the flow direction. The shear flow near the surface of the substrate immobilised the NWs and aligned them along the flow. At high flow rates, larger shear forces were produced and led to better alignment. This technique provided a controlled NW density and a flexibility to meet complex device configurations. However, the alignment process was attainable only for NWs with diameter <15 nm, it required the fabrication of microfluidic channels, it was challenging to scale up the process to large wafers, it was difficult to control the number of the aligned NWs across the source-drain FET electrodes and no lateral nanowire alignment was achievable [28, 29].

The electrostatic interaction method for nanowire assembly was developed by Heo et al. [30], and it relied on the electrostatic interactions of the positively charged surfaces of the semiconducting nanomaterials with the negatively charged surface of the substrate. Si NWs were functionalised with amine-terminated aminopropyltriethoxysilane (APTS) self-assembled monolayer (SAM) and well dispersed in aqueous solution. Then Si NWs were deposited on negatively charged substrates (i.e. SiO$_2$) with hydrophobic octadecyltrichlorosilane patterns. Therefore, the positively charged NWs were attracted and aligned by the negatively charged APTS surface regions of the substrate. This technique was able to prepare arbitrarily shaped patterns using conventional microfabrication facilities; nonetheless it required the removal of the APTS SAM on the Si NWs with buffer oxide etching process.

A nanowire contact printing method was developed by et al. [31] which utilises the shear forces generated by mechanically sliding two solid surfaces, giving a high degree of order of assembled NWs. In this method two substrates are needed, namely, the donor and the receiver substrate. The donor substrate is covered with a dense "lawn" of NWs, while the receiver is coated with lithographically patterned resist. The method is based on a contact printing process by sliding the surfaces of the two substrates against each other under gentle pressure (**Figure 4a**). Also, lubricant is used to minimise the NW-NW mechanical friction and their uncontrolled breakage during the sliding process. During printing, NWs are transferred from the donor substrate to the receiver substrate by the van der Waals interactions, resulting in the direct alignment of a dense monolayer array of NWs (**Figure 4b–e**). This technique offers the ability to transfer monolayer arrays of NWs on both rigid and flexible substrates with a controllable density. The disadvantage of this technique is the lack of control of the number of the aligned NWs across the source-drain FET electrodes, and NWs tend to break during the transfer process [29, 31].

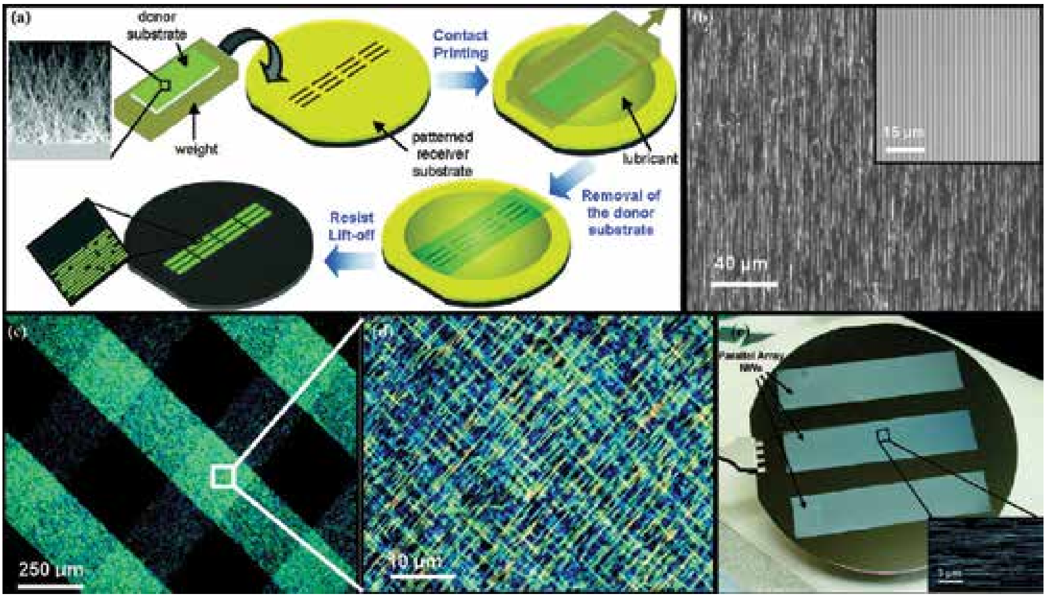

Figure 4. (a) A schematic illustration of the contact printing method. (b) Optical image of the assembly of Ge NWs on a Si/SiO_2 substrate. (c–d) Optical images of a cross assembly printing of Si NWs. (e) Printed Ge NWs on a 4 inch Si/SiO_2 wafer, including an inset SEM image of the printed NWs [31]. © 2008 American Chemical Society.

The electric field-assisted assembly known as dielectrophoresis (DEP) is currently the most promising nanowire assembly technique for the self-alignment of nanomaterials. During a DEP process, a polarisable nanoparticle, suspended in a liquid, is subjected to a non-uniform alternating electric field (AC), and its charges separate and accumulate at the surface, forming a dipole, which experiences the force dependent on the gradient of the electric field resulting in NW self-assembly across the electrode gap [32, 33]. The working principle of DEP is based on the balancing of NW-NW interaction and dielectrophoretic and opposing hydrodynamic drag forces. When the NW "ink" (nanowire dispersion) flows over the electrode gap with applied AC electric field, it gets polarised and attracted to the regions with the strongest electric field gradient, resulting in nanowire deposition across the electrode gap by means of dielectrophoretic forces (F_{DEP}), as illustrated in **Figure 5a**. The deposition of NWs across the FET source-drain electrodes mainly depends on the difference in the dielectric properties (ε) of the nanomaterial and the medium, based on the Clausius-Mossotti factor (CMF) and the electric field gradient. As opposed to previously mentioned nanowire assembly techniques, the DEP method requires very small volumes of NW dispersion (a few μL per DEP alignment), and it offers a precise, dense and controllable deposition of NW monolayer arrays on predefined electrode structures with a high degree of orientation control as shown in **Figure 5b–d**. The NW density can be controlled by tailoring the NW concentration in the formulation and the applied DEP signal voltage [33, 34].

3.2. Self-assembly and purification of nanowires

Some of the key challenges in solution-processed NW applications are the simultaneous purification, selection, and alignment of NWs on the desired substrate areas, which have attracted

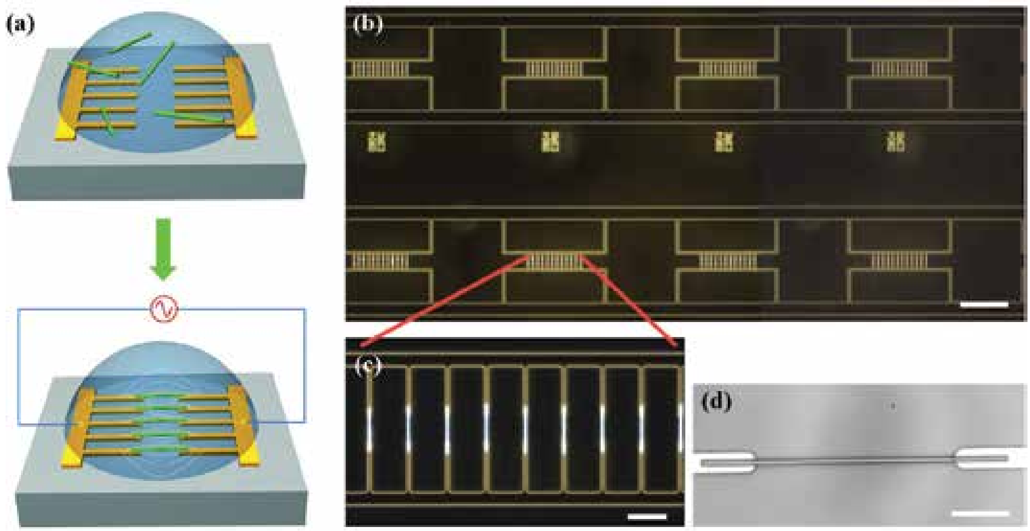

Figure 5. (a) Graphical illustration of dielectrophoretic assembly [1]. © 2012 American Chemical Society. (b) Optical image of NW assembly on eight multi-finger electrode arrays of total 96 sites (scale bar, 200 μm). (c) Precision alignment of NWs on a single sense array (scale bar, 20 μm). (d) Deep ultraviolet image of a NW aligned on a single electrode (scale bar, 4 μm) [34]. © 2010 Macmillan Publishers Limited.

a significant research effort. Despite the substantial progress in NW assembly demonstrated with LB, BBF, flow-directed assembly, electrostatic interactions and mechanical shear forces, the simultaneous precise deposition of NWs with respect to device electrodes and the selective deposition of NWs based on morphological or electrical properties received little attention, and NWs were typically deposited as-synthesised, which affected device reproducibility, performance and reliability.

The first precise orientation positioning, selective deposition and separation of single Si NWs based on their electrical quality from a mixture of other types of nanowires were demonstrated using DEP with capillary assembly by Collet et al. [35]. The combination of both DEP and capillary assembly involved dragging the liquid meniscus of the NW solution on top of the substrate, with a controlled velocity and temperature which led to the trapping of single NWs by the DEP forces on predefined locations coupled with the capillary force acting to align the nanowires. The DEP force trapped the NWs and also adjusted their orientation at the surface of the electrodes followed by the liquid evaporation. A mixture of monodispersed Si, ZnO and InAs nanowires dispersed in isopropanol was used in this study.

The precise orientation of the NWs was achieved by employing stronger electronic polarisation along the long NW axis as compared to the short axis under the application of the AC electric field. In the case of Si NWs, the optimum capture frequency was obtained at 50 kHz and for InAs and ZnO were 500 kHz and 2 MHz, respectively. The authors argued that each NW exhibits its own specific signature based on their electrical properties, which leads to the assembly of different nanostructures at different frequencies. As a proof of concept, the authors provided separation and precise alignment of single Si and InAs nanowires from NW mixture containing both types of nanowires, into alternating columns on the substrate, by switching the applied frequency between 50 and 500 kHz in each column of DEP electrodes, once the meniscus of the NW solution reached the desired set of electrodes. This work has successfully demonstrated a separation of nanowires with different electrical conductivities by examining their optimum capture frequency, which is influenced by the conductivity and level of doping.

Key progress in DEP nanowire selection and purification was demonstrated by Constantinou et al. [33] by developing a scalable one-step solution process for the selection, collection and ordered assembly of Si NW arrays (**Figure 6a**) with desired electrical properties from a polydisperse as-synthesised NW dispersions. The method was applied to SFLS-grown Si NWs with various lengths, diameters and electrical conductivities. The technique utilised the fluidic shear forces coupled with DEP self-alignment to position high-quality NWs with the lowest level of traps across the electrode gap and to remove weakly interacting NWs and

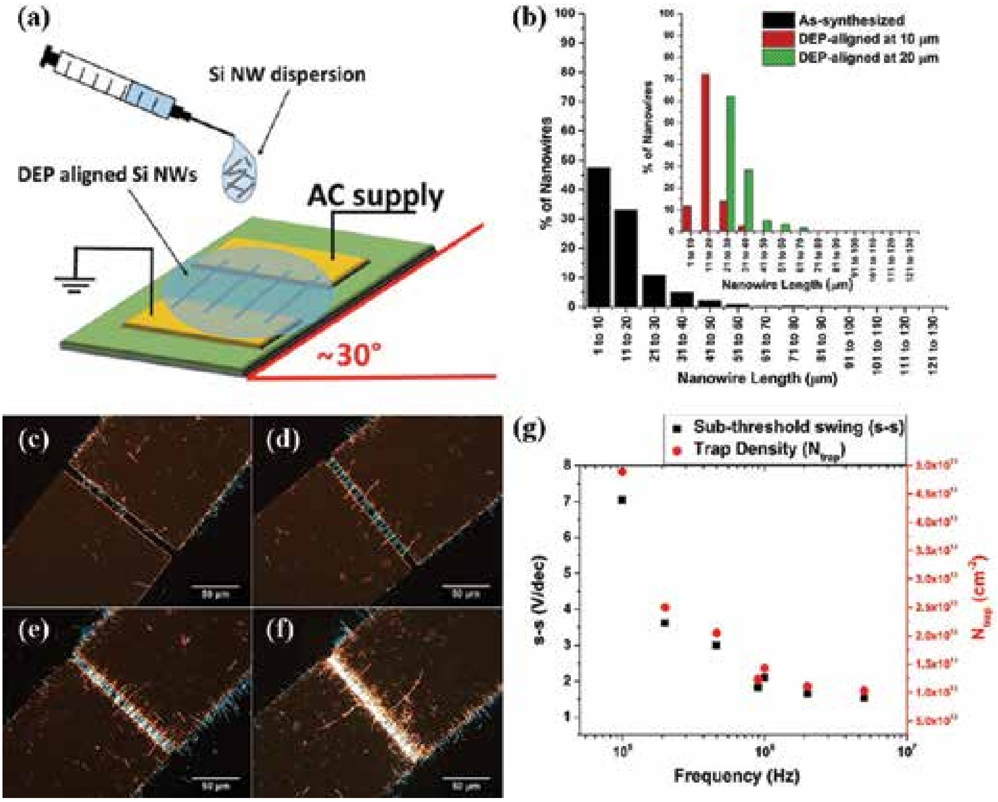

Figure 6. (a) Graphical illustration of the fluidic shear force with DEP technique used for the NW deposition and DEP alignment. The substrate was tilted at approximately 30° angle (versus horizontal plane) to provide gravity-assisted flow of NW dispersion. (b) Length histogram of NWs collected by DEP across two different electrode gaps, 10 and 20 μm. Controllable DEP alignment of SFLS Si NWs across parallel electrode bas with 10 μm spacing at (c) 5 V, (d) 10 V, (e) 15 V and (f) 20 V. (g) Subthreshold swing (s-s) and NW trap density (N_{trap}) data extracted from transfer characteristics of FETs for NWs collected from 100 kHz to 5 MHz [33]. © 2016 American Chemical Society.

impurities from the device channel region. The DEP assembly process employed a drop-cast method on an inclined substrate to provide a gravity-assisted slow flow of NW formulations perpendicular to the pre-patterned DEP electrode gap after the DEP sinusoidal signal was applied (**Figure 6c–f**). The DEP selectivity based on the NW electrical parameters was controlled by altering the frequency dependence of the DEP force. The DEP method coupled with fluidic shear forces offered a high degree of flexibility for NW positioning with NWs being oriented along the channel and perpendicular to the electrode edges. Importantly, the DEP also served as a nanowire length selection tool by providing the strongest interactions for the NWs with lengths at least the same size as the electrode gap or slightly longer opening the possibility for a sequential separation of NWs by length (**Figure 6b**). Main advancement of the method was in systematical examination of the electrical response of the Si NWs aligned at various DEP signal frequencies. It was highlighted that the F_{DEP} is frequency dependent and the level of polarisability is related to the conductivity of the nanostructure, allowing the selection of highly conducting NWs by altering the applied DEP frequency. Thus, lower frequency range collects NWs with various qualities including poor quality that may contain defects and associated traps, while high frequencies induce the collection of only the highest quality, low-defect semiconducting Si NWs, with higher conductivity. The electrical properties of the NWs aligned at various frequencies were compared using FET devices by extracting both subthreshold swing (s-s) and trap density (Ntrap) data as shown in **Figure 6g** and via conducting atomic force microscopy analysis. As a proof of concept, high-performance Si NW FETs with excellent performance were demonstrated with high FET on-currents in the mA range and low subthreshold swing (s-s) and trap density.

The proposed methodology enables the effective selection and assembly of heterogeneous nanowires of any type and provides a printed electronic fabrication approach that can be scaled up for industrial applications.

4. Surface modification approaches for nanowire FETs

The undesirable electrical hysteresis effect in NW FETs is one of the main sources for performance instabilities, which affects the reproducibility and potential applications of NW FETs such as sensors, circuits elements and logic gates, that causes a shift in the threshold voltage (V_{TH}) during normal device operation under gate bias stress. In most FET applications, besides memory devices, even a small degree of hysteresis is unwanted.

The hysteresis behaviour mainly originates from electron or hole trapping/detrapping at the semiconductor/insulator interface due to dielectric surface functionalities and adsorbed small molecules (e.g. oxygen and water). Typically such interface trapping is very strongly pronounced in bottom-gate NW FETs with SiO_2 gate dielectric [36], where silanol groups trap charges at the interfacial layer between the semiconductor material and the gate dielectric [37]. In NW FETs, the hysteresis also originates from the NW surface traps, and it is observed in moisture-free environments and ambient air conditions, highlighting the demand for NW passivation. In this section, we describe NW surface passivation methods with an oxide shell for minimising hysteresis effects.

4.1. Silicon nanowire surface passivation methods

The majority of the NW surface passivation methods include high-temperature annealing which is not suitable for plastic electronic applications. However, successful passivation results for Chemical Vapour Deposition grown Si NWs have been demonstrated by Kawashima et al. [38] and Wang et al. [39]. Both approaches focused on the synthesis of core-shell Si NWs with the core acting as a channel and the shell acting as a gate dielectric.

Kawashima et al. [38] investigated the growth of a 24-nm thermal oxide layer on the surface of Si NWs (forming a core-shell structure) using rapid thermal processing in an oxygen atmosphere at 1100°C for 2–6 min. The authors compared the I–V characteristics of bare and core-shell Si NW FETs, although hysteresis appeared in both cases with a much smaller effect on the core-shell Si NW FETs than the bare Si NW FETs. The results proved that the hysteresis is drastically reduced by the formation of the oxide shell around the Si NW core, effectively passivating the Si NW surface and preventing the adsorption of oxygen and moisture which cause hysteresis. In a similar approach by Wang et al. [39], a silicon nanowire core was covered with a 10-nm-thick SiO_2 shell at lower annealing temperature (700°C) but for a much longer time duration (4 h), also resulting in near-zero hysteresis in devices.

A different approach [40] demonstrated thermal oxidation using ozone for forming a good quality 5-nm-thick SiO_2 shell layer obtained at 600°C processing temperature. However, such high-temperature annealing is not fully suitable for printed electronic applications, and a low-temperature process is still required.

A very efficient method for nanowire passivation that results in a dramatic reduction of surface trap states on Si NWs was demonstrated by Constantinou et al. [41]. This method is ideally suited for nanomaterials intended for printed electronic applications, as it is quick, fully solution based and conducted at room temperature and normal pressure. The passivation phenomenon was directly linked to the interfacial mild oxidation effect induced by the processing solvent.

Dimethylformamide (DMF) solvent treatment was used to directly reduce the hysteresis effect in solution-processed SFLS-grown Si NW FET devices [41]. The choice of solvents for the NW dispersion had a dramatic impact on the NW surface trap density and on the hysteresis effect. The undoped Si NWs were dispersed in both anisole and DMF, with DMF solvent-processed FETs exhibiting significantly low hysteresis of ~3 V, with the lowest reported hysteresis value being 0.1 V (**Figure 7a**), whereas the average hysteresis values of FETs based on nanowires dispersed in anisole were 25–32 V. Thus, DMF passivation effect of the Si NW shell resulted in a drastically suppressed NW FET hysteresis with up to 300 times (from 32 to 0.1 V) reduction as compared to anisole dispersion solvent [41]. For the investigation of the NW surface passivation, high-resolution X-ray photoelectron spectroscopy (XPS) technique was used to analyse the surface of the DMF- and anisole-treated Si NWs. It was observed that DMF-treated Si NWs showed a significant 35% increase of SiO_2 composition of NW shell around the core compared to the reference sample (dry NWs) as shown in **Figure 7b**. The formation of a SiO_2 -rich shell passivates the Si core channel area and provides stability against environmental ageing and prevents the adsorption of water molecules that are responsible for the hysteretic behaviour of the Si NW FETs (**Figure 7c**). As a further study, the DMF-treated devices were exposed to

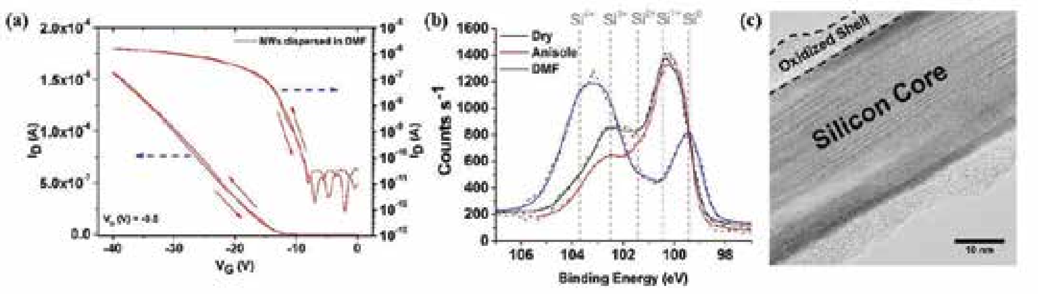

Figure 7. (a) I–V characteristics of DMF-treated Si NW FET showing a very low hysteresis of 0.1 V. (b) XPS high-resolution spectrum of the Si2p region of SFLS-grown Si NWs dispersed in anisole and DMF. (c) HRTEM image of Si NW dispersed in DMF showing a single crystal silicon core with 30 nm diameter and 5–8-nm-thick amorphous oxidised polyphenylsilane shell [41]. © 2015 American Chemical Society.

ambient conditions for 1000 h showing environmental stability, with a marginal increase of the hysteresis. In summary, the simplicity and effectiveness of solution-based mild oxidation methods offer fast passivation technological solution for printable nanowire-based electronics.

5. Scanning probe microscopy techniques for the characterisation of nanowires and devices

5.1. Introduction to conducting atomic force microscopy

Scanning probe microscopy (SPM) techniques evolved quite rapidly over the last two decades for incorporating additional modes beyond conventional topography [42, 43] and were able to provide additional characterisation information in comparison with traditional nanomaterial electron microscopy techniques such scanning electron microscopy. Driven by the introduction of novel one-dimensional conducting and semiconducting nanomaterials, SPM coupled with electrical modes became an integral part for the development and further understanding of these materials due to the unique capability of extracting critical information about the electrical properties of nanoparticles with a spatial resolution comparable to their nanoscale size [44, 45]. By combining this new level of information with conventional topography data [46], a correlation between structural and electrical properties can be established, thus enabling further optimisation of nanoparticles' growth and device integration mechanisms. In this section, the discussion will focus on recent advances in the field of conductive atomic force microscopy (c-AFM) for nanowire characterisation.

c-AFM is a current-based sensing technique for mapping the conductivity variations in samples. It utilises a conductive AFM tip which is brought in contact with a biased sample. During the scan, any current flowing through the sample and into the tip is recorded, forming a current map of the scanned surface (**Figure 8**). c-AFM can simultaneously map the topography and current distribution of a sample (**Figure 9**), thus making it ideal for evaluating defects formed during the fabrication of functional devices made with conducting or semiconducting NW networks.

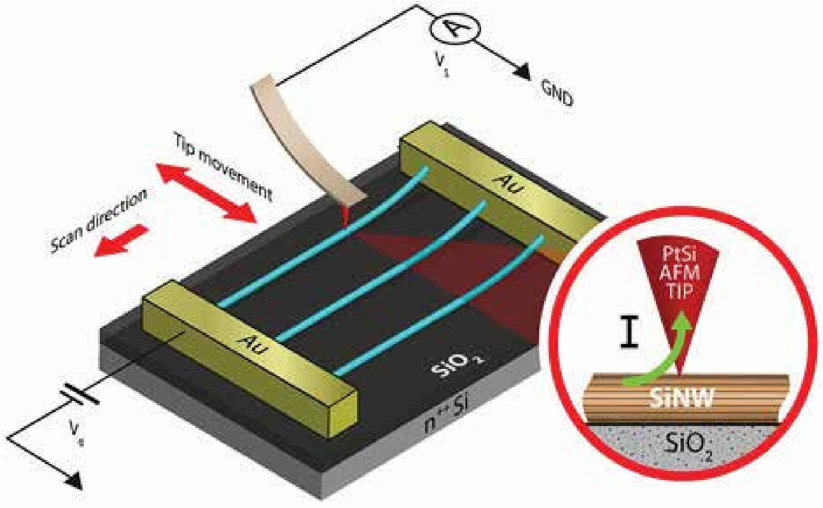

Figure 8. Schematic of c-AFM operating principle [33]. © 2016 American Chemical Society.

In the pursue of solution processed, high conductivity and transparent alternatives to the ITO electrodes, commonly used in optoelectronic devices, metallic NWs were extensively studied [47–49]. One of the main fabrication challenges was the ability of the entire NW network to conduct and thus to minimise the effective sheet resistivity. Bridging the naturally occurring gaps between isolated nanowires during deposition (**Figure 9**) was considered of high importance, and several optimisation approaches were suggested [48, 50, 51]. While conventional measurement techniques can be employed for evaluating the conductivity improvement of these methods on the macroscopic scale, nanoscopic evaluation of the nanowire-to-nanowire connections requires a special approach. One of recent examples was based on using reduced graphene oxide (rGO) as a way of connecting discontinuities in silver nanowire (AgNW) networks [51]. c-AFM was successfully used for imaging these junctions and for proving the bridging effect induced by rGO flakes.

Example of metallic NWs acting as the electrode layer represents one of the most straightforward systems to be examined with c-AFM. Solution-processed nanowire electronics relies heavily on the active layers of the devices consisting of semiconducting NWs. Thus, efficient characterisation of nanowires, including FET device components and any defects on nanowires or contact areas, is essential for the advancement of printed electronics.

5.2. c-AFM characterisation of nanowires with high spatial resolution

As discussed in Section 3, the purification of NWs based on their electrical properties is essential for their efficient incorporation in functional devices. Establishing a relation between the nanowire deposition methods and the properties of assembled nanowires, with very high spatial resolution, is key for high-performance printable nanowire-based FETs. Recently, c-AFM technique was employed for probing the electrical properties of polydispersed Si NWs, after selection processes using different dielectrophoretic signal frequencies [33]. In order to

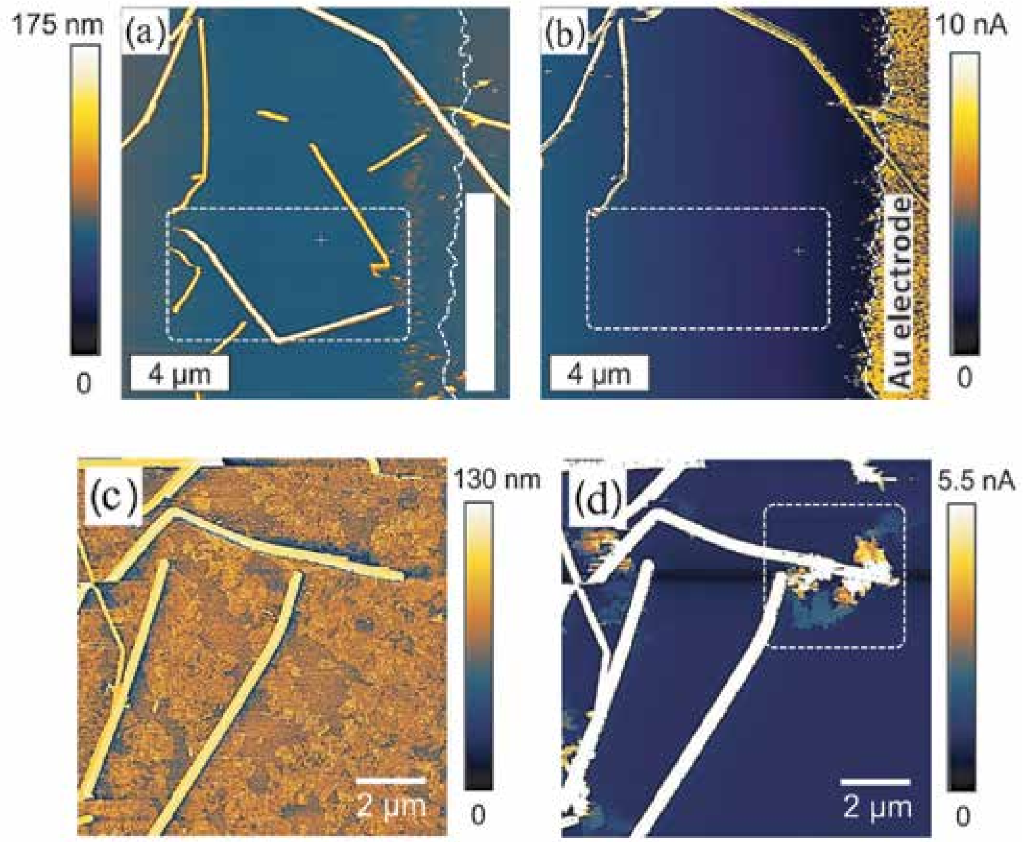

Figure 9. (a–b) c-AFM images including topography (a) and current maps (b) obtained for an AgNW network at a tip bias of 1.6 V. As deposited NWs may result in discontinuities which affect the sheet resistance of the layer. (c–d) Topography (c) and current maps (d) of isolated AgNWs, electrically connected using rGO [51]. © 2016 AIP Publishing.

investigate the conductivity of the low- and high-DEP frequency-selected NWs, c-AFM measurements were conducted with Si NW channels in real FETs. The devices were prepared with Si NWs assembled at DEP frequencies of 220 kHz and 5 MHz. The samples were biased at the drain electrode of the structure, as shown in **Figure 8**, with the conductive platinum-silicide AFM tip being in contact with the Si NWs to act as a ground electrode. Such two-terminal current measurement allows probing the NW conductivity directly, as a function of position. The material for the tip was chosen in order to reduce the contact resistance with the underlying semiconducting nanostructures, without increasing the cantilever deflection and thus allowing soft contact with the sample. By keeping the bias constant at 0.5 V and maintaining constant force applied to the AFM tip, the current maps for NW samples deposited at various DEP signal frequencies were obtained by scanning the samples in contact mode in the direction perpendicular to the NWs. Both conducting AFM current data and AFM topological data were collected at the same time allowing to differentiate the NWs deposited in the channel, but not electrically connected to the contacts, from NWs that were fully electrically connected.

Figure 10 demonstrates typical images obtained for both height (AFM mode) and current (conducting mode) measurements of Si NWs aligned at different DEP frequencies. During the measurement, a common trend was observed that NWs collected using a high, 5 MHz, DEP signal showed ~14 times higher current than the ones collected at low, 220 kHz, frequency. Current levels up to 233 pA were obtained for the NWs aligned at 5 MHz (**Figure 10b**), while peak

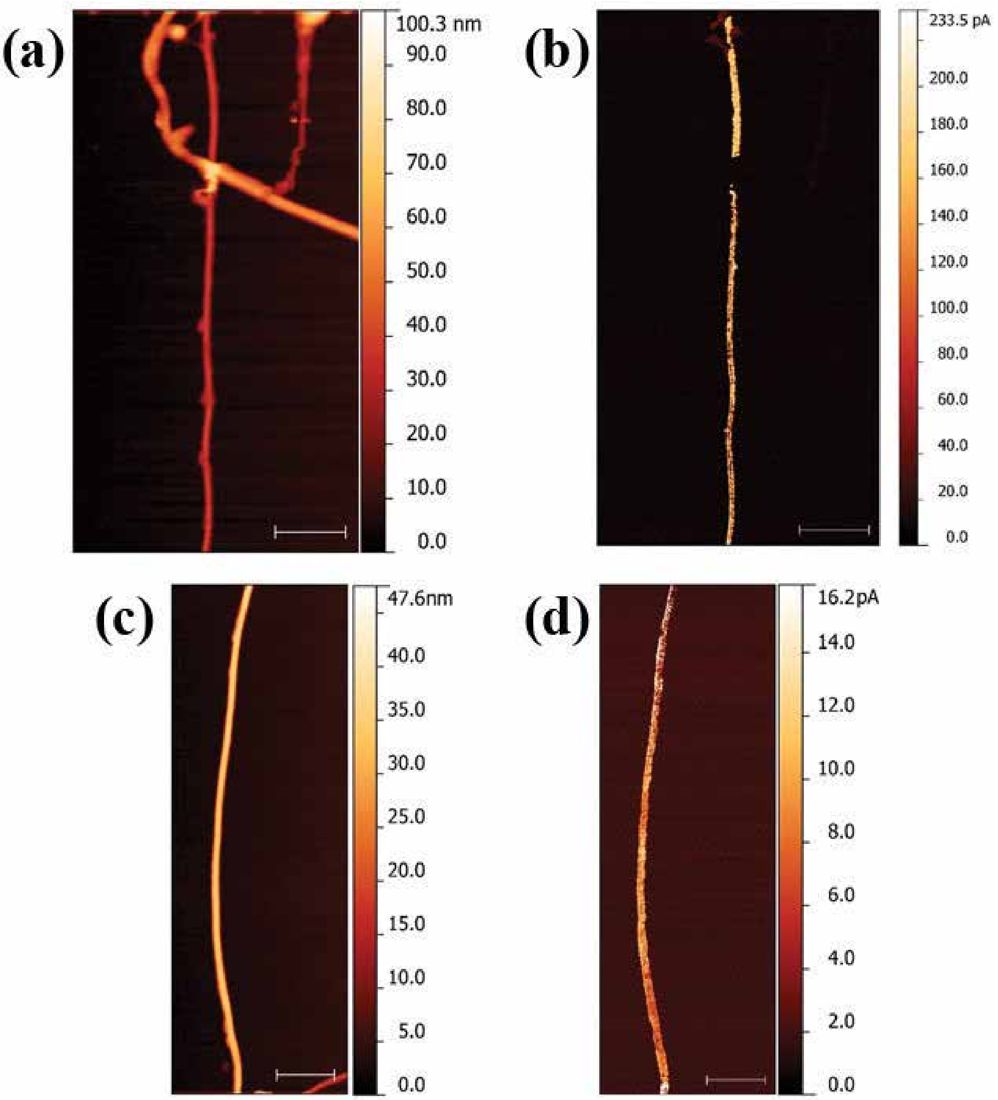

Figure 10. c-AFM data. (a) Height map of Si NWs aligned at 5 MHz and (b) the corresponding current map. Only one straight, fully electrically connected NW is visible in the image. (c) Height map of a NW aligned at 220 kHz and (d) its current map. Scale bars are 1 μm. Conducting Si NWs have similar diameters, (a) 33 nm and (c) 34 nm. All the images were obtained in the trace mode with a pixel size of 5.9 nm. NWs aligned at higher frequency showed higher peak currents up to 233 pA (b), compared to the 16-pA peak current found in the lower frequency assembled NWs (d) [33]. © 2016 American Chemical Society.

current values of 16 pA were measured for the ones assembled at 220 kHz (**Figure 10d**). These current differences between the NWs collected at high and low DEP signal frequencies were fully consistent with the transistor measurements, demonstrating that selective nanoparticle assembly at various dielectrophoretic frequencies is directly correlated with the conductivity of the NWs.

Incorporation of semiconducting NWs into functional devices requires to consider surface oxide properties as well, to enable the efficient coupling of these nanowires with the rest of the device components [52]. In Si NWs, for example, native or intentionally grown surface oxide can act as an insulator or as a poor charge transport medium with limited conduction [53]. In such cases, the uniformity of this oxide layer can be of fundamental importance for the overall functionality of the device. Conventional approaches for imaging any defects in the oxide shell, such as transmission electron microscopy, rely on the observed structural uniformity only and may lead to incorrect assumptions regarding its electrical characteristics.

In a work published in 2008, Stratakis et al. [54] compared the differences between oxide grown on planar Si and Si NWs, in an attempt to evaluate the reliability of these nanostructures for future applications. By examining several nanowires, it was found that the interface barrier for electron injection from silicon core into the oxide shell was similar to planar oxides. Trap density however was susceptible to the non-uniformities of the oxide shell, which, despite appearing to be planar under conventional topography or TEM, had localised weaknesses (**Figure 11**). These weakness areas did not appear to lower substantially the threshold for current leakage through the oxide, but they were potential reliability hazards in nanowire-based devices. This work demonstrated quite successfully that electrical characteristics in NWs may vary significantly depending on the growth conditions of the shell layer. It can also serve as an example of the level of information that can be extracted using advanced SPM techniques.

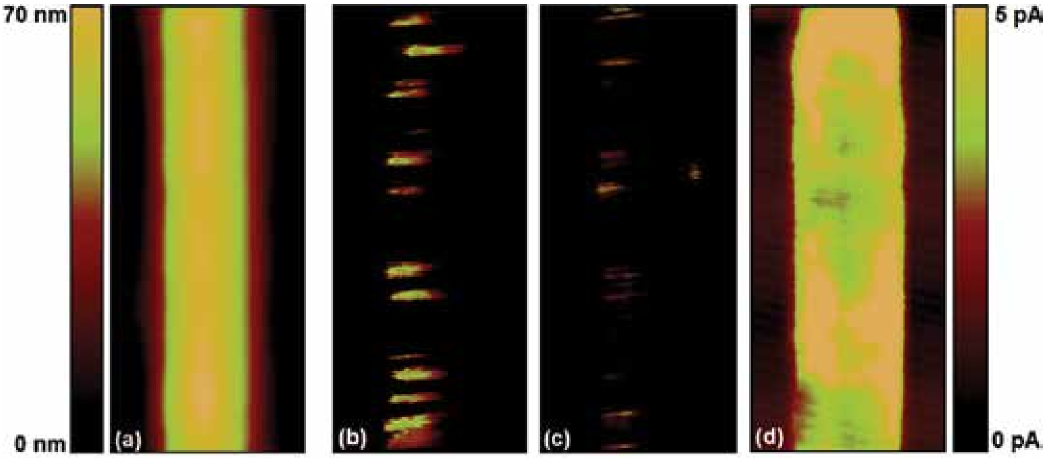

Figure 11. c-AFM current through NW oxide. (a) AFM topography image of part of a NW. Images b, c and d are current maps of the same part of the wire. At the pristine state of this wire, current was first detected at a bias of 13 V (b). Emission is inhomogeneous. Reduced average current in the second scan (c) is attributed to electron trapping in the oxide. At a higher voltage (16 V), increased current density appears from the entire surface of the nanowire (d) [54]. © 2008 American Chemical Society.

6. Conclusions

Solution-processed nanowire field-effect transistors have reached the threshold of being commercially viable due to the developments in nanowires controllable assembly. The main criticism for nanowire-based electronics was linked in the past to the lack of control of a number of nanowires between the device electrodes, thus limiting the devices reproducibility. Recent developments in the field, focusing on solvent-based reproducible and controllable positioning, orientation and placement of nanowires on predefined substrate locations, also coupled with nanowires' purification and selection methods, have provided the necessary breakthroughs to enable scalable fabrication of nanowire devices, including FETs.

For some time, the main target in NW assembly was to reach a high deposition yield and well-aligned nanostructures over large areas as an attempt to achieve superior device performances and reproducibility. However, more precise control of nanowire properties in fabricated devices can only be achieved by full integration of separation and purification processes for nanomaterials, based on their electrical and morphological properties. Currently, the only assembly technique offering all of these features is electric-field–assisted dielectrophoresis. This method is scalable and can be applied in large-area device deposition. Scanning probe microscopy characterisation techniques, such as conductive AFM, capable of simultaneous topological and conductivity measurements of nanowire active channels in electronic devices with high special resolution, have helped to optimise the nanowire properties and the corresponding selection and deposition methods.

In summary, solution-processed nanowire field-effect transistors represent a powerful technological platform with high potential for low-cost large-area electronics with applications targeting chemical, biological and tensile sensing; flexible circuits; memory; displays; and photonic devices.

Author details

Maxim Shkunov*, Grigorios Rigas and Marios Constantinou

*Address all correspondence to: m.shkunov@surrey.ac.uk

Advanced Technology Institute, Electrical and Electronic Engineering, University of Surrey, Guildford, UK

References

[1] Liu X, Long Y-Z, Liao L, Duan X, Fan Z. Large-scale integration of semiconductor nano wires for high-performance flexible electronics. ACS Nano. 2012;**6**(3):1888-1900. DOI:10.1021/nn204848r

[2] Cui Y, Wei QQ, Park HK, Lieber CM. Nanowire nanosensors for highly sensitive and selective detection of biological and chemical species. Science. Aug 2001;**293** (5533):1289-1292. DOI: 10.1126/science.1062711

[3] Patolsky F, Lieber CM. Nanowire nanosensors. Materials Today. Apr 2005;**8**(4):20-28. DOI: 10.1016/S1369-7021(05)00791-1

[4] Gao AR, et al. Enhanced sensing of nucleic acids with silicon nanowire field effect transistor biosensors. Nano Letters. Oct 2012;**12**(10):5262-5268. DOI: 10.1021/nl302476h

[5] Tian B, Kempa TJ, Lieber CM. Single nanowire photovoltaics. Chemical Society Reviews. 2009;**38**(1):16-24. DOI: 10.1039/B718703N

[6] Song JH, Zhou J, Wang ZL. Piezoelectric and semiconducting coupled power generating process of a single ZnO belt/wire. A technology for harvesting electricity from the environment. Nano Letters. Aug 2006;**6**(8):1656-1662. DOI:10.1021/nl060820v

[7] Seo M-H, et al. Versatile transfer of an ultralong and seamless nanowire array crystallized at high temperature for use in high-performance flexible devices. ACS Nano. 2017;**11**(2):1520-1529. DOI: 10.1021/acsnano.6b06842

[8] Pregl S, Heinzig A, Baraban L, Cuniberti G, Mikolajick T, Weber WM. Printable parallel arrays of Si nanowire Schottky-Barrier-FETs with tunable polarity for complementary logic, IEEE Transactions on Nanotechnology. May 2016;**15**(3):549-556. DOI:10.1109/TNANO.2016.2542525

[9] Peng K, et al. Single nanowire photoconductive terahertz detectors. Nano Letters. Jan 2015;**15**(1):206-210. DOI:10.1021/nl5033843

[10] Peng K, Parkinson P, Gao Q, Boland JL, Li Z, Wang F, Mokkapati S, Fu L, Johnston MB, Tan HH, Jagadish C., Single n^+ -i-n^+ InP nanowires for highly sensitive terahertz detection. Nanotechnology. 2017;**28**(12):125202. DOI:10.1088/1361-6528/aa5d80

[11] Yang B, Buddharaju KD, Teo SHG, Singh N, Lo GQ, Kwong DL, Vertical silicon-nanowire formation and gate-all-around MOSFET. Ieee Electron Device Letters. Jul 2008;**29**(7):791-794. DOI:10.1109/LED.2008.2000617

[12] Takei K, et al. Nanowire active-matrix circuitry for low-voltage macroscale artificial skin. Nature Materials. Oct 2010;**9**(10):821-826. DOI:10.1038/nmat2835

[13] Ju SY, et al. Fabrication of fully transparent nanowire transistors for transparent and flexible electronics. Nature Nanotechnology. Jun 2007;**2**(6):378-384. DOI:10.1038/nmat2835

[14] Gudiksen MS, Lauhon LJ, Wang J, Smith DC, Lieber CM. Growth of nanowire superlattice structures for nanoscale photonics and electronics. Nature. Feb 7 2002;**415**(6872):617-620. DOI: 10.1038/415617a

[15] Duan XF, Huang Y, Agarwal R, Lieber CM. Single-nanowire electrically driven lasers. Nature. Jan 2003;**421**(6920):241-245. DOI: 10.1038/nature01353

[16] Feng C, Xu Z, Wang X, Yang H, Zheng L, Fu H. Organic-nanowire–SiO2 core–shell microlasers with highly polarized and narrow emissions for biological imaging. ACS Applied Materials & Interfaces. 2017;**9**(8):7385-7391. DOI:10.1021/acsami.6b13387

[17] Kennedy T, Brandon M, Ryan KM. Advances in the application of silicon and germanium nanowires for high-performance lithium-ion batteries. Advanced Materials. Jul 2016;**28**(27):5696-5704. DOI:10.1002/adma.201503978

[18] Noh YY, Cheng XY, Sirringhaus H, Sohn JI, Welland ME, Kang DJ. Ink-jet printed ZnO nanowire field effect transistors. Applied Physics Letters. Jul 2007;**91**(4):p. 3. DOI: 10.1063/1.2760041

[19] Opoku C, Chen L, Meyer F, Shkunov M. Solution processable nanowire field-effect transistors. MRS Proceedings. 2011;**1287**:69-74

[20] Opoku C, Hoettges KF, Hughes MP, Stolojan V, Silva SRP, Shkunov M. Solution processable multi-channel ZnO nanowire field-effect transistors with organic gate dielectric. Nanotechnology. Oct 2013;**24**(40). Art. no. 405203. DOI: 10.1088/0957-4484/24/40/405203

[21] Hanrath T, Korgel BA. Supercritical fluid–liquid–solid (SFLS) synthesis of Si and Ge nanowires seeded by colloidal metal nanocrystals. Advanced Materials. 2003;**15**(5):437-440. DOI: 10.1002/adma.200390101

[22] Hu J, Bando Y, Liu Q, Golberg D, Laser-ablation growth and optical properties of wide and long single-crystal SnO2 ribbons. Advanced Functional Materials. 2003;**13**(6):493-496. DOI: 10.1002/adfm.200304327

[23] Kim F, Kwan S, Akana J, Yang P. Langmuir-Blodgett nanorod assembly. Journal of the American Chemical Society. 2001;**123**(18):4360-4361. DOI: 10.1021/ja0059138

[24] Yang P, Nanotechnology: Wires on water. Nature. 2003;**425**(6955):243-244. DOI: 10.1038/425243a

[25] Tao A, et al. Langmuir-Blodgett silver nanowire monolayers for molecular sensing using surface-enhanced Raman spectroscopy. Nano Letters. 2003;**3**(9):1229-1233. DOI: 10.1021/nl0344209

[26] Whang D, Jin S, Wu Y, Lieber CM. Large-scale hierarchical organization of nanowire arrays for integrated nanosystems. Nano Letters. 2003;**3**(9):1255-1259. DOI: 10.1021/nl0345062

[27] Yu G, Li X, Lieber CM, Cao A. Nanomaterial-incorporated blown bubble films for large-area, aligned nanostructures. Journal of Materials Chemistry. 2008;**18**(7):728-734. DOI: 10.1039/B713697H

[28] Huang Y, Duan X, Wei Q, Lieber CM. Directed assembly of one-dimensional nanostructures into functional networks. Science. 2001;**291**(5504):630-633. DOI: 10.1126/science.291.5504.630

[29] Yu G, Lieber CM. Assembly and integration of semiconductor nanowires for functional nanosystems. Pure and Applied Chemistry. 2010;**82**(12):2295-2314. DOI: 10.1351/PAC-CON-10-07-06

[30] Heo K, et al. Large-scale assembly of silicon nanowire network-based devices using conventional microfabrication facilities. Nano Letters. 2008;**8**(12):4523-4527. DOI: 10.1021/nl802570m

[31] Fan Z, et al. Wafer-scale assembly of highly ordered semiconductor nanowire arrays by contact printing. Nano Letters. 2008;**8**(1):20-25. DOI: 10.1021/nl071626r

[32] Hughes MP, Nanoelectromechanics in Engineering and Biology. CRC Press; 2002, Boca Raton, FL. ISBN 9780849311833

[33] Constantinou M, et al. Simultaneous tunable selection and self-assembly of Si nanowires from heterogeneous feedstock. ACS Nano. Apr 2016;**10**(4):4384-4394. DOI: 10.1021/acsnano.6b00005

[34] Freer EM, Grachev O, Duan X, Martin S, Stumbo DP. High-yield self-limiting single-nanowire assembly with dielectrophoresis. Nature Nanotechnology. 2010;**5**(7):525-530. DOI: 10.1038/nnano.2010.106

[35] Collet M, et al. Large-scale assembly of single nanowires through capillary-assisted dielectrophoresis. Advanced Materials. 2015;**27**(7):1268-1273. DOI: 10.1002/adma.201403039

[36] Paska Y, Haick H. Interactive effect of hysteresis and surface chemistry on gated silicon nanowire gas sensors. ACS Applied Materials & Interfaces. May 2012;**4**(5):2604-2617. DOI: 10.1021/am300288z

[37] Kim SH, et al. Hysteresis behaviour of low-voltage organic field-effect transistors employing high dielectric constant polymer gate dielectrics. Journal of Physics D: Applied Physics. 2010;**43**(46):465102. DOI:10.1088/0022-3727/43/46/465102

[38] Kawashima T, Saitoh T, Komori K, Fujii M. Synthesis of Si nanowires with a thermally oxidized shell and effects of the shell on transistor characteristics. Thin Solid Films. 2009;**517**(16):4520-4526. DOI: 10.1016/j.tsf.2008.12.042

[39] Wang Y, Lew K-K, Mattzela J, Redwing J, Mayer T. Top-gated field effect devices using oxidized silicon nanowires. In: Device Research Conference Digest, 2005. DRC'05. 63rd;**1**: IEEE; 2005. pp. 159-160. DOI: 10.1109/DRC.2005.1553101

[40] Fukata N, Kaminaga J, Takiguchi R, Rurali R, Dutta M, Murakami K. Interaction of boron and phosphorus impurities in silicon nanowires during low-temperature ozone oxidation. The Journal of Physical Chemistry C. 2013;**117**(39):20300-20307. DOI: 10.1021/jp406713p

[41] Constantinou M, et al. Interface passivation and trap reduction via a solution-based method for near-zero hysteresis nanowire field-effect transistors. ACS Applied Materials & Interfaces. 2015;**7**(40):22115-22120. DOI: 10.1021/acsami.5b07140

[42] Giridharagopal R, Cox PA, Ginger DS. Functional scanning probe imaging of nanostructured solar energy materials. Accounts of Chemical Research. Sep 2016;**49**(9):1769-1776. DOI: 10.1021/acs.accounts.6b00255

[43] Tsoi WC, et al. Surface and subsurface morphology of operating nanowire: fullerene solar cells revealed by photoconductive-AFM. Energy & Environmental Science. Sep 2011;**4**(9):3646-3651. DOI: 10.1039/C1EE01944A

[44] Kopanski JJ. Electrical scanning probe microscopes to address industrial nano-metrology needs of integrated circuits and nanoelectronic devices. In 29th Conference on Precision Electromagnetic Measurements (CPEM 2014); 2014. pp. 214-215. DOI: 10.1109/CPEM.2014.6898335

[45] Berger R, Butt HJ, Retschke MB, Weber SAL. Electrical modes in scanning probe microscopy. Macromolecular Rapid Communications. Jul 2009;**30**(14):1167-1178. DOI: 10.1002/marc.200900220

[46] Kalinin SV, et al. Big, deep, and smart data in scanning probe microscopy. ACS Nano. Oct 2016;**10**(10):9068-9086. DOI: 10.1021/acsnano.6b04212

[47] Leem DS, Edwards A, Faist M, Nelson J, Bradley DDC, de Mello JC. Efficient organic solar cells with solution-processed silver nanowire electrodes. Advanced Materials. Oct 2011;**23**(38):4371. DOI: 10.1002/adma.201100871

[48] Sannicolo T, Lagrange M, Cabos A, Celle C, Simonato JP, Bellet D. Metallic nanowire-based transparent electrodes for next generation flexible devices: A review. Small. Nov 2016;**12**(44:6052-6075. DOI: 10.1002/smll.201602581

[49] Langley D, Giusti G, Mayousse C, Celle C, Bellet D, Simonato J-P. Flexible transparent conductive materials based on silver nanowire networks: A reviewNanotechnology. Nov 15 2013;**24**(45). Art. no. 452001. DOI: 10.1088/0957-4484/24/45/452001

[50] Kim SH, Choi WI, Kim KH, Yang DJ, Heo S, Yun DJ. Nanoscale chemical and electrical stabilities of graphene-covered silver nanowire networks for transparent conducting electrodes, Scientific Reports. Sep 2016;**6**. Art. no. 33074. DOI: 10.1038/srep33074

[51] Shaw JE, Perumal A, Bradley DDC, Stavrinou PN, Anthopoulos TD. Nanoscale current spreading analysis in solution-processed graphene oxide/silver nanowire transparent electrodes via conductive atomic force microscopy. Journal of Applied Physics. May 2016;**119**(19). Art. no. 195501. DOI: 10.1063/1.4949502

[52] Li Y, Qian F, Xiang J, Lieber CM. Nanowire electronic and optoelectronic devices. Materials Today. Oct 2006;**9**(10):18-27. DOI: 10.1016/S1369-7021(06)71650-9

[53] Vogel EM. Technology and metrology of new electronic materials and devices. Nature Nanotechnology. Jan 2007;**2**(1):25-32. DOI: 10.1038/nnano.2006.142

[54] Stratakis E, et al. Imaging dielectric properties of Si nanowire oxide with conductive atomic force microscopy complemented with femtosecond laser illumination. Nano Letters. Jul 2008;**8**(7):1949-1953. DOI: 10.1021/nl0807171

Chapter 6

Semiconductor Nanowire MOSFETs and Applications

Hao Zhu

Additional information is available at the end of the chapter

http://dx.doi.org/10.5772/67446

Abstract

Semiconductor nanowires have aroused a lot of scientific interest and have been regarded as one of the most promising candidates that would make possible building blocks in future nanoscale devices and integrated circuits. Employing nanowire as metal-oxide-semiconductor field-effect transistor (MOSFET) channel can enable a gate-surrounding structure allowing an excellent electrostatic gate control over the channel for reducing the short-channel effects. This chapter introduces the basic physics of semiconductor nanowires and addresses the problem of how to synthesize semiconductor nanowires with low-cost, high-efficiency and bottom-up approaches. Effective integration of nanowires in modern complementary metal-oxide-semiconductor (CMOS) technology, specifically in MOSFET devices, and non-volatile memory applications is also reviewed. By extending the nanowire MOSFET structure into a universal device architecture, various novel semiconductor materials can be investigated. Semiconductor nanowire MOSFETs have been proved to be a strong and useful platform to study the physical and electrical properties of the novel material. In this chapter, we will also review the investigations on topological insulator materials by employing the nanowire field-effect transistor (FET) device structure.

Keywords: semiconductor nanowire, gate-surrounding, MOSFET, self-assembly, flash-like non-volatile memory, topological insulator nanowire FETs

1. Introduction

Since the invention of integrated circuit in the 1950s, the scaling of metal-oxide-semiconductor field-effect transistor (MOSFET) continues with the emergence of new technologies to extend complementary metal-oxide-semiconductor (CMOS) down to ever smaller technology node. However, the CMOS scaling has deviated from the trends predicted by Moore and the scaling rules set forth by Dennard et al. due to fundamental physical and technical limitations [1, 2]. Limitations such as heat dissipation, leakage current and channel length modulation have become a major concern that will inevitably lead to the slowing down in CMOS scaling when approaching atomic dimension. Thus, there is an urgent need to develop new semiconductor technology to solve the issues including cost, speed, density, reliability and power dissipation. A great deal of efforts has been made, and among all the candidates, nanoelectronics involved with replacing existing silicon-based technology has risen to be one of the most promising solutions towards continuous CMOS scaling.

During the past decades, semiconductor nanowires synthesized by bottom-up techniques and derived field-effect transistor (FET) devices have been intensively studied as the fundamental building blocks for nanoelectronic devices and circuit technologies [3–7]. Compared to planar devices based on bulk materials, the nanowires have a smaller channel and large surface-to-volume ratio. In addition, the gate-surrounding or gate-all-around (GAA) structure that can be formed in the nanowire FET allows excellent electrostatic gate control over the nanowire channel. Moreover, the GAA nanowire transistors enable ultimate CMOS device scaling with the best possible short-channel control considering the quantum confinement effects and the scattering at atomic dimensions. The GAA horizontal nanowire FET architecture exhibits high similarities to the FinFET, which is the predominant technology in the current 10 nm or even 7 nm process node. Thus, GAA FETs are very promising candidates in the sub-7 nm nodes to extend the scalability beyond the limits imposed by the FinFET technology with much less complexity compared to the alternative scaling approaches [8].

Till date, nanowire FETs have mainly been fabricated using the "top-down" approaches based on advanced lithography with nanowire prepared by dry/wet etching which usually yields well-oriented nanowire arrays [9, 10]. However, it has been well recognized that nanowires synthesized by "bottom-up" techniques such as chemical vapour deposition (CVD) can have lower cost and higher quality compared to the"top-down" methods [11]. Thus, it would be very attractive to develop an approach to manufacture such nanowire FETs with an excellent performance. Nevertheless, the technique to fabricate FETs from CVD grown silicon nanowires remains a barrier to the development of devices with optimized performance. Current approaches are primarily based on the harvesting and positioning the as-grown nanowires using aligning methods such as fluidic alignment, dielectrophoresis or nanoscale probe methods [12–17]. Such methods will inevitably introduce contaminants to the nanowire surfaces, which will adversely influence the device interface state density and possibly the nanowire surface roughness, and the device performance will be deteriorated as a result.

In this chapter, we first review the fundamentals of semiconductor nanowires and synthetic strategies. Then we introduce a novel self-alignment fabrication process for nanowire FET applications. The high-quality self-aligned nanowire channels possess clean surface and the fabricated FET devices exhibit excellent performance including large on/off ratio, small subthreshold slope and small leakage current. Such an effective nanowire integration scenario is very attractive for different materials and device investigations. We focus on the flash memory based on the self-aligned Si nanowire FETs and the study of topological insulator nanowire FETs using the self-alignment techniques. The results demonstrate that by employing the one-dimensional nanowire as the active component in the electronic devices, the flash memory performance has been significantly improved such as lower operation voltage and better reliability, and the basic principles behind the topological insulators have been manifested strongly enabling more delicate characterizations to understand the physics of the specific material. We believe that nanowire MOSFETs will open up a suit of potential applications in future sub-10 nm semiconductor technology as well as solutions towards emerging micro and nanoelectronic device challenges.

2. Review of physics of semiconductor nanowires

The theory of nanowires will be briefly reviewed with a focus on silicon nanowires since the features discussed here can be extended to other types of semiconductor nanowires. The structural and mechanical properties of silicon nanowires will be reviewed first, and then the electronic properties will be discussed in which we will also consider the device-related issues and limitations.

2.1. Structural and mechanical properties

The Si nanowires are intriguing mostly due to the extra high surface-to-volume ratio and the well-defined single crystalline orientation. The nanowire growth direction has been widely studied, and the connection between the diameter and the favoured crystal direction has been established [18]. It has been reported both experimentally and theoretically that the catalyst-assisted Si nanowires with smallest diameter prefer the <110> direction, while the nanowires with larger diameter favours the <111> direction [19–21]. The growth direction determines the nanowire cross section to some extent. A pentagonal cross section has been observed from the ground-state structure for Si nanowires up to 5 nm [22, 23]. This cross section due to the joint of five prisms cut of a Si (110) plane has rarely been reported. A more well-known structure in good agreement with experimental work is the hexagonal cross section for <110> Si nanowires with a bulk core [18, 24].

Mechanical properties of Si become quite different when reaching nanoscale with lower dimension. Due to the compressive surface stress, the Young's modulus of <100> Si nanowires softens as the surface-to-volume ratio increases and a steep decrease has been detected on shrinking of the nanowire diameter to 2–2.5 nm [25]. It was further discovered that the Young's modulus of Si nanowires is strongly anisotropic [26]. Different from the <100> nanowires, which exhibit lowest values, the wires grown along <110> direction give the highest values. These results are also in good agreement with the experimental work [27]. Currently, the mechanical properties of nanowires have become a promising research direction. Static and dynamic nanowire bending with atomistic simulations, which relies on periodic boundary conditions, reveals the influence of surface stress more clearly and provides valuable information for nanowire-based device designs.

2.2. Electronic properties

It is widely recognized that bulk Si has an indirect band gap, with the valence band maximum at the Γ point and the conduction minimum at about 85% along the Γ and X direction.

However, Si nanowires grown along most orientations have a direct band gap, with the maximum of the valence band and the minimum of the conduction band aligned at the same point in k-space. As a result, such nanowire materials have become encouraging candidates in optoelectronics or photonics applications [28].

The electronic properties of nanowires depend on the nanowire growth direction, cross section and diameter. However, it is interesting to find that the band gap of Si nanowire is insensitive to the shape of cross section. The band gap of a 1 nm nanowire was found constant with change less than 0.09 eV by simulating cross sections that are even utterly different, as long as providing the same surface-to-volume ratio [29, 30].

Different types of Si nanowire based electronic devices have been fabricated and studied for a variety of application purposes. An important cause of electrical conductance degradation in such devices is the scattering occurring at the surface with the presence of surface defects or surface roughness [31, 32]. Generally, the surface roughness disorder induces irregularities in the density of states along the nanowire axis, resulting in the carrier reflection and reduction in conductance. A more detailed study shows that the backscattering due to the surface roughness strongly depends on the nanowire orientation, and the anisotropy comes from the difference in band structure [33, 34]. In particular, electrons are less sensitive to surface roughness in <110> nanowires, and the transfer of holes is more smooth in <111> nanowires. Other electronic transport parameters such as the mean free path, length and the localization length can be better explained with the above incorporated differences.

Despite the defects or roughness from the nanowire surface, the existence of impurities is another major source of scattering, especially when the nanowire size is scaled down below 10 nm. Unlike the bulk in which the carriers are just slowed down by the impurities, the trajectories of the carriers in an extremely thin one-dimensional medium can be entirely backscattered because the scattering potential often extends throughout most of the cross sections of the thin wire [34]. Impurities can be originated from imperfect growth or intentional doping for targeted electrical properties when referred to semiconductors. For the dopants in Si nanowires, impurities like donor impurities, either segregate to the surface forming electrically inactive components or stay in the wire producing a strong backscattering, both will lead to the decreased conductance.

3. Silicon nanowire synthesis and field-effect transistors

3.1. Silicon nanowire synthesis

There has been a large number of reported works on the nanowire synthesis of a wide spectrum of semiconductor materials during the past decades. Both chemical and physical methods are intensively studied. Understanding the growth mechanism of these synthesis approaches is helpful in developing one-dimensional nanostructures of the desired materials and derivative electrical devices.

Solution phase synthesis of nanowires is a low cost yet high yield method in which selective capping agents are often employed, especially in an anisotropic growth, for the kinetic control of the evolving nanostructure to allow elongation along certain axis by preferentially adsorbing to specific crystal facets [35–37]. The major limitation of such solution phase synthesis lies in the empirical trial-and-error methodology for capping agents. Template-assisted electrochemical synthesis is another popular approach to grow one-dimensional nanostructures. Synthesis of metals, semiconductors and conductive polymers and oxides has been reported by using templates such as anodic aluminium oxide (AAO) and polycarbonate membranes [38, 39]. This method shares the advantages such as low-cost, well-orientation, ambient temperature, pressure operation and feasibility of batch fabrication of nanowire array. However, complete template filling still remains a challenge for the nanowire synthesis through electrodeposition. Template-assisted synthesis has been more utilized in the formation of hollow nanotube and core-shell nanowire structures in combination with atomic layer deposition (ALD) technique [40, 41].

Vapour phase synthesis of one-dimensional nanostructure is probably the most extensively explored approach. Numerous techniques have been developed to grow nanowire from gas precursors. Among all the vapour phase methods, the most widely studied and successful approach in generating high-quality single-crystal nanowires in large quantities is the vapour-liquid-solid (VLS) mechanism [4]. We will be focusing on this method in this section, and the following contents reviewed in this chapter are based on the nanowires synthesized by using the VLS approach.

A typical VLS process starts from the dissolution of vapour reactants into a catalytic alloy phase, followed by the crystal nucleation at the liquid-solid interface. As illustrated in **Figure 1**, gold nanoparticles are commonly used as catalyst for Si nanowire growth by the

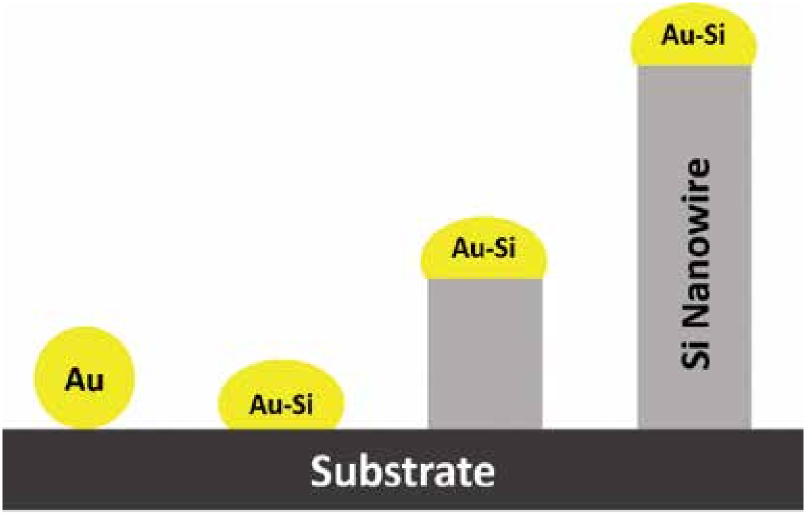

Figure 1. Schematic illustration of the VLS mechanism for Si nanowire synthesis using Au nanoparticle as catalyst.

VLS mechanism. The Au particles catalyze the gas precursor (e.g. SiH_4) and reacts with the Si atoms from the vapour phase, forming Au-Si eutectic droplets. Si was introduced from the vapour and adsorbed onto the liquid surface, then diffused into the droplet leading to a supersaturated state where the Si atoms precipitate and the nanowire starts nucleating. In the growth, the droplet serves as the "seeds" limiting the lateral growth of individual nanowires, and the droplet size remains unchanged during the growth which determines the diameter of the subsequent nanowires.

The VLS process has become a widely used growth method for one-dimensional nanostructures of a broad variety of materials. In addition to elemental semiconductors such as Si and Ge, binary compounds including III-V semiconductors (e.g. GaN, GaAs and InAs), oxides (e.g. ZnO, SiO_2 and ITO) and chalcogenides (e.g. Bi_2Se_3, In_2Se_3 and CdS) have also been fabricated and studied in nanowire morphology following the VLS mechanism.

3.2. Silicon nanowire field-effect transistors

In this section, we review the fabrication and characterization of Si nanowire FETs prepared by using a self-alignment method based on VLS synthesis mechanism [42]. Unlike the traditional nanowire harvesting and alignment methods, the self-alignment approach not only enables simultaneous batch fabrication of reproducible and homogeneous nanowire devices of high quality, but also limits the contaminations of the nanowire during the fabrication process. The fabricated self-aligned Si nanowire FETs exhibit excellent current-voltage (I-V) characteristics, high on/off current ratio and small subthreshold slope providing an excellent platform for other devices and material investigations and applications.

3.2.1. FET fabrication

The Si nanowire FETs are fabricated using the directed self-alignment process as shown in **Figure 2**. The main concept of this fabrication approach is that Si nanowires are synthesized from Au catalysts on predefined locations as on wafers and well aligned with the source/drain and gate electrodes by photolithographic processes without harvesting the nanowires. At the first step of the fabrication process, a thin layer of Au catalyst (~1 nm) was deposited on the SiO_2/Si substrate and patterned by photolithography and lift-off processes. The Si nanowires were grown from the catalyst at the defined locations in a low-pressure chemical vapour deposition (LPCVD) furnace at 440°C for 2 hours with an ambient SiH_4 stream under a pressure of 500 mTorr. The nanowires are typically 20 μm in length and 20 nm in diameter. Immediately after the VLS growth, the Si nanowires were loaded in a dry oxidation furnace and oxidized at 750°C for 30 minutes in O_2 to form a ≈ 3 nm thick SiO_2 which was expected to provide a good interface between the nanowire and the subsequent top gate dielectric stack [42]. Photolithographic and lift-off processes were then performed to form the source and drain contacts. To facilitate proper contact formation, a 2% HF wet etch was applied to remove the oxides from the Si nanowires at the source/drain region before electrode metal (Al in this case) deposition. The next step is to deposit top gate dielectric (25 nm HfO_2) by ALD at 250°C, followed by a deposition of 5 nm of Al_2O_3 to improve the interface with the

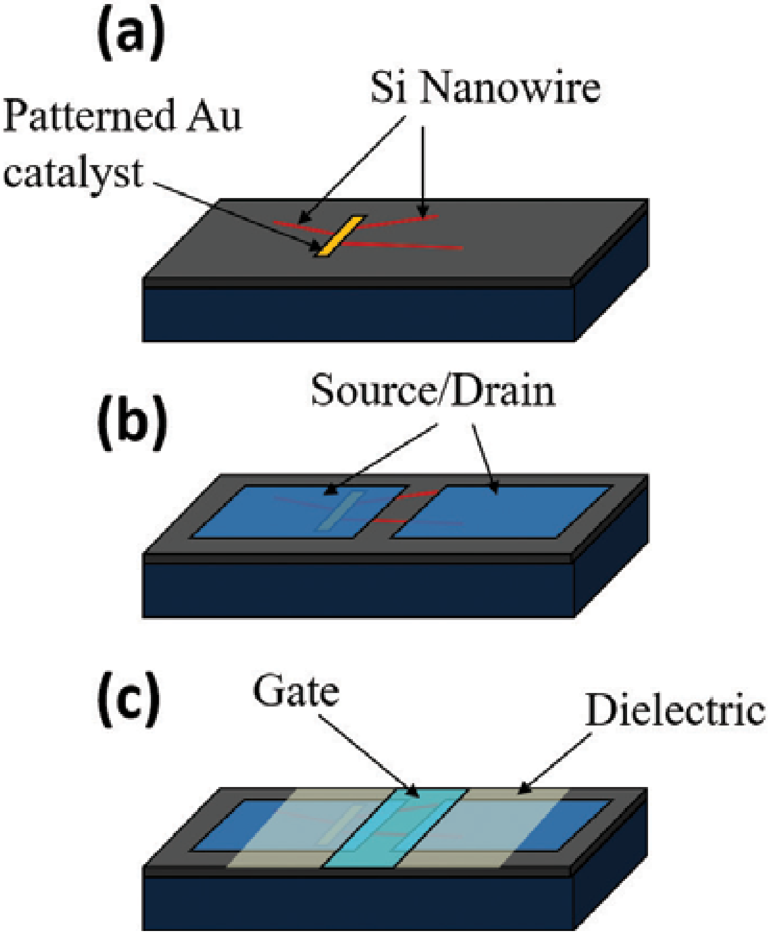

Figure 2. Self-alignment fabrication process: (a) patterned Au catalyst on SiO_2; (b) synthesis of Si nanowire from the Au catalyst, nanowire oxidation and alignment of source/drain contacts; (c) deposition of gate dielectric and pattern of top gate electrode [42].

Al top gate which was formed by the same lift-off process as of the source/drain electrodes. The final devices were annealed in forming gas (5% H_2 in N_2) at 325°C for 5 minutes to reduce the interface trap density between the nanowire and dielectric layer, as well as to improve the contact between the Al metal to the Si nanowire and HfO_2. **Figure 3** shows the top-view scanning electron microscopy (SEM) image of a finished self-aligned Si nanowire FET with gate length of 2 μm.

3.2.2. Electrical characterizations

Si nanowire FET with single or multiple nanowire channels is expected to exhibit better performance than planer bulk Si. The Gate-surrounding structure can be enabled allowing excellent electrostatic gate control over the channel for reduced short-channel effects.

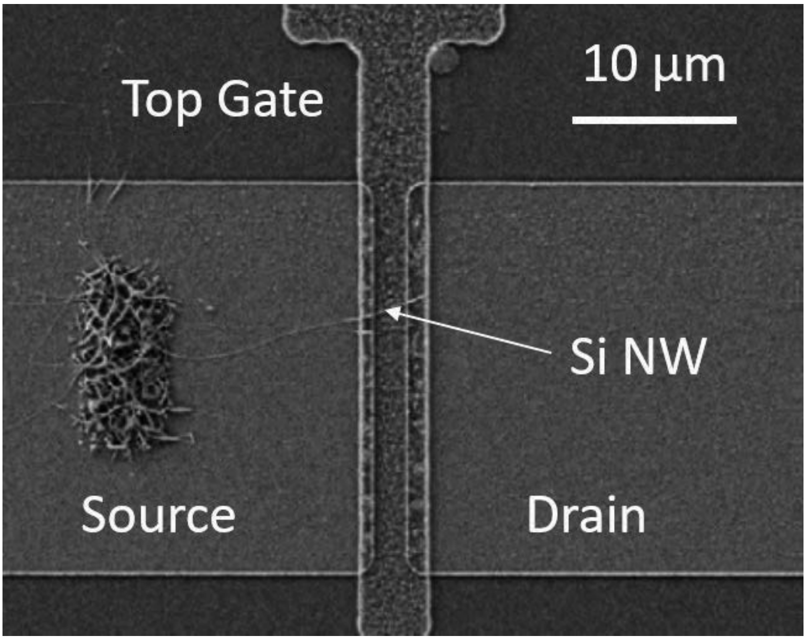

Figure 3. Top-view SEM image of a typical self-aligned Si nanowire FET with gate length of 2 μm [42].

The following equations define the minimum gate length to avoid short-channel effects for single-gate, double-gate and surrounding-gate structures:

$$\lambda_{\text{single-gate}} = \sqrt{\frac{\varepsilon_{Si}\, t_{ox}\, t_{Si}}{\varepsilon_{ox}}} \tag{1}$$

$$\lambda_{\text{double-gate}} = \sqrt{\frac{\varepsilon_{Si}\, t_{ox}\, t_{Si}}{2\,\varepsilon_{ox}}} \tag{2}$$

$$\lambda_{\text{surrounding-gate}} = \sqrt{\frac{2\,\varepsilon_{Si}\, t_{Si}^{\,2} \ln\left(1+\frac{2\,t_{ox}}{t_{Si}}\right) + \varepsilon_{ox}\, t_{Si}^{\,2}}{16\,\varepsilon_{ox}}} \tag{3}$$

where t_{Si}, ε_{Si}, t_{ox} and ε_{ox} are the thickness and permittivity of Si and gate oxide, respectively [43]. The above equations demonstrate that the surrounding gate structure offers the best characteristics for controlling the short-channel effects.

Figure 4a and **b** shows the output characteristics of a self-aligned Si nanowire FET in both linear and logarithmic scale. From the drain current (I_{DS}) versus drain voltage (V_{DS}) curves, the leakage-affected region, weak, moderate and strong inversion operation regions of the FET are clearly shown in **Figure 4b**. In the weak inversion region, I_{DS} increases exponentially with gate voltage (V_{GS}) due to the diffusion of carriers (holes) and is saturated at 3 ϕ_t (~78 mV at room temperature, ϕ_t = kT/q is the thermal voltage). In moderate inversion region, I_{DS} varies by a couple of orders of magnitude, changing gradually from one form of functional dependence to the other. In strong inversion region, I_{DS} approximately follows the quadratic law and is proportional to $(V_{GS} - V_{TH})^2$ with saturation at $V_{DS} = V_{GS} - V_{TH}$. These curves demonstrate that the self-aligned Si nanowire FET has similar electrical behaviours to those of conventional MOSFETs, even though it has much simpler device structure and no source/drain junction doping. It should be noted that the I_{DS}–V_{DS} curves increase sharply in the linear region, indicating a small source and drain contact resistance.

Due to the Schottky contacts between the Al contacts and the intrinsic Si nanowire, Schottky-barrier pMOSFET characteristics are expected for these FETs. **Figure 5** shows typical transfer characteristics of self-aligned Si nanowire FET with V_{DS} of −50, −100 and −150 mV, respectively.

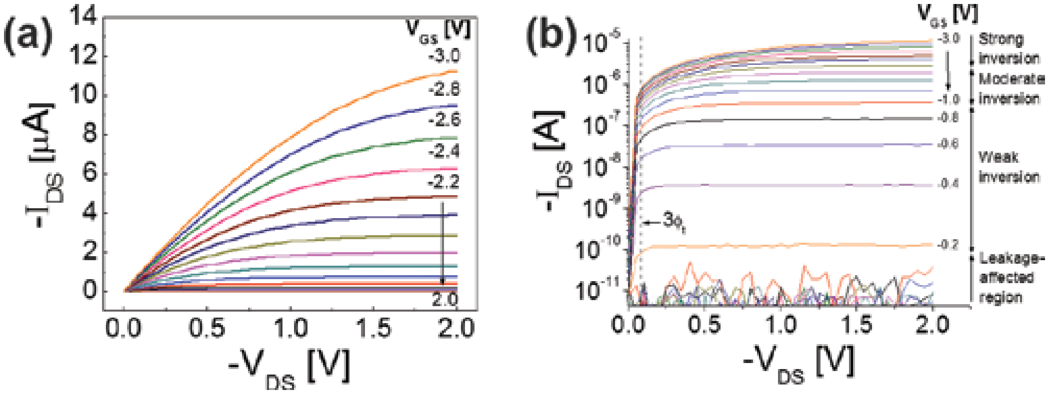

Figure 4. Output characteristics of the self-aligned Si nanowire FET in (a) linear and (b) logarithmic scale [42].

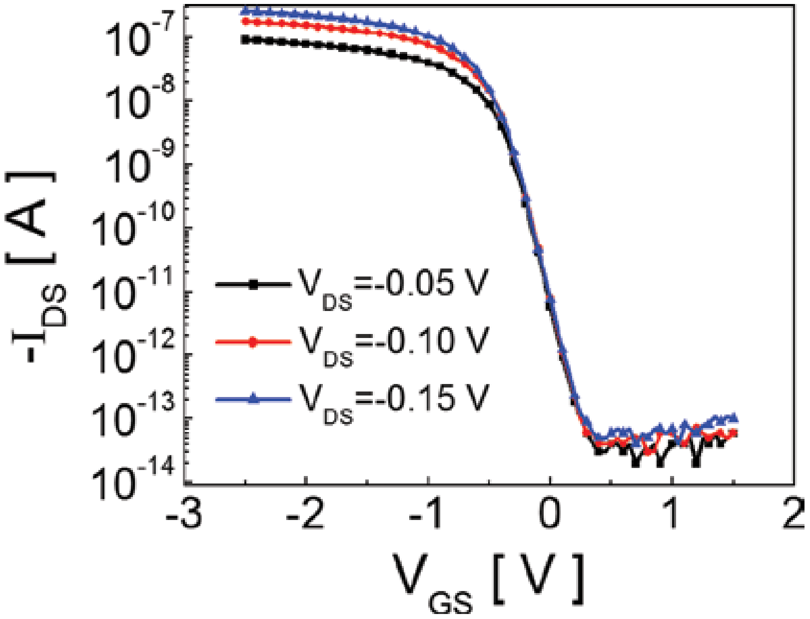

Figure 5. Transfer characteristics of the Si nanowire FET, with V_{DS} value of −50, −100 and −150 mV, respectively [42].

The on/off current ratio is ~10^8 within a 1.2 V V_{GS} window and no ambipolar behaviour is observed. The carrier mobility can be calculated from the linear region of the transconductance when $V_{DS} = -50$ mV with a presumed diameter of 20 nm for the nanowire channel. The calculated results show that the fabricated Si nanowire FETs have a relatively consistent hole mobility around 100 cm^2/Vs. The subthreshold swing (SS) can be extracted from the subthreshold region of I_{DS} in the log-scale I_{DS}–V_{GS} curves. The SS values of the Si nanowire FETs are as low as 75 mV/dec, which is quite small as compared to most reported results on nanowire FETs and poly-Si thin-film transistors [42].

The Si nanowire FETs fabricated through the self-alignment approach exhibit excellent performance as indicated by a high on/off current ratio (~10^8), small leakage current ($<10^{-14}$ A), good carrier mobility (~100 cm^2/Vs) and small subthreshold slope (75 mV/dec). These excellent characteristics are due to the clean interfaces formed in the self-alignment fabrication process, and such Si nanowire FETs are very attractive for future nanoelectronic device applications.

4. Silicon nanowire-based flash-like non-volatile memory

4.1. Introduction of flash-like non-volatile memory

Today, computing architectures and electronic systems built on CMOS components are still pursuing without any sign of slowing down of requirements for low power, fast speed and high density alternatives. Up to now, electronic systems whose main function is to focus on date computing and storage take up more than half of the semiconductor market, and the demand is still growing explosively in areas such as portable electronic devices and systems. Solid-state mass storage occupies a large portion of this market, due to their compatibility with CMOS scaling technology, suitability for harsh environment without mechanical parts and the fact that most types of memory are non-volatile.

Non-volatile memory is typically employed for the task of secondary storage or long-term storage, which usually does not require fast operation speed or integration density. The current primary storage or on-chip memory still relies upon volatile forms of random-access memory. During the past decades, the size of cache memory in the central processing unit (CPU), which is also known as the static random-access memory (SRAM) has been doubled several times as a feasible strategy to increase the CPU capability. However, increasing SRAM will decrease CPU net information throughput because it is volatile and occupies a large chip floor space. Thus, it will be a revolutionary breakthrough in microelectronics if a truly non-volatile memory can be implemented as the on-chip memory in CPUs replacing SRAM.

4.1.1. Basic memory concepts and scaling challenges

Among all the non-volatile memory candidates for primary storage applications, flash memory is the most widely studied and electrically accessible form and is the most promising non-volatile memory in the electronics market. Flash memory has fast read access times, good retention and reliability and CMOS compatible fabrication process [44–46].

Also known as the floating-gate memory (shown in **Figure 6**), a flash memory device stores the trapped electrons in the floating gate until they are removed by another application of electrical field. Because the floating gate is insulated from the control gate and the MOSFET channel by a relatively thick blocking oxide and a thin tunnelling oxide, respectively, the trapped electrons can be retained for many years, and logical "0" and "1" states can be defined according to the presence or absence of electrons trapped in the floating gate. In the past years, the flash capacity, integrated density and performance have been continued to increase with lower manufacturing cost. Due to its compatibility with conventional CMOS process, it is easier and more reliable to integrate flash memory than other forms of non-volatile memory in logic and analog devices with increasing embedded and stand-alone memory to achieve higher chip performance.

However, current flash memory also exhibit disadvantages such as relatively slow write/erase speed and medium endurance, which make it far below the standards of on-chip memory applications. In a conventional floating-gate memory, the tunnelling oxide can hardly be scaled below 7 nm due to the requirement of data retention. Moreover, ultra-thin tunnelling oxide will lead to severe stress-induced leakage current (SILC) issue. On the other hand, the conventional floating-gate materials, poly Si and oxynitride operate at large programming voltages and endure only 10^5 operation cycles. Even though some new flash technologies are promising for low-voltage operations, the voltage supply is in excess of the working voltage standard of the advanced processes, and the gap between the operation voltage of memory device and CMOS logic continues to be broadened.

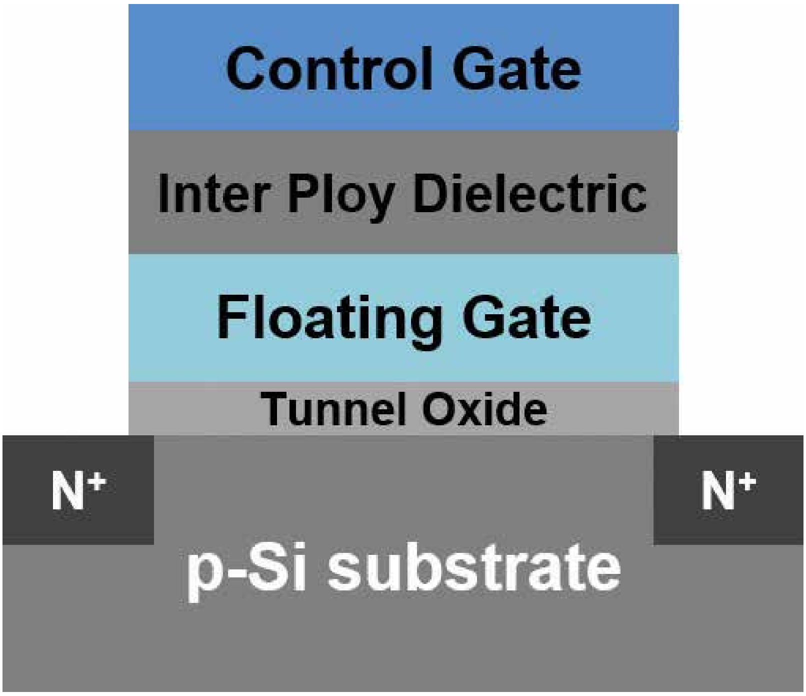

Figure 6. Schematic diagram of a floating-gate flash memory.

4.1.2. SONOS type charge-trapping memory

In recent decades, polysilicon-oxide-nitride-oxide-silicon (SONOS) type charge-trapping non-volatile memory has attracted intensive attention to replace the conventional floating-gate memory due to their advantages such as lower consumption, better reliability and scalability, and simpler structure and fabrication process [47–49]. **Figure 7** demonstrates the schematic structure of a SONOS charge-trapping memory, in which the electrons tunnel through the tunnelling layer and stored in the nitride layer. However, the conventional charge-trapping materials in SONOS memory are not compatible with the dimensional scaling and lead to poor performance in speed, retention and endurance. Furthermore, to achieve faster speed, the tunnelling oxide must be shrinking to enhance the electric field across it while the blocking oxide should be thicker to suppress the leakage current. But thinner tunnelling layer may in turn cause poor stability and reliability, and thicker blocking layer requires larger working voltages. Great efforts have been made for good memory characteristics via various approaches to gain a trade-off between speed and data retention. An effective strategy is to use non-planar channel such as nanotubes and nanowires, to enhance the gate control over the channel. Compared to planar devices based on bulk materials, the nanowires have larger surface-to-volume ratio, therefore, it requires less stored charges to induce the same memory window for nanowire-based flash memory.

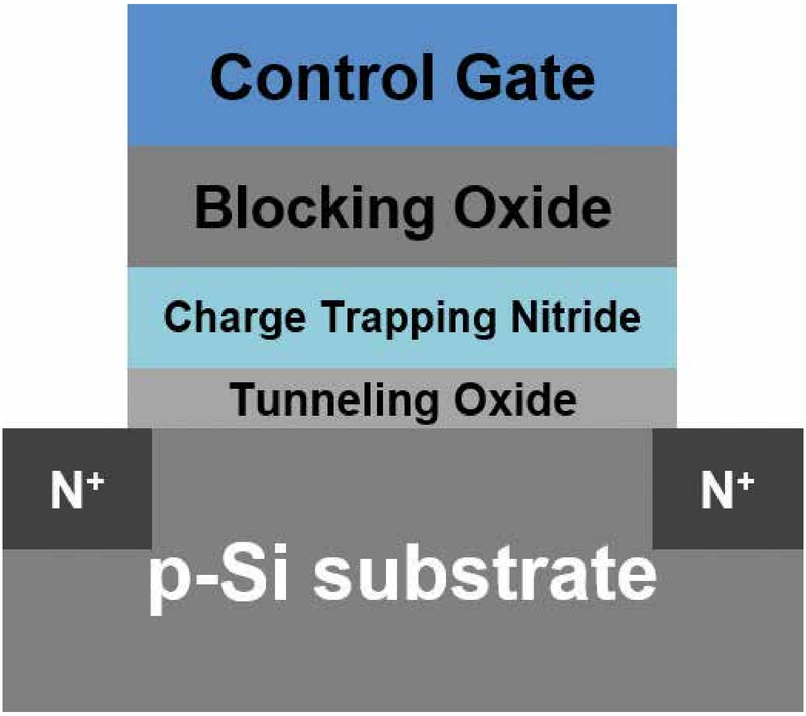

Figure 7. Schematic diagram of a SONOS-type charge-trapping flash memory.

http://dx.doi.org/10.5772/67446

The following in this section reviews the work on the device engineering of flash memory with novel dielectric materials and redox molecules as charge trapping medium based on the Si nanowire FETs. As compared with planar structure memory devise, much better performances have been achieved by utilizing the one-dimensional nanowire channel in the memory devices.

4.2. Silicon nanowire-based dielectric charge-trapping memory

4.2.1. History of one-dimensional nanostructure based charge-trapping memory

The first non-volatile memory cell was demonstrated in 2002 by Fuhrer et al. with one-dimensional nanostructure as the active channel component based on carbon nanotube [50]. Sufficient memory window was witnessed, and Fuhrer et al. predicted that the charge detection of such narrow and high mobility nanotube FETs will outperform planar FET cells [50]. In 2003, Choi et al. reported a carbon nanotube based non-volatile memory with oxide-nitride-oxide (ONO) dielectric stack [51]. A high electric field was generated by 5 V top gate voltage surrounding the surface of 3 nm nanotube, which was sufficiently high to produce Fowler-Nordheim tunnelling.

In 2006, Cha et al. reported a non-volatile flash memory having GaN nanowires with SiO_2 as a charge trapping material, and the operation mechanism was also investigated [52]. It was reported that the electric field distribution in the gate dielectric was different at the centre and the edge beneath the gate. The field is uniform under the centre of the gate across the oxide, and the field distribution at the edge changes along the distance. Non-volatile memory cells based on Si nanowire with CMOS compatible gate dielectric were reported by Zhu et al. in 2011 [53]. HfO_2 was used for charge storage, the thickness of which does not affect the electric field across the tunnelling oxide. The programming speed and retention time have been significantly improved through the surrounding gate structure.

Various high-k materials such as Y_2O_3, Gd_2O_3 and ZrO_2 have been proposed and studied as charge-trapping layer for better reliability and speed [54–56]. Using thicker high-k dielectric with relatively larger band gap as the blocking oxide can be expected to lower the electric field across the blocking layer. Integration of novel dielectric materials as the gate stack in the nanowire FET architecture is therefore very promising to realize practical applications of flash memory with faster speed, higher density, smaller size and better reliability.

4.2.2. Device fabrication

The Si nanowire FET based dielectric charge-trapping flash memory is prepared by following the self-alignment method [57]. Typically, a 300 nm SiO_2 was first grown on Si substrate by dry oxidation. Then a thin film of Au catalyst (1–3 nm) was deposited on patterned area pre-defined by photolithography. Then the Si nanowires were grown from the catalyst following the VLS mechanism and were oxidized at 750°C for 30 minutes to form a ≈ 3 nm SiO_2 which will function as the tunnelling layer. The 3/100 (unit: nm) Ti/Pt source and drain electrodes were then patterned with photolithography and deposited by e-beam evaporation. The channel length between the source/drain electrodes was controlled to be 5 μm. The following process is the deposition of charge-trapping layer and blocking oxide dielectric. Different charge-trapping layer and stacks were fabricated—Ta_2O_5, $Ta_2O_5/Al_2O_3/Ta_2O_5$ (TAT) and a reference HfO_2, with thickness of 20, 6/8/6, 20 nm, respectively [57]. The blocking oxide for all memory devices was selected to be 25 nm for Al_2O_3. Ta_2O_5 was deposited by sputtering, whereas Al_2O_3 and HfO_2 layers were deposited by ALD with TMA and TEMAH as precursors, respectively. Finally, a 100 nm Pd top gate was formed by the same photolithographic and lift-off processes as the source/drain electrodes.

4.2.3. Characterization and performance discussion

Three SONOS-like charge-trapping flash memory devices with structures of metal/Al_2O_3/Ta_2O_5/Al_2O_3/Ta_2O_5/SiO_2/Si (MATATOS), metal/Al_2O_3/Ta_2O_5/SiO_2/Si (MATOS) and metal/Al_2O_3/HfO_2/SiO_2/Si (MAHOS) have been fabricated and electrically characterized [57]. **Figure 8** shows the schematic top view and a cross-sectional transmission electron microscope (TEM) image of a MATATOS device.

Typical output characteristics (I_{DS}–V_{DS}) of the self-aligned Si nanowire FET based flash memory are shown in **Figure 9a** (MATATOS) with smooth and well-saturated drain current curves and a small source and drain contact resistance. **Figure 9b–d** shows the transfer characteristics of the three memory devices with counterclockwise hysteresis loops suggesting the charging and discharging behaviour. By comparing the memory window, the MATATOS and MATOS devices show larger values than the MAHOS device [57].

The programming and erasing (P/E) operations on the MATATOS memory were measured by studying the threshold voltage shift (ΔV_{Th}) under different P/E operations and were

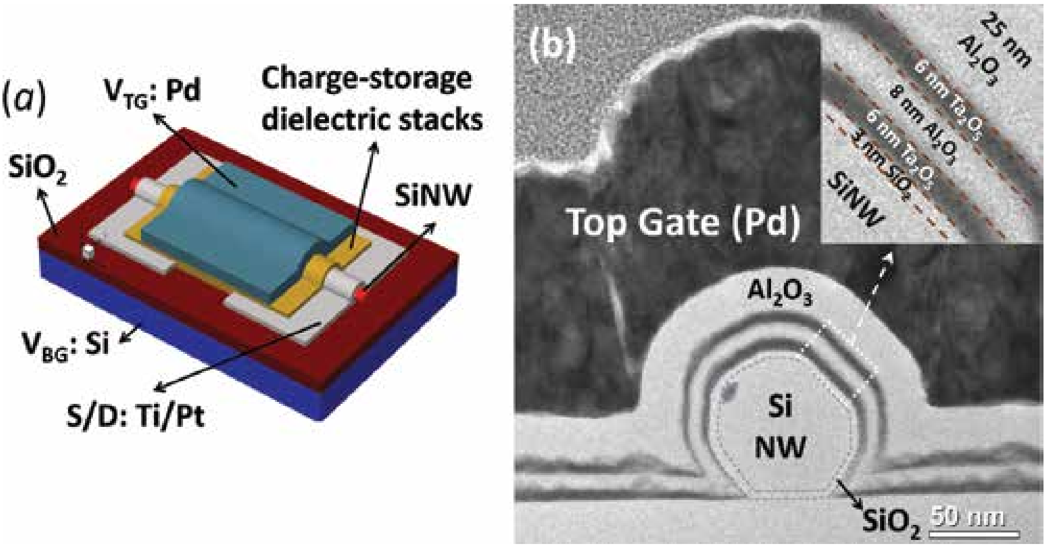

Figure 8. (a) Schematic of top-view of the dielectric charge-trapping flash memory based on Si nanowire FET; (b) cross-sectional TEM image of the dielectric flash memory with TAT charge-trapping layer [57].

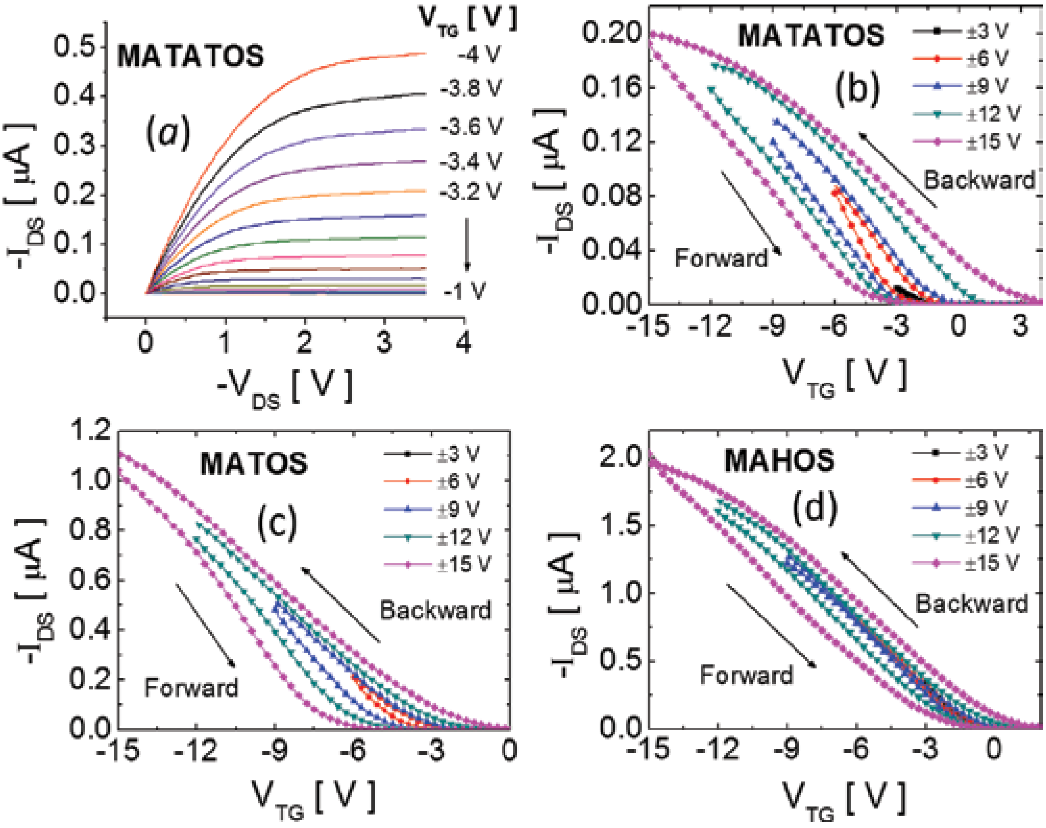

Figure 9. (a) Output characteristics of MATATOS device for V_{GS} from −4 to −1 V with 0.2 V step; transfer characteristics of (b) MATATOS, (c) MATOS, and (d) MAHOS devices, showing counterclockwise hysteresis loops under different V_{GS} sweep ranges [57].

illustrated in **Figure 10**. The I_{DS}–V_{GS} curves show clear ΔV_{Th} under accumulative rectangular gate voltage pulses but exhibiting same subthreshold slope (~300 mV/dec) before and after the programming or erasing operations. This indicates that the ΔV_{Th} is due to the fixed charges in the charge-trapping layers instead of the interface states. By stressing a positive gate voltage, the electrons will tunnel through the tunnelling oxide from the Si nanowire and get trapped in the charge-trapping layers. This corresponds to the programming operations, which will result into a V_{Th} shift towards the positive direction. Negative gate voltage will reversely shift the V_{Th} in the opposite direction by removing the pre-trapped electrons from the charge-trapping layer to the Si nanowire. This is defined as the erasing operations. By comparing the ΔV_{Th} under different P/E gate voltages, it was found that both MATATOS and MATOS devices showed faster speed than the MAHOS device, and MATOS device showed a larger ΔV_{Th} for a long P/E time due to the thicker charge-trapping layer.

Figure 11a shows the charge retention properties of the devices. Less than 25% charge loss was observed for both MATATOS and MATOS devices. **Figure 11b** demonstrated the

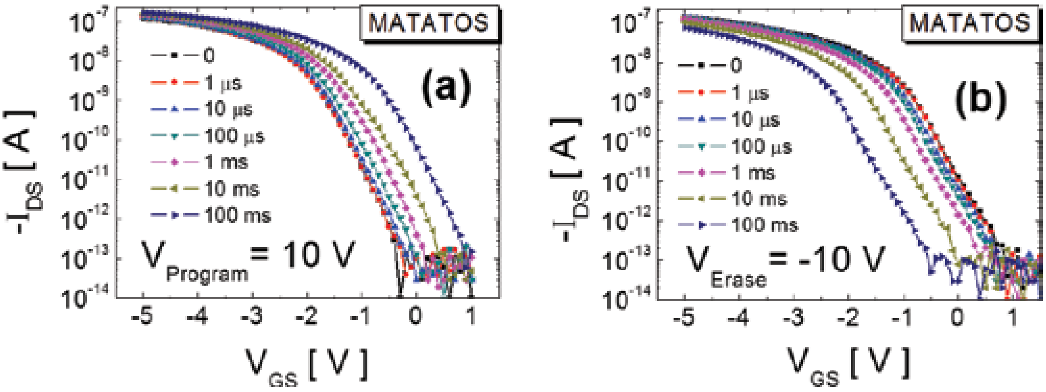

Figure 10. (a) Programming and (b) erasing operations with accumulated P/E time at ±10 V gate voltage pulses on the MATATOS flash memory device [57].

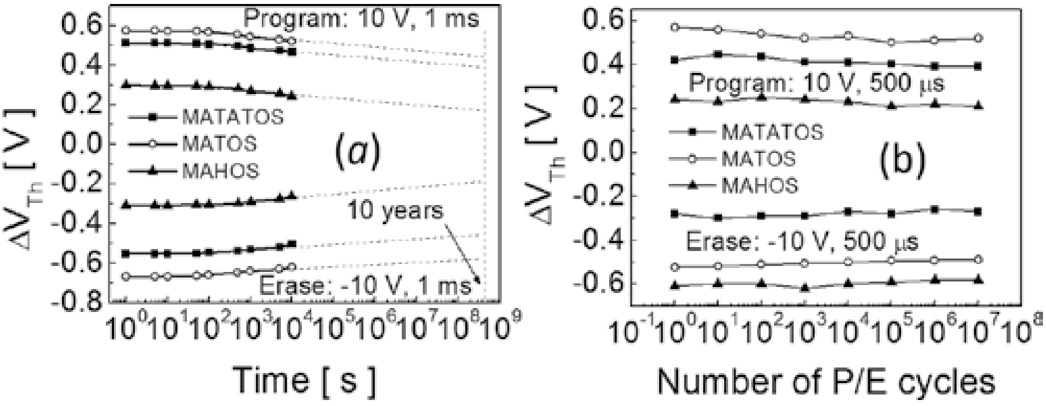

Figure 11. (a) Retention and (b) endurance characteristics of three flash memory devices [57].

endurance properties of the three devices. Very small memory window degradations were observed for all the devices after 10^7 P/E cycles. Such good endurance behaviour arises from the good interface between the Si nanowire and the high-k stacks formed in the self-alignment fabrication process.

The design of the TAT charging-trapping stack with an Al_2O_3 layer sandwiched between two Ta_2O_5 layers is for the multiple charge storage, in which the Al_2O_3 layer functions as the blocking oxide for the first Ta_2O_5 layer and tunnelling oxide for the second Ta_2O_5 layer. As shown in **Figure 12**, clear two-step charging behaviour is successfully observed in the MATATOS device. The first step around 10 V gate voltage is due to the charge storage in the first Ta_2O_5 layer, and the second step at around 20 V is observed indicating the charge-trapping centres in both Ta_2O_5 layers have been filled with electrons. The charge density of the two Ta_2O_5 layers are calculated to be 1.75×10^{19} and 4.98×10^{19} cm^{-3}, respectively.

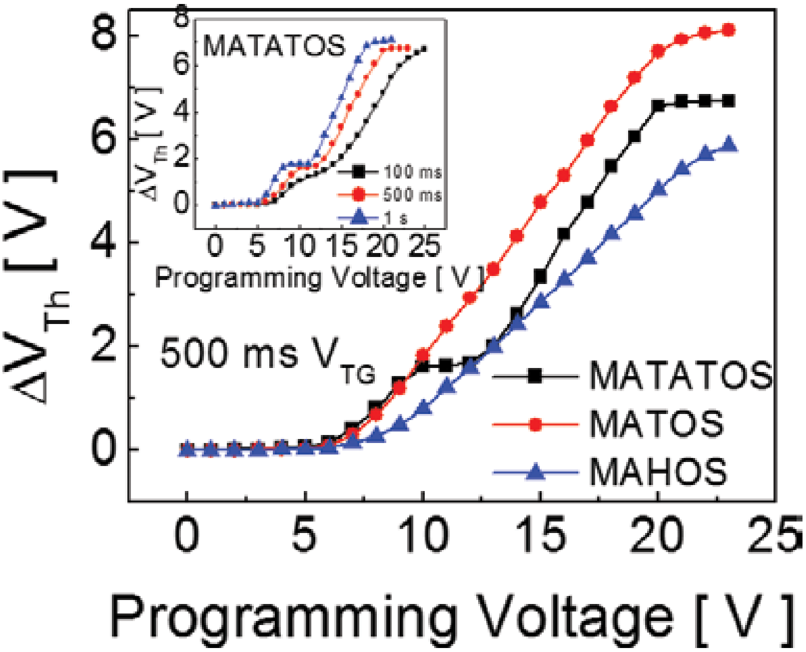

Figure 12. ΔV_{Th} as a function of programming voltage of the three devices. MATATOS device shows a two-step charging storage behaviour. Inset: ΔV_{Th} versus programming voltage of the MATATOS device under gate voltage pulse with different width [57].

By comparing the above results from the flash memory based on Si nanowire FET to the electrical performance of planar capacitor structure with same gate dielectric stack, the nanowire FET-based flash memory exhibits faster speed, better endurance and more remarkable discrete multi-bit memory storage at lower operation voltages [58]. The scaling from planar Si to nanoscale Si nanowire channel effectively enhance the gate electric field introduced by the gate-surrounding structure, enabling faster speed and lower operation voltage. The device reliability is improved with the clean nanowire surface and dielectric interfaces formed by using the self-alignment technique. Such a high-performance and CMOS compatible flash memory is very attractive for future multi-bit non-volatile memory applications.

4.3. Silicon nanowire-based molecular charge-trapping memory

4.3.1. Introduction of redox-active molecules

CMOS and semiconductor non-volatile memory scaling have generated various approaches towards building memory devices with higher scalability and better performance. The hybrid silicon/molecular approach is very attractive as a technology that leverages advantages afforded by a molecule-based active medium with the vast infrastructure of traditional MOS technology.

In reduction-oxidation, redox-active molecules can be attached on various surfaces such as Si and SiO_2 by forming a self-assembled monolayer (SAM) or multiple layers with simple and low-cost processes. Due to the inherent reduction and oxidation of the redox centres, such molecules can exhibit distinct charged and discharged states which can represent the logic on and off states. It has been demonstrated that the redox-active molecules attached on Si structures are stable and can endure more than 10^{12} P/E cycles [59]. Such an excellent reliability is derived from the intrinsic properties of redox molecules. Thus, incorporating redox-active molecules as charge-storage medium in a Si-based flash memory is quite interesting. By taking advantage of the high-quality thin oxide surrounding the Si nanowire, which is readily feasible in various chemical functionalizations, a molecular flash memory with redox molecules attached on the Si nanowire surface serving as the charge storage medium can have even better memory performance including lower operation voltage, faster speed, better device scalability and better reliability.

4.3.2. Redox-active molecules attachment and memory device fabrication

Two redox-active molecules were integrated and studied in the molecular flash memory: α-ferrocenylethanol (referred as ferrocene) and $Ru_2(ap)_4(C_2C_6H_4P(O)(OH)_2)$ (referred as Ru_2), in which ap = 2-anilinopyridinate, with the molecular structures shown in **Figure 13** [60].

The molecular flash memory device fabrication follows the self-alignment Si nanowire FET process as well. After the catalyst patterning, nanowire growth and oxidation and source/drain electrode formation, the molecules SAM attachment on the nanowire was performed by placing droplets of a solution of dichloromethane with 3-mM ferrocene and 2 mM Ru_2 on the active areas separately [60]. Each drop was in place for 3–4 minutes and the samples were held at 100°C in an N_2 environment during the attachment. Saturated SAM will be formed after ~30 minutes. After the self-assembly process, dichloromethane was used to rinse the substrates to remove any residual molecules that are not bonded to the SiO_2 surface. Then, the samples were immediately loaded into the ALD chamber for a deposition of 25 nm Al_2O_3 with TMA and H_2O as precursors at 100°C. Finally, a 100 nm Pd top gate was formed with photolithographic and lift-off processes. A reference sample without molecules was fabricated for comparative study.

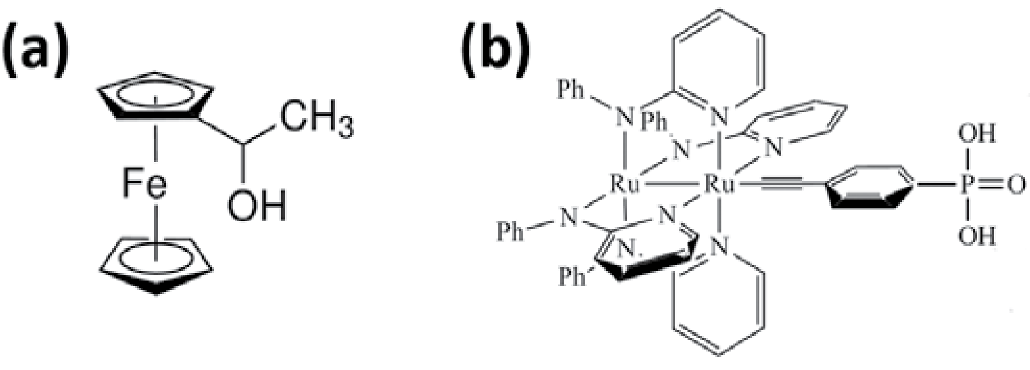

Figure 13. Molecular structure of (a) α-ferrocenylethanol and (b) $Ru_2(ap)_4(C_2C_6H_4P(O)(OH)_2)$ [60].

4.3.3. Electrical characterization and memory performance

Schematic structure of a completed molecular flash memory device was shown in **Figure 14a**. **Figure 14b** shows the TEM image of the cross-section of a ferrocene-attached molecular flash memory. A clear gate surrounding structure has been obtained, with an "intermixed" region observed (indicated by the red dash line). Schottky-barrier p-type MOSFET characteristics have been observed for the Si nanowire based molecular flash memory cells as the source/drain was engineered as Schottky junction. **Figure 15a** and **b** shows the output characteristics of a typical ferrocene molecular flash memory. Smooth and well saturated I_{DS}–V_{DS} curves have been observed with clear leakage-affected region and the weak, moderate and strong inversion operation regions. From the I_{DS}–V_{GS} curves shown in **Figure 15c** and **d**, counterclockwise hysteresis loops were obtained for both devices, suggesting the charge trapping mechanism. The log-scale transfer characteristics shown in the insets demonstrated an on/off ratio as high as ~10^7. The inset (ii) in **Figure 15c** shows the I_{DS}–V_{GS} curves of the reference sample (without molecules), and a negligible memory window was observed, ruling out the possibility of charge storage in the Al_2O_3 dielectric traps.

The P/E speed characterizations of the ferrocene flash memory were shown in **Figure 16a** and **b**. Threshold voltage shift towards the positive (negative) direction was observed during the programming (erasing) operations, indicating the electrons (holes) were injected from the Si nanowire through the SiO_2 and stored in the centres of the molecules. From **Figure 16c** and **d**, both molecular memory devices showed fast P/E speed, which arises from the intrinsic fast speed of the charging behaviour of the molecules and the strong electric field induced through the top gate control over the channel in the gate-surrounding structure.

Similar to the multiple charging behaviour demonstrated in the previous dielectric flash memory, the Ru_2 molecular flash memory is also designed and expected for the application

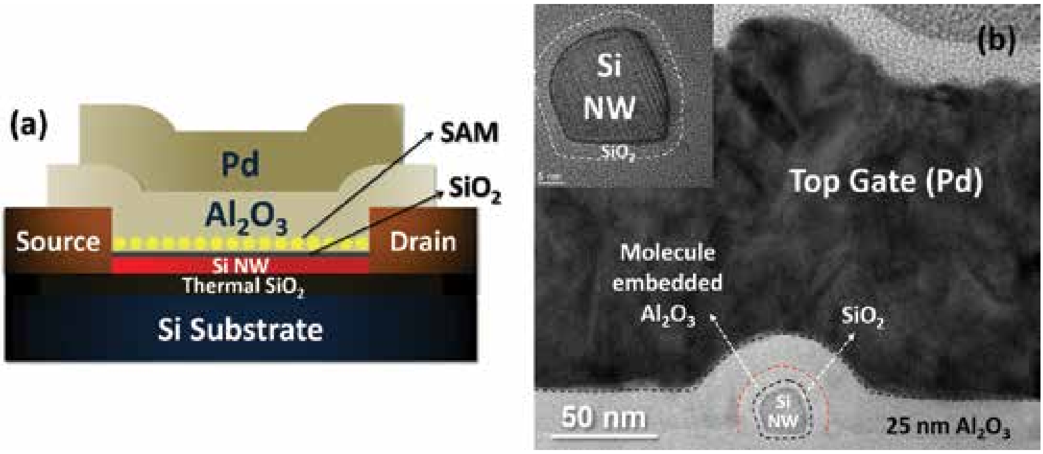

Figure 14. (a) Schematic structure of a completed molecular flash memory device based on Si nanowire FET; (b) TEM image of the cross section of a ferrocene-attached molecular flash memory. The red dashed line indicates the ferrocene-embedded Al_2O_3 region. Inset: Cross section of the nanowire channel, with SiO_2 layer indicated by the dashed line [60].

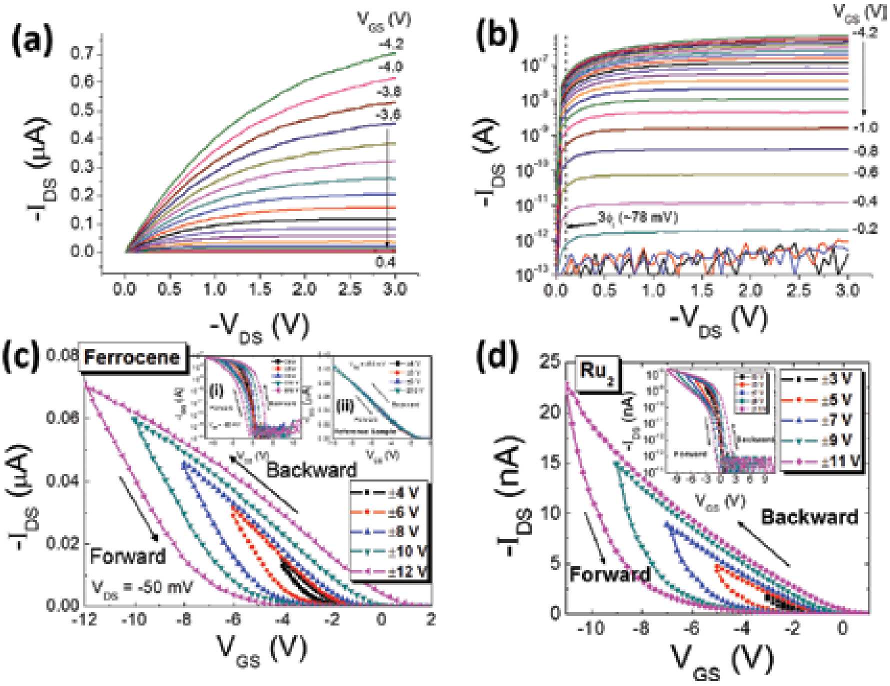

Figure 15. (a) Linear and (b) log-scale output characteristics of ferrocene molecular flash memory; I_{DS}–V_{GS} of the (c) ferrocene and (d) Ru_2 molecular flash memory with the insets showing the log-scale transfer curves. Inset (ii) in (c) shows the I_{DS}–V_{GS} curves of the reference sample with negligible hysteresis observed [60].

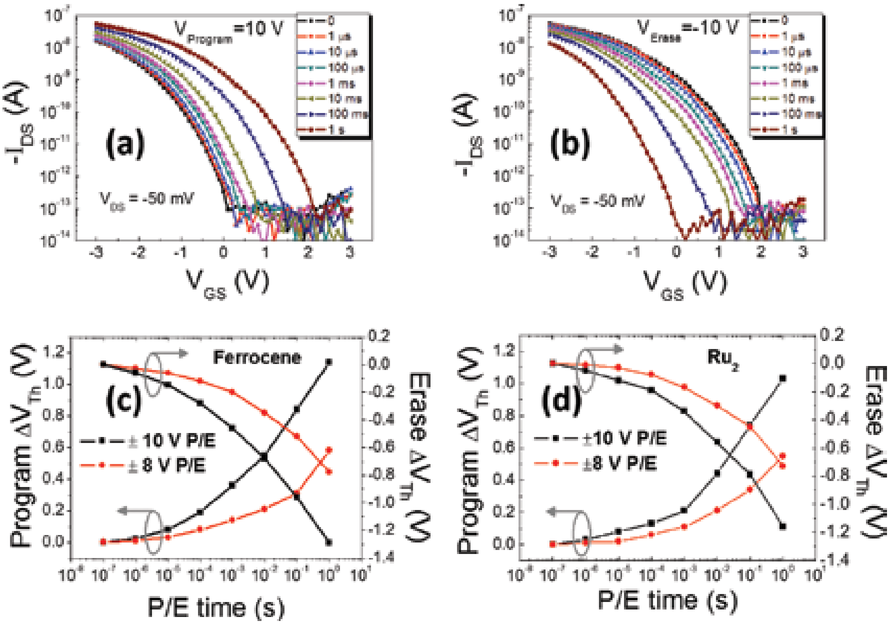

Figure 16. (a) Programming and (b) erasing operations of the ferrocene molecular memory under accumulative rectangular P/E gate voltage pulses. Speed characterizations of the (c) ferrocene and (d) Ru_2 molecular flash memory [60].

of multi-bit memory storage due to the two redox centres, which can exhibit stable and distinct charged states at different voltage levels [57, 60]. As shown in **Figure 17b**, two charged steps were observed at around 10 and 14 V, respectively. The overall charging density of the Ru_2 SAM was calculated to be 1.12×10^{13} cm^{-2}, which is sufficiently high for discrete multi-bit memory applications. One of the most intriguing features of a molecular flash memory is the reliability. **Figure 17c–f** shows the date retention and the endurance properties of the

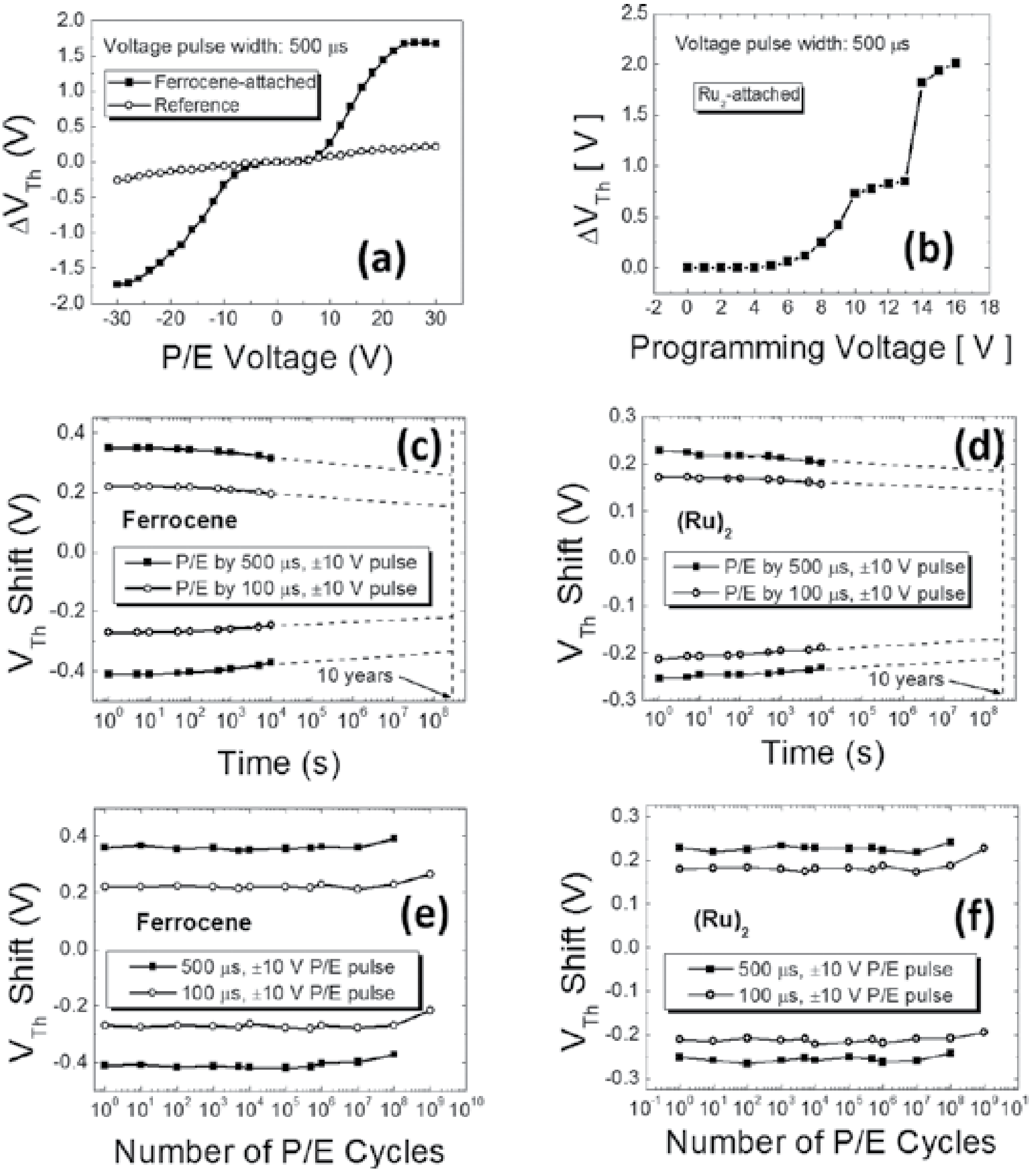

Figure 17. ΔV_{Th} of (a) ferrocene and reference sample and (b) Ru_2 flash memory as a function of P/E voltage. Room temperature retention characteristics of (c) ferrocene and (d) Ru_2 flash memory. Endurance properties of (e) ferrocene and (f) Ru_2 flash memory [60].

ferrocene and Ru_2 flash memory devices, respectively. The projected 10 year memory window showed a charge loss of only 20%, and the excellent endurance characteristics were demonstrated by the negligible memory window degradation after 10^9 P/E cycles, which is about 10,000 times better than that of the conventional floating gate memory [60]. Such a good reliability is due to the intrinsic stable redox behaviour of the molecules and the high-quality tunnelling oxide with clean solid/molecule and dielectric interfaces by using the self-aligned nanowire FET fabrication process. The nanowire FET based molecular flash memory is thus very attractive for future fast speed, high-endurance and high-density on-chip non-volatile memory applications.

5. Nanowire field-effect transistor as a platform for novel materials research

Semiconductor nanowires have shown unique properties in the manner of both physics and technology. The significance of nanowires over planar materials has been more and more discovered and focussed through various interesting and fundamental phenomena, when nanowires have nanoscale diameter at or even below the characteristic length scale of such basic parameters as phonon mean free path, exciton Bohr radius, magnetic domain size, exciton diffusion length and so forth [61]. Many physical properties of semiconductor nanowire are utterly different from the planar bulk materials due to the confines of nanowire surface. Moreover, the large surface-to-volume ratio of nanowires allows for distinct structural, electrical and transport behaviours, as well as advanced technological applications.

This section focuses on the applications of nanowire MOSFETs as a platform for novel materials research. Topological insulator materials and devices are discussed here as an example illustrating the significance of semiconductor with nanowire morphology in the understanding and implementation of fundamental physics and properties behind the materials.

5.1. Introduction to topological insulators

Topological insulators are characterized as a new class of materials having insulating band gaps in the bulk but gapless surface states topologically protected by time-reversal symmetry [62, 63]. Recently discovered three-dimensional topological insulators such as Bi_2Se_3, Bi_2Te_3 and Sb_2Te_3 have been intensively investigated both theoretically and experimentally [64, 65]. Most current experimental research focuses on the surface states of thin films grown by a molecular beam epitaxy (MBE) or mechanically exfoliated from bulk materials. For example, the gapless surface states featuring helical Dirac electrons have been observed by angle-resolved photoemission spectroscopy (ARPES) and scanning tunnelling microscopy (STEM) techniques. A few groups have reported the modification of surface conduction of such materials by doping, electrical gating or polarized light [66–68]. But there has rarely been reported of high-performance nanoelectronic devices based on topological insulators such as the analog of MOSFET. For conventional CMOS devices, the Si surface conduction is protected by thermal SiO_2 to optimize the inversion properties for good transistor performance. For topological insulators, the gapless surface state is derived from the inherent material properties and maintains a robust surface conduction. Therefore, it will be very attractive to integrate the topological insulators as the active conducting channel in MOSFETs.

However, despite the significant efforts made in engineering of materials and devices based on bulk topological insulators, it is always a challenge to modulate the surface conduction due to the dominant contribution from bulk conduction. Topological insulator nanowires can be expected to greatly enhance the surface conduction due to their extra-high surface-to-volume ratio. Here, we will review the work on MOSFET devices based on topological insulator nanowires and the effective separation of surface conduction from the bulk conduction by an external electrical means [69].

5.2. VLS nanowire synthesis of topological insulator Bi_2Se_3 nanowires

The Bi_2Se_3 topological insulator nanowire FETs were fabricated by following the self-alignment process, similar to that of previous Si nanowire FETs [69]. The essential steps are as follows: the SiO_2/Si substrates with patterned Au catalyst were loaded in the downstream end in a horizontal tube furnace while Bi_2Se_3 source powder was located at the heating centre. The furnace was heated to a temperature in a range of 500–550°C and kept for 2 hours with a 50 sccm flow of Ar gas as a carrier gas. The Bi_2Se_3 nanowires were grown following the VLS route at pre-defined locations with typical length of 20 μm and 50 nm in diameter. Ti (3 nm)/Pt (100 nm) source/drain electrodes were formed by photolithography. A layer of 30 nm HfO_2 was then deposited at 250°C by ALD covering the nanowire channel and also a part of source/drain electrodes. The final step is the formation of 100 nm Pd top gate electrode.

Figure 18a shows the SEM image of the as-synthesized Bi_2Se_3 nanowires. Au nanoparticles were found at the top end of each wire, indicating the VLS mechanism. The high-resolution TEM (HRTEM) image shown in **Figure 18** demonstrates that the Bi_2Se_3 nanowires are in a well-defined single-crystal rhombohedral phase with growth direction close to $[11\bar{2}0]$. From the cross-sectional TEM image (**Figure 18d**); it is clear that the hexagonal nanowire core is surrounded by the insulating HfO_2 and the Omega-shaped top gate [69].

5.3. Characterizations of Bi_2Se_3 nanowire FET

The Bi_2Se_3 nanowire FET shows excellent transfer characteristics, as shown in **Figure 19**, such as close-to-zero cutoff current, strong-inversion-like on state current and over 10^8 on/off ratio within 1.0 V gate voltage. The nanowire FET has unipolar current dominated by electron conduction, which is similar to a conventional long-channel Schottky-barrier MOSFET with either electron or hole conduction determined by the unipolar Schottky junctions at the source and drain. **Figure 19b** and **c** shows well-saturated and smooth I_{DS}–V_{DS} curves. I_{DS} saturates roughly at $V_{DS} = V_{GS} - V_{Th}$ in the highly conductive region but does not saturate at $V_{DS} \approx 3\phi_t$ in the weak/moderate conductive region. Instead, I_{DS} keeps increasing significantly after $3\phi_t$, suggesting the fact that the Bi_2Se_3 nanowire FET does not follow the diffusion current model as described for the conventional MOSFETs. It is believed that I_{DS} in the weak/moderate conductive regions is also dominated by drift current [69].

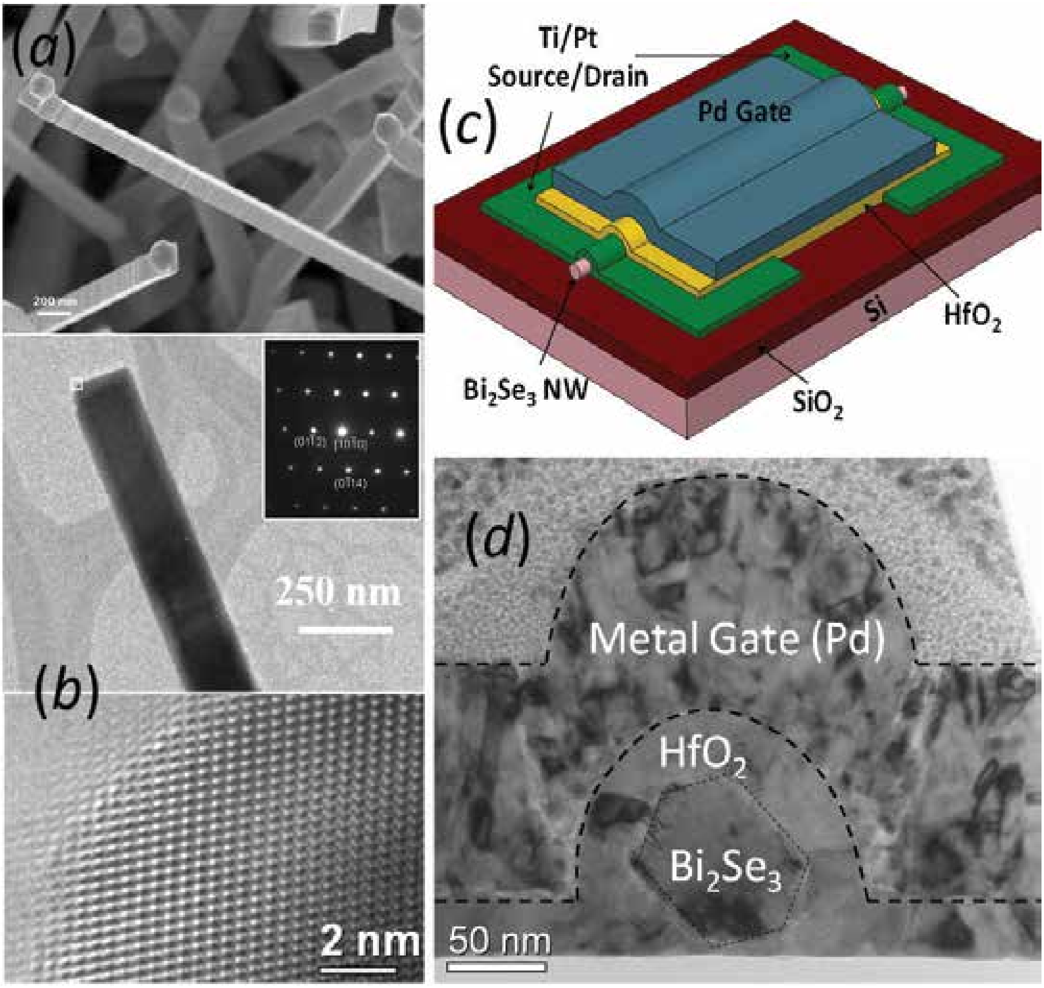

Figure 18. (a) SEM image of Bi_2Se_3 nanowires synthesized by following the VLS mechanism; (b) HRTEM image of Bi_2Se_3 nanowire showing the $[11\bar{2}0]$ growth direction. Inset: Magnified region of the nanowire; (c) schematic structure of a Bi_2Se_3 nanowire FET; (d) cross-sectional TEM image of a Bi_2Se_3 nanowire FET [69].

Further characterizations at different temperatures confirm that the saturation of I_{DS} is due to the electron velocity saturation at the source end instead of the pinch-off at the drain end of the nanowire channel, because a linear relationship was observed between the saturation drain current and the over-threshold voltage (V_{GS}–V_{Th}) as shown in **Figure 19**. By comparing the transfer characteristics at different temperatures (**Figure 20a**), it was found that I_{DS}–V_{GS} curves obtained at temperatures lower than 240 K show a clear cutoff region with higher on/off ratio. The off state current for temperatures greater than 240 K flattens and saturates at negative voltages much below V_{Th}. Such temperature dependence indicates metallic conduction in the on state and insulating behaviour in the off state. By fitting the strongly activated temperature-dependent current to $I_{DS,Off} = I_0 e^{-E_a/kT}$ where E_a is the activation energy, k is

Boltzmann's constant and I_0 is a constant prefactor. E_a value of about 0.33 eV was obtained which is very close to the reported band gap value of bulk Bi_2Se_3 [69].

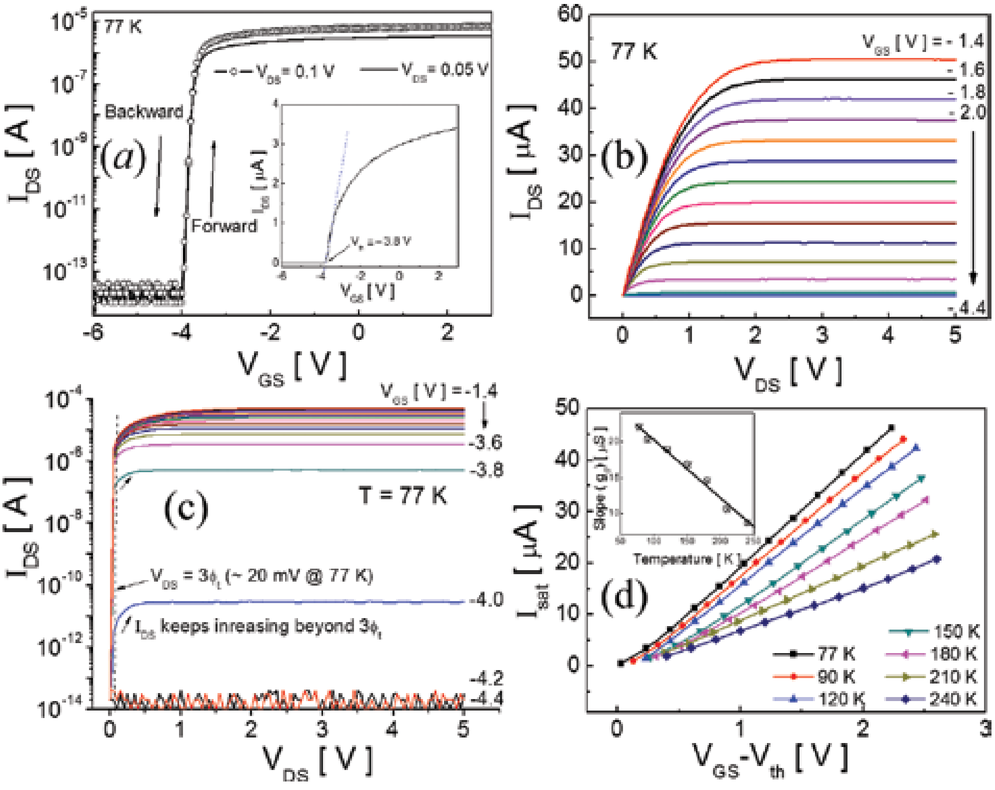

Figure 19. (a) Transfer characteristics and (b and c) output characteristics of the Bi_2Se_3 nanowire FET at 77 K. (d) I_{DS} as a function of over-threshold voltage. Inset: Linear fit slope versus temperature [69].

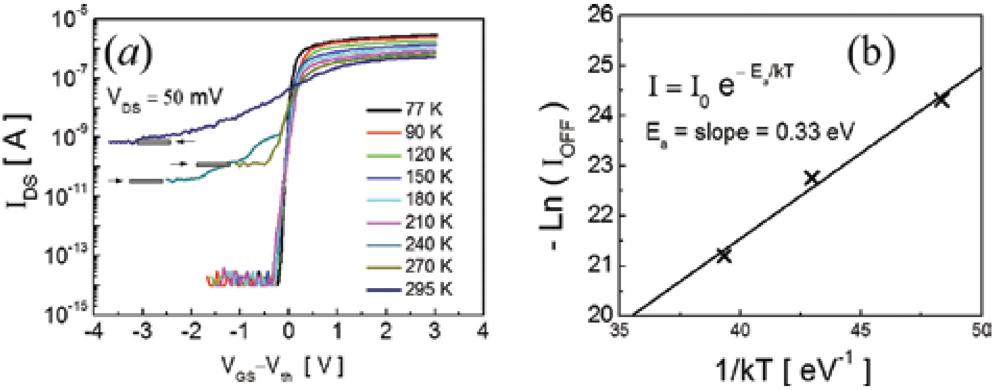

Figure 20. (a) I_{DS}–V_{GS} curves at different temperature; (b) ln(I_{DS}) at off state versus 1/kT above 240 K and its fit to $I_{DS,Off} = I_0 e^{-E_a/kT}$. [69].

5.4. Performance discussion

In the off state, the gate voltage is large enough to fully deplete the electrons from the nanowire, and the small temperature-dependent off-state current is due to the thermal excitations across the energy band gap of the bulk of Bi_2Se_3 nanowire. This further indicates the fact that the electric field generated surround the gate by the gate voltage below the threshold is strong enough to modify the spectrum of the nanowire and destroy the surface conduction channels [69]. Different with the conventional semiconductor nanowires, the saturated current of the Bi_2Se_3 nanowire FET in the on state is linear in gate voltage, indicating metallic conduction and is most likely flowing at the nanowire surface. Such interpretation also agrees with the temperature dependence shown in **Figure 20a**. The most significant achievement is that the surface metallic conduction and the insulating switch-off can be controlled by a surprisingly small gate voltage, resulting from the excellent gate control by the surrounding gate nanowire FET structure.

The above electrical performance obtained from the Bi_2Se_3 topological insulator nanowire FET is very impressive by taking advantages of the nanowire surrounding gate structure, leading to an enhanced gate control over the nanowire channel to realize electrical behaviour that have not been observed on planar counterparts. For example, the sharp switching from cutoff to surface conduction and saturation current by a gate voltage of a few volts is neither expected nor has been previously reported. Since the spin and momentum are locked in the surface states of topological insulators, possibilities of electric manipulation of spin current using gate voltage as well as novel circuit applications may be opened up using such one-dimensional topological insulator materials.

6. Conclusions

The physics and operation principles of nanowire materials and device have been systematically studied. Semiconductor nanowires enable the surrounding-gate structures, which significantly enhance the gate control over the channel in the electrical devices, leading to quite distinct and interesting device behaviours compared with the planar or bulk materials. The "self-alignment" approach enables simultaneous batch fabrication of large numbers of nanowire devices, while effectively reducing the processing steps in which nanowire surfaces might be contaminated. Si nanowire FETs with excellent electrical performances have been used as the platform to fabricate novel flash non-volatile memory devices. Both high-k dielectric and molecular charge-trapping memory demonstrate excellent memory behaviour and are very interesting for future on-chip non-volatile memory applications. The "self-alignment" method and the nanowire FET device architecture have been proved to be an effective platform and approach to be implemented and study other novel materials. High-performance topological insulator Bi_2Se_3 nanowire FET has been fabricated and investigated. The surface states are successfully separated from the bulk conduction within a small range of gate voltage due to the strong electric field induced through the surrounding-gate structure formed in the self-alignment fabrication process. Such a high-performance nanoelectronic device and the analysis on surface conduction have never been previously reported. Therefore, the nanowire MOSFETs not only exhibit their potential in future CMOS scaling at advanced technology nodes but also provide an excellent approach for novel materials research towards next-generation micro and nanoelectronic devices.

Author details

Hao Zhu

Address all correspondence to: hao_zhu@fudan.edu.cn

School of Microelectronics, Fudan University, Shanghai, P.R. China

References

[1] Dennard R.H., Gaensslen F.H., Yu H.N., Rideout V.L., Bassous E., Leblanc A.R. Proceedings of the IEEE. 1999;**87**:668-678.

[2] Moore G.E. IEDM Technical Digest. 1975;11-13.

[3] Tans S.J., Verschueren A.R.M., Dekker C. Nature. 1998;**393**:49-52.

[4] Wagner R.S., Ellis W.C. Applied Physics Letters. 1964;**4**:89-90.

[5] Ucjikoga S. MRS Bulletin. 2002;**27**:881-886.

[6] Duan X..F, Niu C.M., Sahi V., Chen J., Parce J.W., Empedocles S., et al. Nature. 2003;**425**:274-278.

[7] Wu Y.C., Chang T.C., Liu P.T., Chou C.W., Wu Y.C., Tu C.H., et al. IEEE Transactions on Nanotechnology. 2006;**5**:157-162.

[8] Mertens H., Ritzenthaler R., Chasin A., Schram T., Kunnen E., Hikavyy A., et al. IEDM Technical Digest. 2016;524-527.

[9] Gunawan O., Sekaric L., Majumdar A., Rooks M., Appenzeller J., Sleight J.W., et al. Nano Letters. 2008;**8**:1566-1571.

[10] Zervas M., Sacchetto D., Micheli G.D., Leblebici Y. Microelectron Engineering. 2011;**88**:3127-3132.

[11] Westwater J., Gosain D.P., Tomiya S., Usui S., Ruda H. Journal of Vacuum Science & Technology B. 1997;**15**:554-557.

[12] Huang Y., Duan X.F., Wei Q.Q., Lieber C.M. Science. 2001;**291**:630-633.

[13] Salalha W., Zussman E. Physics Fluids. 2005;**17**:063301.

[14] Evoy S., DiLello N., Deshpande V., Narayanan A., Liu H., Riegelman M., et al. Microelectron Engineering. 2004;**75**:31-42.

[15] Papadakis S.J., Hoffmann J.A., Deglau D., Chen A., Tyagi P., Gracias D.H. Nanoscale. 2011;**3**:1059-1065.

[16] Li Q.L., Koo S.M., Richter C.A., Edelstein M.D., Bonevich J.E., Kopanski J.J., et al. IEEE Transactions on Nanotechnology. 2007;**6**:256-262.

[17] Hertel T., Martel R., Avouris P. Journal of Physical Chemistry B. 1998;**102**:910-915.

[18] Wu Y., Cui Y., Huynh L., Barrelet C.J., Bell D.C., Lieber C.M. Nano Letters. 2004;**4**:433-436.

[19] Schmidt, V., Senz S., Gosele U. Nano Letters. 2005;**5**:931-935.

[20] Wang C.X., Hirano M., Hosono H. Nano Letters. 2006;**6**:1552-1555.

[21] Akiyama T., Nakamura K., Tomonori I. Physical Review B. 2006;**74**:033307.

[22] Zhao Y., Yakobson B.I. Physical Review Letters. 2003;**91**:035501.

[23] Marks L.D. Reports on Progress in Physics. 1994;**57**:603-649.

[24] Ma D.D.D., Lee C.S., Au F.C.K., Tong S.Y., Lee S.T. Science. 2003;**299**:1874-1877.

[25] Lee B., Rudd R.E. Physical Review B. 2007;**75**:041305.

[26] Ma L., Wang J., Zhao J., Wang G. Chemical Physics Letters. 2008;**452**:183-187.

[27] Leu P.W., Svizhenko A., Cho K. Physical Review B. 2008;**77**:235305.

[28] Canham L.T. Applied Physics Letters. 1990;**57**:1046-1048.

[29] Ng M.F., Zhou L., Yang S.W., Sim L.Y., Tan V.B.C., Wu P. Physical Review B. 2007;**76**:155435.

[30] Yao D., Zhang G., Li B. Nano Letters. 2008;**8**:4557-4561.

[31] Wang J., Polizzi E., Ghosh A., Datta S., Lundstrom M. Applied Physics Letters. 2005;**87**:043101.

[32] Luisier M., Schenk A., Fichtner W. Applied Physics Letters. 2007;**90**:102103.

[33] Persson M.P., Lherbier A., Niquet Y.M., Triozon F., Roche S. Nano Letters. 2008;**8**:4146-4150.

[34] Lherbier A., Persson M.P., Niquet Y.M., Triozon F., Roche S. Physical Review B. 2008;**77**:085301.

[35] Geaney H., Mullane E., Ryan K.M. Journal of Materials Chemistry C. 2013;**1**:4996-5007.

[36] Kornienko N., Whitmore D.D., Yu Y., Leone S.R., Yang P. ACS Nano. 2015;**9**:3951-3960.

[37] Zhang D., Eaton S.W., Yu Y., Dou L., Yang P. Journal of the American Chemical Society. 2015;**137**:9230-9233.

[38] Furneaux R.C., Rigby W.R., Davidson A.P. Nature. 1989;**337**:147-149.

[39] Fleisher R.L., Price P.B., Walker R.M. Nuclear Tracks in Solids. Berkeley: University of California Press; 1975.

[40] Wang C.C., Kei C.C., Yu Y.W., Perng T.P. Nano Letters. 2007;**7**:1566-1569.

[41] Kemell M., Pore V., Tupala J., Ritala M., Leskela M. Chemistry of Materials. 2007;**19**:1816-1820.

[42] Zhu H., Li Q., Yuan H., Baumgart H., Ioannou D.E., Richter C.A. Solid-State Electronics. 2012;**78**:92-96.

[43] Colinge J.P. Solid-State Electronics. 2004;**48**:897-905.

[44] Atwood G. IEEE Transactions on Device and Materials Reliability. 2004;**4**:301-305.

[45] Lai S.K. IBM Journal of Research and Development. 2008;**52**:529-535.

[46] Pavan P., Bez R., Olivo P., Zanoni E. Proceedings of the IEEE. 1997;**85**:1248-1271.

[47] Wu K.H., Chien H.C., Chan C.C., Chen T.S., Kao C.H. IEEE Transactions on Electron Devices. 2005;**52**:987-992.

[48] Honda K., Hashimoto S., Cho Y. Applied Physics Letters. 2005;**86**:063515.

[49] Wrazien S.J., Zhao Y.J., Krayer J.D., White M.H. Solid-State Electronics. 2003;**47**:885-891.

[50] Fuhrer M.S., Kim B.M., Brintlinger T. Nano Letters. 2002;**2**:755-759.

[51] Choi W.B., Chae S., Bae E., Lee J.W., Cheong B.H., Kim J.R., Kim J.J. Applied Physics Letters. 2003;**82**:275-277.

[52] Cha H.Y., Wu H., Chae S., Spencer M.G. Journal of Applied Physics. 2006;**100**:024307.

[53] Zhu X., Li Q., Ioannou D.E., Gu D., Bonevich J.E., Baumgart H., et al. Nanotechnology. 2011;**22**:254020.

[54] Wang Y.Q., Hwang W.S., Zhang G., Samudra G., Yeo Y.C., Yoo W.J. IEEE Transactions on Electron Devices. 2007;**54**:2699-2705.

[55] Huang X.D., Lai P.T., Liu L., Xu J.P. Applied Physics Letters. 2011;**98**:242905.

[56] Huang X.D., Liu L., Xu J.P., Lai P.T. Applied Physics Letters. 2011;**99**:112903.

[57] Zhu H., Bonevich J.E., Li H., Richter C.A., Yuan H., Kirillov O., et al. Applied Physics Letters. 2014;**104**:233504.

[58] Zhu H., Yuan H., Li H., Richter C.A., Kirillov O., Ioannou D.E., Li Q. IEEE Transaction on Nanotechnology. 2013;**12**:1151-1157.

[59] Liu Z.M., Yasseri A.A., Lindsey J.S., Bocian D.F. Science. 2003;**302**:1543-1545.

[60] Zhu H., Pookpanratana S.J., Bonevich J.E., Natoli S.N., Hacker C.A., Ren T., et al. ACS Applied Material and Interfaces. 2015;**7**:27306-27313.

[61] Hochbaum A.I., Yang P. Chemical Reviews. 2010;**110**:527-546.

[62] Bernevig B.A., Hughe, T.L., Zhang S.C. Science. 2006;**314**:1757-1761.

[63] Zhang H., Liu C.X., Qi X.L., Dai X., Fang Z., Zhang S.C. Nature Physics. 2009;**5**:438-442.

[64] Hasan M.Z., Kane C.L. Reviews of Modern Physics. 2010;**82**:3045-3067.

[65] Qi X.L., Zhang S.C. Reviews of Modern Physics. 2011;**83**:1057-1110.

[66] Kong D., Chen Y., Cha J.J., Zhang Q., Analytis J.G., Lai K., et al. Nature Nanotechnology. 2011;**6**:705-709.

[67] Steinberg H., Gardner D.R., Lee Y.S., Jarillo-Herrero P. Nano Letters. 2010;**10**:5032-5036.

[68] Cho S., Butch N.P., Paglione J., Fuhrer M.S. Nano Letters. 2011;**11**:1925-1927.

[69] Zhu H., Richter C.A., Zhao E., Bonevich J.E., Kimes W.A., Jang H.J., et al. Scientific Reports. 2013;**3**:1757.

Chapter 7

Silicon Quasi-One-Dimensional Nanostructures for Photovoltaic Applications

Rosaria Anna Puglisi, Valentina Lombardo and
Sebastiano Caccamo

Additional information is available at the end of the chapter

http://dx.doi.org/10.5772/67749

Abstract

Thanks to the silicon abundance, stability, non-toxicity and well known electronic properties, Si based solar cells have represented the leading actors in the photovoltaic market and future projections confirm this predominance. However, half of the module cost is due to the material consumption and processing. In order to decrease the costs, a cut in the Si consumption must be operated, with consequent decrement in the optical absorption, generated current and device efficiency. To keep the performance level, a proper Si surface design with the objective to trap the light, has been developed. One of the most popular approaches is to use silicon nanowires embedded in the solar cell emitter where they play the role of optically and electrically active layer, thanks to their excellent optical absorption properties. However, also another material has been the terminus of the light-trapping materials, the silicon nanoholes. Their mechanical robustness is superior, making their integration inside the cell easier and cost-effective. The review will bring about all of the most common methods to fabricate these two types of nanostructures when used for solar cells applications, their optical properties and some critical aspects related to their high surface to volume ratio which modify the recombination processes.

Keywords: silicon, nanowires, nanoholes, synthesis, solar cells

1. Introduction

Silicon nanowires (SiNWs) are very popular in the third-generation solar cells because of their outstanding electrooptical properties [1–4]. Once integrated within the cell active area, they: (i) increase the solar spectrum optical absorption, thanks to light-trapping mechanisms, thus increasing the electron-hole generation and consequently, the device short circuit current [2, 5]; (ii) due to spatial confinement, improve the coupling with certain wavelengths [6, 7]; (iii) their radial symmetry allows for the formation of core-shell junctions, which decouple the light path from carrier path, improving independently the absorption and the electricity collection [8, 9]. Currently, another quasi-one-dimensional (1D) material is overlooking the panorama of the solar cells latest generation: nanoholes [10, 11]. These nanowire "mirror" structures offer all their advantages but are more robust and then easily integrable. The review aims to give an overview of all the synthesis methods and electrooptical properties of both structures, for the first time, presently proposed in the literature giving a space to the issues still open. The two complementary materials, SiNWs and silicon nanoholes (SiNHs), are first described in terms of the synthesis methods. As far as SiNWs are concerned, various techniques are present in the literature, mostly based on growth or etch, both assisted by metals. The vapor-liquid-solid (VLS) method [12, 13] is among the most popular methods to grow the nanowires (NWs). In this process, a liquid eutectic droplet is formed by a metal catalyst particle and the solid Si substrate brought at high temperature. A vapor Si precursor reacts with the liquid eutectic by dissociating the Si adatom, which then diffuses inside it to precipitate and form the 1D NWs. Many aspects dramatically controlling the NW morphology like the precursor flow gas [14], the substrate type, and crystallographic orientation [8, 12, 15]; the SiNWs growth direction [12] and substrate surface chemical conditions [16] will be reviewed and discussed. When SiNWs are deposited by using plasma enhanced chemical vapor deposition (CVD) systems, also the plasma power plays an important role in the formation of SiNWs [17]. The most common metal exploited as a catalyst is gold, thanks to its low eutectic temperature. A part of the literature recognizes the importance to remove the Au catalyst droplets, residual after the growth, because they create deep level traps in Si and increase carrier recombination [18, 19]. To avoid the electronic defects introduced by Au, also other catalysts will be discussed [20]. The review will also address the metal-assisted chemical etching (MAE), another very popular method to obtain SiNW arrays [6, 21–27]. MAE is based on a redox reaction in which a metal with a suitable reduction potential, e.g. Ag, catalyzes the Si oxidation through a highly oxidant agent, such as peroxide aqueous solution. The so-formed silicon oxide is thus removed by the etchant agent. Again the substrate properties such as the synthesis process conditions, the doping type, and concentration will be examined [22, 24]. Nanosphere lithography (NSL) is usually applied together with the MAE process to obtain the ordered SiNWs. It exploits the self-assembly of water-dispersed polystyrene (PS) nanoparticles onto a substrate, where they spontaneously arrange in a hexagonal pattern. A metal layer is then thermally evaporated, acting as a catalyst for successive MAE etch in the regions not protected by the PS particles, which leads to the formation of the nanostructures [26]. SiNWs are excellent platforms to build core-shell architectures, where the inner part of the 1D Si nanostructure is doped of one type, while the external shell is doped of the opposite type [8]. This geometry allows to separate the electrical carrier path, which proceeds along the NW radial direction, from the optical absorption, which takes place along the axial one. In this way, the carrier collection distance is smaller or close to the minority carrier diffusion length. A few approaches presented in the literature propose to add a layer of intrinsic Si between the inner and outer regions, forming a p-i-n coaxial junction [9], in order to increase the effect of the electric field of the depleted region during the charge separation process. Regarding the doping methods for the SiNWs, conventional routes, such as gas source-based techniques or ion implantation [18], will be described, as well as the new cost-effective approach called molecular monolayer doping (MD), consisting in immersing the Si to be doped inside a liquid solution with dopant chemical precursors [28]. The techniques of formation SiNHs will be then considered [10, 29]. Etching in this case is the only key process, typically assisted by metal nanoparticles or in a more standard approach through dry etch machines. The lithographic masks are used if ordered NHs are targeted. As for the NW formation, the metal-assisted etching is a very popular method to create NHs for its versatility and affordability. The size of the holes obtained is strictly related to the metal amount, substrate orientation, and etching duration [11, 21, 30]. The roughness left by the etching process is well recognized in the literature as an issue for the application of solar cells because of its impact on the carrier recombination, thus different surface passivation procedures are developed [11, 31]. UV lithography merged with the MAE etch is proposed in the literature as one of the most conventional strategies for the synthesis of an ordered nanoporous pattern [10]. As alternative strategies, many interesting nonconventional lithographies proposed in the literature will be reviewed. Among the others, nanoimprinting lithography (NIL) is a high-throughput and low-cost technique and not limited by the effects of wave diffraction or scattering which instead occur in the photolithographic methods. For these reasons, this technique can be considered as a promising candidate for mass production [32, 33]. Block copolymer (BCP) lithography is another useful alternative, thanks to its simplicity, low cost, and suitability for the semiconductor industry [34]. The basic principle is the self-assembly of block-copolymers: when a BCP solution is spun onto a solid substrate, it can lead to the formation of a specific template over the whole sample area. The realized pattern can act as a soft mask for the successive pattern transfer to underlying substrates. A less known method to fabricate NHs will be also described, the focused ion beam (FIB) which lets to obtain diameters below few nm [33]. After the synthesis the SiNHs, optical properties [35–38] will be presented, highlighting for the first time the pros and cons of both structures.

2. Silicon nanowires

The VLS method is one of the predominant techniques to form SiNWs. In the VLS method, the Si precursor gas, typically silane, is introduced into a CVD or a physical vapor deposition chamber where liquid metal catalyst particles, forming an eutectic with the substrate, react with the Si precursor atoms. Inside the liquid metal droplet, the Si atoms undergo to supersaturation and diffuse toward the crystalline Si growing interface. The nucleation of SiNWs depends on the deposition temperature and the partial pressure of the precursor gas. At low pressures, the chemical potential of the wire is higher than that of the vapor phase due to the high surface-to-volume ratio, and this prevents the wire nucleation in small eutectic droplets

[39]. When the pressure increases, the steam chemical potential increases as well and the growth of small nanowires becomes possible [40, 41]. SiNWs grown by the VLS method can change dramatically their morphology by changing also the precursor gas flow [14]. SiNWs have been grown directly on a p-type <111> Si substrate. Gold catalysts were deposited by sputtering in Ar plasma. The size of Au nanoparticles was controlled by the sputtering conditions and the thickness of Au film. After the metal deposition, SiNWs were grown using SiH_4 and N_2 as a carrier gas and changing flow gas ratio (SiH_4:N_2) as in the following: 1:3.2, 1:6, and 1:8. Scanning electron microscopy (SEM) and X-ray diffraction (XRD) results showed that with the second dilution (1:6) the density obtained was the highest, the size of NWs more uniform and the crystalline structure more pronounced than in the other cases. With respect to thermal CVD, plasma-enhanced CVD systems present the advantage to decompose the precursor gas by using the plasma energy instead of the high temperature. Moreover, in an inductively coupled plasma (ICP) CVD reactor, the high plasma density and the absence of acceleration of ions toward the substrate grant the absence of structural substrate damage. In reference [17], different plasma power values between 0 and 1000 W were explored to study its role on the Si NWs growth. Morphological results showed that three growth regimes can be identified: a low plasma region from 0 to 60 W, where only 1D SiNW structures were grown, an intermediate region from 60 to 100 W where both 1D and 2D films were obtained, and a third zone at high plasma power (from 100 to 1000 W) where SiNWs were absent and only continuous uncatalyzed Si layer was obtained. When deposited by VLS onto thermally oxidized Si substrates [12], a percentage of 44% of SiNWs with radius smaller than 10 nm showed by high-resolution Transmission Electron Microscopy (HRTEM) a diamond-like structure, while this characteristic was not present in those with larger diameters, which presented the wurtzite structure confirmed also by Raman measurements. In order to explain this result, a thermodynamic analysis was carried out considering the difference in standard free energy between diamond and wurtzite structure in NWs and the contribution due to the surface energy and stress. They found that the final structure is produced by the large stress in the surface curvature developed during the Si precipitation and nucleation with the catalyst. The surface pressure during the successive growth is reduced by the development of facets. VLS is also used to fabricate hexagonally faceted SiNWs as large as 30 μm in diameter [13]. SiNWs were grown on Si <111> substrates by Au catalyzed VLS process by using $SiCl_4$ as a precursor and H_2 as a carrier gas. The metal catalyst was first deposited onto the substrate by thermal evaporation and then annealed. The SiNWs obtained by this process present hexagonal facets and have diameters ranging between 30 nm and 30 μm, with lengths larger than 50 μm. After the deposition, they dispersed the SiNWs by sonication on an n-type Si wafer and doped the NW by p-type Al diffusion. Then deposited by lithography four metallic contacts to perform four-point-probe measurements on a single NW. They demonstrate ohmic n-type behavior and measure the contact resistance, the effective resistivity and the doping level. They found that bulk resistivities ranged from 0.02 to 0.08 Ω cm, corresponding to 1×10^{18} to 1×10^{17} cm^{-3} electrically active dopants. P- and n-type doped SiNWs have also been obtained by VLS growth in CVD with SiH_4 [15]. The doping process took place during the growth by adding PH_3 or B_2H_6 to the process gas. B-doped Si <111> substrates or borosilicate glass substrates with a thin B-doped multicrystalline Si layer on top were used. The NWs were grown and doped under identical conditions for both substrate types. Morphological characterization showed no differences in

the SiNWs despite the different substrates, with lengths of about 3–6 μm and diameters of about 20–100 nm with a 2-nm thick SiO_2 shell. SiNWs can be grown by VLS also on stainless steel foil substrates [8]. In this case, the experiment started with a 5-nm thick Au film deposited as a catalyst layer over the stainless steel substrate. Then p-type SiNWs have been synthesized in a CVD chamber at 650°C by using silane, hydrogen, hydrochloric acid, and trimethylboron as the dopant precursor gas. The obtained SiNWs show diameters of about 100 nm and a length of about 16 μm. The array was first oxidized and then dipped in HF to remove the grown oxide, in order to expose a part of the SiNWs to the deposition of a thin n-type a-Si conformal layer by plasma enhanced CVD (PECVD) using PH_3 as a doping gas. In such a way, a core-shell structure is formed. It presents the advantage to separate the electrical carrier path, which travels along the NW radius, from the optical absorption, which takes place along the NW length. The deposition of the amorphous Si layer is proposed by the authors as an effective strategy to passivate the NWs through the minimization of the nonradiative surface recombination. The introduction of an intrinsic layer in the p-i-n coaxial SiNWs array for fabrication of solar cells has also been suggested in the literature [9], with the advantage to increase the effect of the electric field in the depleted region during the charge separation process. The p-type core of SiNW was fabricated by the VLS method, while the intrinsic and n-type shells were produced by chemical vapor deposition using in the external shell phosphine as a precursor. The outer portions were grown at temperatures higher than the core to suppress the eutectic mediated growth and allow the deposition the NW surface. TEM analysis showed that the p core of SiNW is monocrystalline, and the shells are polycrystalline. An average value of SiNW diameter was measured to be 300 nm. Then p-i-n coaxial SiNW solar cells were fabricated and characterized under air mass 1.5 global (AM 1.5G) illumination. I–V showed an open circuit voltage V_{oc} of 0.260 V, a short circuit current I_{sc} of 0.503 nA, a fill factor FF of 55.0%, and an efficiency of 3.4%. Much more complicated structures are proposed in reference [42]. In this chapter, the authors fabricated four different coaxial SiNW architectures, respectively, p/n, p/in, p/pn, and p/pin. The SiNWs core was grown by the Au-catalyzed VLS method, while the shell was grown by the vapor solid (VS) method using SiH_4, B_2H_6, and PH_3. The core diameters were 100 nm. High-resolution transmission electron microscopy (HRTEM) is used to understand a crystal orientation <112> of the core along the length of the NW. The external NW surfaces were instead assigned to two {111} planes, two {011} planes, and four {113} planes. Energy Dispersive X-Ray Spectroscopy (EDX) was used to characterize the phosphorous dopant and oxygen profiles in the p/pin sample. The O and P profiles and the spatial maps of the P X-ray counts exhibited signals at the edges of the outer n-shell, with the P peaks shifted by 10–15 nm inward with respect to the O ones, thus indicating that the phosphorus atoms are localized at the interface with the oxidized shell. The location of dopant active atoms in SiNWs fabricated by VLS was also studied after one or more steps of chemical oxidation and etching which reduced controllably the SiNWs diameter [43]. The n-type (p-type) SiNWs were synthesized using SiH_4, PH_3 (B_2H_6), and H_2 (He and Ar). Subsequent cycles of chemical wet oxidation/etching were carried out in order to remove 3 nm of material for each cycle. The SiNWs were integrated inside a field effect transistor (FET) device and the electrical characterization showed that, after the removal of the surface layer in SiNWs with diameter smaller than 22 nm, the electrical characteristics strongly changed, revealing the segregation of the dopant atoms on the surface of the SiNWs. Conversely, for diameters larger than 22 nm, the characterization showed that the core of the NWs instead contained dopant atoms. In relation to the *ex-situ* methods to dope the SiNWs, reference [18] demonstrates how the doping of SiNWs is possible by ion implantation, and from this system, a possible functional device is fabricated. This study is realized on three different SiNWs: (1) n doped, (2) n doped at the top and p doped at the bottom, and (3) p doped at the top and n doped at the bottom. The SiNWs were grown by Au catalyzed VLS in an electron beam evaporation system. NWs were 250–500 nm long and 150–400 nm in diameter. The implantation was performed by using B and P ions. The energy was chosen in order for the ion depth to match the NWs length. The NWs were tilted of a few degrees to avoid channeling effects. After ion implantation, a thermal process was necessary in order to remove the implantation damage. In reference [44], the authors present an innovative approach to dope SiNWs in order to fabricate solar cells. SiNWs have been fabricated by the VLS method in an ICP-CVD chamber and showed lengths of about 500 nm and diameters between 2.5 and 70 nm. After the NWs synthesis, the native SiO_2 was removed by HF and the sample immersed in aqua regia in order to etch away the gold agglomerates. Morphological characterization showed the successful elimination of the residual gold agglomerates. SiNWs were doped by molecular monolayer doping, an innovative method that consists in immersing the Si substrate to be doped inside a liquid solution composed of the chemical precursor of the dopant at high temperature [28]. This process leads to the formation of a monolayer of molecules containing the dopant atoms. The sample was then covered with a SiO_2 layer and annealed to diffuse dopant atoms into the substrate. The cell was completed with front and back contacts realized with Ag paste and sputtered Al. I-V measurements in dark showed a rectifying behavior of the diodes but with a high value of the reverse saturation current. This was attributed to the presence of Au residuals, from the VLS process, inside the bulk of the wafer. The high temperature process used in a group of samples for the dopant diffusion let increase the leakage current, probably due to the structural damage induced by the high temperature on the SiNWs. Under solar simulator illumination, the cells showed a photovoltaic effect. I_{sc} presented higher values in the SiNW cells with respect to the planar reference cell, as expected thanks to the improved optical absorption of the nanostructures. However, the increment was also related to the better coupling between the nanostructured surface and the Ag paste than with the planar Si case. Another study is focused on the removal of gold catalyst [19]. In this chapter, SiNW arrays were fabricated by the VLS method from a <111> Si wafer patterned by lithography to define the regions where the Au catalyst was deposited. The SiNWs obtained under these conditions were vertically oriented and 50 μm long, with an average diameter of 2.6 μm. The SiNW array was HF etched and Au was then removed using a commercial etchant. Energy Dispersive X-Ray Spectroscopy (EDX) measurement was performed and Au was detected on the NWs tip and within the Si matrix. To remove these inclusions, multiple cycles of thermal oxidation and etching steps were performed. As it is clear that the literature underlines the importance of the residual Au removal, because it creates deep level traps in the Si band gap, producing phenomena of charge recombination and hopping conductivity, thus deteriorating the carriers transport. Besides gold, other catalysts have also been explored. In or Sn has been used for the SiNWs synthesis on the glass substrate by the VLS method [20] using SiH_4 plasma at 300–600°C. The morphology, density, and properties of the array during the growth were studied as a function of the growth parameters, such as temperature and dilution of Si source in H_2. Energy dispersive X-ray (EDX) analysis was also performed to investigate the residual metal catalyst concentration after the growth. The authors highlighted that the solubility of In is poor in Si, indeed the In content in the NWs was found to be below the EDX limit of detection, while on the top of the nanowire reaches concentrations of 5%. This behavior shows the advantages of these metal catalysts when compared with gold. The role of the interface between In and the substrate was also investigated. In one case, In nanodots (NDs) were thermally evaporated over a Si <111> substrate and then transferred to the growth chamber, while in a second case, they were deposited by Radio frequency (RF) magnetron sputtering and the NWs growth process followed without air breaking [16]. Morphological characterization of the catalyst particles revealed a spherical shape, in the first case, thus indicating a large contact angle with the substrate. The main reason was attributed to the presence of a thin oxide layer at the interface between the In catalyst particles and the Si substrate. This layer hampered the precipitation of Si atoms through the eutectic liquid, causing a low density of SiNWs.

In the second experiment, as a result of elimination of the air breaking, no oxide layer formed at the In/Si interface. This optimization produced a decrease of the In particles contact angle from 140 to 80°. As a result, the NWs density increased with respect to the first process. **Figure 1(a)** shows the results of this last experiment, where the contact angle is measured by SEM observation in tilted view of the In catalyst particles deposited over the Si substrate. Vertically aligned <111> oriented SiNWs were obtained (**Figure 1b**) with a uniform diameter of about 18 nm and a length of approximately 100 nm, as observed by TEM (**Figure 1c**). The diffraction analysis (**Figure 1e** and **f**) confirmed their epitaxial orientation with respect to the

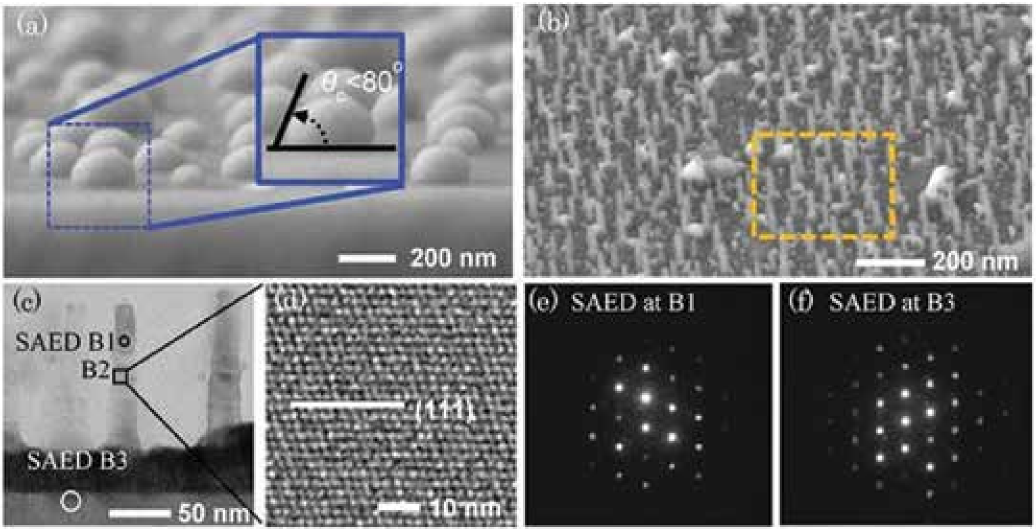

Figure 1. (a) SEM images of In NDs grown by In sputtering, (b) SEM image of Si NWs grown at TS = 600 1C for 60 min. The magnified image in the dotted rectangular area is shown in **Figure 4b**. (c) TEM micrograph of the vertically aligned Si NWs fabricated using In NDs, (d) HR-TEM micrograph of the as-grown (111) oriented Si NWs taken at point "B1" of (c), (e), and (f) shows the SAED patterns taken at points"B1" and "B3," respectively, of (c) [16].

substrate. One of the alternative methods proposed in the literature to synthesize SiNWs is the combination of VLS and laser ablation [45]. The authors compare the method to the one used for the synthesis of carbon nanotubes [46]: a vacuum furnace with a solid source of Si mixed with Fe and a cold finger were used for the SiNWs deposition. The target was kept at 1200°C and the laser pulsed for tens of nanoseconds. The growth took place by evaporating the material from the target, which in vacuum combined to form the liquid catalyst-Si phase and then the supersaturated solid SiNWs. The nanostructures deposited as a net on the furnace inner walls close to the cold finger. This approach then provides template-free SiNWs. TEM images showed that SiNWs were curved, with length of few hundreds of μm and external diameters ranging from 3 to 43 nm with a peak distribution at 16 nm. A 5-nm amorphous shell over the crystalline core was also found. Raman spectra at 521 cm^{-1} of the nanowires showed a tail at lower wavelength numbers, attributed by the authors, to the presence of internal defects besides the SiNWs small size.

MAE is another widespread method to obtain SiNW array [6, 21–27]. A metal catalyst and an etchant solution of HF/H_2O_2 in various ratios are used. MAE has two evidence sources: the first one is that the chemical etching occurs only under the portion covered by the metal, and second is that the "holes" dug into the substrate have the same diameter of the catalyst particles. Peng et al. [20] describe the MAE working principles as a "catalytic conversion of chemical free energy into propulsive mechanical power." Indeed, they explain that the metal basically acts as not just a catalyst but also as a galvanic cell. When deposited onto a Si substrate, we can distinguish two interfaces: the first one is the Ag/etchant solution, which is constituted by the oxidant agent (H_2O_2) and the etchant, HF. This interface works as the cathode of the cell, thus promoting the reduction of the peroxide to water through the consumption of both protons and electrons. Vice versa, the second interface, Si substrate/Ag, works as the anode of the galvanic cell. Here, two reactions play: one is the oxidation of Si, which turns in SiO_2, and the latter one is the etching of Si oxide by the HF, which forms the soluble H_2SiF_6 species. This process depends on both aqueous HF and H_2O_2 species: indeed the electrokinetic model proposed by the authors effectively works only in the presence of both chemicals, and etching rate increases with increasing the concentration of both species. Alternatively, a solution of silver nitrate, fluoridric acid, and water can be applied [6, 22–27]. The particularity of the MAE samples is that the SiNWs are epitaxial, i.e., show single crystal cores and the crystallographic orientation is the same of the used wafer, and maintain the same type and doping level as the starting wafer. As a counterpart, the NW surface is usually very rough due to the fact that it is produced by a chemical etch. The following redox reaction: $Si + 2H_2O_2 + 6HF \rightarrow H_2SiF_6 + 4H_2O$ is explicitly indicated as the base of the NWs formation [22]. A systematic study on the dependence of the MAE SiNW formation process has been performed [22]. They explored six different substrates, p- and n-type, with several degrees of doping levels. A 0.4 M (0.15 M) solution of H_2O_2 for lightly and heavily doped wafers was used. The etching process was performed in dark and at room temperature. The samples were cleaned to dissolve the Ag catalyst and the grown oxide layer. The length and diameter of SiNWs demonstrate a dependence on the doping level of the original substrate: the NWs in heavily doped wafer were smaller than the lightly doped ones and in both cases were several μm in length and 50–200 nm in diameter. The reason whereby heavily doped Si was more active than the lightly doped one was ascribed to the high carrier concentration favoring the electrons transfer [22]. Oblique SiNWs can also be obtained by MAE [23]. A p-type Si <111> wafer previously cleaned was subjected to the evaporation of a net-like layer of 10–50 nm of silver nanoparticles. Successively, the sample was immersed in a solution of DI water, HF (4.6 M) and H_2O_2 (0.44 M) from room temperature to 80°C and various times to modulate the NWs length. The final SiNWs present oblique orientations with two preferential directions, the <100> and <110>. The authors attribute this morphology to the anisotropic etching of silicon and to the competition existing during the catalytic etching along different directions. Besides oblique NWs, zigzag SiNWs can also be produced by immersing cleaned Si wafers in aqueous HF solution (4.6 M) with 0.01 or 0.04 M silver nitrate ($AgNO_3$) solution for 40 min at different temperatures [24]. The array formation using the same solution 0.01 M $AgNO_3$ at two different temperatures (25 and at 55°C) was first focalized. Results showed that at lower temperatures, Ag dots created arrays of straight SiNWs, while at 55°C, the Ag dots produced curved SiNWs. Then a 0.04 M solution at 45–55°C was used and three types of curved SiNWs were obtained (**Figure 2**): I type with a turning angle of 150°, longitudinal orientations on <111> and <113>; II type with 125°, <100> and <111> orientation; III 90° and a longitudinal orientation that alternates between two orthogonal <100> directions (**Figure 2c**).

Two possible etching mechanisms were proposed to explain the results: (1) single-particle etching mechanism in which the Ag nanodots can move, as a result of perturbations, from the <111> direction to the <113> direction (I group). Since the last direction is not energetically favorite, the dots switch back to <111>; (2) a multiparticle etching mechanism in which the higher etching temperature/silver ion concentration enhances the etching activity, so the Ag

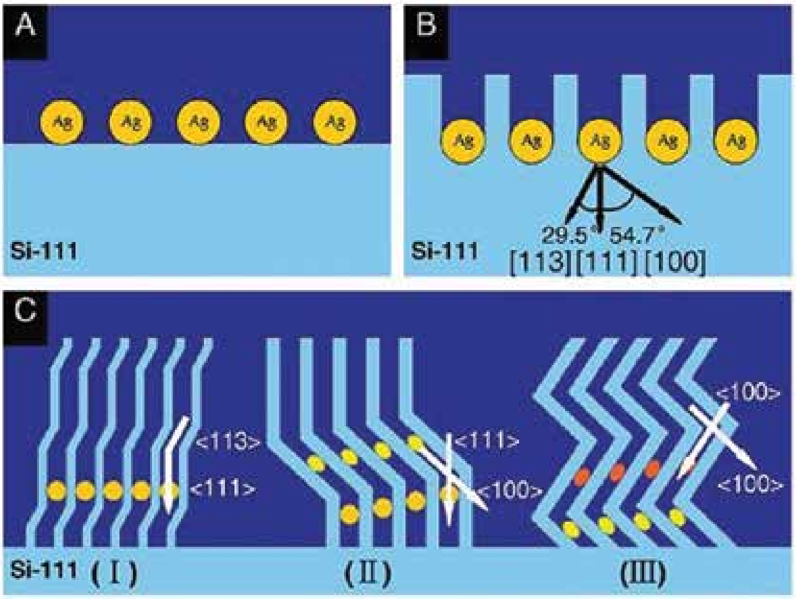

Figure 2. The proposed growth or etching process of the zigzag Si nanowires [24].

particles can move from the <111> direction to the three different <100> directions (groups II and III).

The MAE process can be coupled to a mask of anodic aluminum oxide (AAO) to obtain an ordered array of vertical aligned SiNWs [25]. From SEM characterization performed on AAO masks, the authors estimated the mask pore diameter, interpore distance, and pore density to be 20 nm, 60 nm and 2.9×10^{10} cm^{-2}, respectively. SEM characterization was used also to study the array after silver removal, and in this case, it was evident that the SiNWs had a different diameter at the top and the bottom parts. This difference was assigned to the dissolution of metal during the etching or to the isotropic etching of Si in HF/H_2O_2 and the different exposure times of the NW parts. The evolution of the NWs diameter was also studied as a function of thickness of the metal film, and the results show that the trend is inversely proportional to the thickness. This behavior was explained by considering the decrease of the original pore diameter when the metal thickness increases, due to the conformality of the deposition. Nano sphere lithography (NSL) exploits the self-assembly of polymeric nanospheres in order to create a soft mask for patterning the surface. When water-dispersed PS nanoparticles are spun onto a substrate, they spontaneously arrange in a hexagonal pattern in which they leave triangular voids between each sphere. A successive dry etch leads to a shrinkage of the PS spheres, which thus exposes a major portion of the substrate surface. A metal layer is then thermally evaporated, covering the unprotected substrate, while the area under each PS particle remains metal-free. Therefore, the polymeric nanospheres are removed by dissolving them into a specific solvent or through a lift-off method thus leaving a metal layer with circular voids. This metallic film acts as a catalyst for successive processes such as the MAE etch, which leads to the formation of SiNWs. The final structure characteristics strictly depend on some geometrical parameters such as the "in solution"-diameter of the polymeric particles, the effective diameter related to the polymer/substrate interaction and finally the space between two neighbor particles after the deposition. In reference [26], the NSL obtained by spreading a monodisperse suspension of PS microspheres onto the substrate was used. The size of the PS spheres was then reduced by reactive ion etching process (RIE). The samples were then subjected to the deposition of a gold thin film, thus producing an anti-dot pattern, and subsequently etched in HF/H_2O_2, which acted only on the regions of Si covered with Au. The sample was then immersed into toluene to dissolve the PS spheres, dried and characterized. The SiNWs have size similar to the ones of the reduced PS spheres, i.e., diameter of 400 nm and a length of about 1 μm. Among the others, they studied the influence of the substrate doping type and concentration. As for reference [22], it is found that the doping type influences the etching rate of Si: the substrate with the lower doping concentration showed deeper etching than highly doped one. Axial junctions can be also obtained if using properly doped substrates [6]. The synthesis of SiNWs started with three evaporation steps of amorphous Si layers on borosilicate glass, respectively, doped by: (1) boron (p+), (2) phosphorus (n), and (3) phosphorus highly doped (n+), followed by crystallization with a diode laser at different wavelengths (depending on the doping types). The recrystallized multilayers showed large Si grains (of the order of a few tens of micrometers). Successively, MAE wet etching was performed in order to obtain a SiNW array, presenting an axial junction p+/n/n+ along their length, with the different doping types as the original multilayers. Optical properties showed a reflectance less than 5% in the wavelength between 300 and 1000 nm. The SiNWs were integrated inside a solar cell with the highest efficiency of 4.4%. In reference [27], the authors have synthesized SiNW arrays by using MAE with silver nitrate, fluoridric acid, and water of an n-type Si substrate. The Si oxide was removed by HF and the SiNWs were then covered with a shell of p-type amorphous Si deposited by low pressure CVD and finally the amorphous layer was crystallized by rapid thermal annealing (RTA). SEM analysis showed vertically aligned core-shell SiNWs with a length of 18 μm, total diameter of 350–400 nm, and a coverage of 50%. TEM results showed that the shell was constituted by nanocrystalline domains of about 5 nm. As recognized by the authors, the large surface roughness typical of the MAE etched SiNWs can lead to enhanced depletion region traps, causing strong carrier recombination effects. SiNWs obtained by MAE have been integrated in a solar cell [1]. The nanostructures have been etched by a p-type Si <100> substrates. The n+ emitter was obtained by $POCl_3$ diffusion at 930°C. Aluminum and silver films were evaporated on the rear contact of the cell, the first to remove the parasitic junction and the second to form the back electrode. The front contact was made by Ti/Pd/Ag grid by mask evaporation. The solar cell presented a V_{oc} of 548.5 mV, an I_{sc} of 26.06 mA, and a FF of 0.6512 and a power conversion efficiency of 9.31%. The photovoltic (PV) conversion was not high if compared to other geometries such as the devices based on slantingly aligned SiNW arrays that have been demonstrated in reference [23]. The difference in efficiency was correlated to the low current collection yield or to enhanced surface electron-hole recombination velocity. VLS grown SiNWs was doped to obtain axial p-i-n junctions [2]. The solar cell was fabricated with a single SiNW and the intrinsic region length was varied from 0 to 4 μm. The I-V data for the intrinsic region of 0, 2, and 4 μm show V_{oc} and I_{sc} values of: 0.12 V and 3.5 pA, 0.24 V and 14.0 pA, and 0.29 V and 31.1 pA, respectively.

The results show a systematic improvement in both V_{oc} and I_{sc} with increasing i-segment length, where the largest increase is observed in moving from the p-n to p-i-n structure. The best value of FF (51%) was shown in p-i-n device with i-region of 4 μm and it yielded a maximum power output per NW of 4.6 pW. The efficiency in the single axial NW cell is calculated by considering the projected active area and results 0.5% less than the coaxial geometry which produced 3.4% [9]. The authors also monitored I_{sc} and V_{oc} as a function of the temperature and found that V_{oc} showed a linear dependence while I_{sc} slightly increased. A tandem structure p-i-n+-p+-i-n (**Figure 3A** and **B**) was also fabricated in order to investigate the behavior of series of single-junction SiNW device. Tandem device was created under the same conditions of the single junction NWs. They finally compared the results of p-i-n axial NW to tandem NW device with the same intrinsic length of 2 μm, the values of V_{oc} and I_{sc} are 0.23 V and 10.2 pA, and 0.39 V and 8.2 pA, respectively. These data showed an increment of 57% of V_{oc} (**Figure 3C**) due to the presence of the tunnel junction n+/p+. However, the increment is not large as expected due to the parasitic series resistances at the tunnel interface [2]. A study on the current collection and generated photovoltage for several NW diameters and consequent junction areas with respect to the minority carrier diffusion length has been also pursued [13]. The p-n junction was formed by depositing and diffusing Al over the eutectic temperature on a single NW. The work results suggest that a trade-off between small NWs (enhancing current collection) and large ones (enhancing photovoltage) can be reached when the NW radius is comparable to the minority carrier diffusion length. One of the processing steps more critical

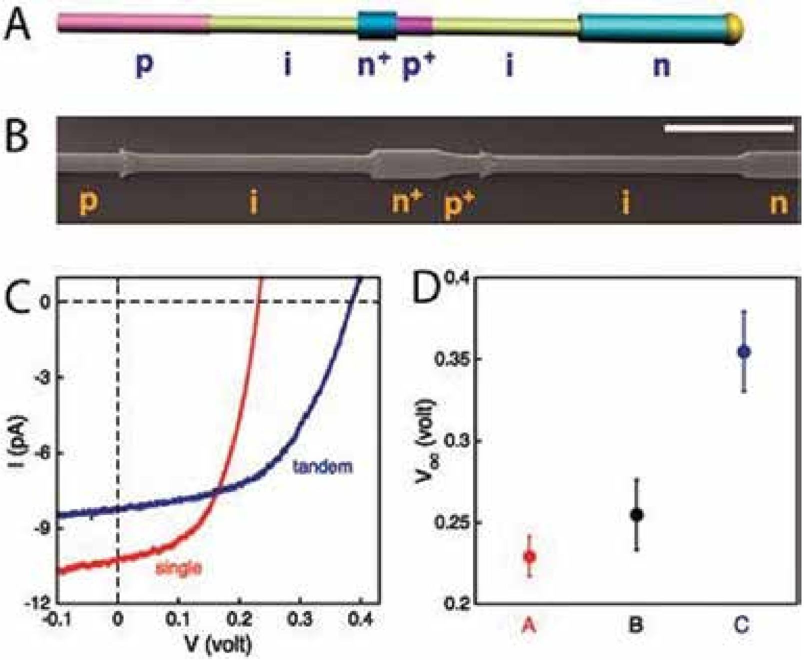

Figure 3. Tandem axial SiNW photovoltaic devices. (A) Schematic of two p-i-n diodes integrated in series on a single NW. (B) SEM images of a selectively etched tandem p-i-n+-p+-i-n SiNW; scale bar is 1 μm. (C) *I-V* responses recorded on p-i (2 μm) -n (single) and p-i-n+-p+-i-n, *i*) 2 μm (tandem) SiNW devices under AM 1.5G illumination. (D) *V*oc for p-i (2 μm) -n (case A), p-i (4 μm) -n (case B), and p-i-n+-p+-i-n, *i*) 2 μm (case C) axial SiNW devices. Error bars are ±1 standard deviation [2].

for the integration of SiNWs inside the solar cells is the passivation process. Indeed, the presence of surface states on the NWs, due to the high surface to volume ratio of these 1D nanostructures, leads to copious carrier recombination events detrimental for the device efficiency. Conductance of SiNWs was investigated before and after a passivation treatment with organic molecules (4-nitrophenyl octadecanoato or tetraethylammonium bromide) [47]. The SiNWs were integrated inside a FET transistor and characterized in terms of the passivation process effects. The treatments with both molecules improved similarly the device on/off ratio, the transconductance and the mobility. The same results were obtained also by changing the first molecule chain lengths. The explanation was based on the fact that the molecules lead to a stable and relatively nonpolar Si-O-C bond, thus reducing the availability of the surface to water hydrolysis, and as a consequence the density of polar surface sites, such as SiO^-.

3. Silicon nanoholes

SiNHs are emerging as promising materials for the fabrication of performing solar cells because of their interesting properties and easy integration in the device processing. Since their first proposal in the solar cells field [10], several examples have appeared in the literature, referring to them as "pores," or "black-Si," "holey structures," and "honeycomb" [48, 49]. Regarding their synthesis, NHs can be realized in Si through electrochemical anodization and oxidation carried in an aqueous electrolyte of HF and H_2O_2 [50]. The process is based on the localization of the electric field on specific substrate sites, due to the depletion layer formed on its surface. The experiments are run onto n-type Si and the surfaces are texturized by applying different electrolyte concentrations and current densities. The pore density can be tuned with the current and HF concentration, while it does not show any clear dependence on the H_2O_2 content. These data have been explained by assuming that the bottleneck process is the removal of the oxidized surfaces rather than their oxidation. The pore depth does not strongly depend on the peroxide concentration, while it increases with the HF. Depths as large as tens of microns can be reached. The oxidation/etching process exploited in the previous case is also employed in MAE, which as for the NW formation is very frequently used to create NHs. The size of the holes obtained is strictly related to both the duration of the metal deposition and etching steps [21]. If compared to the electrochemical anodization, MAE is assisted by a metallic catalyst while the first one is boosted by an external current which supplies the carriers to the Si surface [50]. The fabrication of NHs by MAE is affected by different factors [30]. As seen in the last reference, the samples are immersed in $AgNO_3$ aqueous solution and the amount of deposited Ag, in terms of dot density and size, increases with the immersion time. The Ag particle density will be higher onto more reactive surfaces (e.g., <111> Si than <100> Si), but for very long deposition times the area covered from metal seems to be independent of the substrate orientation. Moreover, this parameter can have a strong effect on the NH morphology: for metal coverage lower than 70%, in the <100> Si substrate the etching path changes abruptly from the vertical to the horizontal direction along the (100) axis, thus showing a clear lateral etching component. While in the case of the <111> Si substrates, the etching process follows a much more irregular path. However, any lateral etching is suppressed for both Si <100> and Si <111> samples when the Ag coverage is higher than 70%. Indeed under these conditions, the nanoparticles sink all together at the bottom of holes and they all follow the equivalent <100> directions, thus forming long, vertical, and aligned structures in the <100> substrate, and oblique pores in the <111> ones [30]. Many interesting approaches found in the literature merge the MAE process with different lithographic techniques to realize ordered patterns. Among these, UV lithography is one of the most conventional strategies proposed [10]. The lithographic steps with the exposure to deep UV light are followed by silver evaporation onto a mask, which undergoes to a lift-off process, thus leaving Ag dots on the Si surface. A MAE wet etching is run by an aqueous oxidant mixture of H_2O_2 and HF, which molds the substrate. After that silver dots are removed with nitric acid from the holes bottom. The morphology shows a regular square-packed NHs array with precise features, such as diameter (800 nm), pitch (≈1 μm), edge-to-edge distance (≈200 nm), and depth (≈1.4 μm) (**Figure 4**). According to this synthetic approach, the lateral dimensions of NHs are strictly conditioned by the specific size of the shadow mask and by the wavelength of the light source used, which can give severe resolution limits when very small sizes are required. As a consequence, the smallest features achievable by the typical UV lithography are on the order of hundreds of nanometers. Differently, the third dimension of the structures can be easily controlled by calibrating the etching time.

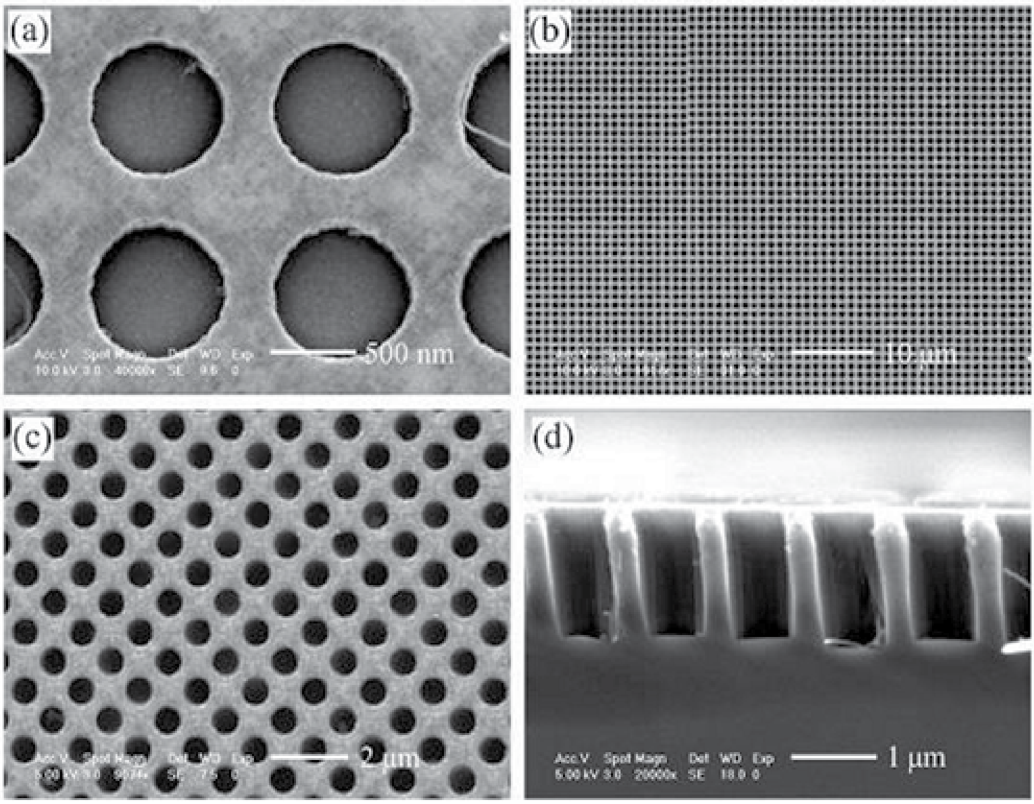

Figure 4. SEM images of silicon nanoholes produced in an 8–12 Ω cm p-Si(100) wafer. (a) Top-view SEM image of ordered, shallow, flat-bottomed pits in Si formed during the initial etching stage. Silver is seen at the bottom of these pits. Marker: 500 nm (b and c): top-view SEM images of ordered silicon nanoholes with large depths after prolonged immersion in HF and H_2O_2 solution. Marker: 10 and 2 μm figure (b) and (c), respectively, (d) cross-sectional view of silicon nanoholes; the hole channels are cylindrical and vertical with respect to the Si surface. Marker: 1 μm [10].

Nanoimprinting lithography (NIL) guarantees the realization of structures with vertical and smooth sidewalls [32, 33]. It consists in the pattern transfer from a hard mold to a resist through mechanical pressure. The replication is then run from the resist to an underlying substrate by successive treatments, such as dry etching. This approach can be exploited for the fabrication of a SiNHs array [51] by using a polydimethylsiloxane (PDMS) mold and poly(methyl methacrylate) (PMMA) resist in order to pattern the surface. The pores are finally realized by etching the Si substrate with SF_6/O_2 gaseous mixture. This approach leads to a regular NH array in which holes have 200 nm of diameter and the aspect ratio >1. BCP lithography allows the formation of nanotemplates by exploiting self-assembling mechanisms. For the sake of simplicity, it will be now considered the behavior of a binary species, which means a linear di-block copolymer containing A and B as repeating units. If A and B blocks have a poor chemical affinity in their molten state, which can be estimated by the Flory-Huggins interaction parameter, an unfavorable excess in the mixing free energy takes place. The energy excess does not entropically support the mixing process between the blocks thus promoting a mesoscopic phase separation between A and B. The shape and size of the phases have a strong dependence on the relative fraction of each polymeric block in the chain and the global molecular weight of the polymer, respectively. An ordered pattern through the BCP self-assembly onto a SiO_2/Si substrate can be realized. The di-block copolymer PS-b-PMMA with a 70:30 ratio, polydispersity 1.1, and molecular weight 67,000 gr/mol is typically used. Before proceeding with the deposition of the PS-b-PMMA, the SiO_2 substrate surface with an analogous random polymer is neutralized. Then the PS-b-PMMA is spun from 1 w/w% toluene solution onto the random layer, and this sample is annealed in a range of 160–190°C for a couple of hours. The annealing promotes the separation of the two polymeric phases thus forming a template in which PMMA cylindrical microdomains are organized in a hexagonal array and embedded into a PS matrix. The exposition of the annealed film to the UV light lets cure the PS chains and thus allows the successive development of the PMMA portions in acetic acid. Therefore, this step leaves a regular porous PS film, which can be exploited by using the standard lithography concepts, taking into account the necessary technical measures. The literature results demonstrated that the thickness of the copolymer layer plays a major role in the self-assembling process [52]. Indeed, it is noted that too thick films lead to a quasi-lamellar morphology, while too thin layers do not reproduce the hexagonal pattern, thus losing the planar order. A suitable range of spin speed for the optimal self-assembly is then identified. Both the annealing temperature and its duration also have a strong role for determining the planar order of the film. Indeed, the annealing must be run over the glass transition temperature of both polymeric blocks in order to give the right mobility for allowing the movements of the chains. However, there is small range of temperatures that can guarantee the lateral order of the domains, thus allowing the diffusion of the molecules and avoiding the order-to-disorder transition. Inside this range of temperature, the self-assembling process can be tuned in order to obtain ordered hexagonal macrodomains as large as microns [53]. The template replication down to the SiO_2 and then to the Si substrate to form NHs can be carried by a CHF_3/Ar gas mixture followed by cycling SF_6/O_2 and CHF_3/Ar according to the procedure of the Bosch process [54]. The choice about the gases mixture and the general approach for both the etching cycles is made in order to promote the anisotropic etching which removes material from the bottom of the structures realized while it protects the sidewall and preserves them from the etching. Indeed, the passivation layer realized by the CHF_3 prevents the enlargement of the structures due to any isotropic etching effect, while SF_6/O_2 acts as a reagent for the etching of the Si substrate. This procedure leads to a hexagonal array of 30 nm-deep SiNHs and an aspect ratio ≈1. NSL is also used for the fabrication of SiNHs. Unlike the process used for the SiNWs formation, here the metallic film acts as a hard mask for successive processes such as the reactive ion etching (RIE) which leads to the formation of the Si holes. PS spheres are spun from a liquid solution on a Si substrates, realizing a monolayer of polymeric spheres with a high hexagonal packed array. The PS spheres diameter is shrunk with a RIE etch which thus increases the separation between them. A metallic film is deposited through a thermal evaporation onto the PS layer while a successive lift-off in a sonication bath removes PS, thus leaving the porous metallic layer that works as a hard mask for the successive dry etching of the Si. Finally, the metallic layer is removed. The PS spheres have also been embedded inside a monomer matrix [55]. A suspension of silica particles in a solution of a specific monomer (ETPTA) is spun onto the Si substrate. After monomer curing, the polymeric mask with silica particles embedded and positioned in hexagonal configuration is obtained. The vertical pressures exerted by the spin coating and the polymerization constrict the PS particles on the substrate to form a nonclose packed array. The polymeric mask is then removed by plasma oxygen, thus leaving a 2D film of silica nanoparticles. A metallic film is deposited onto the colloidal pattern via e-beam technique and it acts as a hard mask after the silica lift-off and during the successive RIE etching. Finally, the mask is removed via etching. SEM characterization shows that the diameter of the SiNHs is equal to the silica particles diameter, $D \approx 320$ nm and it is correlated to the center-to-center distance, d, since $d = 1.4$ D. In the work of Jiang et al., SiNHs are five times smaller with respect to those ones obtained by Hulteen et al. [56]. It is found that by using particles with $D = 264$ nm, the in-plane particle diameter, a, is ≈0.23 D, while the interparticles spacing, $d \approx 0.6$ D, and it does not depend on the substrate [56]. SiNHs can also be realized by two other uncommon techniques, the fast atoms bombardment (FAB) and FIB. In the first approach, SF_6 beam is used to erode the Si surface [57]. This method first requires a partial protection of the Si surface with a mask, for example with the alumina AAO mask: the sample is soaked in an oxalic solution and electrically oxidized at a constant voltage to obtain an ordered porous array with a periodicity of approximately 100 nm. FAB is thus performed using SF_6 gas under an acceleration voltage of 2.0 kV, to transfer the porous texture from alumina to the underlying Si, keeping both the directionality and in-plane hexagonal array of the alumina mask. FIB is also exploited in order to manufacture NHs with diameters below 5 nm. The approach is also called the "ion beam sculpting technique" [32]. Nanopores of about 100 nm diameter are drilled by the focused beam of the FIB onto a low-stress SiN layer supported by a Si substrate. After multiple beam scans on the pore and its surrounding areas, a strong reduction of the diameter of the NHs is observed, down to 5 nm. The authors speculate that the holes shrink because of a mass flow finalized to the minimization of the surface tension energy, when temperature and entropy are locally increased by the high-energy electron beam, although the explanation is not complete. If pore diameter smaller than 5 nm is desired, the above process becomes uncontrolled and the authors suggest to use a 200-keV beam of a TEM equipment, as a more controllable sculpting process. Using this second strategy, pores with less than 1 nm diameter can be fabricated. Despite the well-known behavior for which high-energy species usually tend to enlarge structures, surprisingly this does not occur in this case. It must be highlighted that this mechanism works as here described when the initial pore diameter is ≤50 nm. In fact, for pores which have ≥80 nm, different dynamics occur [58].

As for the SiNWs, the passivation process is a critical step and it has been addressed in the literature with several solutions. The SiNHs surface can be passivated with a defects removal etching (DRE) process, with the objective to remove the ion bombardment defects [31]. The DRE process is performed onto the sample using an oxidant aqueous solution of $HF:HNO_3$ which works through two different steps: (1) nitric acid oxides Si to SiO_2 and (2) HF removes the oxide formed. DRE duration strongly influences the depth of the SiNHs since the longer the etching, the deeper the holes obtained. Oh et al. [11] also recognize the strategic importance of surface passivation and treat the NHs sample by immersing it into an aqueous solution of 1% of tetramethylammonium hydroxide (TMAH), to decrease the area of the realized texture and the structural defects due to the MAE wet etching [11]. Despite the passivation issues not yet fully overcome, the electrooptical properties of the NH arrays are extremely interesting. Indeed as reported in the literature, a periodic array with subwavelength dimensions, such as the SiNHs, manifests antireflecting behaviors. When an electromagnetic radiation passes from a lower refractive index medium (e.g., air) to another one that has a higher optical density (i.e., Si), an abrupt variation of the optical parameter occurs. In this case, the transmitted "power" of the incident light is partially lost through the reflections. Differently, when the refractive index changes gradually, the losses due to external reflections can be minimized since the incident light sees the surface as a continuous system in which the power is transferred from the air to the bulk "layer by layer." This effect is more evident in deep surface textures, for which the reflectance reduction is also explained by the light-trapping effect, which means that multiple internal reflections increase the light path inside the structures and lead to the absorption enhancement. Koynov et al. investigate the optical response of a textured surface throughout the entire spectrum range of interest for photovoltaics from 350 to 1000 nm [35]. They find a very strong reduction of the reflectance that passes from 35 to 45% of the flat reference to very low values (5%) for the random textured sample. At the same time, the total transmittance, T, does not change within 350–1000 nm. Since $A + T + R = 1$, where A is the absorption and R is the total reflectance, these results imply that the absorption of a textured Si surface must be higher than that of the untreated sample. R decreases with increasing the pore depth [36] and, for each value of depth, R is about constant into the spectral range from 250 to 1000 nm. After 1000 nm, the reflectance increases and this occurs for each structure and independently of the depth, also in accordance with other experimental data [37]. From these results, the authors provide the universal law correlating the reflectance to the depth of nanostructures and to the wavelength of the incident light, $R\ (d, \lambda)$. The universal scaling-law is an exponential decay: $R(d, \lambda) = R_0(\lambda)\, e^{-C(\frac{d}{\lambda})}$ where $R_0(\lambda)$ is the wavelength depending-reflectance of the flat reference, d is the depth of the NHs, λ is the wavelength of the incident light, and C is a constant. Such subwavelength structures can be designed in order to increase the optical absorption of materials [38]. For instance, the indirect band gap of Si is the main cause of its low absorption in the IR region, which can be thus improved by the surface texturing. About this, geometrical features of the nanopattern employed can play a role in the reflectance reduction. For example, when the optical properties of SiNWs and SiNHs with the same dimensions are compared, it is possible to see that the latter ones show superior optical properties, thanks to a more efficient light-trapping capability. These results are deduced by the reflectance measurements of both SiNHs and SiNWs arrays (**Figure 5**).

The reflectance of a shallow NHs array can decrease until 5% within 300–1100 nm wavelength and it is always lower for NHs than for NWs of comparable size. The reflectance can be further reduced by increasing depth/length of the structures and it reaches the minimum value in the UV region while its maximum is always achieved in the IR range. Similar to SiNWs, SiNHs can represent the base for radial p-n junctions, with the carrier channel being placed in between the hole interspacing, rather than in the inner core of the nanostructure. The doping can be performed only by *ex-situ* methods, by using the standard gas source [10] or by MD [29]. The last one allows the optimization of the doping step since it avoids the typical stochastic spatial distribution or the crystal damage, leading instead to a high conformality. Authors in

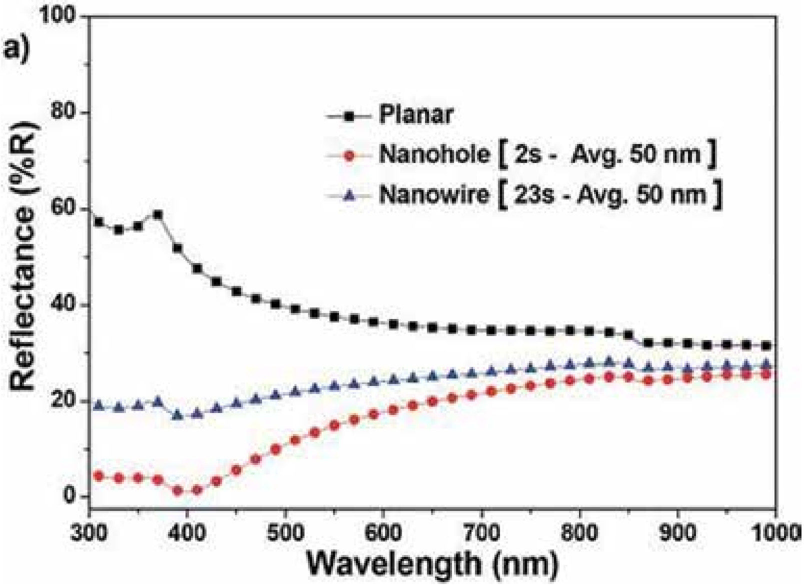

Figure 5. a) The optical reflectance of SiNW and SiNH arrays measured by the integrating sphere, including the reflectance average lengths of 50 nm. All the figures are show here with the reflectance of referenced polished n-type Si wafer [38].

reference [29] investigate the doping profile by spreading resistance measurements for two different annealing temperatures. They find a boron concentration peak of 10^{19} cm^{-3} and a junction depth of about 20 nm for a diffusion process at 950°C, while, when the annealing temperature is 1050°C, the carrier peak concentration slightly decreases and a junction depth of 70 nm is obtained. In the case of small SiNHs, a smaller thermal budget could modulate the diffusion depth in order to properly design the carrier channel width.

4. Conclusions

In this work, various SiNWs synthesis methods have been reviewed, the most common based on the VLS catalyzed growth. The advantages are control of external impurities by use of vacuum instrumentation, low surface roughness, control over structural and morphological properties, crystallinity. When the growth takes place in a plasma-based CVD chamber, the additional benefits consist in the low temperatures and high growth rate. The substrate crystallographic orientation determines the NW directions. Among the methods examined those based on the combination of the catalyzed growth and the laser induction do not allow the manufacture of the cell, as the NWs obtained are free-standing and have no contact with the substrate. The NWs have been exploited as building blocks for the formation of core-shell metallurgical junctions. A large variety of designs have been proposed, where the intrinsic layer plays the relevant role to improve the cell efficiency. One of the issues largely debated is about the efficient removal of the metallic catalyst from the SiNWs, because it is related to the electrical performance deterioration. Regarding the optical properties, light trapping by multiple reflections in the case of forest-like configuration, and increased absorption in the UV in the case of structures smaller than 5 nm have emerged. SiNHs are frequently fabricated directly by MAE which leads to random nanostructures or by lithographic approaches and successive etching to obtain recurring patterns. A wide range of diameter sizes going from hundreds of nm, attainable by common lithographies, down to 30 nm, by BCP, can be achieved. Smaller SiNHs can be synthesized by FIB with drawbacks for the wafer scalability of the process. The most interesting SiNHs optical properties manifest drop in reflectance down to 5%, demonstrated for randomic structures with 50 nm of diameter. Even for these mirror structures, it is possible to build core-shell p-n layers and innovative *ex-situ* techniques are proposed providing conformality and cost-effective solutions.

Acknowledgements

R.A.P. wish to mention the National Program PON R&C 2007–2013, project “Tecnologie per l’ENERGia e l’Efficienza energETICa (ENERGETIC)” (PON02_00355_3391233) for financial support.

Author details

Rosaria Anna Puglisi[1*], Valentina Lombardo[1,2] and Sebastiano Caccamo[1,2]

*Address all correspondence to: rosaria.puglisi@imm.cnr.it

1 Consiglio Nazionale delle Ricerche – Istituto per la Microelettronica e Microsistemi Strada Ottava, Catania, Italy

2 Dipartimento di Fisica, università degli Studi di Catania, Catania, Italy

References

[1] Peng K, Xu Y, Wu Y, et al. Alligned single-crystalline Si nanowire array for photovoltaic applications. Small. 2005;**1**(11):1062-1067. DOI: 10.1002/smll.200500137

[2] Kempa TJ, Tian B, Kim DR, et al. Single and tandem axial p-i-n nanowire photovoltaic devices. Nano Letters. 2008;**8**(10):3456-3460. DOI: 10.1021/nl8023438

[3] Schmidt BV, Wittemann JV, Senz S, Go U. Silicon nanowires: A review on aspects of their growth and their electrical properties. Advanced Materials. 2009;**21**:2681-2702. DOI: 10.1002/adma.200803754

[4] Ramanujam J, Shiri D, Verma A. Silicon nanowire growth and properties: A review. Materials Express. 2011;**1**(2):105-126. DOI: 10.1166/mex.2011.1013

[5] Kelzenberg MD, Boettcher SW, Petykiewicz JA, et al. Enhanced absorption and carrier collection in Si wire arrays for photovoltaic applications. Nature Materials. 2010;**9**(3):239-244. DOI: 10.1038/nmat2635

[6] Sivakov V, Andrä G, Gawlik A, et al. Silicon nanowire-based solar cells on glass: Synthesis, optical properties, and cell parameters. Nano Letters. 2009;**9**(4):1549-1554. DOI: 10.1021/nl803641f

[7] Zhang RQ, Hou C, Gao N, et al. Multi-field effect on the electronic properties of silicon nanowires. ChemPhysChem. 2011;**12**(7):1302-1309. DOI: 10.1002/cphc.201100030

[8] Tsakalakos L, Balch J, Fronheiser J, et al. Silicon nanowire solar cells. Applied Physics Letters. 2007;**91**:233117-1. DOI: 10.1063/1.2821113

[9] Tian B, Zheng X, Kempa TJ, et al. Coaxial silicon nanowires as solar cells and nanoelectronic power sources. Nature. 2007;449:885-889. DOI: 10.1038/nature06181

[10] Peng K, Wang X, Li L, et al. High-performance silicon nanohole solar cells. Journal of the American Chemical Society. 2010;**132**:6872-6873. DOI: 10.1021/ja910082y

[11] Oh J, Yuan H, Branz HM. An 18.2%-efficient black-silicon solar cell achieved through control of carrier recombination in nanostructures. Nature Nanotechnology. 2012;**7**:743-748. DOI: 10.1038/nnano.2012.166

[12] Fontcuberta i Morral A, Arbiol J, Prades JD, et al. Synthesis of silicon nanowires with wurtzite crystalline structure by using standard chemical vapor deposition. Advanced Materials. 2007;**19**:1347-1351. DOI: 10.1002/adma.200602318

[13] Kelzenberg MD, Turner-Evans DB, Kayes BM, et al. Photovoltaic measurements in single-nanowire Si solar cells. Nano Letters. 2008;**8**:710-714. DOI: 10.1021/nl072622p

[14] Yung Kuo C, Gau C, Tong Dai B. Photovoltaic characteristics of silicon nanowire arrays synthesized by vapor liquid solid process. Solar Energy Materials & Solar Cells. 2011;**95**(1):154-157. DOI: 10.1016/j.solmat.2010.04.028

[15] Yu L, Rigutti L, Tchernycheva M, et al. Silicon nanowire-based solar cells. Nanotechnology. 2008;**19**:295203. DOI: 10.1088/0957-4484/19/29/295203

[16] Ajmal Khan M, Ishikawa Y, Kita I, et al. Control of verticality and (111) orientation of In-catalyzed silicon nanowires grown in the vapour–liquid–solid mode for nanoscale device applications. Journal of Materials Chemistry C. 2015;**3**:11577-11580. DOI: 10.1039/C5TC01338K

[17] Garozzo C, La Magna A, Mannino G, et al. Competition between uncatalyzed and catalyzed growth during the plasma synthesis of Si nanowires and its role on their optical properties. Journal of Applied Physics. 2013;**113**(21):214311-214317. DOI: 10.1063/1.4809557

[18] Hoffmann S, Bauer J, Ronning C, et al. Axial p-n junctions realized in silicon nanowires by ion implantation. Nano Letters. 2009;**9**(4):1341-1344. DOI: 10.1021/nl802977m

[19] Kendrick CE, Yoon HP, Yuwen YA, et al. Radial junction silicon wire array solar cells fabricated by gold-catalyzed vapor-liquid-solid growth. Applied Physics Letters. 2010;**97**(14):42-45. DOI: 10.1063/1.3496044

[20] Yu L, O'Donnell B, Alet PJ, et al. All-in-situ fabrication and characterization of silicon nanowires on TCO/glass substrates for photovoltaic application. Solar Energy Materials & Solar Cells. 2010;**94**(11):1855-1859. DOI: 10.1016/j.solmat.2010.06.021

[21] Peng BK, Lu A, Zhang R, et al. Motility of metal nanoparticles in silicon and induced anisotropic silicon etching. Advanced Functional Materials. 2008;**18**:3026-3035. DOI: 10.1002/adfm.200800371

[22] Zhang ML, Peng KQ, Fan X, et al. Preparation of large-area uniform silicon nanowires arrays through metal-assisted chemical etching. Journal of Physical Chemistry C. 2008;**112**(12):4444-4450. DOI: 10.1021/jp077053o

[23] Fang H, Li X, Song S, et al. Fabrication of slantingly-aligned silicon nanowire arrays for solar cell applications. Nanotechnology. 2008;**19**(25):255703. DOI: 10.1088/0957-4484/19/25/255703

[24] Chen H, Wang H, Zhang XH, et al. Wafer-scale synthesis of single-crystal zigzag silicon nanowire arrays with controlled turning angles. Nano Letters. 2010;**10**(3):864-868. DOI: 10.1021/nl903391x

[25] Huang Z, Zhang X, Reiche M, et al. Extended arrays of vertically aligned Sub-10 nm diameter [100] Si nanowires by metal-assisted chemical etching. Nano Letters. 2008;**8**(9):3046-3051. DOI: 10.1021/nl802324y

[26] Mikhael B, Elise B, Xavier M, et al. New silicon architectures by gold-assisted chemical etching. ACS Applied Materials & Interfaces. 2011;**3**(10):3866-3873. DOI: 10.1021/am200948p

[27] Garnett EC, Yang P, Garnett EC, et al. Silicon nanowire radial p-n junction solar cells. Journal of the American Chemical Society. 2008;**130**:9224-9225. DOI: 10.1021/ja8032907

[28] Puglisi RA, Caccamo S, D'Urso L, et al. A comprehensive Study on the physicochemical and electrical properties of Si doped with the molecular doping method. Physics of the Status Solid A. 2015;**1694**(8):1685-1694. DOI: 10.1002/pssa.201532030

[29] Garozzo C, Giannazzo F, Italia M, et al. Radial junctions formed by conformal chemical doping for innovative hole-based solar cells. Materials Science and Engineering: B. 2013;**178**:686-690. DOI: 10.1016/j.mseb.2012.11.019

[30] Milazzo RG, Arrigo GD, Spinella C, et al. Ag-Assisted chemical etching of (100) and (111) n-type silicon substrates by varying the amount of deposited metal. Journal of the Electrochemical Society. 2012;**159**(9):521-525. DOI: 10.1149/2.008209jes

[31] Chen T, Yu P, Chen S, et al. Characteristics of large-scale nanohole arrays for thin-silicon photovoltaics. Progress in Photovoltaics: Research and Applications. 2014;**22**:452-461. DOI: 10.1002/pip.2291

[32] Lo CJ, Aref T, Bezryadin A. Fabrication of symmetric sub-5 nm nanopores using focused ion and electron beams. Nanotechnology. 2006;**17**:3264-3267. DOI: 10.1088/0957-4484/17/13/031

[33] Chen J, Shi J, Decanini D, et al. Gold nanohole arrays for biochemical sensing fabricated by soft UV nanoimprint lithography. Microelectronic Engineering. 2009;**86**:632-635. DOI: 10.1016/j.mee.2008.12.093

[34] Bates FS, Fredrickson GH. Block copolymers—Designer soft materials. Physics Today. 1999;**52**(2):32. DOI: 10.1063/1.882522

[35] Koynov S, Brandt MS, Stutzmann M. Black nonreflecting silicon surfaces for solar cells. Applied Physics Letters. 2006;**88**:203107(1-3). DOI: 10.1063/1.2204573

[36] Branz HM, Yost VE, Ward S, et al. Nanostructured black silicon and the optical reflectance of graded-density surfaces. Applied Physics Letters. 2009;**94**(23):1-4. DOI: 10.1063/1.3152244

[37] Hadobas K, Kirsch S, Carl A, et al. Reflection properties of nanostructure-arrayed silicon. Nanotechnology. 2000;**11**:161-164. DOI: 0957-4484/00/030161

[38] Thiyagu S, Syu H, Hsueh C, et al. Optical trapping enhancement from high density silicon nanohole and nanowire arrays for efficient hybrid organic–inorganic solar cells. RSC Advances. 2015;**5**:13224-13233. DOI: 10.1039/C4RA13536A

[39] Wagner RS and Ellis WC. Vapor liquid solid mechanism of single crystal growth. Applied Physics Letters. 1964;**4**(5):89-90. DOI: 10.1063/1.1753975

[40] Westwater J, Gosain DP, Tomiya S, et al. Growth of silicon nanowires via gold/silane vapor–liquid–solid reaction. Journal of Vacuum Science & Technology. B. 1997;**15**(3): 554-557. DOI: 10.1116/1.589291

[41] Puglisi RA, Mannino G, Scalese S, et al. Silicon nanowires obtained by low temperature plasma-based chemical vapor deposition. Materials Research Society Symposium Proceedings. 2012;**1408**:139-144. DOI: 10.1557/opl.2012.718

[42] Kempa TJ, Cahoon JF, Kim S-K, et al. Coaxial multishell nanowires with high-quality electronic interfaces and tunable optical cavities for ultrathin photovoltaics. Proceedings of the National Academy of Sciences. 2012;**109**(5):1407-1412. DOI: 10.1073/pnas.1120415109

[43] Xie P, Hu Y, Fang Y, Huang J, Lieber CM. Diameter-dependent dopant location in silicon and germanium nanowires. Proceedings of the National Academy of Sciences. 2009;**106**(36):15254-15258. DOI: 10.1073/pnas.0906943106

[44] Puglisi RA, Garozzo C, Bongiorno C, et al. Molecular doping applied to Si nanowires array based solar cells. Solar Energy Materials & Solar Cells. 2015;**132**:118-122. DOI: 10.1016/j.solmat.2014.08.040

[45] Zhang YF, Tang YH, Wang N, et al. Silicon nanowires prepared by laser ablation at high temperature. Applied Physics Letters. 1998;**72**(15): 1835-1837. DOI: 10.1063/1.121199

[46] Yu DP, Sun XS, Lee CS, et al. Synthesis of boron nitride nanotubes by means of excimer laser ablation at high temperature. Applied Physics Letters. 1998;**1966**:1-4. DOI: 10.1063/1.121236

[47] Cui Y, Zhong ZH, Wang DL, et al. High performance silicon nanowire field effect transistors. Nano Letters. 2003;**3**(2):149-152. DOI: 10.1021/nl025875l

[48] Zhao J, Wang A, Ferrazza MAG, Zhao J, et al. Silicon solar cells monocrystalline silicon solar cells. Applied Physics Letters. 1998;**73**(14):1991-1994. DOI: 10.1063/1.122345

[49] Hauser H, Michl B, Schwarzkopf S, et al. Honeycomb texturing of silicon via nanoimprint lithography for solar cell applications. IEEE Journal of Photovoltaics. 2012;**2**(2):114-122. DOI: 10.1109/JPHOTOV.2012.2184265

[50] Martins GF, Thompson AJR, Goller B, et al. Fabrication of "finger-geometry" silicon solar cells by electrochemical anodisation. Journal of Materials Science. 2013;**48**:2977-2985. DOI: 10.1007/s10853-012-7075-x

[51] Hamouda F, Barbillon G, Held S, et al. Nanoholes by soft UV nanoimprint lithography applied to study of membrane proteins. Microelectronic Engineering. 2009;**86**:583-585. DOI: 10.1016/j.mee.2008.11.086

[52] Guarini KW, Black CT, Milkove KR, et al. Nanoscale patterning using self-assembled polymers for semiconductor applications. Journal of Vacuum Science & Technology B. 2001;**19**(6):2784-2788. DOI: 10.1116/1.1421551

[53] Puglisi RA, La Fata P, Lombardo S. Tailoring the long-range order of block copolymer based nanomasks on flat substrates. Applied Physics Letters. 2007;**91**:0531041-3. DOI: 10.1063/1.2766694

[54] Puglisi RA. Towards ordered silicon nanostructures through self-assembling mechanisms and processes. Journal of Nanomaterials. 2015;**2015**:1-20. DOI: 10.1155/2015/586458

[55] Jiang P, McFarland MJ. Wafer-Scale periodic nanohole arrays templated from two-dimensional nonclose-packed colloidal crystals. Journal of the American Chemical Society. 2005:**127**;3710-3711. DOI: 10.1021/ja042789

[56] Hulteen JC, Duyne RP Van, Hulteen JC, et al. Nanosphere lithography: A materials general fabrication process for periodic particle array surfaces. Journal of Vacuum Science and Technology A. 1995;**2011**:1553-1558. DOI: 10.1116/1.579726

[57] Sai H, Fujii H, Arafune K, et al. Antireflective subwavelength structures on crystalline Si fabricated using directly formed anodic porous alumina masks. Applied Physics Letters. 2006;**88**:201116(1-4). DOI: 10.1063/1.2205173

[58] Storm AJ, Chen JH, Ling XS, et al. Fabrication of solid-state nanopores with single-nanometre precision. Nature Materials. 2003;**2**:537-541. DOI: 10.1038/nmat941

Chapter 8

Opportunities of Scanning Probe Microscopy for Electrical, Mechanical and Electromechanical Research of Semiconductor Nanowires

Pavel Geydt, Mikhail S. Dunaevskiy and
Erkki Lähderanta

Additional information is available at the end of the chapter

http://dx.doi.org/10.5772/intechopen.68162

Abstract

In this chapter, three types of phenomena (electrical, mechanical, and electromechanical) that can be investigated in individual III–V semiconductor nanowires with scanning probe microscope are presented. Transport measurements in GaAs nanowires based on stable electric connection provided opportunity to study individual vertical freestanding nanowires under gentle precisely controlled force. Latter approach appears superior to studies of horizontally fixed nanowires because studying vertical as-grown nanowires avoids charge leakage into the substrate and impact of defects caused by breakage of nanowires. Principles of thermionic emission theory are used to characterize electrical effects in individual as-grown nanowires. Effects of SiO_2 protective layer, surface passivation layers, illumination, and influence of sweeping rate of current-voltage recording are analyzed. Elastic studies are performed for individual InP nanowires affixed at one end. Bending of the tapered nanowires with diameters of a narrow free end either 10 or 20 nm was performed under different loading forces. It allowed calculation of flexibility coefficient profiles along the nanowires' axes. Improved numerical model for tapered nanowires leads to the finding of Young's modulus of wurtzite InP material in nanowires. Piezoelectric measurements permitting registration of reverse piezo effect with opportunities of direct piezo response recording for individual wurtzite GaAs nanowires are briefly described.

Keywords: scanning probe microscopy, AFM, PFM, current-voltage characteristics, Young's modulus

1. Introduction

Recent technological challenges of nanotechnology and industry are lying in two main fields: characterization and production of nanostructures. In order to enhance the quality of nanodevices, it is vital to know properties of the nanostructures involved and specific features that are attributed to their scaling. Since nanowires (NWs) are one of the most prominent objects of nanoscience, significant attention is being paid to their properties and throughput investigation [1–7].

However, already choosing an appropriate method for studying NWs is hard due to their small size and fragility. NWs are quasi one-dimensional structures with nanoscale width possessing properties that dramatically change due to the size effects [8]. Diameter of NWs is approximately 10–100 nm with considerable value of length-to-diameter ratio. In addition, surface-to-volume ratio of NWs defines their strong dependence from the surface effects [1]. Typically, well-established massive methods of investigation are used to characterize the entire arrays of NWs [2, 5]: photoluminescence (PL), X-ray diffraction (XRD), scanning electron microscopy (SEM), transmission electron microscopy (TEM), optical methods, etc. All above-mentioned techniques have limitations on spatial resolution and type of information provided by each certain technique. Definitely, a precise and accurate method focused onto single-object study and revealing features of individual nanostructures should be proposed to support inductive reasoning over properties of NWs inside arrays. Furthermore, if properties of an individual object will be revealed in details, it seems achievable to tune the object's properties and then replicate improved structures into a regular array. Later, such "perfect" array of NWs can be used to create advanced devices based on NWs. Thus, detailed understanding of structure's parameters and its material's properties is expected to benefit innovative technologies. Nanowire-based devices already attract significant attention as units establishing new energy sources [3, 9–11], sensors [12–14], transistors [7, 15], NEMS [16, 17], etc.

Due to the challenges associated with NWs, a novel multifunctional helping hand needs to be utilized for their systematic study. Exactly scanning probe microscopy (SPM) as a family of research methods provides visualization, examination, and even changing of properties of individual nanostructures [18–20]. SPM-based methods were successfully performing this challenging role for NWs as reported previously [21–26]. For example, exactly SPMs are enthusiastically used in studies of new materials and assemblies in modern field of piezotronics [10, 27, 28]. However, description of prospects of electromechanical SPM methods for NWs seems not properly structured yet. Moreover, SPM is an intensively progressing tool, which regularly establishes new and enhanced opportunities for an advanced research [29–31]. We will try to represent accumulated knowledge and our experience in NWs and SPM to help in further studies of NWs. This is done with aspiration that adequate description of SPM methods will stimulate designing and R&D of NW-based devices. Thus, we will represent our results of studies of an individual III-V semiconductor NWs within an enhanced experimental methodology.

Primary issue in such work is establishing of classification under which a comprehensive study will be presented. Among different variants: (1) by composition of material used in NWs (GaAs, InP, GaN); (2) by microscopic method (force spectroscopy, quantitative nanomechanical mapping (QNM), conductive atomic force microscopy (C-AFM), Kelvin probe force microscopy (KPFM), piezoresponse force microscopy (PFM), etc.); (3) by geometrical orientation of the NWs (vertical, horizontal, inclined, or stumps rest after breakage of NWs); and (4) by properties of interest; we preferred the latter class. Therefore, the chapter consists of three following sections: electrical, mechanical, and electromechanical properties of NWs and represents methods of their investigation by modern SPM approaches. Latter means that magnetic [32–35], optical [29, 36–39], acoustic [10, 40–45], catalytic [46], and other properties [47–49] will not be reflected in recent chapter due to format limitations but are proposed to be accessed from the denoted comprehensive works.

NWs described in Sections 2 and 3 were grown by vapor-liquid-solid (VLS) mechanism [4] in metaloxide vapor phase epitaxy (MOVPE) chamber. Catalytic golden droplets were sputtered on substrate under the temperature ~450°C followed by the initiation of a volatile precursor's flow in a predefined protocol [50]. Diameters of NWs were ~100 nm in accordance with width of the Au droplets. Lengths were controlled by duration of the precursor's flow: ~1 μm for vertical structures, ~5 μm for horizontal NWs, and ~3 μm for inclined NWs. NWs for electrical studies were highly p-doped ($\sim 10^{19}$ cm^{-3}) by diethylzinc flow. Comprehensive details about fabrication setup and technique can be accessed from [50]. Samples with horizontal NWs in Section 2 were prepared by a procedure similar to the above described, although after fabrication, the NWs were broken from the substrate and dispersed in distilled water. Acquired suspension was placed onto clean SiO_2 substrate. When water has evaporated, NWs appeared fixed to the substrate by adhesive force. This step was followed by optical lithography, which finally connected separate NWs into electric circuit connected with macro-sized electrodes. Circuiting has been initially checked by SEM and verified by SPM performed afterward. Inclined InP NWs were fabricated on silicon wafers without intentional doping to preserve the pure wurtzite crystal structure of InP.

Subsequent studies were carried out on standard SPM Multimode 8 (Bruker, USA) equipped with additional modules, e.g., either PeakForce KPFM or PeakForce TUNA [51]. Both regimes were accompanied by quantitative nanomechanical mapping (QNM). Separately, few types of spectroscopies were executed. This means that individual single-point-oriented studies were performed with SPM, e.g., force-distance spectroscopy $F(z)$, current-voltage spectroscopy (I–V curves), or current-time spectroscopy $I(t)$.

PFM studies presented in Section 4 were done for wurtzite GaAs NWs fabricated with molecular beam epitaxy (MBE) method (details can be found in [52]). Measurements were performed in standard protocol, where specific AC voltage (frequency ~30 kHz, amplitude 10 V) was applied to the substrate. This has induced mechanical oscillations of the piezo responsive phase in studied NWs, which was registered by high-frequency lock-in of the SPM controller. In a modified version of piezo experiment, we observed current instead of mechanical oscillations. NWs were stressed, but not broken and piezo potential was induced in them. Therefore, mapping of current flowing through the area with NWs was performed under the gentle force. In such approach, piezoelectric NWs are bended and can generate an observable electric current.

2. Electrical measurements

Industrial importance of electrical characterization of NWs defined that electrical measurements of NWs are broadly studied and reported nowadays [7, 53–55]. Indeed, GaAs and InP NWs are proposed for next-generation NW-based solar cells [9, 25, 56–58], while their efficiency is characterized from current-voltage characteristics of an array of NWs (rarely from single individual NW [11]). SPM electrical measurements can be classified into two main types. First one is registration of electric current and its dependence from voltage applied between contacting probe and sample [7] by C-AFM or PeakForce Tuna methods. Secondly, registration of surface electric potential of a sample (i.e. work function of a NW's surface combined with visualization of injected electrostatic charge), is achievable in lift scan of KPFM.

For proper electrical measurements of NWs, substrate must be highly conductive (**Figure 1a**). Obviously, resistance of a wafer should be significantly smaller than resistance of the NW connected in series with substrate (not more than few Ohms). Therefore, substrates' resistance can be neglected [7, 25] (**Figure 1b**). While probe-NW contact resistance is also neglected and shunting is avoided, the I–V characteristics indicate Schottky barrier near zero voltage [7] and linear resistance of a NW (when Schottky barrier becomes open as will be discussed further in 2.1.1.). Connection to a bias source should be direct and not leading to any significant RLC elaboration. Additionally, SPM probes should be highly conductive with uniform thickness of stable rigid conductive coating. It is important to know the shape of a probe's tip apex and utilize probes with height of the tip pyramid applicable for micrometer-tall NWs. For example, KPFM studies are routinely done by probes with height of a pyramidal tip ~2.5 μm. Such probes must not be used for studies of NWs with heights above ~2.0 μm, because a cantilever's beam would strike NW instead of scanning done appropriately with the tip's apex. Morphology of a sample should be considered from established growth procedure or with subsequent visualization techniques, e.g., SEM or TEM. Moreover, following less articulated phenomena should be kept in mind for accurate measurement.

- "Plowing effect" [59], i.e., sliding of the location of probe-sample contact in opposite direction from the cantilever's holder after probe is approaching onto a sample. Referred contact is arranged between the end of tip's apex and a sample. Sliding between them emerges due to the lateral force acting onto the probe's tip mounted on a cantilever affixed at on end. Such sliding (i.e. plowing) occurs every time when the SPM probe approaches the surface, e.g. during initial engage onto the sample, and in each tapping cycle. Plowing/sliding length can reach tens of nanometers depending on setpoint force and is able to damage the surface of flat soft samples. This phenomenon must be considered to understand where exactly the current-voltage spectrum is being registered.
- Influence of setpoint force of push by SPM probe onto stability of contact and forcing, i.e., penetrating, through a surface oxide and chemisorbed water layers.
- Flexibility of a cantilever with related possibility that both vertical and torsional bends will be represented under dissimilar setpoint forces.
- Geometry of a contact between the round top part of an NW (**Figure 1c**) and rounded SPM probe's tip elongated into a pyramid.

Aforementioned features should be taken into account with environmental conditions of specific experiment, i.e., pressure of ambient gas or vacuum level, composition and humidity of this surrounding medium, temperature of the system, and illumination of certain individual NW under the study. Consideration of these factors is important because environment, e.g. air

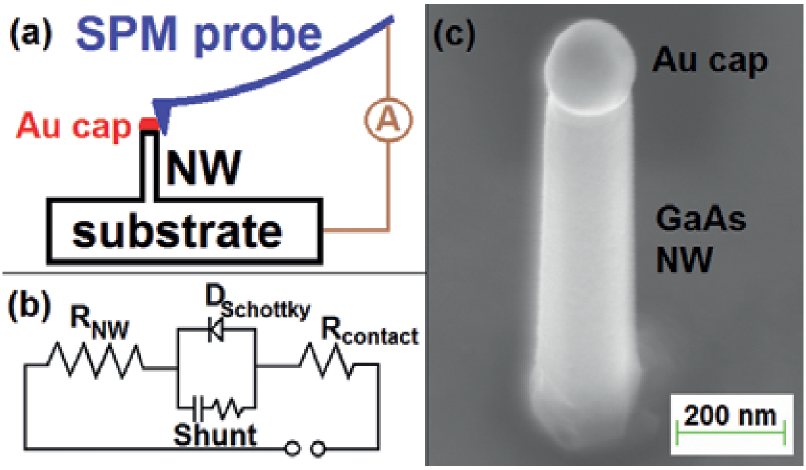

Figure 1. (a) Scheme of the electroconductive experiment by SPM probe in contact with an NW's metal cap. (b) Equivalent electric circuit proposed for the electrical conductivity of a semiconductor NW with a metal cap. (c) Single vertical p^{+}-GaAs NW on p^{++}-GaAs substrate.

in an AFM laboratory room, leads to surface oxidation and covering of NWs by a layer of water. Therefore, electrical, mechanical, and other properties of NWs experience aging. In practice, aging in GaAs is more intensive than for InP, but deterioration of NW can be decelerated by passivation with AlGaAs, GaN, GaP, or other thin coatings [56, 60].

2.1. Electrical conductivity of vertical and horizontal nanowires

Electrical resistance of the conductive channel [7, 56] in a semiconductor NW can be measured when bias is arranged between SPM's probe and a NW positioned in direct contact. Later evaluation of transconductance can be done in terms of the thermionic emission theory [7]. It should be noted that high amount of surface states are one of the most widely known disadvantages of GaAs as a material [55]. Indeed, charges can be trapped by NW's surface due to the defective nature of surface of nanostructures. These trapped carriers induce electric charge that hampers transport of mobile carriers through the conduction channel. Moreover, layer of a nonstoichiometric oxide grows on bulk semiconductor material of the NW. This oxide layer similarly acts as a charge-trapping agent blocking the carrier's transport in the NW, i.e., decreasing width of the conductive channel [61].

SPM controller allows measuring small current flowing through the system when contact is arranged with single individual NW. It should be noted that since SPM controller is solely measuring the electric current signal, an adequate model should be used to interpret the obtained signal (**Figure 1b**). Reason is that shunt or parasitic conductance through undesired coatings, e.g. chemisorbed water layer (from moisture content), nonstoichiometric oxide, or passivation layer can influence the obtained I–V characteristics. Capability to measure the as-grown vertical NWs is the main advantage of SPM techniques in comparison to methods requiring breakage and postgrown processing, which affect properties of these nanostructures. Additionally, SPM is preferential to massive methods, where parameters are registered for an array containing hundreds to millions of NWs, and further experimental values are averaged. Indeed, massive approaches do not allow qualifying the growth quality of NWs and examination of their local features, e.g., properties of Schottky barrier located between metal cap and a semiconductor NW. Thus, the prominent advantage of SPM in research of NWs is exactly in studying of local properties of individual structures.

2.1.1. Obtaining the current-voltage characteristics

Approach of taking I–V curves initiates from scanning the area covered by NWs (**Figure 2a**), while DC bias ~1 V is applied between SPM probe and a substrate. In modern microscopes, it is possible to record few channels of data simultaneously during a single scan. This provides obtaining of maps demarcating independent records of properties of a studied material when SPM data scan file is analyzed. Later, it becomes possible to correlate features from different channels, e.g., *topography* and *current*, and understand details of certain features observed in overall morphology. Vertical NW appears as pyramids in *topography* (**Figure 2b**) due to convolution effect of pyramidal tip and cylindrical or hexagonal NW. Preliminary map of currents in close proximity to a conductive NW typically represents an ensemble of conductive points or distinctive regions with regular shape indicating currents responsible for different facets of the SPM probe tip's pyramid (**Figure 2b** and **c**).

C-AFM study is considerably less expensive and more automated than similar studies performed on SEM with full metal probe or practice of STM with visualization of movements by the station's SEM [62–64]. Noteworthy that in C-AFM, it is only necessary to choose the location where current is maximum and to perform spectroscopy of current at this specified spot (**Figure 3**). Typically, position of the spot is situated at a distance approximately tens of nanometers from the top part of a vertical NW's metal cap visible from *topography* (**Figure 2b**). Reason here is that the most conductive area only indicates position where contact resistance $R_{CONTACT}$ between probe and NW is the smallest.

Capability to observe conductance of long vertical NWs (**Figure 2b** and **3**) highlights benefits of C-AFM technique in comparison to measurements of those done on horizontal NWs connected by lithography. Advantages include simplicity of procedure, availability of standard conductive probes, and absence of necessity in costly additional visualizing SEM. Moreover, utilization of such SEM is associated with bombardment of the nanostructures with focused high-energy electron beam. It can affect conductivity of NWs both when beam is switched on and off. When SEM is performing visualization, the amount of charge carriers within the certain observed NW increases by injection of electrons in SEM observation procedure. Moreover, if SEM beam is switched off, localized charges can persist in surface oxide and spoil the entire sample and measurement. On the contrary, C-AFM is based on standard AFM. A flexible cantilever with highly responsive piezo scanner and bias control system is used in this regime. These features allow measuring morphology and conductivity of fragile nanoobjects with heights more than 5 μm without their breakage. It is possible to arrange experiments with electric bias applied by SPM, although unfortunately, the aforementioned deterioration of NWs by localized charges can still exist.

Nevertheless, few shortcomings arise in SPM method of I–V spectroscopy. As we have noticed from experimental work, drift of the sample occurs during the scanning, so that the spot of measurements moves toward hardly predictable location. It leads to decline of reproducibility

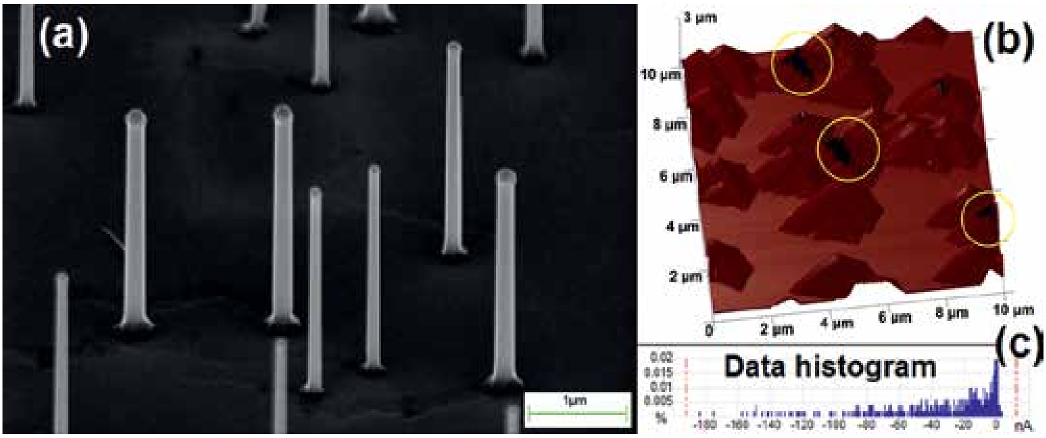

Figure 2. (a) SEM image of an array of vertical GaAs NWs. (b) 3D model of topography of an array of vertical GaAs NWs, where NWs are seen as pyramids due to shape convolution. Electric current map is overplayed on 3D topography indicating regions with high current density near the NW tops as black spots marked with circles. (c) Distribution of values of electric currents in an array of NWs obtained by PeakForce Tuna module, where highest absolute values indicate stable electric contact.

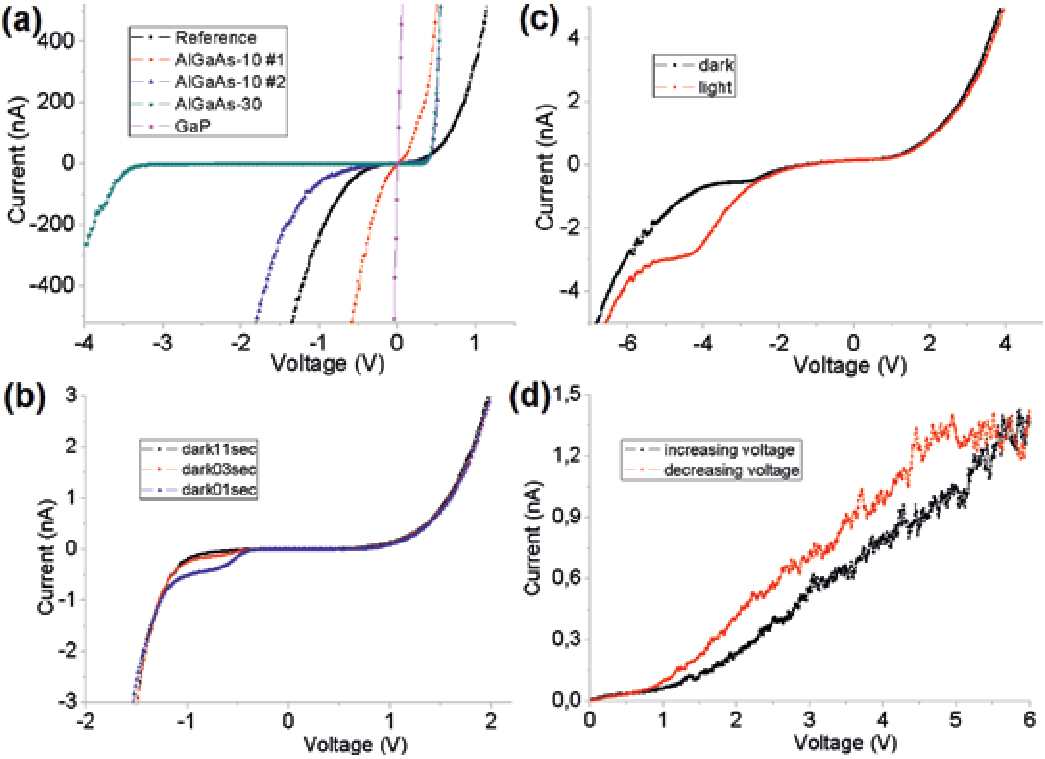

Figure 3. I–V curves for vertical (a)–(c) and horizontal (d) GaAs NWs taken by SPM. (a) Comparison of different passivating shells. (b) Indication of effects of sweeping duration onto accumulation of charges in NWs for 1 s, 3 s, and 11 s. (c) Comparison between electric output of the same pGaAs NW on nGaAs substrate in light and dark conditions. (d) Hysteresis of electric current for GaAs NW.

of I–V curves for same NW after long series of measurements. This can be solved by obtaining more representative statistics of measurements, repeating the tests by fresh probes and with significant suppression of a setpoint force acting during I–V spectroscopy acquisition.

Analysis of the I–V spectra [7] (**Figure 3**) acquired by SPM controller for certain individual NWs in a series of samples prepared with different treatments can be done. It is possible to evaluate effects of passivating shell onto conductive behavior of NWs. For example, in **Figure 3a**, two passivating compounds are compared for vertical GaAs NWs, i.e., GaP and AlGaAs. It is noticeable that current through the NW in region of forward bias increases for both of them in comparison with unpassivated reference NWs. We studied these passivating shells in details previously [65, 66]. GaP appeared to be the most advantageous passivating material from experimental measurements of GaAs NWs. This conclusion is obvious from I–V curves taken on vertical NWs since I–V spectra for sample with GaP ultrathin shell demonstrate neither a specific knee in region of forward bias nor the junction voltage parameter. Reason for that is decrease of concentration of surface states at the surface of vertical NWs, which widens the conduction channel in NWs. Practically, I–V curves for GaP passivated NWs were almost linear, so that quasi-Ohmic contact was formed between Au cap and highly doped GaAs crystal part of the NW.

Indeed, latter contact area should arrange a Schottky junction, and NW system should resemble the rectifying shape of I–V curve for a Schottky diode [7, 67] in accordance with the diode law

$$I = I_0\left(e^{\frac{eV}{kT}} - 1\right) \tag{1}$$

where I_0 is a reverse-bias leakage current (A), q is an elementary charge 1.6×10^{-19} C, k is the Boltzmann constant 1.23×10^{-23} J/K, and T is an absolute temperature (K).

It is considered that explanation for phenomenon of negligence of Schottky input is that Fermi-level pinning is reduced in highly doped NW [68]. In fact, level of doping can be quantified from the linear serial resistance region of I–V curves. The slope equals to resistance of a system by Ohm's law and following equation

$$R = \frac{l}{eN_A \mu \pi r_{\mathrm{NW}}^2} \tag{2}$$

where length of the NW, L, is approximately 1 μm, elementary charge $q = 1.6 \times 10^{-19}$ C, mobility of carriers $\mu = 400$ cm^2/V s, and NW's radius r_{NW} is approximately 50 nm, while carrier concentration is N_{A}. Since resistance of GaP-passivated p-GaAs NWs is ~100 kΩ from the slope, the doping level N_{A} is approximately 10^{19} cm^{-3}, verifying the value anticipated from fabrication protocol of VLS growth.

Passivation by GaP [69] or AlGaAs [70] was previously found among the most advantageous methods to decrease the density of surface states in GaAs NWs by other authors. Interestingly, it is possible to distinguish instabilities of quality of passivation for NWs over the single sample as visible for two I–V curves taken on two separate GaAs NWs with equal 10-nm AlGaAs-passivating shells. In fact, sizes of NWs have specific distribution as can be seen in **Figure 2a**. From AlGaAs passivation results obtained for NW#1 (red curve) and NW#2 (blue curve), it is possible to conclude that thin AlGaAs passivation is also advantageous for GaAs NWs, although effect of passivation is less pronounced comparing with NWs shelled by GaP. However, summarized effect of the surface states (fast traps and slow traps) of native oxide significantly depends on NW's diameter. I–V curve for NW with AlGaAs shell passivation layer with thickness 30 nm (cyan curve) already resembles the shape characteristic for a diode.

Such NWs have forward threshold voltage (junction voltage) approximately 0.2 V and indicate leakage current and reverse breakdown voltage lower than −3 V. Therefore, such thick shell passivation approach is detrimental for NWs. Reason for that is accumulation of electric charge at the shell and its capacitive adverse input blocking the conduction channel of the NW. Moreover, inclination of all curves in regions of linear resistance is equal because it represents the concentration of charge carriers, i.e., same doping level [65, 66].

Furthermore, analysis of curves recorded with different sweeping rates indicates that charge accumulation and redistribution effects can be visualized for GaP-passivated pGaAs NWs on nGaAs substrates (**Figure 3b**). Corresponding curves represent both Schottky barrier input and p–n junction barrier. It should be noted that detailed shape of I–V curves depends not only on sweeping rate (duration of registration of a spectra) but also on starting voltage of such registration and cycle. Latter means that hysteresis effects can be observed from I–V curves of NWs. Therefore, all curves in **Figure 3a–c** were shown for sweeping from maximum voltage, i.e. while bias was consistently shifted toward negative potential. Additionally, illumination effects can be observed for certain NW systems with p-n barrier. As it is seen from **Figure 3c** for unpassivated pGaAs NW on nGaAs substrate, over-lighted conditions led to intensive rise in current through NW. In addition, the serial linear resistance regions for unpassivated NW (**Figure 3c**) are significantly further from 0 V comparing with passivated NWs (**Figure 3b**). Partly, the observed increase of current can be explained by the stimulation of photo-induced conductivity. Availability to register I–V curves is more impressive for vertical NWs but can be done also for horizontal NWs. In this respect, for example, resistivity and charge accumulation near the Schottky barrier (near the interface between the NW and each electrode) can be (**Figure 3d**).

2.1.2. Mapping of electric current (C-AFM in contact mode, PeakForce TUNA in semicontact mode)

Another option is performing the C-AFM scanning without further spectroscopy, while DC bias between probe and sample is being manually or programmably changed. This possesses registering the map of values of current for each manually specified bias. The approach is time-consuming, but can allow plotting of considerable amount of data points on I–V plot and later reconstruction of detailed shape of I–V curves. Advantage of the mapping approach is elimination of the adverse drift, because it is possible to reconstruct the location of a NW's cap independently in every scan. This location of maximum current would be defined to consider and plot exactly current values from the locations of maximum currents. It should be noted that high-aspect ratio, i.e., so-called lent-shaped scans are proposed to be done. These rectangular shape scans with low amount of scan lines along the slow scan axis reduce duration of

SPM measurements. Another advantage is that mapping approach allows obtaining statistics to characterize the distribution and repeatability of conductance of NWs in an array. Unfortunately, mapping approach accelerates degradation of the SPM probe by wearing its conductive coating and can result into damage or breakage of the NW. This is due to significant forces (in the order of hundreds to thousands of nanonewtons) acting onto NWs in contact mode of C-AFM. Stability of conductive coating of SPM probes from wearing can be verified as unfailing of maximum values of registered electric current with time during a series of scans.

Therefore, the most advantageous procedure of measurements of NW's resistance should be based on method, where force of interaction is minimized and controlled. Most of recent SPM setups provide this opportunity, which appeared initially as PeakForce™ mode (Bruker). PeakForce is based on ScanAsyst feature allowing automated calculation of optimal setpoint force and feedback gain. Here, it should be noted that the regime combining both accurate measurement of topography and measurement of current is called PeakForce TUNA mode. The regime is realized as additional mode of our standard SPM microscope. It is beneficial in comparison to C-AFM because considerably smaller force of interaction can be established and controlled, i.e., force is controlled with precision ~0.01 nN instead of few nN in C-AFM. Simultaneously, current is being registered in the range up to 500 nA with outstanding accuracy ~65 fA, which is also two order of magnitude more accurate than C-AFM with its high noise level. Practically, measurements of morphology of vertical NWs are done in such a way that force of interaction onto flexible few micrometer-tall NWs can be controlled to be approximately 0.1 nN.

Since PeakForce Tuna is a semicontact regime, electric current is being measured in every act of tapping. Direct contact established during a single tap lasts approximately tens of microseconds (depending on setpoint force and tapping frequency), but this duration is enough for modern electronics to register current precisely with picoampere accuracy. This approach allows measurements of long and thin NWs (length ~4 μm and diameter ~10 nm) without damaging the NWs as was shown in our previous works [65, 66]. Last important detail is exactly the composition of conductive coating on SPM probes utilized for electric measurements. Industrial techniques of fabrication of SPM probes are consistently developing. Old types of coating materials, e.g., so-called diamond-like coated probes (DCP), are becoming more rigid and reliable. Simultaneously, noble metals are being used for coatings, e.g., alloy of Pt/Ir (Bruker) or Au. These coatings have thickness approximately tens of nanometers and tend to be defaced when significant forces or electrical biases above 2 V are applied. It leads to decline in repeatability of results for excessive biases or insufficient scale of applied electric potential for I–V curves. We consider that most reliable results can be obtained with modern DCP probes (NT-MDT), or AFM probes made entirely of highly conductive inert metal, e.g., full metal platinum probes (Rocky mountain nanotechnology) or with SPM probes covered with tungsten semicarbide W_2C (ScanSens). All of these types of probes are available in market representing various resonant frequencies and spring constants. Still unfortunately, progress of SPM probes seems less significant than predicted by corresponding roadmaps for technologies [71]. Hence, a holdback in one of the nanotechnologies decelerates research of others as happens in the study of NWs.

2.2. Electrostatic surface potential and charging of horizontal NWs

KPFM is a method of registration of surface electric potential originated from a classical experimental technique invented in late nineteenth century. Its principle of operation utilizes control of electric potential field between measuring probe and studied sample [72]. SPM probe moves in predetermined pattern above the surface with constant lift height and performs mapping of surface's electric potential with millivolt-level accuracy. The advanced SPM version of Kelvin probe setup is KPFM operated in frequency modulation regime. Lateral resolution of imaging is in the order of radius of the SPM tip, while most recent conductive SPM tips have radius approximately 20 nm. Indeed, KPFM can be acclaimed as one of the most important and informative tools to study electrostatic effects in NWs. In a forefront KPFM experimental procedure, scanning is being done in a single pass, simultaneously mapping *topography* and *potential*. This feature is called PeakForce KPFM FM, and it reduces the duration of experiment twice in comparison to two-pass method [73]. Thus, major achievements in this method were reached during latest two decades as a result of advanced nanotechnology and modern computing. It should be noted that resolution of KPFM is strongly dependent on quality factor of SPM's probe oscillations Q. Parameter Q increases in vacuum due to depressed damping of induced mechanical vibrations of SPM cantilever that significantly improve signal-to-noise ratio. Common resolution in ambient air conditions is limited by tens of nanometers partly due to the moisture and water layer covering surfaces of both sample and SPM probes.

KPFM experiments with horizontal NWs fixed in metal-semiconductor-metal (MSM) geometry are well established and were described in previous works [74]. However, it seems worth adding few vital previously unreported details to disclose the procedure of surface potential microscopy in even more comprehensive way. Optimal procedure of KPFM measurements assumes that horizontally lying NW (see marked area in **Figure 4a**) should be oriented perpendicularly to the plane of the vertical deflection of an SPM cantilever (see scheme in **Figure 4b**). Typically, this is achieved by manual rotating of the sample itself or sample's holder in desired direction before the measurements. Scanning should be done with fast scanning direction coincident with long axis of an NW, which is done by insertion of scan angle of 90°. These methodical improvements result into elimination of influence of shape of the pyramidal SPM tip because front and back angles of the tip pyramid are typically different, while the two other side angles are identical. Another benefit is a significant suppression of parasitic capacitive influence of massive SPM tip onto lateral resolution [75]. Moreover, such arrangement routinely eliminates spikes related to topography roughness of NWs visible in lift pass of the double pass KPFM mode. This is because typical surface profile of the NW in the direction of fast scanning is a smooth flat line. Latter allows decreasing the lift scan distance below 20 nm without any risk of accidental contacting the NW in a noncontact pass. Cantilever and the pyramidal tip should be as small as allowed by features of topology and roughness. In addition, tip radius need to be as small as possible on probe with stable conductive coating. Consideration of all aforementioned factors can allow sub-nanometer resolution of KPFM imaging [72].

Injection of electric charge with its subsequent registration by SPM involves the following steps. Electric bias should be switched on and adjusted to zero with feedback system recording

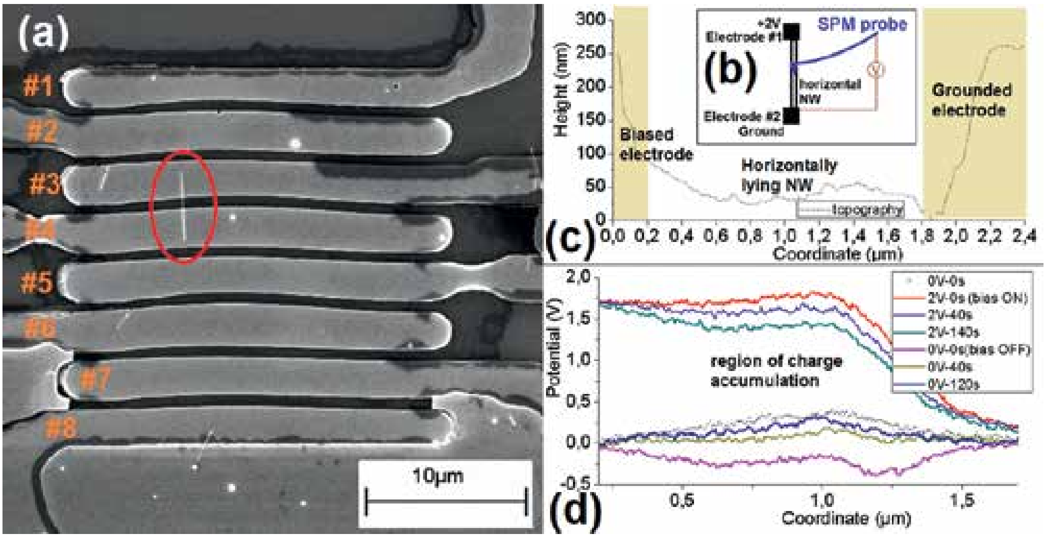

Figure 4. (a) SEM image of a microscheme with pGaAs NW covered by Zn-Au micropads grown by optical lithography. Red mark indicates an NW circuiting the pads #3 and #4, which were used for biasing and grounding. (b) Scheme of the surface potential experiment by SPM probe lifted above the horizontally lying NW. NW is rotated on scheme to represent perpendicular direction of its axis to bending plane of the SPM's probe. (c) Topography profile of the horizontal pGaAs NW. (d) Surface electrical profiles for bias 2 V applied followed by 0 V applied to the left electrode, i.e., to electric micropad #3.

electric *potential* of a sample. First, surface *potential* map should clearly indicate position and orientation of an NW on a substrate in *topography* (**Figure 4c**). It is expected that *potential* profile of the NW should be smooth and flat (**Figure 4d**). If NW is properly connected to microelectrodes and further massive electric feed source, then *potential* of the electrodes should immediately reflect the established parameter of DC bias (i.e., zero if grounded). It should be highlighted that surface *potential* profile of the NW would follow the set value of electric potential of an electrode. It is remarkable that the profile can change in time due to accumulation of electric charges so that shape of profile evolves depending on barrier and NW (**Figure 4d**). Moreover, shape of the profile qualifies this energy barrier at the border between two materials, which indicates certain type of electric contact, i.e., Ohmic [65–67] or Schottky (**Figure 4d**).

Furthermore, potential of both electrodes immediately returns to initial value when bias is switched off, but the distribution of surface electric potential profile of an NW in KPFM occurs with finite observable rate (**Figure 4d**). It means that exactly the charge injected into the NW is visible in profile. Reason is that accumulated charge whose highest concentration is located at coordinate of maximum $U_{MAX}(x)$ is distributed according to (1) diffusive transport model, (2) tunneling into substrate, and (3) considering Coulomb repulsion [76]. In other words, electric charges become redistributed and dynamics of this process are restricted by certain major distribution mechanism. The major mechanism of charge distribution in semiconductor NWs should be diffusion. If charge is leaking, then transistors and energy sources produced on base of such NWs would be ineffective. This means that for properly arranged transport measurements with SPM $dU(t)$ should be proportional to square root of time. From $U_{\mathrm{MAX}}(t)$ dependence and full-width at half-maximum of $U_{\mathrm{MAX}}(t)$ plot, it becomes possible to characterize the mobility of charge carriers and location of defects in NWs. It should be noted that experiments in horizontal NWs and recording their surface potential profiles are preferable to be done for NWs fixed at two ends in a "bridge geometry" [77, 78]. The "bridge geometry" arrangement is laborious in fabrication, although superior to the horizontal MSM arrangement. Reason is that in bridge geometry, the NW is not in electrical contact with a substrate, which eradicates possibility of charge tunneling into the substrate. Similar KPFM investigation over the length of the NW can be proposed also for vertical or inclined NWs, although the substrate with such NWs must be cleaved and then tilted so that SPM probe would have access to the side surface of the NW instead of solely the NW's metal cap. Potentially, electrical studies of NWs can be done by an SPM probe oriented horizontally [79] but not with vertical standard AFM and STM probe tips. In addition, multiprobe techniques already allow advanced operation with vertical NWs [80], but such measuring stations are nowadays expensive and rare.

3. Evaluation of mechanical strength for inclined NWs

Evaluation of strength characteristics of nanoscale objects is a nontrivial task, particularly because it is impeded by properties of their surface, geometry of a measurement, and physical effects of scaling. In this respect, studies of NWs by SPM are challenging because these structures are highly bendable, oscillate with own frequency due to thermal vibrations, and because properties along the NW can be unevenly distributed. Another challenge is that NWs kept in atmospheric environment become partly oxidized, and their properties tend to resemble features of nanocomposites. One of the major details that are widely neglected is that NWs represent specific degree of tapering (**Figures 1c**, **2a**, and **5a**). Reason for that is parasitical input of vapor-solid input of crystal growth [52], which occurs concurrently with VLS mechanism. Tapering of group III–V semiconductor NWs is more pronounced under high-temperature fabrication and for excessive values for relation of V/III precursor sources inside a MOVPE chamber [50]. We will pay special attention to the impact of tapering onto measurement of properties of NWs in this section.

Few methods possessing nanoscale accuracy enable measurements of 1D nanostructures. One of the noncontact approaches makes use of in-situ TEM in order to measure amplitude of free and induced mechanical oscillations of an NW fixed at one end [81]. To certain degree of accuracy, it is possible to calculate elastic parameters with such TEM or high-resolution SEM visualization. Typically, it is only needed to calculate elastic modulus from abovementioned amplitude and geometrical parameters with known density of the NW's material. However, first, certain degree of inaccuracy arises from inexactness of measured geometry and vibrational output. Second, the major reason for error can be that no adequate models were proposed for tapered structures and their mechanics. It should be noted that flexibility coefficient of such tapered NWs is variable along the length.

Methods based on SPM employ direct mechanical contact between structure and a probe and have advantage in their locality. In fact, the only SPM approach presented in literature is when the

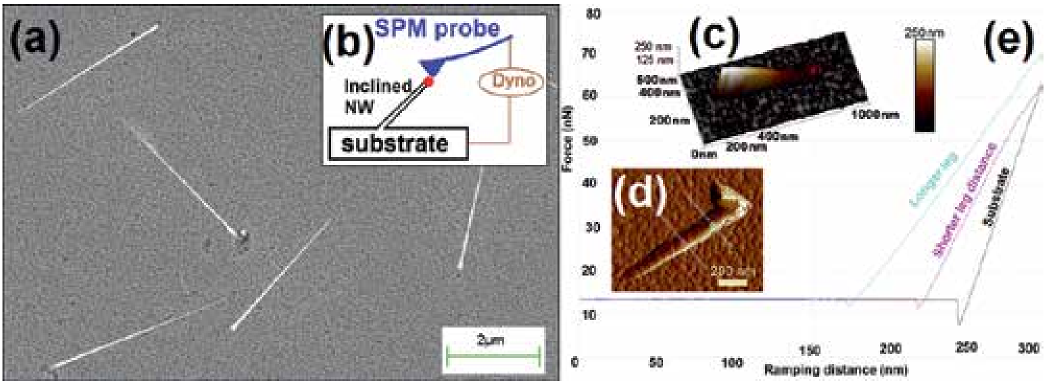

Figure 5. (a) SEM image of an array of inclined tapered wurtzite InP NWs on Si substrate. (b) Scheme of the bending experiment by SPM probe brought in contact with inclined NW. (c) 3D topography model of an inclined NW representing angle 22° for visualization of the NW under small setpoint force. (d) PeakForce error channel representing NW's fixed end at lower left and free end at upper right. Force spectroscopy was performed according to the coordinates seen by color marks. (e) force-load curves $F(z)$ for substrate, middle of NW, and free end of NW.

probe is bending an NW in a definite leg distance point [82, 83]. Leg distance and NW's diameter should be accurately measured in order to evaluate the Young's modulus. We will describe this simple approach in detail at first and then represent our original approach based on mapping of elastic parameters. Latter allows precise control of setpoint force that provides significantly more accurate and precise results for tapered NWs, also entitled as conical NWs or nanocones [84].

3.1. Method of force-load curves F(z)

The simplest approach is based on bending of an NW by SPM probe in exactly defined position [85]. This experiment can be performed on inclined cylindrical NWs (**Figure 5a–c**). Procedure involves measurement of *topography* and defining the location, where stable contact for bending can be established at farthest distance from the NW's fixed end (**Figure 5d**). Longer leg distance provides higher values of displacement and thereof bigger amount of data points plotting the $F(z)$ curve without breaking the NW.

SPM probe for such experiments needs to be flexible and dull, i.e., tip radius is desirable to be considerably more than 30 nm. Initially, cantilever becomes bended on any flat rigid substrate (see black curve on **Figure 5e**), e.g., in proximity to the NW. When spring constant of SPM cantilever becomes precisely recognized, the measurement is called calibrated conferring the force-distant curve $F(z)$ and its slope. Afterward, bending of the desired structure is performed. It is clearly visible that magenta and turquoise curves (**Figure 5e**) taken correspondingly for location near the middle length of the NW and closer to the free end indicate two different slopes. For a highly bendable structure, measured force-load curve $F(z)$ will consist of two components, i.e,. bending of a cantilever and own bend of the NW [85]. For finest evaluation of the NW's spring constant, it is preferable to choose a cantilever with spring constant similar to the anticipated stiffness of the NW. Since spring constant of cantilever k_{CANT} is known from calibration, the other component is exactly spring constant of the NW k_{NW} [85].

First difficulty of this one-point spectroscopy approach is that NWs can be tapered to specific extent. Their diameter d_{NW} is depending on leg distance x, but since $d_{NW}(x)$ is changing along the length of the NW, then their k_{NW} is nonlinearly dependent from leg distance as $k_{NW}(x)$, where $x \in [0;L]$. Despite that, k_{NW} characterizing elastic properties of a studied NW is adequately obtained only for one coordinate situated considerably far from NW's end. Second, it does not seem achievable to recognize this leg distance x precisely, because inclined NWs are partly merged with the substrate at the fixed end, which is an artifact of fabrication procedure (**Figure 5d**). However, it is obvious that SPM probe is unable to visualize any area beneath the structure (**Figure 5c**). Third, since diameter strongly affects the value of elastic modulus, inaccuracy of a diameter is crucial. Finally, such measurement can hardly be qualified as stable, because sliding effect is significant, so repeatability over time is also a significant drawback. Nonetheless, with this technique authors of [82, 83, 85] have successfully measured and reported elastic moduli of 1D nanostructures with reasonable accuracy. In was achievable because method of force-load curves is adequate for thick long nanostructures.

3.2. Advanced QNM for bendable nanostructures

We have generalized an advanced procedure allowing measurements of inclined NWs to be carried out with significant accuracy [86]. Measurements are proposed to be performed with the help of SPM equipped by a module registering setpoint force at each moment, e.g., QNM. In fact, major SPM manufacturers had promoted concurrent methods analogous to QNM (HybriD from NT-MDT, pulsed force mode from WITec and jumping mode from Nanotec Electronica) independently, while Bruker firstly introduced their QNM™ in 2009. As a result, this advanced experimental technique is now attainable by plenty of research teams with various microscopes worldwide. Let us describe our experimental approach with theoretical background and associated limitations, which will be formulated in terminology of the Bruker's QNM mode.

Initially, it is possible to find individual NWs by built-in optical microscope providing magnification 200x. In fact, even location of thin NWs having diameters 10 nm can be visualized by optical microscope, because they scatter the light. Such NWs become visible as single grey pixel routinely resolvable by optical matrix (**Figure 6a**). The scanning is done by the blunt flexible SPM probe moving along the long axis of an inclined NW. It should be noted that specific probes can have a tip shape allowing to settle on the nanostructure and arrange a stable mechanical contact. For example, manufactured NP-STT10 probes (Bruker) with two tip apexes are proposed for stabilization of contact between NW and SPM probe and to avoid sliding effect (see two tip apexes in **Figure 6b**). Separately, ordinary flexible one-apex probes should be used for surface visualization. QNM measurements of bendable NWs are proposed to be performed under different setpoint forces (**Figure 6c** and **d**) in order to obtain significant statistics to calculate flexibility coefficients (**Figure 6e**) and model the Young's modulus. Interestingly, such remarkably precise scanning requires not more than 10 min with rectangular scans described in Section 2.1.2. Entire profile of a flexibility coefficient is obtained instead of low representative single data point in the method of force-load curves (**Figure 5e**). These data are reproducible during the scan, for different forces and by probes with different spring constants.

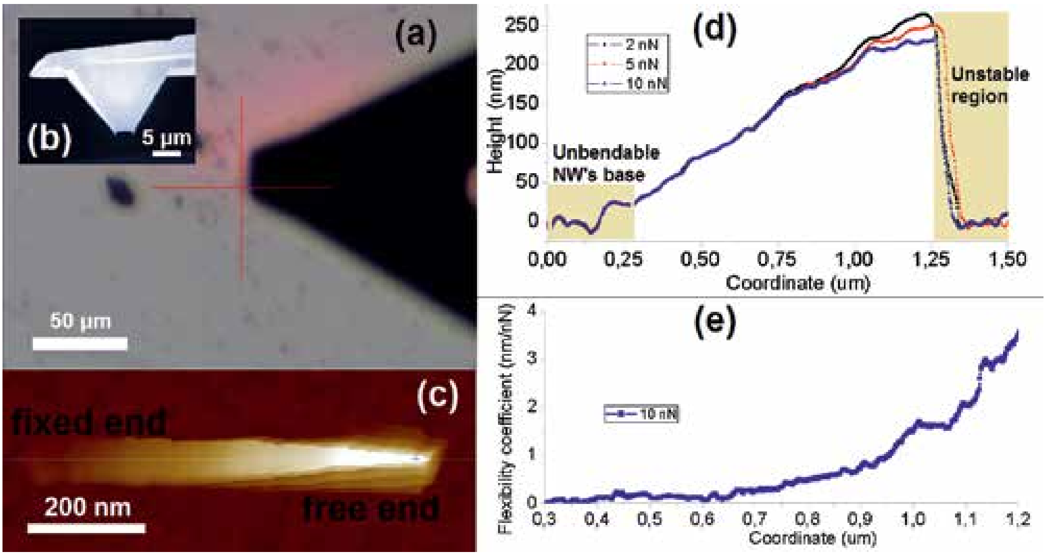

Figure 6. (a) Optical image 125 × 80 µm representing individual NWs as grey spots near the triangle-shaped SPM cantilever. (b) SEM image of BRUKER NP-STT10 probe with two apexes at the end of the tip and an arc between them. (c) High resolution rectangular shaped 2D topography image of an inclined InP NW under significant force setpoint 10 nN. (d) Comparison of topography profiles for bending of inclined InP NW under different forces. (e) Bending profile representing flexibility spectra of a single bendable NW along its length, where fixed end is on left and free end is on right side.

Our approach is based on Hooke's law and Euler-Bernoulli theory. The body compression law (seventeenth century Hooke's law) states that

$$F = k\delta \tag{3}$$

where k is a linear stiffness coefficient, i.e., spring constant, of a structure and δ is a linear displacement, i.e., deformation, by the force F acting on same axis with deformation.

In case of a NW, which is bended down by specific setpoint force F until the NW's "bended position", the equation for deflection ω should be written as follows

$$F = \mathrm{k}_{NW}(x) \cdot \omega_{NW,\ F}(x) \tag{4}$$

Noteworthy that the "spring constant" k_{NW} is not invariable along the NW structure in bending experiment, but depends from a distance to the fixed end $x \in [0,L]$, where L is length of NW.

Deflection of NW $\omega_{\mathrm{NW,F}}$ under certain applied force F is a parameter measurable from SPM topography data (**Figure 6d**)

$$\omega_{NW,F}(x) = \Delta\text{height} = h_F(x) - h_0(x) \tag{5}$$

where h is a registered height, so that $h_{\mathrm{10nN}}(x)$ is the height observed by SPM when the probe pushes with a setpoint force 10 nN at a certain coordinate $x \in [0,L]$.

It should be noted that F is a fixed parameter and this setpoint force is established with piconewton accuracy in QNM. The spring constant k is known as dependent from the leg distance x, so that relation between k and x is cubic for a cylindrical beam $k \sim x^3$ similar to experimental plot of flexibility profile f(x) in **Figure 6e**. We will later calculate how exactly k is related with x for a tapered beam with the cone angle 2α and diameter in the middle of the NW's length D_{MID}. Height $h_0(x)$ is typically considered as the height of a structure scanned by SPM. Despite that, the topography is always measured under specific setpoint force applied by SPM. Therefore, the force for $h_0(x)$ is neglected. SPM setpoint force is ~10 pN for a gentle scanning, which is affordably small.

Euler-Bernoulli theory introduced in eighteenth century defines bending of an isotropic beam [87], depending on composition (by elastic modulus) and geometrical shape of a beam (e.g., by length L and diameter D)

$$\frac{d^2}{dx^2}\left(EI\frac{d^2\omega}{dx^2}\right) = q \tag{6}$$

where $I(x)$ is second moment of inertia of a beam.

The equation for deflection of an NW by a point contact established by an SPM probe along the location in NW $x \in [0,L]$

$$E\frac{d^2}{dx^2}\left(I(x)\frac{d^2\omega}{dx^2}\right) = 0 \tag{7}$$

The boundary conditions appropriate for our model are

$$\omega(0) = 0;\ \omega'(0) = 0;\ \omega''(L) = 0;\ \omega'''(L) = -\frac{F}{EI(X)} \tag{8}$$

Accounting these boundary conditions, the generalized form of a solution of Eq. (7) is

$$\omega_{\mathrm{NW,F}}(x) = \frac{F}{6EI(x)}(3Lx^2 - x^3) \tag{9}$$

The second moment of inertia for a cross-section of a conical beam is described as

$$I(x) = \frac{\pi D_{\mathrm{MID}}^4}{64}\left(1 + \frac{\alpha}{D_{\mathrm{MID}}}(2x - L)\right) \tag{10}$$

We now can formulate the dependence of flexibility of a tapered NW:

$$f_{\mathrm{NW}}(x) = \frac{1}{k_{\mathrm{NW}}(x)} = \frac{\text{Deflection}}{\text{Force}} = \frac{\omega_{\mathrm{NW,F}}(x)}{F} = \frac{1}{E_{\mathrm{mat}}}\cdot[\mathrm{coeff}(x, L, D_{\mathrm{MID}}, \alpha)] \tag{11}$$

where flexibility coefficient $f_{\mathrm{NW}}(x)$ is presented as a function of material (E), location of applied force (x), and the shape of a structure (L, D_{MID}, α).

Finally, the formula for calculation of the Young's modulus of a tapered NW in our model is the following

$$E_{\text{mat}} = \frac{64}{3\pi} \frac{1}{f_{NW}(x)} \frac{1}{D_{\text{mid}}^4} x^3 \frac{1}{(1 + \frac{\alpha}{D_{\text{mid}}}(2x - L))(1 - \frac{\alpha L}{D_{\text{mid}}})^3} \tag{12}$$

It must be noted that for appropriate application of any model, it is vital to consider not only the generalized form of relation between variables, but also assumptions of the model, defining its limits of use. Two of such assumptions for Euler-Bernoulli theory are isotropy of the material and elastic regime of bending. Material of the NW is considered isotropic across its entire length, discarding e.g., surface effects, possible defects in crystal structure, etc. In reality, defects act as deformation accelerators and result into spikes visible on bending profile. Elastic regime of bending means that object's deformation should be very small with the force applied. In addition, elastic modulus in our model is considered independent from temperature and speed of bending. In fact, Young's modulus E descends with heating [88], although it is not considered in our model. Indeed, any physical body becomes heated when the work is applied upon it. Therefore, bending by SPM probe performed in a regular manner 2000 times per second can be seem to add heat into the studied NW. Reason for ignoring the possible thermal input is that NWs have considerably high thermal conductivity and small length, so that heat is rapidly distributed into the substrate and dissipated in atmosphere.

Remarkably, the value of Young's modulus is obtained for one-single NW from a substantial series of data points $\omega_{\text{NW,F}}(x)$ recorded by SPM. Indeed, each of these values is already appropriate to define E, but the series of data values contains ~400 informative data records providing high reproducibility of a result. Furthermore, each setpoint force provides specific bending to verify that deflection is within the linearity range. If multiplied by amount of data values for each applied setpoint force, then significant approximation of flexibility coefficient is achieved, providing unprecedented accuracy of this approach.

Unfortunately, the model involves few geometrical parameters of NWs, which are difficult for estimation with significant accuracy. Visualization techniques, e.g., SEM or SPM topography measurement, were used to provide L, D_{MID}, and α. Due to limitations of lateral resolution of SEM scanning (~2 nm) inaccuracy of measurement of diameters of the studied NWs was significant. Moreover, relative error of diameter evaluation increases for thin NWs, while we have studied NWs with diameter of top part as small as 10 nm. Therefore, a special protocol of estimation of diameter of the NWs was utilized to correct the values. Initially, sizes were controlled during fabrication with accuracy approximately ±3 nm. After the fabrication, diameters were controlled by SEM. After that we performed breakage of few NWs from an array to estimate their height, while NWs were lying on flat substrate. As a result, for NWs with $D_{\text{MID}} = 40$ nm, relative error of estimation of Young's modulus was ±40%. Therefore, we performed the HR-SEM investigation and numerical modeling that decreases the relative error until approximately 20%.

This level of accuracy allowed defining that the Young's modulus of InP in thinner NWs increased from 60±7 GPa until 140±30 GPa. Remarkably, 62 GPa is exactly the value of Young's modulus of zinc blende InP. The result was obtained from a series of 16 inclined

NWs. This means that Young's modulus of wurtzite InP is approximately twice bigger than that of zinc blende InP. Wurtzite structure of NWs was verified by TEM and microPL analysis. Already this, i.e., estimation of Young's moduli of wurtzite InP, is a challenging achievement, which can be acquired only in thin NWs. Reason is that wurtzite InP phase is unstable with increasing of the sample's size, so that bulk material transforms into zinc blende structure while the NWs under our studies were affordably thin. Own scaling effects of Young's modulus of wurtzite phase can be separately investigated when size of the material becomes lower than 50 nm in diameter. Another issue to highlight is that a proper model of tapered NWs was proposed and used [86], which was not performed by other authors. The results were achieved for NWs with upper diameter (width of Au caps) ~10 nm.

In order to understand the unlikeness of experiment with bendable objects, it is essentially important to differentiate between "stiffness of the structure" and "rigidity of the material within a structure". Such distinguishing seems necessary because *deformation* channel data are calculated only in the case when both force applied and material's stress occur at the same location. These calculations for SPM in QNM are done in accordance with Derjaguin-Muller-Toporov (DMT) elastic model [24], used as built-in in QNM mode. Indeed, DMT model was introduced in SPM to be mainly used for characterization of flat surfaces and the method succeeded in this pursue. However, for bendable objects, DMT channel data and underlying model are inapplicable. This is explained considering that the stress occurs solely at the fixed end of a bendable structure possessing one fixed end. Therefore, the location of stress (fixed end) is situated micrometers away from location of force applied by SPM probe. In QNM, while DMT model is used, the deformation is quantified from adhesion data, while setpoint force is precisely controlled by feedback system. Topography is being registered routinely, but highly bendable NWs are twisting down during their scanning. Thus, bending reflects on registered topography. Similar conclusion that morphology depends on setpoint force applied by SPM probe was previously demonstrated in studies of exceedingly soft materials [89]. Force needs to be kept in such small range that deformation is consistently ~1 nm across the entire flat surface of a sample. Lastly, topography must be measured in appropriate time moment of PeakForce procedure. The sync distance parameter needs to be manually adjusted to be approximately 6 μs (for PeakForce frequency 2 kHz) later [86] than established automatically during the first engaging onto a sample prior to scanning. Autofitting of time moment of the PeakForce value for each tapping cycle can solve this problem and probably will be introduced in forthcoming versions of SPM software.

Considering other types of experiments possible to be realized with SPM, classical indentation can be mentioned. For indentation measurements, sharp and extremely stiff SPM probes are required. Unfortunately, elastic deformation and indentation models consider different geometries and types of stress and should not be compared. Elastic models include stretching, squeezing, and torsional stress, while indentation results depend on a shape of the indenter, etc. Interesting summary of results obtained by these various methods of ZnO NWs was prepared by authors of [90]. They have shown that elastic modulus of ZnO measured by different groups with different methods varied by almost twice.

Summarizing that the above-described elastic profile mapping approach is significantly more advanced in comparison with spectroscopic method of investigation of Force-Load curves. It is first because diameter D is not considered constant due to tapering of NWs. Secondly, because $k_{NW}(L)$ is being evaluated at plenty of definitely established positions, but not at one single location (typically at the oscillating free end of NW and in disfavoring semicontact tapping mode). Our approach allows precise definition of coordinates of the fixed end necessary for the evaluation of the leg distance for each definite data point from hundreds of those measured experimentally. Even though defining these coordinates is not possible for SPM visualization, it is reachable for fitting procedure in our numerical model. Accuracy of evaluation of Young's modulus seems to be approximately 5 GPa for NWs with radius above 30 nm. Finally, our approach is easily applicable for conical NWs. The presented comparatively easy SPM procedure of measurements of elastic characteristics is proposed to be used for various one-dimensional nanostructures and conical nanoobjects.

4. Studying piezo response

Piezoelectricity in NWs is an electromechanical phenomenon [91], so we left it to last section of this chapter. Piezophototronic devices based on NWs are widely discussed as sources that would replace both solar cells and windmills in the distant future. Therefore, such nanogenerators based on piezo responsive NWs represent a new generation of sustainable energy sources and must be studied in details. Interestingly, SPM is exactly the instrument that is used by plethora of research teams in the field of nanogenerators of electricity. Previously, we reflected two types of experiments, i.e., spectroscopy and mapping. Being consistent with this methodological assemblage, two self-determined PFM approaches will be discussed in this section for wurtzite GaAs NWs (**Figure 7a** and **b**). First type is a standard PFM oriented toward detection of reverse piezo coefficient. Second type is registration of piezo current and indirect evaluation of piezo coefficient, although reasons for generation of current in this case are not entirely understood up to recent moment.

4.1. Reverse piezo coefficient studies of horizontal NWs and nanowire stumps

Experiment requires reliable contact to be arranged between a sample and a dull probe mounted on a stiff cantilever. This is one of the methodical differences comparing to all other experiments described in this chapter where flexible levers were much preferable. Hard contact commonly leads to destruction of vertical and inclined NWs due to significant forces applied to the sample and fragility of NWs. Thus, the method is applicable either for horizontal NWs or for "stumps" (**Figure 7b** insets (i) and (iii), correspondingly). Stump structure is a residue of NW left after its upper part was broken due to application of excessive force (nonelastic stress). The part left is lower than initial NW, so its thermal oscillations are less intensive in lateral direction. Unfortunately, it seems impossible to predict existence of piezo responsive phase in the stump after the breakage. Nevertheless, this becomes explicit from PFM imaging, where studies are performed in C-AFM contact regime.

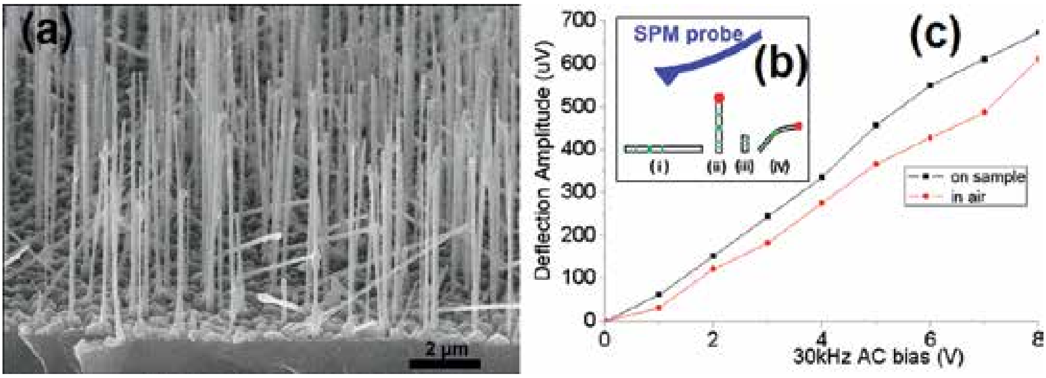

Figure 7. (a) SEM image of an array of vertical wurtzite GaAs NWs grown by MBE on Si substrate. (b) Schemes of the PFM experiment by SPM probe for horizontal (i), vertical (ii) and inclined (iv) NWs and NW stump (iii). (c) Comparison between PFM amplitude output from a stump of wurtzite GaAs NW and air 5 μm above the NW.

4.1.1. Spectroscopy of surface oscillations in comparison with non-piezoelectric phase and air

In spectroscopic PFM method (**Figure 7c**), it is necessary to establish a point-like contact (area of contact is few tens of square nanometers) with NW's segment containing piezo responsive phase. Then, high-frequency variable bias V_{AC} is being applied to the substrate. Frequency of the voltage applied f_{AC} should be different from the resonant frequency of the SPM probe contacting sample under certain force. After that, mechanical oscillations [$\mu V_{\mathrm{DER}}/V_{AC}$] are registered by high-frequency feedback amplifier of photodetector's signal. Indeed, all signals obtained in SPM are processed as relation of *derivative microvolts* μV_{DER} of signal, but if measurement is properly calibrated considering sensitivity of photodetector as [μV_{DER}/nm], then result would be represented in [nm/V_{AC}]. In addition, flexibility of the SPM cantilever can be easily calibrated in [nN/nm] (see probe calibration protocol in Section 3.1), which would provide a value of inverse piezo coefficient of a studied material in [nN/V_{AC}]. Unfortunately, given force in [nN] does not represent the value of elastic response correctly in contact mode AFM, but is used only as guiding parameter of force. However, if standard test sample with known piezo coefficient is used for comparison of its piezo response with data recorded for unknown material, then result for sample would be recorded in standard layout [nN/V_{AC}]. In such a way, it becomes possible to compare properties of new materials with references and tabulated data for d_{33} vertical piezo coefficient for stumps or d_{13} and d_{15} coefficients for horizontal NWs.

It should be noted that measurements of both piezo active phase and nonpiezo active phase in same conditions should be compared to eliminate the influence of background noise onto derived signal and evaluate solely input of piezo response (**Figure 7c**). This is due to capacitive effects influencing the compelled resonant mechanical oscillations of an SPM probe situated in micrometer distance from the sample. Obtained dependence of mechanical oscillations from applied potential can be wrongly interpreted as pure piezoresponse signal (**Figure 7c**). The logic here should be that if signal in certain NW is different from measurements of nonpiezoelectric material with same geometry and composition, then piezo phase exists in the NW. Fortunately, single experimental measurement requires few minutes, which permits quick finding the NW stumps with piezo phase. Significant drawback of this approach is that it is almost impossible to characterize thickness of the piezo active inclusion in the stump, while all remaining part of NW cannot consist of piezo active material. Therefore, additional tools are required to characterize its structure and composition.

4.1.2. Mapping of mechanical oscillations induced by AC voltage

Method of mapping allows avoiding the sample's drift and builds up a map of piezo response (**Figure 8**). Such map indicates more intensive contrast for areas with stronger piezo signal.

If a sample is homogeneous or provides areas with homogeneous piezo response, e.g., on surface of horizontal NWs, then such areas provide significantly representative array of data. Thus, measurements in PFM mapping approach are more accurate comparing with PFM spectroscopy. Drawbacks of this approach are that sample and probe are more intensively worn and torsional movements are strengthened due to friction. Moreover, triboelectric effect arising from friction between SPM probe and surface can influence the result [92]. Triboelectric effect can generate localized charges of opposite signs in the NW and SPM probe after each tap due to friction and difference in work functions between the sample and the probe. These charges can shift surface potential of a sample and lead to generation of adverse current. However, such current is detrimental solely for evaluation of piezo coefficient. Intriguing new field of NW technology was formulated during last decade focused on production of current with triboelectric effect. For comprehensive analysis of prospects of triboelectric nanogenerators, reader should access [92].

4.2. Piezo current visualization for vertical and inclined NWs

Instead of reverse piezo effect, it can be more beneficial for applied science and industry to evaluate useful electric current produced by NWs containing piezo responsive phase. We will briefly describe its phenomenological value. Visualization of electric current for thick, vertical, and inclined NWs (see insets (ii) and (iv) in **Figure 7b**, correspondingly) is considered uncomplicated for SPM with force control (see Section 3.2). Latter can be crucial for testing of NWs fabricated from new materials with the following two techniques.

4.2.1. Recording of current during mechanical bending in local point contact geometry

In the method of force-load curves (discussed in Section 3.1), it is possible to perform spectroscopy of current in time $I(t)$. If registration of current flowing through the system is switched on, then it becomes possible to measure electric current flowing through an individual NW in every moment of its bending (see Section 2.1.2) (**Figure 9**). It must be admitted that current spikes were registered while no bias was applied to the sample. However, the electric current observed by SPM can be associated with increase of concentration of photo induced carriers [93, 94]. Parasitic electrically induced potential can also lead to adverse stimulation of carriers. Since laser beam falling onto the SPM cantilever near the probe can over-illuminate the measured NW then both of these mechanisms can lead to observation of electrical spots during C-AFM spectroscopy or mapping. These influences can be overcomed with adequate grounding and performing the experiments in dark conditions [93, 94].

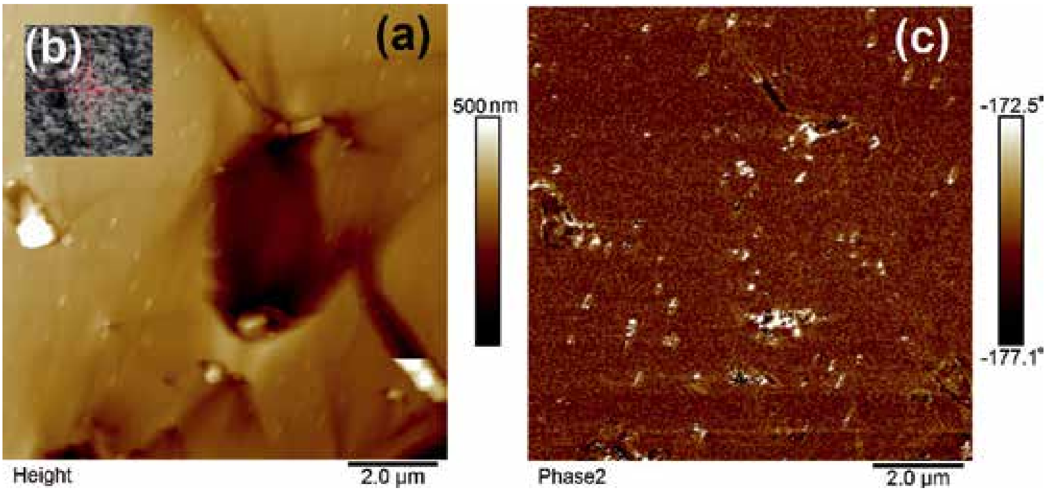

Figure 8. (a) 2D topography of a field with stumps left from an array of wurtzite GaAs NWs. (b) Optical image 100 × 100 μm representing square shaped field left after the breakage of vertical wurtzite GaAs NWs. (c) 2D image with a map of phase of the oscillations in lateral direction for a field with wurtzite GaAs stumps seen on (a) image. White spots indicate areas with higher amplitude indicating individual stumps.

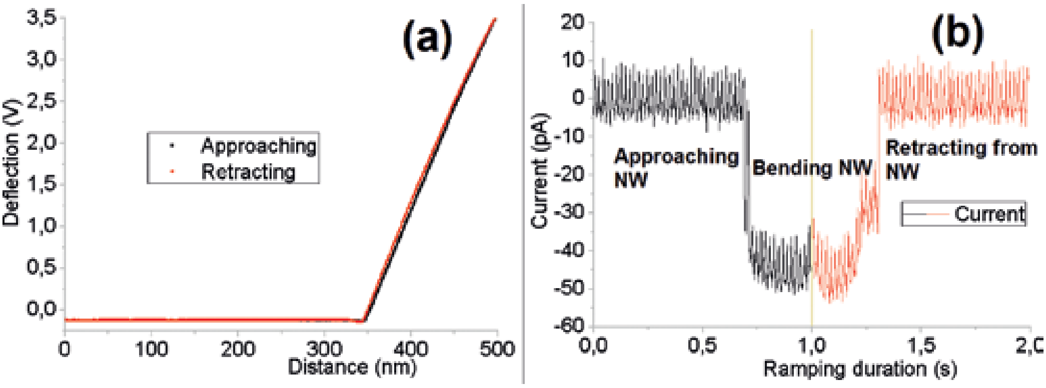

Figure 9. (a) Plot of F(z) for approaching and retracting from the sample where wurtzite NW was bended. (b) Current-time spectra $I(t)$ registered during the bending of wurtzite GaAs NW.

Additionally, since these measurements are performed during almost seconds (while the value of current is considerably stable), it is potentially possible to evaluate the charge transferred $q[C]$ and power $P[pW]$. This gives path to evaluation of performance of piezotronic devices with help of SPM by assessment of single NWs.

4.2.2. Mapping of electrical current in NWs induced by controlled mechanical bending

Mapping of electric current in principle can help to visualize certain NWs producing higher values of electric current See **Figure 10** taken under 0 V applied bias on WZ GaAs, where black spots are supposedly representing the current spikes measured in contact by SPM probe and generated due

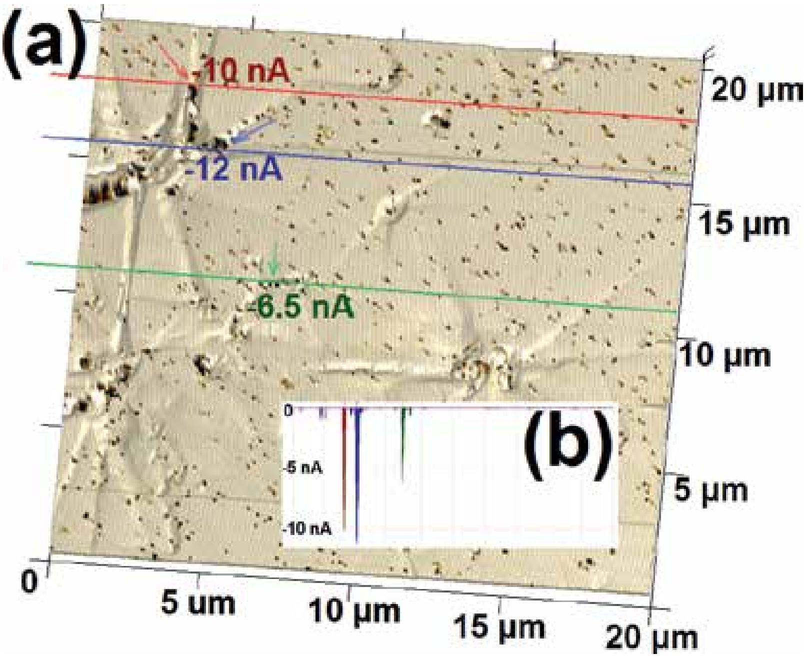

Figure 10. (a) 3D topography model of surface covered by stumps of wurtzite GaAs NWs seen as black spots due to overlaying of electric current map onto 3D topography. (b) Comparison of profiles of electric current taken for spots with highest electric current on from (a) image.

to mechanical stress of piezo responsive WZ GaAs material. This might indicate statistics about level of fabrication defects and overall quality of an array. Unfortunately, this approach is highly dependent from definite recognition of properties of energy barriers involved. Both Schottky barrier at the top part of NW and diffusion barrier at the bottom of NW (existing if materials of NW and substrate are different, e.g., Si and GaAs) can affect the result. In addition, triboelectricity can be an adverse factor during mapping of mechanical oscillations and it is aggravated for mapping in comparison with spectroscopy. Thus, triboelectric effect elaborates calculation of the input of piezo current and further evaluation of direct piezo coefficient of NW in nonvertical axis.

Shift of electric potential, which is registered as piezo response of the NWs' material, is suggested to be the result of redistribution of charge carriers inside NWs during their scanning/bending. Correspondingly, electric current that can be measured for piezoelectric NWs in PeakForce Tuna microscopy should indicate transfer of above-mentioned electric charges, i.e., electric current. Order of magnitude for such current is approximately few nanoamperes (**Figure 10b**). In addition, it can be possible to recalculate the current into potential, if resistance of the system is known. Unfortunately, heterojunction at the contact area between NW and a substrate obscures the transport mechanisms in such NWs. Revealing of mechanism of generation of electric current requires a separate comprehensive methodical study. This study should be performed on NWs with negligible energy barrier at its bottom contact with a substrate.

When aforementioned methodical difficulties will be overcomed, a map of current density generated from each individual NW from an array would be visualized. In this respect, it should be considered that force of push onto the NWs affects the value of electric potential induced in NWs. At the same time, altering rate of a setpoint force regulates the value of electric current produced by NW-based nanogenerators. Integer of current from single NW in time by its physical meaning defines the charge transferred into the SPM probe and recorded by SPM controller. Moreover, current from an array of NWs can be summed. Anticipated current output from an array containing plenty of NWs can be substantial for functioning of NW-based devices and can be characterized by current per certain area of an energy source [A/cm^2]. Applicability of latter approach needs to be approved by experiments with properly arranged massive electrode grown above an array. Therefore, we can conclude that local methods still need to be strengthened by massive methods of research of NWs. The proposed concept of registering the piezo current presented here has debatable arguments but provides a room for improvements. If it would be realized in near future, it seems prolific for quick and accurate estimation of electricity generated by piezoelectric materials and NWs.

5. Conclusion

To summarize, nine types of experiments were described in this chapter with associated advantages and drawbacks of the SPM techniques. Different types of SPM probes paired as sharp/dull and flexible/stiff were specified for certain experiments with NWs. Congregation of methodical information was motivated toward better understanding of opportunities of microscopic techniques for studies of NWs. Comprehensive usage of these techniques depends on measuring systems available for certain research groups interested in study of NWs. While SPM systems continuously develop in latest decades, we emphasize that SPM is essentially useful, precise, and versatile tool for abovementioned purposes when properly operated. SPM allows studying electrical, mechanical, piezo properties, in addition to magnetic and optical properties, biocompatibility for medicine, chemical reactivity, etc.

In the course of our SPM research work, few significant findings were obtained in materials science. GaP should be preferably chosen as passivation material for GaAs NWs, while AlGaAs appeared also beneficial. Second, transparent protective medium of SiO_2 has a complex influence onto conductive properties of NWs, i.e., energy barrier is reduced for unpassivated NWs, while it is strengthened for GaP-passivated NWs. These results were first obtained due to possibilities of SPM force control. Additionally, few methodical improvements were proposed. In the field of mechanics, the original mapping procedure of studies of tapered 10 nm thin NWs fixed at one end has been established. This allowed to first measurement of Young's modulus of wurtzite InP material, which exists recently only in nanothin state, i.e., solely in NWs. Therefore, it is a remarkable example of gathering a promising exotic nanomaterial and the only technique that can correctly describe its properties. Moreover, few original SPM experiments were proposed for comprehensive characterization of piezo properties of piezoelectric NWs in the field of electromechanics. Individual wurtzite GaAs NWs were experimentally investigated on the basis of proposed methodical electromechanical concepts. Lastly, studies of electrical conductivity of as-grown NWs are possible only with SPM. We developed the methodology of examination of as-grown vertical NWs and analysis of their I–V curves. The presented approach doe not require an objectionable stage of the breakage of the

NWs followed by their fixation in horizontal lithographic MSM pattern for analyses as was done previously by other authors.

Considering the further outlook of SPM methods in studies of NWs, described approaches can be partly adapted to nonsemiconductor classes of materials, e.g., metals, polymers, insulators, ceramics, carbon ribbons, etc. Modern computational tools with proper procedures can assist standard microscope stations in realization of fast measurements and data recognition. Furthermore, components of SPM and experimental practices tend to be developed to an automated stage, resulting in even more powerful technique for studying versatile one-dimensional structures. Utilization of SPM allows obtaining of vital information about NWs, their individual and even local properties, which helps to better understanding of properties of an array of NWs and to design future devices based on NWs.

Acknowledgements

Authors wish to thank a research group in Department of Micro and Nanosciences, Micronova, operating in Aalto University, Finland for fabrication and SEM visualization of vertical, horizontal and inclined NWs presented in Sections 2 and 3. Additionally, we thank the group of Laboratory of Nanoelectronics from St. Petersburg Academic University, St. Petersburg, Russia for growth and TEM visualization of piezo responsive GaAs NWs. PG thanks Dr. Prokhor Alekseev for thorough discussions providing significant contribution to the final version of the manuscript, Alina Lomenkova for help with graphical data analysis and Andrey Shubin from ScanSens Gmbh for assistance with tungsten semicarbide probes. This work was supported by EU project Horizon2020-MSCA-RISE-691010 Hunter.

Author details

Pavel Geydt[1]*, Mikhail S. Dunaevskiy[2] and Erkki Lähderanta[1]

*Address all correspondence to: pavel.geydt@lut.fi

1 Lappeenranta University of Technology, Lappeenranta, Finland

2 Ioffe Institute, St. Petersburg, Russia

References

[1] Xia Y, Yang P, Sun Y, Wu Y, Mayers B, Gates B, Yin Y, Kim F, Yan H. One-dimensional nanostructures: Synthesis, characterization, and applications. Advances Materials. 2003;**15**(5):353–389. DOI: 10.1002/adma.200390087

[2] Dasgupta NP, Sun J, Liu C, Brittman S, Andrews SC, Lim J, Gao H, Yan R, Yang P. 25th anniversary article: Semiconductor nanowires – synthesis, characterization, and applications. Advances Materials. 2004;**26**(14):2137–2184. DOI: 10.1002/adma.201305929

[3] Hochbaum AI, Yang P. Semiconductor nanowires for energy conversion. Chemical Reviews. 2010;**110**(1):527–546. DOI: 10.1021/cr900075v

[4] Lu W, Xiang J, editors. Semiconductor Nanowires: From Next-Generation Electronics to Sustainable Energy. London, United Kingdom: RSC Publishing; 2015. p. 448. DOI: 10.1039/9781782625209

[5] Arbiol J, Xiong Q, editors. Semiconductor Nanowires: Materials, Synthesis, Characterization and Applications. 1st ed. United Kingdom: Woodhead Publishing; 2015. p. 572. DOI: 10.1016/B978-1-78242-253-2.01001-X

[6] Prete P, editor. Nanowires. Croatia: InTech; 2010. p. 428. DOI: 10.5772/3457

[7] Zhang Z, Yao K, Liu Y, Jin C, Liang X, Chen Q, Peng L-M. Quantitative analysis of current–voltage characteristics of semiconducting nanowires: Decoupling of contact effects. Advanced Functional Materials. 2007;**17**:2478–2489. DOI: 10.1002/adfm.200600475

[8] Arzt E. Size effects in materials due to microstructural and dimensional constraints: A comparative review. Acta Materials. 1998;**46**(16):5611–5626. DOI: 10.1016/S1359-6454(98)00231-6

[9] Duan X, Huang Y, Cui Y, Wang J, Lieber CM. Indium phosphide nanowires as building blocks for nanoscale electronic and optoelectronic devices. Nature. 2001;**409**:66–69. DOI: 10.1038/35051047

[10] Wang ZL, Song J. Piezoelectric nanogenerators based on zinc oxide nanowire arrays. Science. 2006;**312**(5771):242–246. DOI: 10.1126/science.1124005

[11] Holm JV, Jørgensen HI, Krogstrup P, Nygård J, Liu H, Aagesen M. Surface-passivated GaAsP single-nanowire solar cells exceeding 10% efficiency grown on silicon. Nature communications. 2013;**4**(1498):1–5. DOI: 10.1038/ncomms2510

[12] Cui Y, Wei Q, Park H, Lieber CM. Nanowire nanosensors for highly sensitive and selective detection of biological and chemical species. Science. 2001;**293**(5533):1289–1292. DOI: 10.1126/science.1062711

[13] Wan Q, Li QH, Chen YJ, Wang TH, He XL, Li JP, Lin CL. Fabrication and ethanol sensing characteristics of ZnO nanowire gas sensors. Applied Physics Latters. 2004;**84**(18):3654–3656. DOI: 10.1063/1.1738932

[14] Patolsky F, Lieber CM. Nanowire nanosensors. Materials Today. 2005;**8**(4):20–28. DOI: 10.1016/S1369-7021(05)00791-1

[15] Lu W, Xie P, Lieber CM. Nanowire transistor performance limits and applications. IEEE Transactions on Electron Devices. 2008;**55**(11):2859–2876. DOI: 10.1109/TED.2008.2005158

[16] Husain A, Hone J, Postma HWC, Huang XMH, Drake T, Barbic M, Scherer A, Roukes ML. Nanowire-based very-high-frequency electromechanical resonator. Applied Physics Latters. 2003;**83**(6):1240–1242. DOI: 10.1063/1.1601311

[17] Feng XL, He R, Yang P, Roukes ML. Very high frequency silicon nanowire electromechanical resonators. Nano Letters. 2007;**7**(7):1953–1959. DOI: 10.1021/nl0706695

[18] Binnig G, Quate CF, Gerber C. Atomic force microscope. Physical Review Letters. 1986;**56**:930–933. DOI: 10.1103/PhysRevLett.56.930

[19] Giessibl FJ. Advances in atomic force microscopy. Reviews of Modern Physics. 2003;**75**:949–983. DOI: 10.1103/RevModPhys.75.949

[20] Bhushan B, Fuchs H, editors. Applied Scanning Probe Methods II—Scanning Probe Microscopy Techniques. 1st ed. Germany: Springer-Verlag Berlin Heidelberg; 2006. p. 420. DOI: 10.1007/b139097

[21] Marszalek PE, Greenleaf WJ, Li H, Oberhauser AF, Fernandez JM. Atomic force microscopy captures quantized plastic deformation in gold nanowires. Proceedings of the National Academy of Sciences USA. 2000;**97**(12):6782–6786. DOI: https://www.ncbi.nlm.nih.gov/pmc/articles/PMC18594/

[22] Dobrokhotov VV, Yazdanpanah MM, Pabba S, Safir A, Cohn RW. Visual force sensing with flexible nanowire buckling springs. Nanotechnology. 2007;**19**(3):035502. DOI: 10.1088/0957-4484/19/03/035502

[23] Wu C-H, Yeh N. Electrical properties and photoresponses of silicon nanowires with selective anchored gold nanoparticles via scanning probe bond breaking nanolithography. Japanese Journal of Applied Physics. 2009;**48**(4S): 04C152. DOI: 10.1143/JJAP.48.04C152

[24] Sahin O. Harmonic Force Microscope: A New Tool for Biomolecular Identification and Material Characterization Based on Nanomechanical Measurements [dissertation]. USA: Stanford University; 2005. p. 113. Available from: https://searchworks.stanford.edu/view/6212100

[25] Beinik I. Electrical Characterization of Semiconductor Nanostructures by Conductive Probe Based Atomic Force Microscopy Techniques [dissertation]. Austria: Montanuniversität Leoben; 2011. p. 118. Available from: http://www.unileoben.ac.at/images/stories/Bibliothek/edoc/AC08511205n01vt.pdf

[26] Sadewasser S, Glatzel T, editors. Kelvin Probe Force Microscopy—Measuring and Compensating Electrostatic Forces. Germany: Springer; 2012. 334 p. DOI: 10.1007/978-3-642-22566-6

[27] Teichert C, Beinik I. Conductive atomic-force microscopy investigation of nanostructures in microelectronics. In: Bhushan B, editor. Scanning Probe Microscopy in Nanoscience and Nanotechnology 2. Germany: Springer Berlin Heidelberg; 2010. pp. 691–721. DOI: 10.1007/978-3-642-10497-8_23

[28] Wang ZL. Nanopiezotronics. Advanced Materials. 2007;**19**(6):889–892. DOI: 10.1002/adma.200602918

[29] Nakayama Y, Pauzauskie PJ, Radenovic A, Onorato RM, Saykally RJ, Liphardt J, Yang P. Tunable nanowire nonlinear optical probe. Nature. 2007;**447**:1098–1101. DOI: 10.1038/nature05921

[30] Rossi N, Braakman FR, Cadeddu D, Vasyukov D, Tütüncüoglu G, i Morral AF, Poggio M. Vectorial scanning force microscopy using a nanowire sensor. Nature Nanotechnology. 2017;**12**(2):150–155. DOI: 10.1038/nnano.2016.189

[31] US Patent 8484756 B2. Bertness KA, Sanford NA, Kabos P, Wallis TM. Tip-Mounted Nanowire Light Source Instrumentation [Internet]. 2011. Available from: https://www.google.com/patents/US8484756 [Accessed: 01.02.2017]

[32] Yang G, Tang J, Kato S, Zhang Q, Qin LC, Woodson M, Liu J, Kim JW, Littlehei PT, Park C, Zhouless O. Magnetic nanowire based high resolution magnetic force microscope probes. Applied Physics Latters. 2005;**87**(12):123507. DOI: 10.1063/1.2043237

[33] Park JJ, Reddy M, Stadler BJH, Flatau AB. Hysteresis measurement of individual multilayered Fe-Ga/Cu nanowires using magnetic force microscopy. Journal of Applied Physics. 2013;**113**(17):17A331. DOI: 10.1063/1.4795818

[34] Tabasum MR, Zighem F, Medina JDLT, Encinas A, Piraux L, Nysten B. Magnetic force microscopy investigation of arrays of nickel nanowires and nanotubes. Nanotechnology. 2014;**25**(24):245707. DOI: 10.1088/0957-4484/25/24/245707

[35] Béron F, dos Santos MVP, de Carvalho PG, Moura KO, Arzuza LCC, Pirota KR. How to characterize cylindrical magnetic nanowires. In: Khan M, editor. Magnetic Materials. Croatia: InTech; 2016. pp. 41–69. DOI: 10.5772/63482

[36] Dresselhaus MS, Lin Y-M, Rabin O, Black MR, Kong J, Dresselhaus G. Nanowires. In: Bhushan B, editor. Springer Handbook of Nanotechnology. Germany: Springer Berlin Heidelberg; 2010. pp. 119–167. DOI: 10.1007/978-3-642-02525-9_4

[37] Yang P, Yan H, Mao S, Russo R, Johnson J, Saykally R, Morris N, Pham J, He R, Choi H-J. Controlled growth of ZnO nanowires and their optical properties. Advanced Functional Materials. 2002;**12**(5):323–331. DOI: 10.1002/1616-3028(20020517)12:5<323::AID-ADFM323>3.0.CO;2-G

[38] Kim DC, Dheeraj DL, Fimland BO, Weman H. Polarization dependent photocurrent spectroscopy of single wurtzite GaAs/AlGaAs core-shell nanowires. Applied Physics Latters. 2013;**102**(14):142107. DOI: 10.1063/1.4801865

[39] Zhang Y, Wu J, Aagesen M, Liu H. III–V nanowires and nanowire optoelectronic devices. Journal Physics D: Applied Physics. 2015;**48**(46):463001. DOI: 10.1088/0022-3727/48/46/463001

[40] Mukdadi OM, Datta SK, Dunn ML. Acoustic-phonon dispersion in nanowires. Journal of Applied Physics. 2005;**97**(7):0743123. DOI: 10.1063/1.1871333

[41] McGary PD, Tan L, Zou J, Stadler BJH, Downey PR, Flatau AB. Magnetic nanowires for acoustic sensors (invited). Journal of Applied Physics. 2006;**99**(8):08B310. DOI: 10.1063/1.2167332

[42] Young ESK, Bouravleuv AD, Cirlin GE, Dhaka V, Lipsanen H, Tchernycheva M, Scherbakov AV, Platonov AV, Akimov AV, Kent AJ. Electrical detection of picosecond acoustic pulses in vertical transport devices with nanowires. Applied Physics Latters. 2014;**104**(6):062102. DOI: 10.1063/1.4864637

[43] Xie Q-Y, Ju Z-Y, Tian H, Xue Q-T, Chen Y-Q, Tao L-Q, Mohammad MA, Zhang X-Y, Yangac Y, Ren T-L. A point acoustic device based on aluminum nanowires. Nanoscale. 2016;**8**:5516–5525. DOI: 10.1039/C5NR06999H

[44] Hernández-Mínguez A, Möller M, Breuer S, Pfüller C, Somaschini C, Lazić S, Brandt O, García-Cristóbal A, de Lima Jr. MM, Cantarero A, Geelhaar L, Riechert H, Santos PV. Acoustically driven photon antibunching in nanowires. Nano Letters. 2012;**12**(1):252–258. DOI: 10.1021/nl203461m

[45] Kargar F, Debnath B, Kakko J-P, Säynätjoki A, Lipsanen H, Nika DL, Lake RK, Balandin AA. Direct observation of confined acoustic phonon polarization branches in free-standing semiconductor nanowires. Nature Communications. 2016;**7**:13400. DOI: doi:10.1038/ncomms13400

[46] Burt DP, Wilson NR, Weaver JMR, Dobson PS, Macpherson JV. Nanowire probes for high resolution combined Scanning electrochemical microscopy—atomic force microscopy. Nano Letters. 2005;**5**(4):639–643. DOI: 10.1021/nl050018d

[47] Hersam MC, Hoole ACF, O'Shea SJ, Welland ME. Potentiometry and repair of electrically stressed nanowires using atomic force microscopy. Applied Physics Latters. 1998;**72**(8):915. DOI: 10.1063/1.120872

[48] Trukhin VN, Buyskikh AS, Kaliteevskaya NA, Bourauleuv AD, Samoilov LL, Samsonenko YB, Cirlin GE, Kaliteevski MA, Gallant AJ. Terahertz generation by GaAs nanowires. Applied Physics Latters. 2013;**103**(7):072108. DOI: 10.1063/1.4818719

[49] Miao X, Chabak K, Zhang C, Mohseni PK, Walker Jr D, Li X. High-speed planar GaAs nanowire arrays with f_{max}> 75 GHz by wafer-scale bottom-up growth. Nano Letters. 2015;**15**(5):2780–2786. DOI: 10.1021/nl503596j

[50] Haggrén T. Nanowire Technology for Optoelectronic Applications [dissertation]. Finland: Aalto University; 2016. p. 76. DOI: https://aaltodoc.aalto.fi/handle/123456789/21918

[51] Bruker Inc. Application Note #132—Simultaneous Electrical and Mechanical Property Mapping at the nanoscale with PeakForce TUNA [Internet]. 2011. Available from: https://www.bruker.com/fileadmin/user_upload/8-PDF-Docs/SurfaceAnalysis/AFM/ApplicationNotes/AN132-RevA0-Simultaneous_Electrical_Mechanical_Property_Mapping_with_PeakForce_TUNA-AppNote.pdf [Accessed: 01.02.2017]

[52] Dubrovskii VG, Cirlin GE, Ustinov VM. Semiconductor nanowhiskers: Synthesis, properties, and applications. Semiconductors+. 2009;**43**(1539):1585–1628. DOI: 10.1134/S106378260912001X

[53] Rojo MM, Calero OC, Lopeandia AF, Rodriguez-Viejob J, Martín-Gonzalez M. Review on measurement techniques of transport properties of nanowires. Nanoscale. 2013;**5**:11526–11544. DOI: 10.1039/C3NR03242F

[54] Kaja K. Development of nano-probe techniques for work function assessment and application to materials for microelectronics [dissertation]. France: Université Joseph-Fourier-Grenoble; 2010. p. 221. DOI: https://tel.archives-ouvertes.fr/tel-00515370/en

[55] Chia ACE. Electrical Characterization and Optimization of Gallium Arsenide Nanowire Ensemble Devices [dissertation]. Canada: McMaster University; 2013. p. 155. DOI: https://macsphere.mcmaster.ca/handle/11375/13335

[56] LaPierre RR, Chia ACE, Gibson SJ, Haapamaki CM, Boulanger J, Yee R, Kuyanov P, Zhang J, Tajik N, Jewell N, Rahman KMA. III–V nanowire photovoltaics: Review of design for high efficiency. Physica Status Solidi Rapid Research Letters. 2013;**7**(10):815–830. DOI: 10.1002/pssr.201307109

[57] van Dam D, van Hoof NJJ, Cui Y, van Veldhoven PJ, Bakkers EPAM, Gómez Rivas J, Haverkort JEM. High-efficiency nanowire solar cells with omnidirectionally enhanced absorption due to self-aligned indium-tin-oxide Mie scatterers. American Chemical Society Nano 2016;**10**:11414−11419. DOI: 10.1021/acsnano.6b06874

[58] Malloroqui AD. Nanowire-Based Solar Cells: Device Design and Implementation [dissertation]. EPFL Lausanne: Switzerland; 2014. p. 108. DOI: https://infoscience.epfl.ch/record/196411

[59] Giordano MA, Schmidt SR. Applications of contact mode AFM to manufacturing processes. In: Bhushan B, editor. Scanning Probe Microscopy in Nanoscience and Nanotechnology 2. Germany: Springer Berlin Heidelberg; 2011. pp. 867–914. DOI: 10.1007/978-3-642-03535-7_25

[60] Tajik N. Sulfur Passivation of III–V Semiconductor Nanowires [dissertation]. Canada: McMaster University; 2013. p. 132. DOI: https://macsphere.mcmaster.ca/handle/11375/12834

[61] Werner F, Limbach F, Carsten M, Denker C, Malindretos J, Rizzi A. Electrical conductivity of InN nanowires and the influence of the native indium oxide formed at their surface. Nano Letters. 2009;**9**(4):1567–1571. DOI: 10.1021/nl8036799

[62] Lin X, He X, Lu J, Gao L, Huan Q, Deng Z, Cheng Z, Shi D, Gao H. Manipulation and four-probe analysis of nanowires in UHV by application of four tunneling microscope tips: a new method for the investigation of electrical transport through nanowires. Surface and Interface Analysis. 2006;**38**(6):1096–1102. DOI: 10.1002/sia.2333

[63] Timm R, Persson O, Engberg DLJ, Fian A, Webb JL, Wallentin J, Jönsson A, Borgström MT, Samuelson, Mikkelsen A. Current–voltage characterization of individual as-grown nanowires using a scanning tunneling microscope. Nano Letters. 2013;**13**(11):5182–5189. DOI: 10.1021/nl402570u

[64] Lord AM, Walton AS, Maffeis TG, Ward MB, Davies P, Wilks SP. ZnO nanowires with Au contacts characterised in the as-grown real device configuration using a local multi-probe method. Nanotechnology. 2014;**25**(42):425706. DOI: 10.1088/0957-4484/25/42/425706

[65] Geydt P, Alekseev PA, Dunaevskiy M, Lähderanta E, Haggrén T, Kakko J-P, Lipsanen H. Observation of linear I–V curves on vertical GaAs nanowires with atomic force microscope. Journal of Physics: Conference Series. 2015;**661**(1):012031. DOI: 10.1088/1742-6596/661/1/012031P

[66] Geydt P, Alekseev PA, Dunaevskiy MS, Haggrén T, Kakko J-P, Lähderanta E, Lipsanen H. Influence of surface passivation on electric properties of individual GaAs nanowires studied by current–voltage AFM measurements. Lithuanian Journal of Physics. 2016;**46** (2):92–101. DOI: 10.3952/physics.v56i2.3305

[67] Ellis JA, Barnes PA. Current–voltage characteristics of a GaAs Schottky diode accounting for leakage paths. Applied Physics Latters. 1999;**76**(1):124. DOI: 10.1063/1.125677

[68] Suyatin DB, Jain V, Nebol'sin VA, Trägårdh J, Messing ME, Wagner JB, Persson O, Timm R, Mikkelsen A, Maximov I, Samuelson L, Pettersson H. Strong Schottky barrier reduction at Au-catalyst/GaAs-nanowire interfaces by electric dipole formation and fermi-level unpinning. Nature Communications. 2014;**5**(3221):1–8. DOI: 10.1038/ncomms4221

[69] Darbandi A, Salehzadeh O, Kuyanov P, La Pierre RR, Watkins SP. Surface passivation of tellurium-doped GaAs nanowires by GaP: Effect on electrical conduction. Journal of Applied Physics. 2014;**115**(23):234305. DOI: 10.1063/1.4883960

[70] Dementyev PA, Dunaevskii MS, Samsonenko YB, Cirlin GE, Titkov AN. Current-voltage characteristics of silicon-doped GaAs nanowhiskers with a protecting AlGaAs coating overgrown with an undoped GaAs layer. Semiconductors+. 2010;**44**(5):610–615. DOI: 10.1134/S1063782610050118

[71] Morita S. Roadmap of Scanning Probe microscopy. 1st ed. Germany: Springer-Verlag Berlin Heidelberg; 2007. p. 201. DOI: 10.1007/978-3-540-34315-8

[72] Melitz W, Shen J, Kummel AC, Lee S. Kelvin probe force microscopy and its application. Surface Science Reports. 2011;**66**(1):1–27. DOI: 10.1016/j.surfrep.2010.10.001

[73] Li G, Mao B, Lan F, Liu L. Practical aspects of single-pass scan Kelvin probe force microscopy. Review of Scientific Instruments 2012;**83**(11):113701. DOI: 10.1063/1.4761922

[74] Prokhor AA. Investigation of Charge and Electric Field Distribution in Nanostructures by Scanning Probe Microscopy (in Russian) [dissertation]. Russian Federation: LETI; 2013. p. 159. Available from: http://fizmathim.com/issledovanie-raspredeleniya-zaryadov-i-

elektricheskih-poley-v-pribornyh-nanostrukturah-metodami-skaniruyuschey-zondovoy-m DOI: http://search.rsl.ru/ru/record/01005535363

[75] Dunaevskiy M, Alekseev P, Girard P, Lashkul A, Lahderanta E, Titkov A. Analysis of the lateral resolution of electrostatic force gradient microscopy. Journal of Applied Physics. 2009;**112**(6):064112. DOI: 10.1063/1.4752430

[76] Hong KM, Noolandi J, Street RA. Theory of radiative recombination by diffusion and tunneling in amorphous Si: H. Physical Review B. 1981;**23**(6):2967. DOI: 10.1103/PhysRevB.23.2967

[77] He R, Gao D, Fan R, Hochbaum AI, Carraro C, Maboudian R, Yang P. Si Nanowire bridges in microtrenches: Integration of growth into device fabrication. Advanced Materials. 2005;**17**(17):2098–2102. DOI: 10.1002/adma.200401959

[78] Yong Oh J, Park J-T, Jang H-J, Cho W-J, Islam MS. 3D-transistor array based on horizontally suspended silicon nano-bridges grown via a bottom-up technique. Advanced Materials. 2014;**26**(14):1929–1934. DOI: 10.1002/adma.201304245

[79] Shi C, Luu DK, Yang Q, Liu J, Chen J, Ru C, Xie S, Luo J, Ge J, Sun Y. Recent advances in nanorobotic manipulation inside scanning electron microscopes. Microsystems & Nanoengineering. 2016;**2**(16024):1–16. DOI: 10.1038/micronano.2016.24

[80] Qin S, Kim T-H, Wang Z, Li A-P. Nanomanipulation and nanofabrication with multi-probe scanning tunneling microscope: From individual atoms to nanowires. Review of Scientific Instruments. 2012;**83**(6):063704. DOI: 10.1063/1.4727878

[81] Wang ZL, Gao RP, Pan ZW, Dai ZR. Nano-scale mechanics of nanotubes, nanowires, and nanobelts. Advanced Engineering Materials. 2001;**3**(9):657–661. DOI: 10.1002/1527-2648(200109)3:9<657::AID-ADEM657>3.0.CO;2-0

[82] Barth S, Harnagea C, Mathur S, Rosei F. The elastic moduli of oriented tin oxide nanowires. Nanotechnology. 2009;**20**(11):115705. DOI: 10.1088/0957-4484/20/11/115705

[83] Chen CQ, Shi Y, Zhang YS, Zhu J, Yan YJ. Size dependence of young's modulus in ZnO nanowires. Physical Review Letters. 2006;**96**:075505. DOI: 10.1103/PhysRevLett.96.075505

[84] Wang B, Stevens E, Leu PW. Strong broadband absorption in GaAs nanocone and nanowire arrays for solar cells. Optics Express. 2014;**22**(S2):A386–395. DOI: 10.1364/OE.22.00A386

[85] Alekseev PA, Dunaevskii MS, Stovpyaga AV, Lepsa M, Titkov AN. Measurement of Young's modulus of GaAs nanowires growing obliquely on a substrate. Semiconductors+. 2012;**46**(5):641–646. DOI: 10.1134/S106378261205003X

[86] Geydt P, Dunaevskiy M, Alekseev P, Kakko J-P, Haggrén T, Lähderanta E, Lipsanen H. Direct measurement of elastic modulus of InP nanowires with Scanning probe microscopy in PeakForce QNM mode. Journal of Physical: Conference Series. 2016;**768**(1):012029. DOI: 10.1088/1742-6596/769/1/012029

[87] Gere JM, Goodno BJ. Mechanics of Materials. 8th ed. Stamford, USA: Cengage Learning; 2013. p. 1098. DOI: http://trove.nla.gov.au/version/185463313

[88] Wachtman Jr JB, Tefft WE, Lam Jr DG, Apstein CS. Exponential temperature dependence of Young's modulus for several oxides. Physical Reviews. 1961;**122**(6):1754. DOI: 10.1103/PhysRev.122.1754

[89] Dokukin ME, Sokolov I. Quantitative mapping of the elastic modulus of soft materials with Harmonix and PeakForce QNM AFM modes. Langmuir. 2012;**8**(46):16060–16071. DOI: 10.1021/la302706b

[90] Xu F, Qin Q, Mishra A, Gu Y, Zhu Y. Mechanical properties of ZnO nanowires under different loading modes. Nano Research. 2010;**3**(4):271–280. DOI: 10.1007/s12274-010-1030-4

[91] Espinosa HD, Bernal RA, Minary-Jolandan M. A review of mechanical and electromechanical properties of piezoelectric nanowires. Advanced Materials. 2012;**24**(34):4656–4675. DOI: 10.1002/adma.201104810

[92] Wang ZL. Triboelectric nanogenerators as new energy technology and self-powered sensors—principles, problems and perspectives. Faraday Discuss. 2014;**176**:447–458. DOI: 10.1039/C4FD00159A

[93] Lin Y-F, Song J, Ding Y, Lu S-Y, Wang ZL. Alternating the output of a CdS nanowire nanogenerator by a white-light-stimulated optoelectronic effect. Advanced Materials. 2008;**20**:3127–3130. DOI: 10.1002/adma.200703236

[94] Song J, Wang X, Liu J, Liu H, Li Y, Wang ZL. Piezoelectric potential output from ZnO nanowire functionalized with p-type oligomer. Nano Letters. 2008;**8**(1):203–207. DOI: 10.1021/nl072440v

Chapter 9

Diluted Magnetic DNA Nanowires

Caner Değer, Vahap Eldem and İzzet Paruğ Duru

Additional information is available at the end of the chapter

http://dx.doi.org/10.5772/67921

Abstract

DNA, as a natural biological nanowire, could be modified by inorganic atoms, either conducting or semi-conducting ones, to render feasible for technological applications and sequencing. Magnetic phase transition of modified DNA (M-DNA) nanowire, similar to diluted magnetic semiconductor (DMS) materials, occurs by changing parameters such as temperature and doping ratio having critical values. Tuning such parameters provide a pleasant control about determination of the magnetic property of M-DNA, particularly room-temperature soft ferromagnetism. In this chapter, a fundamental theory for anti-ferromagnetic Cr^{3+}-doped M-DNA nanowire named as diluted magnetic organic structures (DMOS) is tried to figure out the interactions representing the exotic behaviour of these type of organometallics. However, authors detailed preparation of nanowire as a global input and overall procedure of simulation based on Markov chain Monte Carlo (MCMC) method.

Keywords: DMOS, M-DNA, dipolar Interaction, hysteresis, organic nanowire, MCMC

1. Introduction

With unique structural features and self-assembly nature, deoxyribonucleic acid (DNA) has long been considered as ubiquitous bionanomaterials. The unique structural patterns and dynamic behaviours of DNA mainly arise from hydrogen bonds between purine and pyrimidine bases which are fundamental building blocks in double helix. Moreover, the editable, modifiable, scalable, and controllable natures of polynucleotides make synthetic DNA an attractive material for several applications at the nanoscale fields, including optoelectronics [1], spintronics [2], nanophotonics [3], nanobiosensors [4, 5] and even data storages such as nucleic acid memory. On the other hand, despite all these advantages, optical, electronic and magnetic properties of bare DNA are not suitable for such applications. Therefore, by doping DNA with divalent metal ions (Cu^{2+}, Ni^{2+}, Zn^{2+}, and Co^{2+}), called "modified DNA (M-DNA)", it is possible to tailor or control the magnetic and electrical properties of DNA. Besides, changing magnetic property of DNA via selective incorporation of metal ions between purine-pyrimidine pairs and hydrogen bonds not only provides a tunable material but also gives a clue about the location of bases. However, Hu et al. [6] investigated the electronic and magnetic properties of graphene and Fe and probe the DNA bases adsorbed by first-principal calculations theoretically to detect DNA bases. As a matter of fact, researchers recently focused on conceiving magnetic properties of M-DNA nanowires even though Azbel [7] derived an explicit formula that provides the consistency of theory and experiments while studying phase transitions in DNA. Alivisatos et al. [8], Mirkin et al. [9], and Braun et al. [10] were the first researchers who studied DNA-templated self-assembly, followed by Richter et al. [11], Park et al. [12] and Keren et al. [13]. Fabrication of DNA nanowires extend the field of workspace generated by organic structures. Park et al. [12] studied detection of nucleic acids with high sensitivity and specificity. Besides fabrication of DNA nanowires, band-gap effects on temperature-dependent magnetism of DNA molecules have been evaluated by Yi [14]. On the other hand, Savin et al. [15] described the thermal properties of DNA, especially heat conductivity of the DNA double helix, constructing a 3D coarse-grain (CG) model. Therefore, some studies have been carried out to reveal magnetic properties of M-DNA, both theoretically and experimentally. Electronic states of metal ion-doped M-DNA (m is Mn, Ni, Mg, Co and Fe) are figured out by optical absorption concluding charge transfer from Fe^{2+} to DNA and transferred charges should be positioned close to bases [16]. Computational models are properly developed to investigate the electrical conduction in DNA nanowires by Panahi and Chitsazanmoghaddam [17] and Behnia and Fathizadeh [18]. The studies performed by Dugasani et al. [19] and Nikiforov et al. [20] discovered that divalent metal ion–doped DNA exhibits soft ferromagnetic (FM) behaviour. Both of the studies claim that the origin of the soft ferromagnetic behaviour is the interaction between doped ions. Long-range interactions have also been proposed as the cause of room-temperature ferromagnetism in M-DNA. On the other hand, a comprehensive theoretical study proposed a new type of Hamiltonian approach suggesting both inorganic and organic structures including M-DNA nanowires [21]. One of the significant terms of Hamiltonian indicates exchange interaction, the ferromagnetic or anti-ferromagnetic interaction between atoms. The effect of ion concentration on the system was investigated to determine the proper ratio for technological applications. The result of the study is also compatible with experimental studies.

2. Constructing modified DNA nanowires

In this section, a simple workflow is introduced for construction of the modified DNA structure doped by a metal ion (Cr^{3+}) to investigate magnetic properties, especially soft ferromagnetism related to doping ratio. Firstly, a set of gene sequences should be designated as a sample group considering the guanine-cytosine (G-C)% content and base composition herewith sequence length. It is important to know the base composition of DNA and the number of hydrogen bounds since dopant ion is replaced with hydrogen atoms. After the determination of sample group (base sequences), base pairs containing organic atoms will be converted to a 3D structure by assigning atomistic coordinates of atoms in Euclidian space. van Dijk and Bonvin [22] developed a model to produce atomistic coordinates with connections of atoms from the singe base sequence of a gene in the mentioned coordinate space using reasonable parameters. The key parameters are roll, tilt and twist during the modelling procedure combined with each other. By the usage of 3D DART modelling tool [23], resulting DNA helical was ready to be modified by a dopant ion. Doping process is required to start after the successful finish of former work. Dugasani et al. [19] suggested the most probable locations of subsequent dopant ions between base pairs and PO4, and at last, the random displacement of dopants instead of hydrogen atoms of N-H-N and N-H-O.

2.1. Preparation of the sample group

G-C base pair has three electrostatic hydrogen bonds between nitrogen and oxygen atoms, while adenine-thymine (A-T) base pairs are connected to each other via two hydrogen bonds in the Watson-Crick model. Duru et al. [21] doped a number of genes with length of 1000 bases whose G-C ratio ranged from 40.8 to 69.5%. Sample group prepared has hydrogen bonds between the G and C bases ranging from 1124 to 2085 and the ratio of A to T content ranging from 610 to 1184. Authors prepared a sample group having different genes and G-C contents to re-simulate the M-DNA. The sample sequences of DNA (1000 bases) in length were obtained from Ensembl Genome browser (www.ensembl.org). Detailed information about the base composition of selected genes is presented in **Table 1**.

2.2. Atomistic structure of DNA

Polynucleotide chains constitute DNA by helical circling which is either right handed or left handed. As the most common form, B-DNA is right handed. There are a major groove and a minor groove through the outer region, respectively. Yet another right-handed helical A-DNA is a more congested molecule. Contrary to A-DNA and B-DNA, Z-DNA is a left-handed helical DNA. Base pairs are seen as zigzags. Moreover, helical structure forms a deep indentation instead of two. The Watson-Crick model, B-DNA, is considered as the normal form. The model is for the damp form due to the high water activity in vivo. That model has 10 base pairs per turn of the double helix, with a rise of 3.4 Å/bp [24], and A-DNA has 11 base pairs per turn and a rise of 2.6 Å/bp [25]. **Table 2** compares some properties of A-DNA, B-DNA and Z-DNA.

Sequences of all genes of the sample group should be used to visualize the atomic coordinates using U-GENE (free open-source cross-platform) separately (can be downloaded from http://ugene.net/). All of the atoms have the same spherical geometry. First, distances between the first 10 nearest neighbours of all atoms in DNA are calculated to provide a reasonable process time during simulation. van Dijk et al. [22] proposed a method to generate a canonical structure including atomic positions of A-DNA and B-DNA. The modelling procedure is clearly detailed in their work. B-DNA should be preferred for simulation process due to the most observed structural form of bare DNA in vivo.

Gene name	Length (bp)	A (%)	T (%)	G (%)	C (%)	%GC	M.W. (Da)
ADGB[a]	1000	32.8	26.4	17.1	23.7	40.8	312,051
AGRN[b]	1000	15.1	15.4	34.7	34.8	69.5	312,177
AK1[c]	1000	25	18.2	24.2	32.6	56.8	313,148
ALB[d]	1000	29.2	28.2	19.8	22.8	42.6	311,340
FOXA1[e]	1000	19.7	13	35.5	31.8	67.3	311,793
MFN1[f]	1000	30.3	27.4	17.6	24.7	42.3	312,046
PODN[g]	1000	21	17.3	33.5	28.2	61.7	311,130
SMOX[h]	1000	21.9	18.8	29.2	30.1	59.3	311,944
SMTN[j]	1000	21.2	14.1	33.4	31.3	64.7	311,929
TESK1[k]	1000	18.6	18.8	31.1	31.5	62.6	311,883

[a] androglobin
[b] agrin
[c] adenylate kinase 1
[d] albumin
[e] forkhead box A1
[f] mitofusin 1
[g] podocan
[h] spermine oxidase
[j] smoothelin
[k] testis-specifc kinase 1 [21].

Table 1. List of genes with different base compositions and molecular weights (M.W.).

	A-DNA	B-DNA	Z-DNA
Helix sense	right-handed	right-handed	left-handed
Repeating unit	1	1	2
Rotation/bp	32.7°	34.3°	60°/2
Inclination of bp to axis	+19°	−1.2°	−9°
Rise/bp along axis	0.26 nm	0.34 nm	0.37 nm
Rise/turn of helix	2.86 nm	3.57 nm	4.56 nm
Mean propeller twist	+18°	+16°	0°
Nucleotide phosphate to phosphate distance	0.59 nm	0.70 nm	C: 0.57 nm, G: 0.61 nm
Diameter	2.3 nm	2.0 nm	1.8 nm

Table 2. Comparing geometries of A-DNA, B-DNA and Z-DNA.

Figure 1 shows A-T and G-C base pairs, including base atoms having spherical geometry and bounds roughly. Furthermore, the flow diagram of the distance calculated between nearest neighbours is given by **Figure 2**. Finalization process of preparing input data would be followed by the doping process explained in the next section.

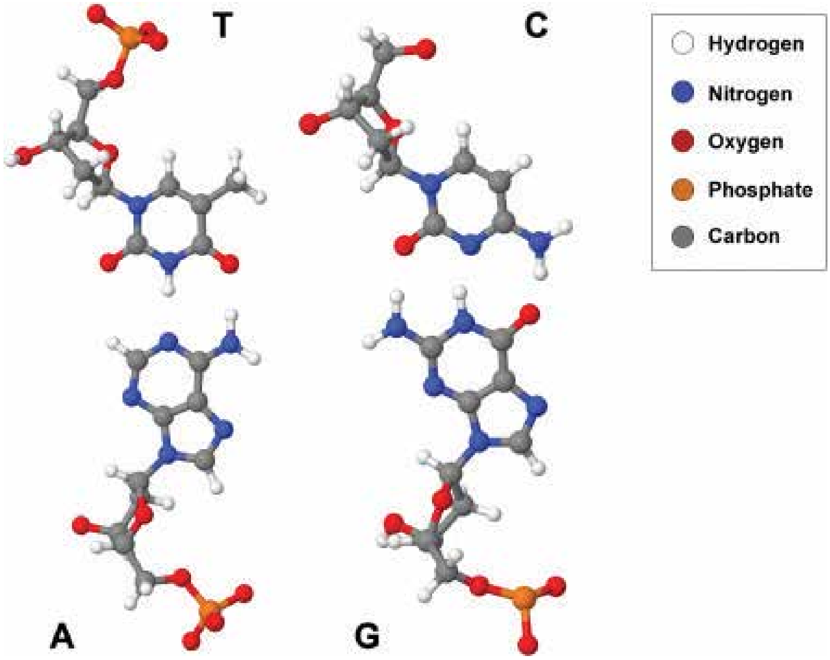

Figure 1. A molecular structure of A-T and C-G base pairs.

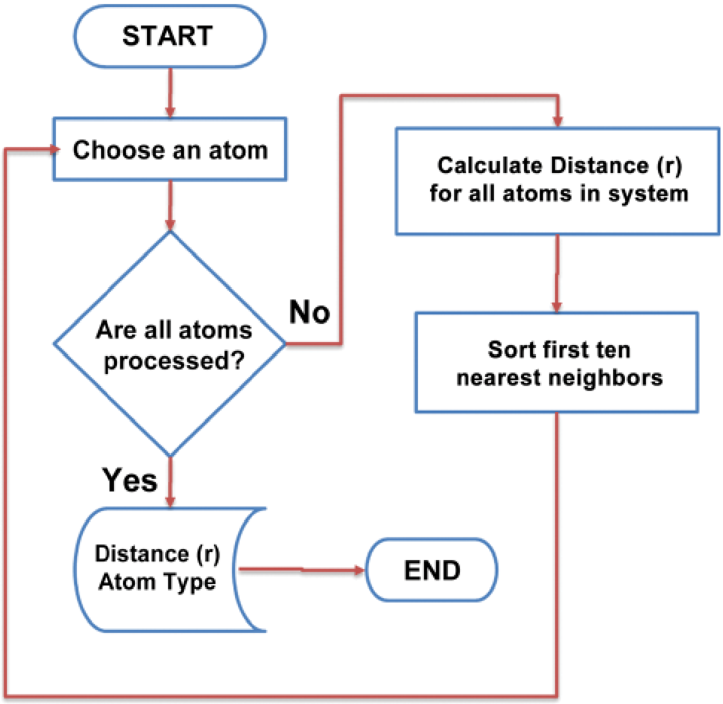

Figure 2. A flow diagram of first 10 nearest neighbours' distance calculation.

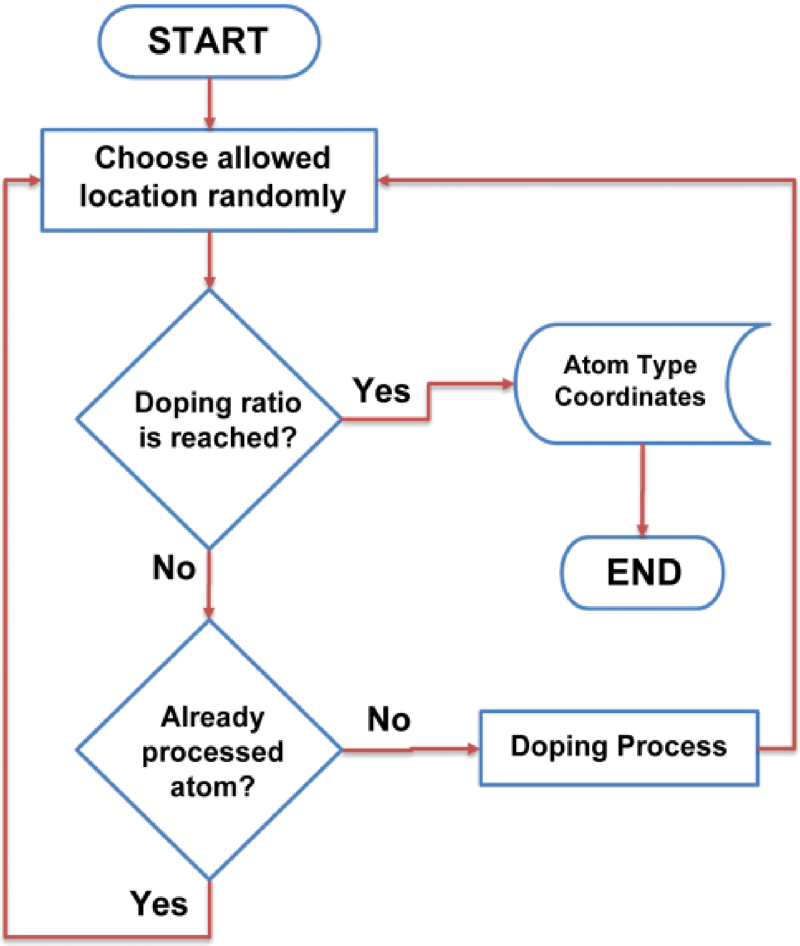

Figure 3. A flow diagram of doping process.

2.3. Doping process

The dopant ions are distributed to DNA almost randomly assuming that the binding probabilities of the dopant to G-C, A-T and $(PO^4)^-$ are similar (33%) in contrast to Dugasani et al. [19].

The number of hydrogen atoms that connects base pairs affects the magnetic phase of M-DNA by changing concentration of metal ions doped to B-DNA [26, 27]. Selection of DNA bases will be investigated and is based on G-C ratio since it includes three hydrogen atoms, while A-T has two bounds of hydrogen. Therefore, G-C ratio of selected DNA is changing from 40.8 to 69.5% to reveal the effect of G-C ratio on doping process and magnetic behaviour.

In the light of recent experimental studies [26–30], dopant ions have different probabilities on where they will bind. **Figures 4** and **5** illustrate the highest probabilities of Cr^{3+} positioning through the DNA helical structure. Hydrogen bind N-N or N-O or N-C atoms existed on the inner edge of pairs of helical structure and have critical importance since researchers mainly say that dopant ion is actually replaced by hydrogen. So, Cr^{3+}ions are located instead of hydrogen binding to a base pair randomly during doping process for a desired value of doping ratio. Flow diagram in **Figure 3** shows the doping process precisely. In **Figure 4**, dash circles represent the probable positions of doped ion, removing relevant hydrogen in G-C and A-T pair, respectively. Also, dopant ion Cr^{3+} binds to phosphate, as illustrated in **Figure 5**. There are probable positions where dopant ions will be located. It is thought that unbounded oxygen of phosphate holds on to the dopant ion according to Dugasani et al. [19]. Other transition metals (Mn, Fe, Co, Ni and Cu) can be doped to DNA, and they can show ferromagnetic behaviour [19, 26].

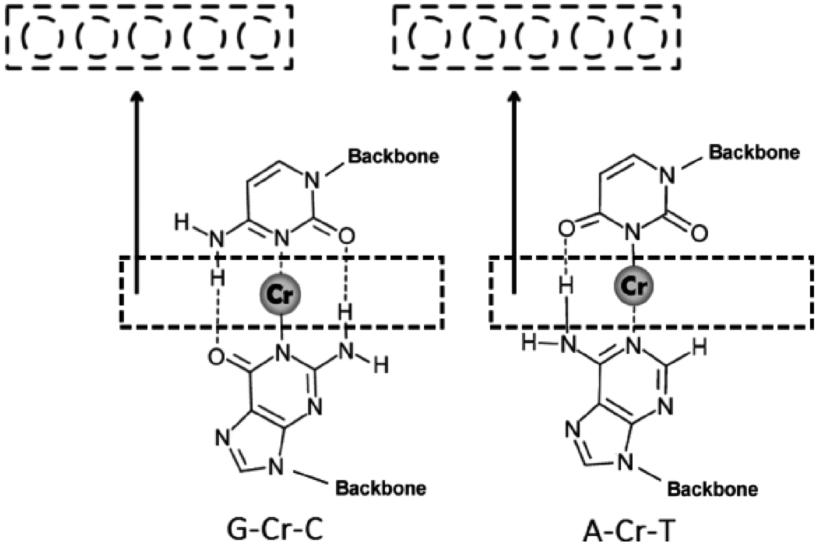

Figure 4. An illustration of probable positions of dopant Cr located instead of hydrogen atom. Dashed circles indicate the possible locations, while grey circle is the most probable one between G-C and A-T base pairs.

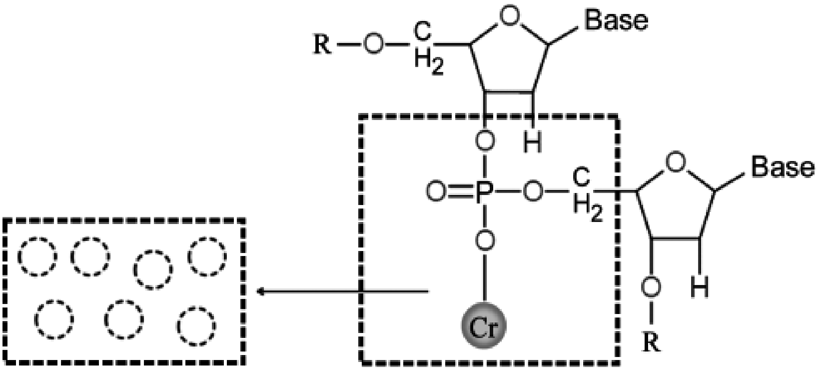

Figure 5. An illustration of probable positions of dopant Cr binding to $(PO_4)^-$. Dashed circles indicate the possible locations, while the grey circle is the most probable one.

3. Simulating the hysteresis

The relationship between applied magnetic field and magnetization is generally explained by using hysteresis loops in solid state physics. A detailed investigation of the hysteresis loop gives immense information about magnetic properties of the material. Saturation magnetization (M_S), described as the maximum value of the magnetization achieved in a sufficiently large magnetic field, can be determined from hysteresis loop. Also, remanent magnetization (M_R), the magnetization that remains in a material when the magnetizing force is zero, and coercive field (H_C), the amount of reverse magnetic field that has to be applied to make the magnetization return to zero, are indicated by hysteresis loop.

Initially, every domain in a ferromagnetic material has an intense magnetization but the whole material is generally unmagnetized because all of the domains are randomly oriented with respect to one another in the absence of magnetic field. The only need is a small external magnetic field to observe ferromagnetism phenomenon. This small magnetic field can cause the magnetic domains to line up with each other and parallel to external magnetic field, the material is now said to be magnetized. In contrast to paramagnets, ferromagnets tend to stay magnetized even if external magnetic field is removed. This tendency is called as "hysteresis". Saturation magnetization, remanent magnetization and coercive field can be viewed in a "*hysteresis loop*" as in **Figure 6**.

3.1. Dipolar Heisenberg Hamiltonian

DNA nanowire is fixed on a glass substrate, and bases adenine, thymine, cytosine and guanine are formed by H, C, O, N, P and dopant Cr^{3+} repeated through z direction in cylindrical coordinates during the simulation process. Glass is chosen because of its non-magnetic property to prevent any external magnetic contribution from another structure except the M-DNA structure since precision in measurement is important. However, doping process affected positions to be changed with little shifts by some perturbations to preserve considerable symmetry and prevent the fall to pieces of the including atoms. The Hamiltonian of the system is described by:

$$\mathcal{H} = -\sum_{<i,j>} J_{\alpha\beta}\left(r_j - r_i\right) S_i^{\alpha} S_j^{\beta} + D \sum_{<i,k>} \left[\frac{S_i^{\alpha} S_k^{\beta}}{r_{ik}^3} - \frac{3\left(S_i^{\alpha} r_{ik}\right)\left(S_k^{\beta} r_{ik}\right)}{r_{ik}^5}\right] - \mu_B g \sum_i B_{\alpha} S_i^{\alpha} \qquad (1)$$

where $J_{\alpha\beta}$ is the exchange coupling constant, B_α ($\alpha = 0$) is the magnetic field applied along the z-direction, μ_B is the Bohr magneton, and g is the gyromagnetic ratio. α is set to zero to apply external uniform magnetic field through –z direction. The exchange term due to uniqueness and "sole" importance while explaining the strange nature of diluted magnetic semiconductor (DMS) structures is required to be assimilated. This term dipolar Heisenberg Hamiltonian represents the exchange interaction and is related to the distance and type of atoms. It is calculated by summing up nearest neighbours over the whole existed atoms in the system. Theory of diluted magnetic organic structures (DMOS) will be detailed in the next section. The second term factorized by D represents the magnetic dipolar interaction. Even though it can be considered as irrelevant to the subject of chapter, dipole-dipole interaction is also critical to the understanding of magnetic dipoles in optical lattices. The significance of dipolar interac-

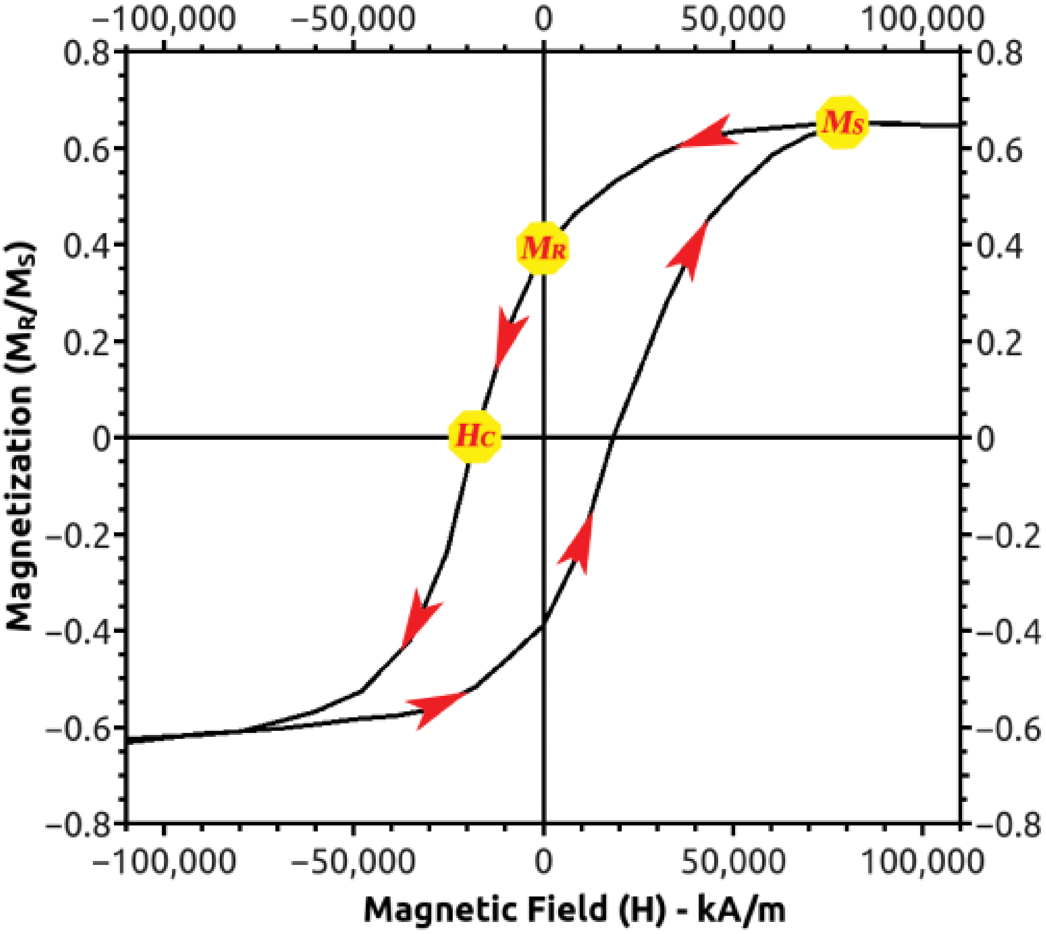

Figure 6. A schematic representation of the hysteresis loop belonging to a ferromagnetic material at a certain temperature (T). H_c= 20,000 (kA/m) and normalized remanent magnetization M_R=0.4.

tion in this theory is intrinsically balancing exchange energy to keep the essence of DMOS dialectic. Finally, the time comes up to talk about the last term, Zeeman energy. The effect of the external field is implicated as the Zeeman energy term by choosing an easy axis for the applied magnetic field. Heisenberg Hamiltonian, as a well-known Hamiltonian, is widely and greatly studied not only in modelling magnetic systems but also there is a distinct scientific "accent" in this theory named diluted magnetic organic structures based on the DMS theory mentioned in [31].

3.2. Theory of diluted magnetic organic structures

Theory of DMOS consists of two basic emphasis on the base of exchange interaction between first 10 nearest neighbours of A, T, C and G atoms in M-DNA helical. First is about the distance-dependent behaviour which means that effect of $J_{\alpha\beta}$ will decrease when distance between interacting neighbours increase. $J_{\alpha\beta} \propto \frac{\delta}{r}$; δ is any positive scalar. The other is that the major assumption of the theory provides a fundamental essence diverging from superexchange (Kramers-Anderson superexchange), Ruderman–Kittel–Kasuya–Yosida (RKKY) and similar ones. Even if the former can be easily understood, one can deal with the second to perceive it properly. The coupling strength of the atoms between the ions and organic atoms is scaled to the ion-ion coupling strength. That was so fast. Let us start again. Consider an exchange interaction that exists between a random determined X (C, H, O, N, P and Cr^{3+}) and Y (C, H, O, N, P and Cr^{3+}). If X and Y are both Cr^{3+}, the interaction type will be anti-ferromagnetic. However, if X and Y are both organic atoms, $J_{\alpha\beta}$ will vanish because extra soft magnetic contribution by organic atoms should be neglected. Lastly, if X (Y) is organic and Y (X) is Cr^{3+}, they will interact as ferromagnetic. Eq. (2) formulizes the mentioned assumption clearly.

$$J_{\alpha\beta}(r) = \begin{cases} -1 & \alpha = \beta = Cr \\ 0 < J(r) \ll 1 & \alpha = Cr,\ \beta = organic \\ 0 & \alpha = organic,\ \beta = organic \end{cases} . \quad (2)$$

According to a theory, the FM interaction between AFM Cr^{3+} ions and organic atoms, besides $J_{\alpha\beta,}$ vanishes for the organic type of atoms. Furthermore, the system will be aware of the anti-ferromagnetic interaction between Cr^{3+}ions. Actually, Duru et al. [21, 31] proposed a very similar method for the interacting atoms of diluted magnetic semiconductors.

In order to investigate effect of interactions between Cr-Cr and Cr-X (X = C, P, H, N and O) ions on magnetic behaviour, the authors have tried different J-coupling constants. During the simulation process, a reasonable exchange coupling constant between the above-mentioned atoms is traced. The aim is providing consistent characteristic results of the experimental studies.

3.3. MCMC simulation method

Markov chain Monte Carlo (MCMC) simulation method based on the metropolis algorithm is explained by defining an organic lattice introduced is Section 2. Metropolis algorithm [32] uses a transition probability related to energy difference between the first and trial state generated randomly. The ordered structured is formed by Monte Carlo method and also is stochastic due to the nature of the methodology. This time-dependent behaviour is defined by a basic equation in stochastic models like Ising model [33]. Eq. (3) shows:

$$\frac{\partial P_n(t)}{\partial t} = -\sum_{n \neq m} \left[P_n(t) W_{n\to m} - P_m(t) W_{m\to n} \right] \quad (3)$$

Actually, P_n is the probability of the state n at a known finite temperature, t and energy E_n.

$$P_n(t) = \frac{e^{-\frac{E_n}{k_B T}}}{Z} \quad (4)$$

Z denotes the partition function. $W_{n\to m}$ represents the transition probability from state n to state m. In the balance condition, $P_n(t) W_{n\to m} = P_m(t) W_{m\to n}$ will be valid since $\frac{\partial P_n(t)}{\partial t} = 0$. It is known as "detailed balance" [34]. Since it is hard to defeat the problem of partition function Z, one should construct a Markov chain [35]: The new state will be generated by the former state.

Therefore, Z became unnecessary and

$$\frac{P_n(t)}{P_m(t)} = \frac{e^{-\frac{E_n}{k_BT}}}{e^{-\frac{E_m}{k_BT}}} = e^{-\frac{E_n-E_m}{k_BT}} \tag{5}$$

$$\Delta E = E_n - E_m \tag{6}$$

Any transition probability agreed with detailed balance should be accepted. The first selection probability in statistical physics is the metropolis algorithm.

$$W_{m\to n} = \begin{cases} \frac{1}{\tau} e^{-\frac{\Delta E}{k_BT}}, & \Delta E > 0 \\ \frac{1}{\tau}, & \Delta E < 0 \end{cases} \tag{7}$$

τ, denotes the time which is required for a spin flip. Besides the ordinary Monte Carlo, it is transformed to a transition probability to avoid the partition function and in a natural way to take us to a well-known form, Markov chain. Expectation value of an observable A should be calculated by $< A > = \sum_n^N A_n P_n$. However, mean value of magnetization can be easily calculated by $< M > = \frac{1}{N} \sum_i^N S_i$. Flow diagram details the simulation process explicitly, which is shown in **Figure 7**. First, a random atom of the M-DNA nanowire is selected to calculate its energy as described by dipolar Hamiltonian. Second, this step is followed by determining a random magnetic moment of the relevant atom in 3D vector space. Simulation world is calling this state as a trial state. Once again, an energy calculation via to trial state is performed to determine the difference between the trial and former one. Then, the system can decide the

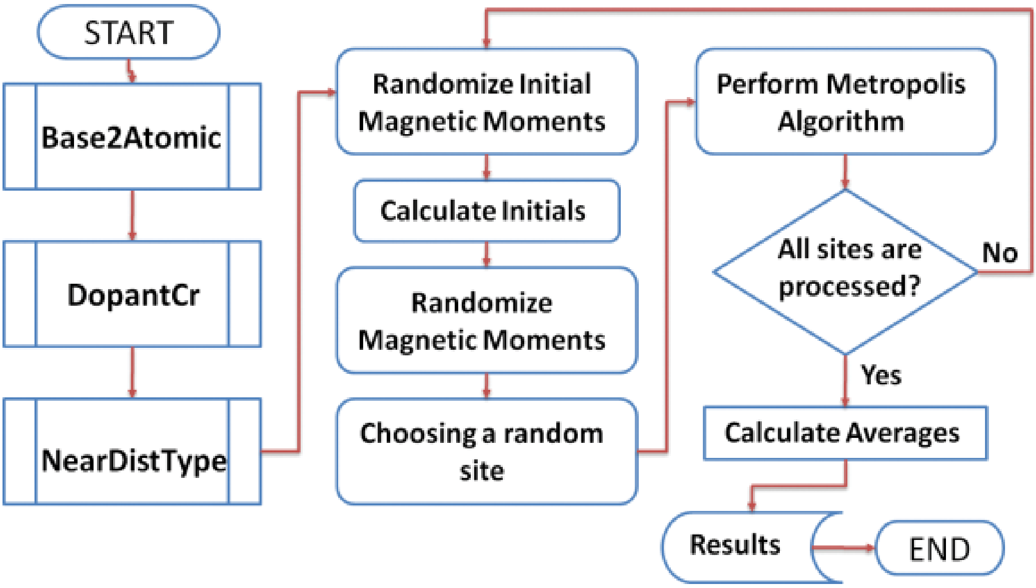

Figure 7. A flow diagram of the simulation process.

new state that will be exist according to the minimization of the energy ($\Delta E < 0$). What if the energy difference is bigger than zero? The answer is Boltzmann statistics. If $\Delta E > 0$, a pseudo random number will be generated and compared with $e^{-\frac{\Delta E}{k_B T}}$. If random number is bigger than $e^{-\frac{\Delta E}{k_B T}}$, trial state will be the new state. In this equation, beta is the inverse temperature included in Boltzmann factor k_B.

4. Magnetic measurements

Magnetic behaviour of materials strongly depends on temperature. Even if magnetic moments are coupled to each other in ferromagnetic materials, thermal agitations can cause random alignment of the magnetic moments in certain temperatures. The thermal agitations tend to keep the atomic moments pointed at random. The result is only partial alignment in the field direction and therefore a small positive susceptibility. The effect of an increase in temperature is an increase of the randomizing effect of thermal agitation that decreases the susceptibility. There is a maximum temperature for all ferromagnets for the disappearance of ferromagnetic property as a result of thermal energy. This critical temperature is called as "Curie temperature". Thermal agitation becomes dominant compared to molecular field upward of Curie temperature. For example, Curie temperatures of iron and cobalt are 1043 and 1400 Kelvin, respectively. Thermal stability of a magnetic material is required to use the material in technological applications. Therefore, determining magnetic properties of a material in different temperatures is the crucial point for the material being a candidate for technological purposes. For our case, room temperature ferromagnetism is the subject so hysteresis loops are measured at room temperature. Magnetization-temperature (M-T) graphs and hysteresis curves of M-DNA can be found in this topic.

4.1. Magnetization-temperature

Two modes are possible for M-T measurements: Zero field cooling (ZFC) and field cooling (FC). In ZFC, the sample is cooled without any applied magnetic field to the desired temperature. Then, the data are collected while heating with certain value of applied magnetic field. In FC, the sample is cooled with some applied magnetic field to the desired temperature. Then, the temperature is increased in the same applied magnetic field. The data can be collected while either the cooling or heating process. The field cooling magnetization-temperature measurement of various samples of M-DNA can be found in **Figures 8** and **9**.

Duru et al. [31] proposed a decrement in the remanent magnetization of the system at temperature $k_B T = 0.01$, from $x = 0.15$ to 0.30, which can be seen in **Figure 8**. The magnetic behaviour of the system strongly depends on the doping ratio (x) because of changing the number of ferromagnetic interactions between the atoms. When a doped atom has all host atomic neighbours, the amount of ferromagnetic coupling for the interacting doped host atoms reaches a maximum. In contrast, decreasing the number of doped-host neighbours and increasing the number of doped-doped neighbours cause the disappearance of ferromagnetism. At the same time, thermal agitations play a well-known role in magnetic systems, especially providing disordered states. A detailed discussion about the effect of doping ratio will be carried out with the information provided by hysteresis curves in the next topic.

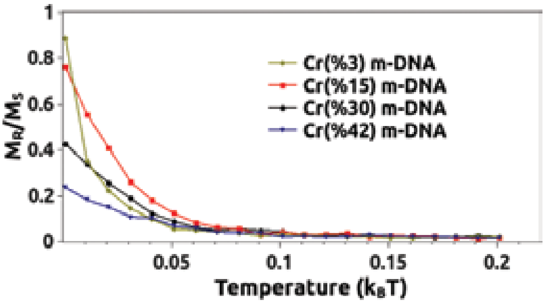

Figure 8. FC of Cr-doped DNA with different doping ratios: 3, 15, 30 and 42%. M_R/M_S ratio of 15%-doped M-DNA is larger when compared to 3, 30 and 42% at 0.02 k_BT.

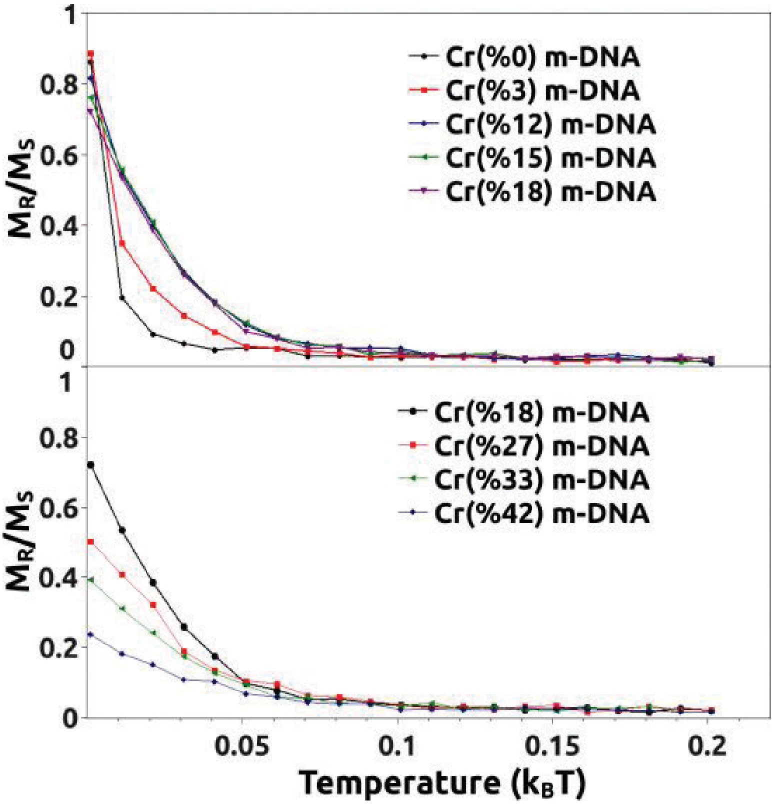

Figure 9. FC of M-DNA doped by Cr **(a)** 0, 3, 12, 15 and 18% **(b)** 18, 27, 33 and 42%.

4.2. Hysteresis curves

The idea of using DNA, a natural nanowire, in magnetism-based technological applications arose when the first paramagnetic resonance signal was observed by Bliumenfeld and Bendersky [36]. The signal explicitly revealed that B-DNA is a paramagnetic material. A hysteresis curve of B-DNA verifies its paramagnetic phase as shown in **Figure 10**. The outputs of the simulation process for B-DNA were also used to calibrate the main parameters of the doped-DNA systems [31].

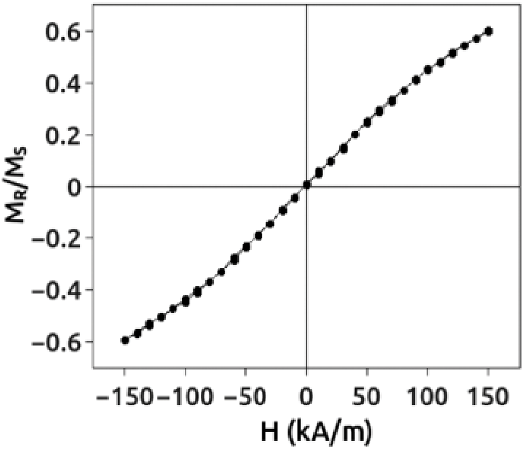

Figure 10. Hysteresis loop of B-DNA at k_BT/J=0.02.

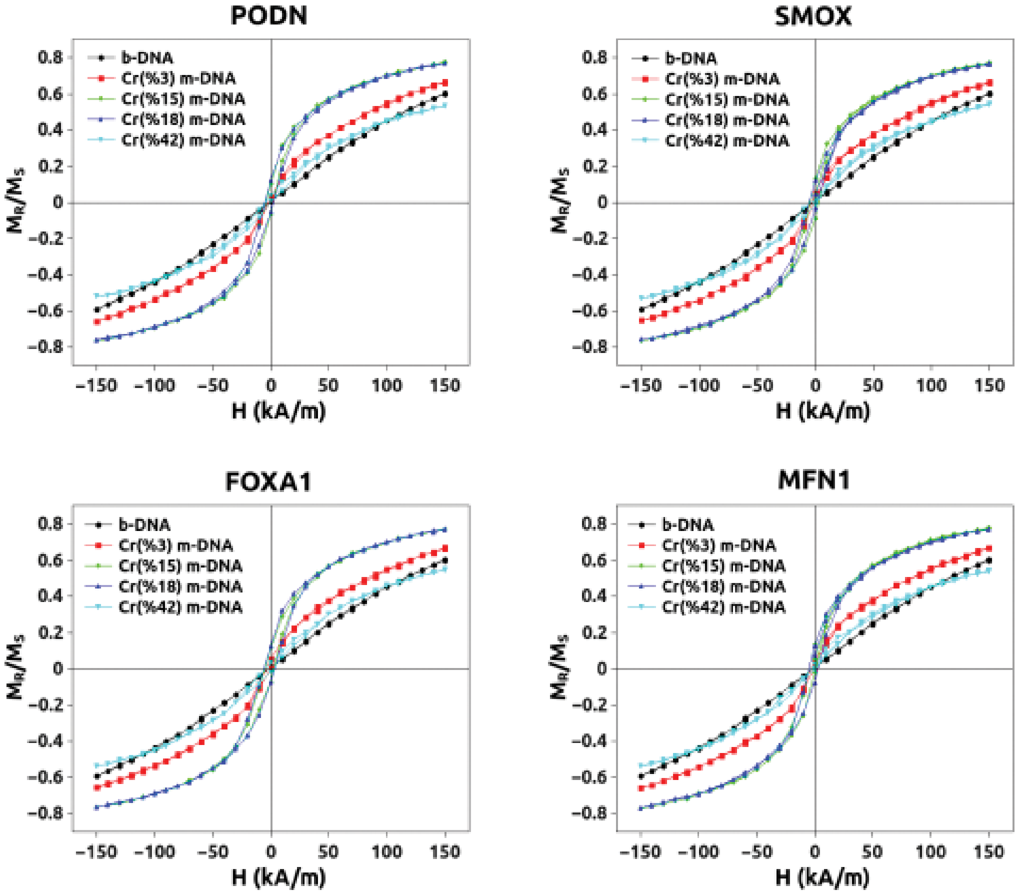

Figure 11. Hysteresis curves of B-DNA and Cr-doped M-DNA at 3, 15, 18 and 42% ratio for PODN, SMOX, FOXA1 and MFN1 gene sequences. The difference between hysteresis loops of various genes is negligible.

Although the Curie temperature of M-DNA is not so far from room temperature, **Figure 11** makes it clear that Cr-doped M-DNA has a relatively higher coercivity for x = 0.15 against other organomagnetic materials [37]. It is supposed that higher Cr concentrations larger than 15% lead the system to a state of disorder. Decrement in the M_R and coercive field indicates a change in the magnetic phase of DNA with increasing the doping ratio after x = 0.15 [31]. Briefly, the system has nonlinear phase transition behaviour with increasing the doping ratio from 0 to 42%: first, it is paramagnetic as in B-DNA and then gains soft ferromagnetic and antiferromagnetic properties, respectively.

Particularly, residual magnetism in system vanishes for x = 0.42, indicating that the ferromagnetic behaviour of the system completely vanishes due to AFM ion coupling, while there is no significant difference between x = 0.15 and 0.18 because of the random distribution of the Cr ions.

When **Figure 12** is roughly skimmed, DMOS behaviour should be understood easily. Remanent magnetization normalized by saturation magnetization has the bigger value near to 15% doping ratio and decreases with increasing doping ratio. Hysteresis and remanent magnetization figures of only four different genes of the sample group are implemented to this section since it is sufficient to verify the theory.

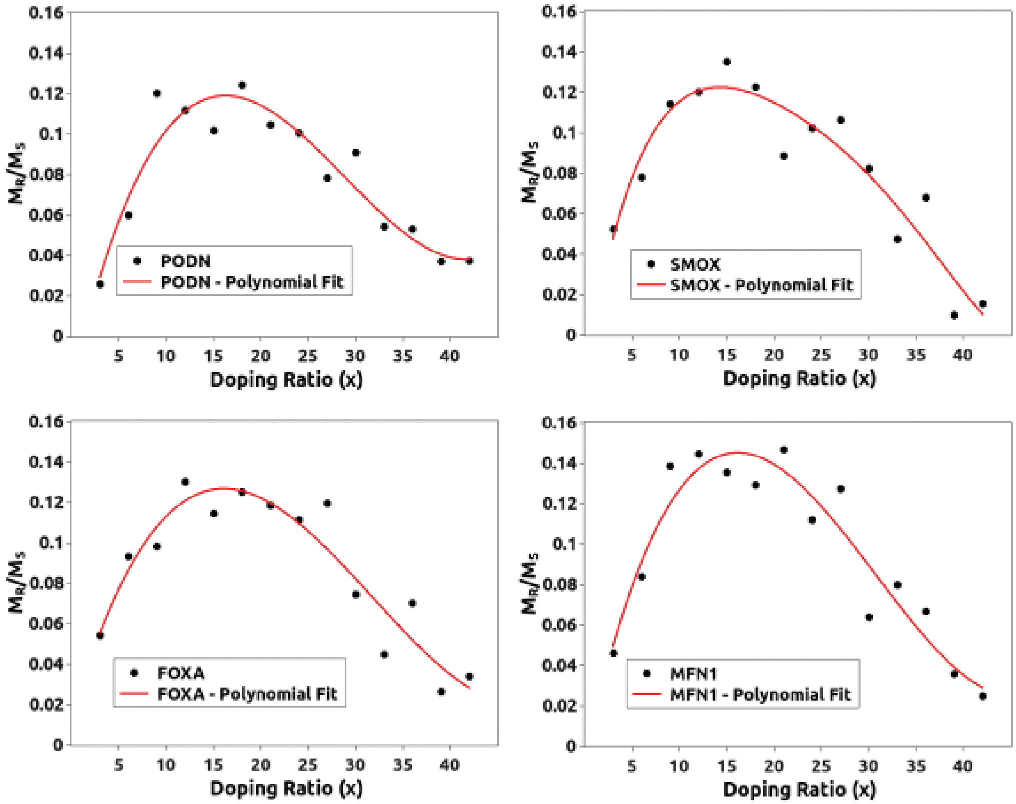

Figure 12. M_R/M_S MR/MS versus doping ratio of Cr-doped M-DNA for PODN, SMOX, FOXA1 and MFN1 gene sequences. The presentation of changing magnetic phase is supported by second-order polynomial fitting to have a clear understanding.

5. Summary

Geometrical structure of B-DNA nanowire in Euclidian space is generated by a given sample set of genes, including non-dispersive base sequences that consist of certain G-C ratio. The modifying process of B-DNA nanowire by doping Cr^{3+} ions is explained clearly and detailed by flow diagram as made from the simulation process of the whole system. However, MCMC method based on metropolis algorithm is used to mimic M-DNA nanowire to discover a proper Hamiltonian in the case of DMOS theory. Existence of a ferromagnetic interaction between Cr-X (X = N, H, O, P and C) and an anti-ferromagnetic interaction between Cr-Cr neighbouring atoms underlies the theory with Heisenberg Hamiltonian-included dipolar interaction. Moreover, hysteresis curves and remanent magnetization versus doping ratio of Cr is presented after critical temperature is determined by simulating of FC. $k_B T/J$ ratio is set to ~0.1 after several trials to calibrate parameters according to the paramagnetic behaviour. Duru et al. proposed a decrement in the remanent magnetization of the system at temperature $k_B T = 0.01$ from $x = 0.15$ to 0.30. Moreover, hysteresis curves reveal the DMS characteristic of M-DNA by Cr^{3+}, and it is not crucially dependent to type of atom. Different type of atom should only change coercive field or doping ratios that system gains ferromagnetic property. One must not forget that the dopants must have conducting property such as metals or semi-conductors.

Acknowledgements

We would like to thank the Scientific Research Commission (BAPKO) of Marmara University supporting this chapter under the research project numbered FEN-A-100616-0275.

Author details

Caner Değer[1], Vahap Eldem[2] and İzzet Paruğ Duru[1]*

*Address all correspondence to: izzetparug.duru@marun.edu.tr

1 Department of Physics, Marmara University, İstanbul, Turkey

2 Department of Biology, İstanbul University, İstanbul, Turkey

References

[1] Dugasani SR, Park B, Gnapareddy B, Pamanji SR, Yoo S, Lee KW, Lee S, Jun SC, Kim JH, Kim C, Park SH. Tunable near white light photoluminescence of lanthanide ion (Dy^{3+}, Eu^{3+} and Tb^{3+}) doped DNA lattices. RSC Advances. 2015;**5**(69):55839-55846. DOI: 10.1039/C5RA07360J

[2] Göhler B, Hamelbeck V, Markus TZ, Kettner M, Hanne GF, Vager Z, Naaman R, Zacharias H. Spin selectivity in electron transmission through self-assembled monolayers of double-stranded DNA. Science. 2011;**331**(6019):894-897. DOI: 10.1126/science.1199339

[3] Steckl AJ. DNA—a new material for photonics? Nature Photonics. 2007;**1**:3-5. DOI: 10.1038/nphoton.2006.56

[4] Nam J-M, Thaxton CS, Mirkin CA. Nanoparticle-based bio-bar codes for the ultrasensitive detection of proteins. Science. 2003;**301**(5641):1884-1886. DOI: 10.1126/science.1088755

[5] Lu Y, Goldsmith BR, Kybert NJ, Johnson ATC. DNA-decorated graphene chemical sensors. Applied Physics Letters. 2010;**97**(8). DOI: 10.1063/1.3483128

[6] Hu J-F (胡建芬), Feng L (冯琳), Zhang W-X (张文星), Li Y (李勇), Lu Y-X (卢亚鑫). Detection of DNA bases using Fe atoms and graphene. Chinese Physics Letters. 2016;**33**(1). DOI: 10.1088/0256-307X

[7] Azbel MY. Phase transitions in DNA. Physical Review A. 1979;**20**(4):1671-1684. DOI: 10.1103/PhysRevA.20.1671

[8] Alivisatos AP, Johnsson KP, Peng X, Wilson TE, Loweth CJ, Bruchez MP Jr, Schultz PG. Organization of "nanocrystal molecules" using DNA. Nature. 1996;**382**:609-611. DOI: 10.1038/382609a0

[9] Mirkin CA, Letsinger RL, Mucic RC, Storhoff JJ. A DNA-based method for rationally assembling nanoparticles into macroscopic materials. Nature. 1996;**382**:607-609. DOI: 10.1038/382607a0

[10] Braun E, Eichen Y, Sivan U, Ben-Yoseph G. DNA-templated assembly and electrode attachment of a conducting silver wire. Nature. 1998;**391**:775-778. DOI: 10.1038/35826

[11] Richter J, Mertig M, Pompe W, Mönch I, Schackert HK. Construction of highly conductive nanowires on a DNA template. Applied Physics Letters. 2001;**78**(4). DOI: 10.1063/1.1338967

[12] Park SJ, Taton TA, Mirkin CA. Array-based electrical detection of DNA with nanoparticle probes. Science. 2002;**295**(5559):1503-1506. DOI: 10.1126/science.1067003

[13] Keren K, Berman RS, Buchstab E, Sivan U, Braun E. DNA-templated carbon nanotube field-effect transistor. Science. 2003;**302**(5649):1380-1382. DOI: 10.1126/science.1091022

[14] Yi J. Emergent paramagnetism of DNA molecules. Physical Review B. 2006;**74**(21):212406. DOI: 10.1103/PhysRevB.74.212406

[15] Savin AV, Mazo MA, Kikot IP, Manevitch LI, Makoto AVO. Heat conductivity of the DNA double. Physical Review B. 2011;**83**(24):245406. DOI: 10.1103/PhysRevB.83.245406

[16] Sakamoto H, Mizoguchi K. Electronic states of DNA and M-DNA studied by optical absorption. Physical Review E. 2014;**89**(2):022719. DOI: 10.1103/PhysRevE.89.022719

[17] Panahi M, Chitsazanmoghaddam M. Comment on "modeling the electrical conduction in DNA nanowires: Charge transfer and lattice fluctuation theories". Physical Review E. 2016;**93**(4):046401. DOI: 10.1103/PhysRevE.93.046401

[18] Behnia S, Fathizadeh S. Modeling the electrical conduction in DNA nanowires: Charge transfer and lattice fluctuation theories. Physical Review E. 2015;**91**(2):022719. DOI: 10.1103/PhysRevE.91.022719

[19] Dugasani SR, Lee N, Lee J, Kim B, Hwang SU, Lee KW, Kang WN, Park SH. Magnetic characteristics of copper ion-modified DNA thin films. Scientific Reports. 2013;**3**(1819). DOI: 10.1038/srep01819

[20] Nikiforov VN, Kuznetsov VD, Yevdokimov YM, Irkhind VY. Magnetic properties of Gd^{3+} ions in the spatially distributed DNA molecules. Journal of Magnetism and Magnetic Materials. 2014;**368**:338-341. DOI: 10.1016/j.jmmm.2014.06.008

[21] Duru IP, Değer C, Eldem V, Kalayci T, Aktas S. Theory of room temperature ferromagnetism in Cr modified DNA nanowire. Journal of Physics D: Applied Physics. 2016;**49**:135004. DOI: 10.1088/0022-3727/49/13/135004

[22] van Dijk M, Bonvin AMJJ. 3D-DART: A DNA structure modelling server. Nucleic Acid Research. 2009;**37**(2). DOI: 10.1093/nar/gkp287

[23] Utrecht Biomolecular Interaction Web Portal. 3DDART@BonvinLab [Internet]. Available from: http://milou.science.uu.nl/services/3DDART/

[24] Watson CD, Crick FHC. Molecular structure of nucleic acids. Nature. 1953;**4356**:737

[25] Franklin R, Gosling RG. The structure of sodium thymonucleate fibres. II. The cylindrically symmetrical Patterson function. Acta Crystallographica. 1953b;**6**:678-685. DOI: 10.1107/S0365110X53001940

[26] Dugasani SR, Kim M, Lee I-y, Kim JA, Gnapareddy B, Lee KW, Kim T, Huh N, Kim G-H, Park SC. Construction and characterization of Cu^{2+}, Ni^{2+}, Zn^{2+}, and Co^{2+} modified-DNA crystals. Nanotechnology. 2015;**26**(27):275604. DOI: 10.1088/0957-4484/26/27/275604

[27] Mizoguchi K. Physical properties of natural DNA and metal ion inserted M-DNA. In: Heckman EM, Singh TB, Yoshida J, editors. Proceedings of SPIE. Nanobiosystems: Processing, Characterization, and Applications; 2008. DOI: 10.1117/12.801478

[28] Dong R, Yan X, Li K, Ban G, Wang M, Cui S, Yang B. Effects of metal ions on conductivity and structure of single DNA molecule in different environmental conditions. Nanoscale Research Letters. 2010;**5**:1431. DOI: 10.1007/s11671-010-9657-3

[29] Park H-Y, Dugasani SR, Kang D-H, Jeon J, Jang SK, Lee S, Roh Y, Park SH, Park J-H. n- and p-type doping phenomenon by artificial DNA and M-DNA on two-dimensional transition metal dichalcogenides. ACS Nano. 2014;**8**(11):11603-11613. DOI: 10.1021/nn5048712

[30] Joseph J, Schuster GB. Long-distance radical cation hopping in DNA: The effect of thymine–Hg(II)–thymine base pairs. Organic Letters. 2007;**9**(10):1843-1846. DOI: 10.1021/ol070135a

[31] Duru İP, Değer C, Kalaycı T, Arucu M. A computational study on magnetic effects of Zn Cr O 1−x x type diluted magnetic semiconductor. Journal of Magnetism and Magnetic Materials. 2015;**396**:268-274. DOI: 10.1016/j.jmmm.2015.08.031

[32] Metropolis N, et al. Journal of Chemical Physics. 1953;**21**:1087

[33] Kawasaki K. In: Domb C, Green MS, editors. Chapter 4.Mode Coupling and Critical Dynamics. Phase Transitions and Critical Phenomena. Vol. 5. London: Academic Press; 1976

[34] Boltzmann L. Lectures on Gas Theory. Berkeley, CA, USA: University of California Press; 1964

[35] Hastings WK. Monte Carlo sampling methods using Markov chains and their applications. Biometrika. 1970;**57**(1):97-109. DOI: 10.1093/biomet/57.1.97. JSTOR 2334940. Zbl 0219.65008

[36] Bliumenfeld LA, Bendersky VA. Magnetic and Dielectric Properties of High-ordered Macromolecular Structures. Doklady Akademii Nauk, SSSR. 1960;133:1451-1454

[37] Jain R, Kabir K, Gilroy JB, Mitchell KAR, Wong K, Hicks RG. High-temperature metal–organic magnets. Nature. 2007;**445:**291-294

Chapter 10

Recent Trends in Plasmonic Nanowire Solar Cells

Mohamed Hussein,
Mohamed Farhat Othman Hameed and
Salah S. A. Obayya

Additional information is available at the end of the chapter

http://dx.doi.org/10.5772/67617

Abstract

Light trapping is crucial for low-cost and highly efficient nanowire (NW) solar cells (SCs). In order to increase the light absorption through the NWSCs, plasmonic materials can be incorporated inside or above the NW design. In this regard, two novel designs of plasmonic NWSCs are reported and analyzed using 3D finite difference time domain method. The geometrical parameters of the reported designs are studied to improve their electrical and optical efficiencies. The ultimate and power conversion efficiencies (PCE) are used to quantify the conversion efficiency of the light into electricity. The first design relies on funnel shaped SiNWs with plasmonic core while the cylindrical NWs of the second design are decorated by Ag diamond shaped. The calculated ultimate efficiency and PCE of the plasmonic funnel design are equal to 44% and 18.9%, respectively with an enhancement of 43.3 % over its cylindrical NWs counterpart. This enhancement can be explained by the coupling between the three optical modes, supported by the upper cylinder, lower cone and plasmonic material. Moreover, the cylindrical SiNWs decorated by Ag diamond offer an ultimate efficiency and short-circuit current density of 25.7%, and 21.03 mA/cm^2, respectively with an improvement of 63% over the conventional cylindrical SiNWs.

Keywords: light trapping, plasmonic solar cells, nanowires, finite-difference time-domain

1. Introduction

It has become obvious that global stability, economic prosperity, and quality of life are linked intimately with sufficient supplies of clean energy. Searching for energy resources to meet the world's growing demand is a major challenge for the next half century. Traditional energy sources are currently depleted at the rate of approximately 4.1 × 10^{20} J/yr, which is equivalent to continuous power consumption of 13 trillion watt [1]. An increase in the global population to 9 billion people, along with the rapid worldwide technology development and economic growth, leads to an inevitable increase of more than double the demand for energy (to 30 TW) by 2050 and above the triple demand (to 40 TW) by the end of this century [2]. Because of the dramatic hydrocarbon-based power consumption, the harmful effects (such as global warming, acid precipitation, air pollution, ozone depletion, and forest destruction) are increasingly in catastrophic forms. In the pursuit of limiting these drawbacks, suitable actions aimed at reducing the dependence on the fossil fuels are mandatory. The most urgent challenge is in the search for clean and renewable alternative energy resources required for the sustainable development of human civilization. The Sun is the primary source for clean and abundant energy, with nearly 120,000 TW of incident radiations on the earth's surface which has the potential for covering the human needs [3, 4]. This contains 1.5×10^{18} KWh of energy; which is larger than that of the traditional reserves of oil, coal, and gas which form 1.75×10^{15}, 1.4×10^{15}, and 5.5×10^{15} KWh, respectively [5, 6]. Hence, solar radiation annually provides over 100 times the energy supplied by the entire known fossil fuel sources. Harvesting solar power has become the modern trend in worldwide research projects reported in the scientific community [5, 6]. The photovoltaics (PVs) or solar cell (SC) devices are considered a promising technology that converts the sunlight directly into electricity on a very large scale without causing pollution [7]. The PVs are considered attractive and a promising candidate that would significantly contribute in the future global renewable energy sources. The main challenge in the PV devices is the cost reduction per watt with respect to the fossil fuel technologies. The cost/watt ratio of the photovoltaic devices is at least 1.5 times higher than the electricity generated from the fossil fuels [8]. The main factor influencing the cost/watt ratio is the size of the active material, mostly crystalline silicon (c-Si), and the manufacturing process. The 30–40% of cost/watt in the c-Si SCs is mainly due to the silicon substrate.

Until now, over 90% of the photovoltaic market is currently dominated by the c-Si solar cells. A maximum power conversion efficiency of 25.6% has been achieved for the c-Si solar cell which is approaching the Shockley-Queisser theoretical limit of 29.4%. Therefore, further improvement in the Si solar cell efficiency is required to compete with the fossil fuels and other alternative sources of energy [9]. Different efficient and reliable avenues have been used to enhance the solar cell efficiency and reduce the cost/watt ratio [9]. In the attempt to do so, different materials have been used, such as crystalline silicon (c-Si) [10], amorphous silicon (a-Si) [11], gallium arsenide (GaAs) [12], copper indium gallium selenide (CIGS) cadmium telluride (CdTe) [9, 13], GaSb/GaAs quantum rings [14], organic material [15], and tandem solar cells by combining several materials [16]. The c-Si material is commercially used because it is cheap and abundant compared to other materials. However, the absorption of the c-Si is poor, and a very large thickness is needed to absorb the solar energy. The bandgap of silicon (1.12 eV) is not at the perfect bandgap for solar spectrum, which severely limits the efficiency of the solar cell. Alternatively, a-Si has a better absorption, and it is usually used for thin-film solar cell materials; however, its efficiency is not higher than the c-Si solar cells. The GaAs has high conversion efficiency up to 30% because its bandgap is close to the optimized bandgap for single absorbed material on the expenses of the high total cost. Also, the cadmium telluride (CdTe) has good conversion efficiency, and the cost can be minimized due to the rapid technology development based on this material. However, the Cd is a highly polluted material, and it has several drawbacks. Recently, different materials can be used to absorb various spectra of solar energy with high efficiency [17, 18]. However, such multi-junction designs need complicated fabrication techniques and expensive manufacturing processes. Thus, the multi-junction solar cells are difficult to be commercialized in the near future.

Currently, the thicknesses of the crystalline silicon wafers used in solar cell market is about 180–300 μm which affects the total cell price due to the silicon materials and processing. Therefore, thin film solar cells attract a great attention, with film thickness in the range of 1–2 μm, as it can be deposited on cheap substrates such as glass, plastic, or stainless steel. However, thin-film solar cell suffers from its weak absorption near the material bandgap especially when using indirect bandgap materials (Si). One of the most alternative important approaches to increase the thin-film solar cell efficiency is the light-trapping techniques to enhance the light absorption into the solar cell active materials. These techniques can increase the light path of the trapped photons in the solar cell materials to generate the electron-hole pair under light illumination. Consequently, the material cost can be minimized by using cheap substrate and solar cell materials with high efficiency. Further, semiconductor nanowires with a few nanometers in diameters can reduce SC material cost with high efficiency. The antireflection layers can be also used to improve the light transmission efficiency [19]. The refractive index of the antireflection layer is chosen between the refractive indices of the active material and surrounding air. The most widely used antireflection materials include SiO_2, SiNx, TiO_2, Al_2O_3, CeO_2, etc. [20]. The antireflection layer can be merged with the textured structures for better light-trapping improvements. The textured silicon surface structures can be etched by various etchants, such as NaOH [21], TMAH [22, 23], and KOH [24]. Different textured structures have been introduced, including the pyramidal textured surfaces [25], inverted pyramidal [26], honeycomb [27], nanowire [28, 29], gratings [30], V-grooved [31], and other types of structures [32–34]. Most of these structures have large size and are not suitable for thin-film SCs with micrometer or sub-micrometer ranges [30]. Recently, the plasmonic SCs attract sharp attention because it can be used for efficient light trapping through the active layer of the SC. Further, it is simple to merge the plasmonic materials into nanowire and thin-film SC designs [35]. Therefore, the plasmonic nanoparticles are considered as pivotal cornerstone in increasing the light trapping in thin-film and nanowire SCs.

Following this introduction, a review of plasmonic light-trapping techniques for solar cell applications will be discussed. In addition, the recent trends in NW SCs are introduced thoroughly. Further, two novel designs of plasmonic NW SCs are presented and analyzed using 3D full-vectorial finite-difference time-domain method (FDTD). In this regard, plasmonic funnel-shaped SiNWs and plasmonic diamond SiNWs are investigated to present the effect of adding plasmonic materials through or above the SiNWs. The performance of the suggested NWSCs has been investigated in terms of the ultimate efficiency and short-circuit current density, open-circuit voltage, power conversion efficiency, and absorbed field profiles. The reported funnel-shaped SiNWs with plasmonic core show an ultimate efficiency of 36.9% which is higher than cylindrical and conical counterparts by 36.7 and 22.2%, respectively. Further, the plasmonic funnel-shaped design has short-circuit current density of 30.2 mA/cm^2 which is greater than 24.5 and 22.12 mA/cm^2 of the conical and cylindrical designs. The enhancement in the ultimate efficiency and hence short-circuit current density apparently can be attributed to the combination between three types of optical modes that are supported by the upper cylinder, the lower tapered cone, and the plasmonic material. On the other hand, the SiNW decorated by Ag diamond shows an ultimate efficiency of 25.7% which is higher than conventional SiNWs without plasmonic material by 63%. Additionally, the reported design with Ag diamond shows short-circuit current density of 21.03% mA/cm^2 which is greater than the conventional counterpart SiNWs with an improvement of 32.6%.

2. Review of plasmonic light trapping for solar cell applications

At the emergence of the eighteenth century, metallic nanoparticles have gained much interest in the research community for their optical properties. Years later, the Raman scattering was enhanced through the utilization of metallic structures [36] which attracted more researchers to the field of plasmonic nanoparticles. Since then, plasmonic resonance, with its fundamental properties, has been introduced to various applications such as integrated optics, biosensing [37, 38], and energy harvesting [39–41]. In metallic nanoparticles, plasmon resonances give rise to a resonance scattering which reduces the reflection over the spectral range. This anti-reflection effect, caused by random and periodic arrays of metallic nanoparticles, has been extensively studied, theoretically and experimentally, for photovoltaic applications [42, 43]. Stuart and Hall have led the research work in the field of light-sensitive devices enhanced by plasmonic resonance where an enhancement factor of 18 has been reported for a silicon-on-insulator photodetector at 800 nm wavelength. This device has a thickness of 165 nm and is covered by silver nanoparticles on its surface [44]. Additionally, Schaadt et al. [45] proposed a highly doped wafer-based solar cells coated by gold nanoparticles on its surface which achieved an enhancement of 80% for the photocurrent at 500 nm wavelength. Gold nanoparticles have been also used in amorphous thin-film silicon SCs, by Derkacs et al. [43], which improved the overall power conversion efficiency (PCE) by 8%. Pillai et al. [46] achieved 19 and 33% increase in the overall photocurrent for wafer-based SCs and 1.25 μm thick silicon-on-insulator design, respectively, using silver nanoparticles on the cells' surface. Ouyang et al. [47] employed self-assembled Ag nanoparticles on the surface of thin-film silicon SCs which enhanced the short-circuit current density by 27%. A relative photocurrent enhancement of 10% was reported by Beck et al. [48] for silicon cell of thickness 22 μm covered by an array of Ag nanoparticles. In recent years, Tan et al. [49] used Ag nanoparticles as a plasmonic back reflector which offered a net short-circuit current density gain of 2 mA/cm^2. Moreover, different types of solar cells have achieved a performance enhancement based on the plasmonic effect of metallic nanoparticles such as organic and dye-sensitized SCs [50, 51]. In a pioneering breakthrough by Ding et al. [52], plasmonic effect was used to enhance the light absorption and hence, the efficiency of dye-sensitized SCs which achieved a PCE of 5.9% [52]. For a dye-sensitized TiO_2 film, reported by Hägglund et al. [53], an enhanced carrier generation was achieved by employing gold nanodisc. Rand et al. [54] also introduced organic SCs based on ultrathin film using tiny silver nanoparticles which enhanced the cell efficiency. Furthermore, an efficiency enhancement of 1.7 in magnitude was reported by Morfa et al.

for organic bulk heterojunction solar cells [55]. Another organic SCs proposed by Chen et al. achieved an improved PCE using Au nanoparticles incorporated into anodic buffer layer [56].

3. State of the art of semiconductor nanowire solar cells

The current crystalline Si cells are widely used in the PV market with efficiency in the proximity of 25% [57]. A major dilemma lies in the high material cost. The use of cheaper materials, such as polycrystalline thin films or organic semiconductors, decreases the material cost. The amount of required absorbing material can be further decreased by increasing the concentration of the light through a small area [58]. A dramatic improvement in the fabrication techniques can further minimize the loss mechanism and hence increase the SC efficiency. The use of semiconductor nanoantennas (NAs) or NWs readily fulfills all these requirements. In this regard, the NW SCs with structures of a few nanometers in diameters have been considered for PV power generation. The semiconductor NWs have advantages in terms of optical absorption enhancement [59]. This is mainly due to the small reflectivity of the NW array (NWA) with large open area on the frontal surface. The light is trapped by multiple total internal reflections through each nanoscale cylindrical NW resonator [60]. In 2007, Hu and Chen [59] introduced the cylindrical SiNWs with an ultimate efficiency of 15.5%. The behavior of the semiconductor NWs strongly depends on their structural geometrical parameters [59]. Consequently, intense theoretical studies of the optical absorption are required to maximize the ultimate efficiency of the NWA-based SCs. The NWAs with optimized parameters apparently offer higher broadband absorption than solid films [61]. As the NW diameter, period, and wavelength are of the same order, strong light scattering and further light trapping occur [61]. The modified design presented by C. Lin and Povinelli [62] have enhanced the ultimate efficiency up to 23.84% through increasing the lattice constant to 600 nm [62]. The ultimate efficiency of 20.44% was obtained using partially aperiodic vertically SiNWs [63]. Li et al. [64] accomplished an ultimate efficiency of 30.5% by tuning silicon nanowire parameters. The NWAs with random orientation, length, diameter, and position have been experimentally investigated in 2008 [65]. It has been shown that reflection or backscattering was detected with slight effects on the absorption. The optical properties of vertically aligned silicon NWAs with three types of structural randomness, i.e., random position, diameters, and lengths, were numerically investigated [66]. The NWAs with random position displayed slight absorption enhancement, while those with random diameter or length exhibited a significant absorption enhancement. Therefore, the structural randomness in vertical nanowire arrays can further enhance the optical absorption compared to ordered nanowire arrays. The substantial reflectance and absorption of slanting silicon NWAs attracted attention due to their established applications in SCs [67]. The slanting NWAs achieve a significant suppression of light reflection and an enhancement of light-harvesting ability than the conventional vertical structure. The slanted NWAs offer an ultimate efficiency of 33.45%, which exceeds the 30.5% of optimum vertical SiNWs [67]. Wanget al. [68] also reported an ultimate efficiency of 29.1% by using elliptical SiNWAs. On top of that, an ultimate efficiency of 39.3% is achieved using SiNWs arranged in a decagonal lattice [28]. Additionally, periodic vertical cone arrays form a promising family of structures that are currently under examination for PV technology. Wang et al. proved that the light absorption can be considerably enhanced by using nanocones [69, 70]. In addition, Ko et al. [71] demonstrated that an ultimate efficiency of 28.9% can be obtained by decreasing the cone bottom diameter to 20 nm. Further, the SiNWs funnel shape achieved an ultimate efficiency of 41.8% [29].

4. Simulation methodology and numerical results

4.1. Plasmonic funnel SiNWs

The optical simulation of the suggested designs is carried out using 3D finite-difference time-domain (FDTD) method via Lumerical FDTD solution software package [72]. The FDTD method is widely used in solar cell applications due to its ability to make the simulation physically realistic through using the multi-coefficient material model. Moreover, the FDTD has the capacity to simulate broadband frequency ranges in a single simulation run. In this study, the 3D FDTD method is employed for investigating the optical properties of the SiNWs over the main region of the solar spectrum [72]. **Figure 1(a)** shows the utilized computational domain for the proposed plasmonic funnel-shaped SiNW unit cell in x-z plane. However, **Figure 1(b)** illustrates the x-y view of the suggested design. The top and bottom of the unit cell are surrounded by perfectly matched layers (PML) boundary conditions, while the unit cell is surrounded by periodic boundary conditions (BCs) along x and y directions to simulate periodic square SiNW array. The width and length of the unit cell are equal to 500 nm, while the height is taken as 4000 nm. In order to achieve high accuracy, fine meshing of $\Delta x = \Delta y = \Delta z = 5$ nm is used, which is less than

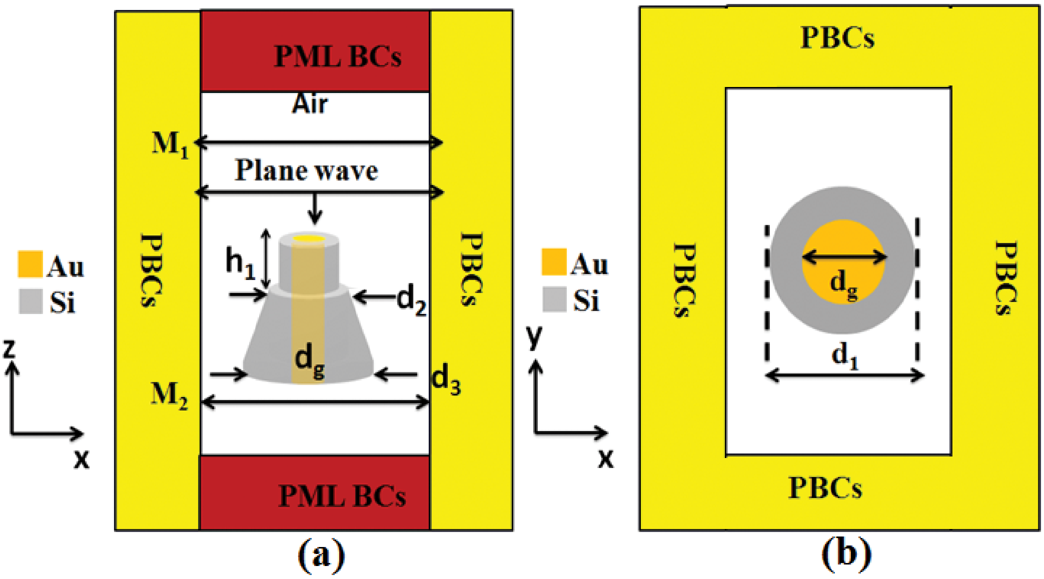

Figure 1. The computational domain of the plasmonic funnel SiNW unit cell in the (a) x-z plane and (b) x-y plane.

1/60 of the shortest wavelength. The proposed plasmonic design is specifically illuminated from the top by a plane wave ranging from 300 to 1100 nm, which covers the main part of the solar spectrum. The incident wave is normal to the x-y plane with the electric field polarized along the x-axis as shown in **Figure 1(a)**. In this study, we only consider lightly doped silicon material. At frequencies above the bandgap, the difference in the optical constants between lightly doped and intrinsic silicon is negligible, which gives us the convenience of using the same optical constants for both p and n regions of the core-shell structure in silicon NW SC [59]. The refractive indices of the SiNWs are taken from experimentally measured optical constants from Ref. [73]. The plasmonic funnel SiNW design shown in **Figure 1** consists of silicon cylinder of height h_1 and a cone of height h_2. The total thickness is equal to h_1+h_2 which is fixed to 2.33 μm that is comparable to the thickness of thin-film solar cell. The Si cylinder has a diameter d_1 with a gold core of diameter d_g, while the cone has upper and lower base diameters of d_2 and d_3, respectively. In this investigation, the NWs are arranged in a square lattice with a periodicity of $\Lambda = 500$ nm.

The amount of the total absorbed power by the suggested design can be calculated as a function of the wavelength λ using the total reflection R (λ) and total transmission T (λ) according to the following relation:

$$A(\lambda) = 1\text{-}R(\lambda)\text{-}T(\lambda) \tag{1}$$

Further, the absorbed power by the SiNWs only is calculated as

$$\alpha(\lambda) = \mathbf{A}(\lambda) - \mathbf{Ag}(\lambda) \tag{2}$$

where Ag(λ) is the absorbed power by the plasmonic material. The wavelength-dependent reflection and transmission are calculated by using two frequency domain monitors (M_1) and (M_2), placed above and below the unit cell, respectively, as shown in **Figure 1(a)**. In order to have a convergent absorption, the source and reflection monitors are placed above the SiNWs at a distance 400 and 600 nm, respectively. However, the transmission monitor is placed below the structure by 300 nm. The ultimate efficiency (η) defined as a figure of merit is used to evaluate the absorption capability of the proposed structures for solar cell applications. The ultimate efficiency is calculated from the following equation [4, 8]:

$$\eta = \frac{\int_{300\,\mathrm{nm}}^{\lambda_g} F_s(\lambda\Big)\, \alpha(\lambda) \frac{\lambda}{\lambda_g}\, d\lambda}{\int_{300\,\mathrm{nm}}^{4000\,\mathrm{nm}} F_s(\lambda)\, d\lambda} \tag{3}$$

where λ is the wavelength of the incident light, E_g is the bandgap wavelength of the Si, and $F_s(\lambda)$ is the photon flux density in the ASTM AM 1.5 solar spectrum [74]. In this study, λ_g is taken as 1100 nm, corresponding to the energy gap of the silicon material. The short-circuit current density (J_{sc}) is related to the ultimate efficiency by assuming perfect carrier collection efficiency, i.e., each photon absorbed with energy higher than the bandgap produces one electron-hole pair, and all generated carriers are collected to produce current without recombination losses [28, 29]. The short-circuit current density J_{sc} of the proposed design can be expressed as [29]

$$J_{sc} = \eta \frac{q\,\lambda_g}{hc} \int_{300\,\mathrm{nm}}^{4000\,\mathrm{nm}} F_s(\lambda\Big)\, d\lambda = 81.83\eta(mA/c\,m^2) \tag{4}$$

where q is the electron charge, h is Planck's constant, η is ultimate efficiency, and c is the speed of light.

The open-circuit voltage can be related to the maximum short-circuit current density by [75]:

$$V_{oc} = \frac{K_B T_c}{q} \ln\left(1 + \frac{J_{sc}}{J_0}\right), \tag{5}$$

where K_B (ev/K) is the Boltzmann constant, T_c is the ambient temperature of the solar cell temperature that is assumed to be equal to the ambient temperature (i.e., 300 K), and J_0 is the dark saturation current density. The semiempirical expression for the dark saturation current density is given by [75]:

$$J_o = 1.5 \times 10^9 \ln\left(-\frac{E_g}{K_B T_c}\right), \tag{6}$$

The fill factor (FF) is defined as [75]

$$FF = \frac{v_{oc} - \ln(v_{oc} + 0.72)}{v_{oc} + 1}, \tag{7}$$

where $v_{oc} = \frac{V_{oc}}{(KT/q)}$,

To quantify the electrical performance of the proposed design, the power conversion efficiency (PCE) is calculated from the following equation:

$$PCE = \frac{v_{oc} J_{sc} FF}{I_{in}}, \tag{8}$$

where I_{in} is the incident power density at AM 1.5 and is equal to 900.14 w/m^2 [76].

Figure 2(a) depicts the absorption spectra of the cylindrical, conical, and proposed plasmonic funnel NWs versus the wavelength. It should be noted that the absorption of the suggested plasmonic design $\alpha(\lambda)$ shown in this figure is due to the Si only. In this study, d_1 = 300 nm, d_2 = 400 nm, d_g = 120 nm, d_3 = 500 nm, h_1 = 500 nm, and h_2 = 1830 nm. Further, the studied three shapes have the same total height of 2330 nm. It is revealed from this figure that the plasmonic funnel shape shows superior absorption than conical and cylindrical counterparts over the

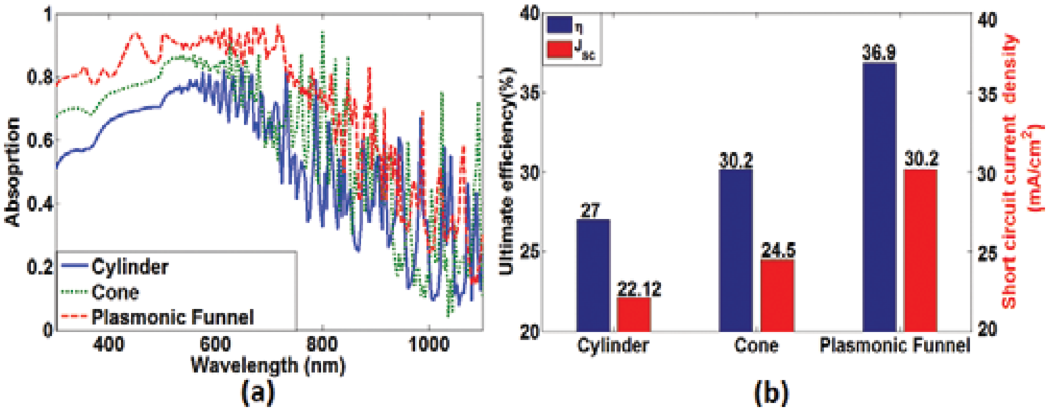

Figure 2. (a) Absorption spectra and (b) ultimate efficiency and short-circuit current density of the cylindrical, conical, and plasmonic funnel NWs.

entire wavelength band. **Figure 2(b)** shows the ultimate efficiency and short-circuit current density of the investigated NWs. The ultimate efficiencies of these structures are equal to 27, 30.2, and 36.9%, respectively. Therefore, it may be noted that the plasmonic funnel-shaped NWs offer an overall enhancement of 36.7 and 22.2% over the cylindrical and conical counterparts. Further, the funnel-shaped design has short-circuit current density of 30.2 mA/cm^2 which is greater than 24.5 and 22.12 mA/cm^2 of the conical and cylindrical designs. The enhancement in the ultimate efficiency and hence short-circuit current density apparently can be attributed to the combination between the modes supported by the upper cylinder and the lower tapered cone along with the plasmonic modes generated by the gold core. Additionally, the proposed design offers continuous reflections between the SiNWs until the incident angle becomes smaller than the critical angle resulting in high light trapping and broadband absorption. Furthermore, the absorption enhancement can be also explained from the waveguide modal dispersion of the NWs [29]. The leaky mode resonance relies on the NW diameter. Therefore, the use of plasmonic funnel-shaped NW with multiple diameters will increase the number of leaky mode resonances. The cylindrical part with small diameter d_1 can absorb short wavelength spectrum. However, the long wavelength spectrum is absorbed by the conical part with upper and lower base diameters d_2 and d_3, respectively. Additionally, the gold core generates plasmonic modes which play an important role for the broadband absorption.

To further confirm the underlying mechanism of the absorption enhancement, the absorbed field profiles inside the cylindrical, conical, and plasmonic funnel shapes have been presented in **Figure 3(a)–(c)**, respectively in x-z plane at λ = 688 nm. It is reveled from these figures that the incident light has more penetration and confinement through the proposed funnel shape with plasmonic core than the conventional conical and cylindrical Si structures. Therefore, the absorption and consequently the ultimate efficiency are enhanced.

In order to ensure that the absorption enhancement of the suggested design is due to the enhanced light trapping in the Si material, the absorption through the plasmonic core and the surrounding Si material are calculated and shown in **Figure 4**. The absorption of the Si NW funnel design [29] without plasmonic material is also plotted in **Figure 4**. It may be noted from this figure that the absorption through the plasmonic metal is small. Further, the plasmonic

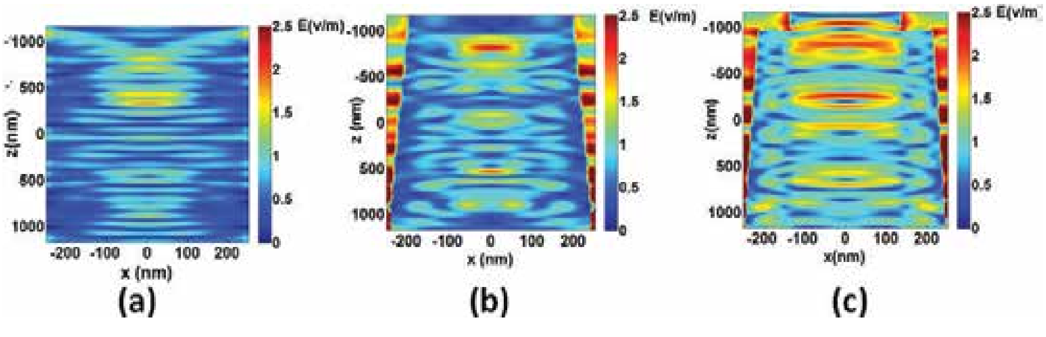

Figure 3. Absorbed field profiles of the (a) cylindrical, (b) conical, and (c) plasmonic funnel SiNWs in x-z plane at λ = 688 nm.

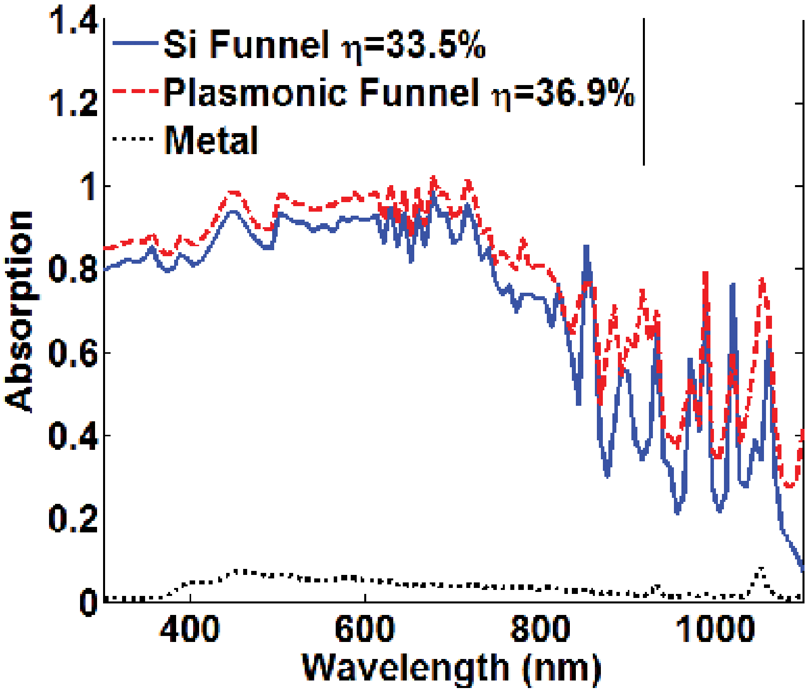

Figure 4. Absorption spectra through the Si funnel [29], metallic layer, and plasmonic funnel NWs.

funnel design has better absorption than that of the Si funnel design [29]. The simulation results also reveal that the plasmonic funnel-shaped NWs achieve an ultimate efficiency of 36.9% which is higher than that of the Si funnel counterpart of ultimate efficiency of 33.5%. The metallic core supports plasmonic modes which increase the light confinement through the silicon NWs. Therefore, the hybrid funnel nanowires improve the light trapping and hence the ultimate efficiency.

To understand the electrical enhancement in the reported design, the ultimate efficiency (η), short-circuit current density (J_{sc}), open-circuit voltage (V_{oc}), fill factor (FF), and power conversion efficiency (PCE) are calculated and shown in **Table 1**. In this table, the calculated values of η, J_{sc}, V_{oc}, FF, and PCE of the cylindrical [66], conical [70], Si funnel [29], and proposed plasmonic funnel SiNWs are listed in detail. It may be noted from this table that the V_{oc} and PCE of the plasmonic funnel shape are higher than that reported in Refs. [29, 66, 70]. Additionally, the PCE of the reported design is higher than that of the cylindrical SiNWs [66] and Si funnel [29] counterparts by 9.95 and 38.2%, respectively. This enhancement is attributed to the better absorption in the plasmonic funnel design which is responsible for enhancing the conversion efficiency. Therefore, the suggested design has a better conversion from optical to electrical power than the previously published design [29, 66, 70].

In order to enhance the absorption capabilities of the proposed funnel-shaped SiNWs with plasmonic core, the effects of the structure geometrical parameters are investigated. **Figure 5(a)** shows the effect of the top cylindrical diameter (d_1) on the ultimate efficiency

Structure	η	J_{sc} (mA/cm^2)	V_{oc} (v)	FF	PCE
Cylindrical SiNWs [66]	27%	22.0941	0.6538	0.8380	13.6405
Conical SiNWs [70]	30.2%	24.7127	0.6567	0.8385	15.3247
Funnel SiNWs [29]	33.5%	27.4131	0.6594	0.8390	17.0687
Plasmonic funnel NWs	36.9%	30.1953	0.6619	0.8395	18.8723

Table 1. The ultimate efficiency (η), short-circuit current density (J_{sc}), open-circuit voltage (V_{oc}), fill factor (FF), and power conversion efficiency (PCE) of different structures.

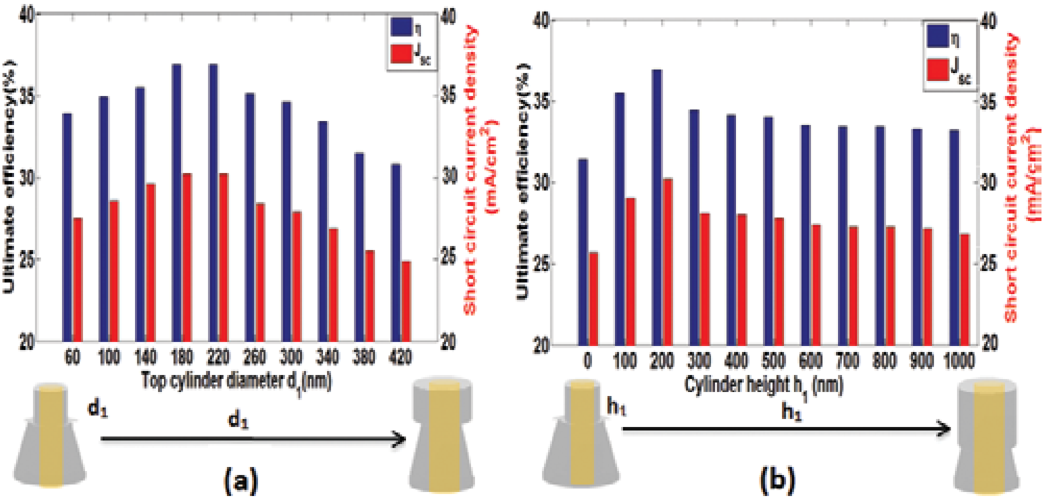

Figure 5. Variation of the short-circuit current density and ultimate efficiency with the (a) cylinder diameter d_1 and (b) cylinder height h_1.

and short-circuit current density for the suggested structure. In this investigation, the other parameters Λ, h_1, d_2, d_3, and h_2 are kept constants at 500, 500, 400, 500, and 1830 nm, respectively. As the diameter (d_1) increases from 60 to 180 nm, the absorption through the SiNWs and hence the ultimate efficiency increase. The ultimate efficiency and short-circuit current density have maximum values of 36.9% and 30.2 mA/cm^2 at d_1 = 180 nm, respectively. As d_1 is further increased, the reflection will be increased, and hence the absorption and ultimate efficiency are decreased. As a result, the short-circuit current density decreases from 30.2 to 24.9 mA/cm^2 by increasing d_1 from 180 to 420 nm, respectively. Therefore, the tuned d_1 = 180 nm will be used for the subsequent simulations. Next, the effect of the cylinder height h_1 of the suggested design is also investigated. As h_1 increases from 0 to 200 nm, the ultimate efficiency and short-circuit current density are increased. Therefore, it is concluded that the funnel shape has a better absorption capability than the conical design at $h_1 = 0$. It may be also seen from **Figure 5(b)** that the cylinder height has a slight effect on the short-circuit current density of the proposed design when $h_1 \geq 300$ nm. This is due to the fixed cylindrical diameter d_1 which faces the incident light. Therefore, the amount of trapped light inside the proposed design is slightly changed with h_1 variation. The maximum ultimate efficiency of 36.9% is obtained at $h_1 = 200$ nm.

Figure 6(a) displays the relation between the short-circuit current density and ultimate efficiency against the cone upper base diameter (d_2) for the suggested design. In this study, the tuned geometrical parameters of the plasmonic design are taken as $d_1 = 180$ nm, $d_3 = 500$, and $h_1 = 200$ nm. As d_2 increases from 160 to 360 nm, the active material increases, and hence higher order optical modes are generated. Therefore, the ultimate efficiency is increased from 33.3 to 36.96%. The tapered shape of the plasmonic design with $d_2 = 360$ nm has maximum ultimate efficiency of 36.9% and J_{sc} of 30.2 mA/cm^2. The effect of the cone base diameter (d_3) is also studied and shown in **Figure 6(b)**. It is revealed from **Figure 6(b)** that as the cone base diameter (d_3) of the plasmonic funnel design increases, the active material will be increased which decreases the transmission through the proposed design. Therefore, the absorption and ultimate efficiency are increased. An optimum ultimate efficiency of 36.9% and J_{sc} of 30.2 mA/cm^2 are obtained at 500 nm cone base diameter.

From the practical point of view, the absorption spectra of the funnel SiNWs with plasmonic core and cylindrical SiNWs decorated on 2 μm Si substrate and Ag back reflector of thickness 200 nm are calculated and shown in **Figure 7**. Compared with the cylindrical SiNWs of ultimate efficiency = 30.6%, the proposed plasmonic design shows an ultimate efficiency of 44% with an enhancements of 43.3% [7]. Additionally, short-circuit current densities of 36 mA/cm^2 and 25.1 mA/cm^2 are achieved by the plasmonic funnel design and cylindrical SiNWs, respectively. This is due to the coupling between the nanowire arrays and underlying substrate which leads to a strong absorption enhancement in the lower energy region as well as good light-trapping improvement in the longer wavelength as displayed in **Figure 7(a)**.

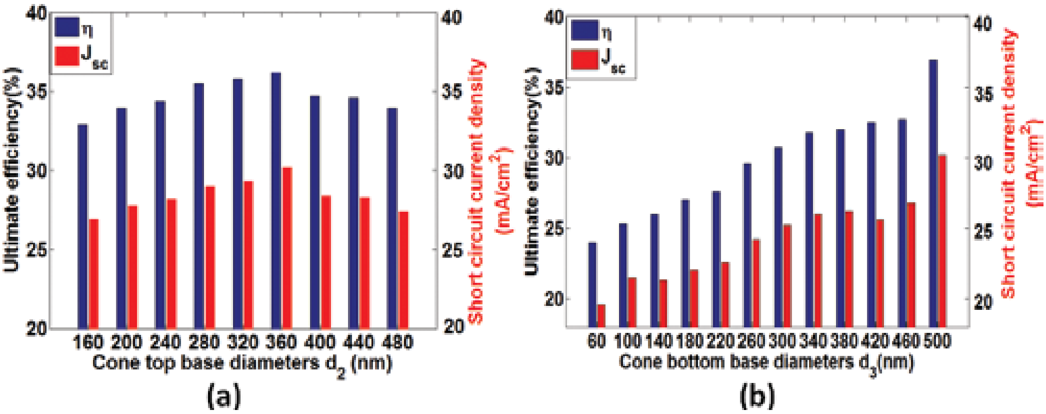

Figure 6. Variation of the short-circuit current density and ultimate efficiency with the cone (a) top diameter d_2 and (b) bottom diameter d_3.

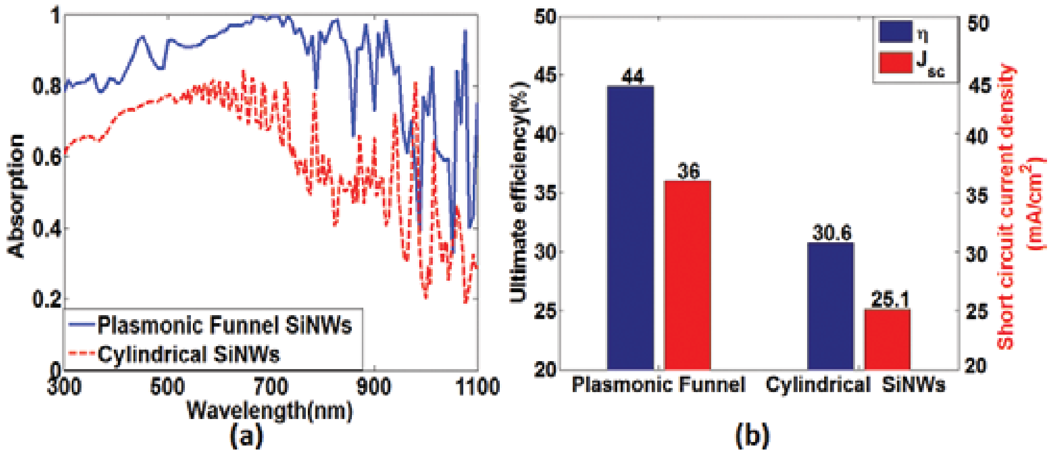

Figure 7. (a) Absorption spectra and (b) ultimate efficiency and short-circuit current density of the proposed plasmonic funnel SiNWs and cylindrical SiNWs with Si substrate and Ag back reflector.

4.2. SiNWs decorated by plasmonic diamond

In order to test the effect of plasmonic material over the NW structure, the cylindrical SiNWs decorated by Ag diamond is studied. **Figure 8(a)** illustrates the computational domain of the proposed plasmonic unit cell in the x-z plane, while **Figure 8(b)** shows the top view of the suggested design. The positive and negative z directions of the unit cell are surrounded by PML boundary conditions, while the unit cell is surrounded by periodic BCs along x

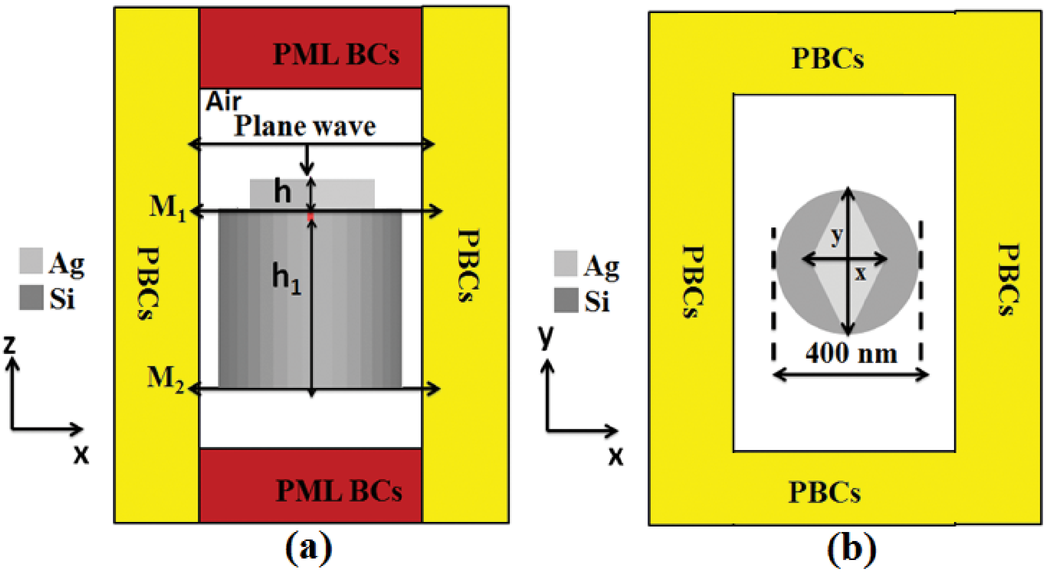

Figure 8. Computational domain of the proposed cylindrical SiNWs decorated by Ag diamond in the (a) x-z plane and (b) x-y plane.

and y directions to simulate periodic square SiNW array. The reported design of the silicon NWs decorated by Ag diamond is specifically illuminated from the top by a plane wave ranging from $\lambda = 300$ to 1100 nm, which covers the main part of the solar spectrum. Two frequency-domain field monitors M_1 and M_2 are placed at the top and bottom of the cell, respectively, to calculate the absorption in the SiNW which is defined by $A_{Si} = M_1 - M_2$. In this study, the height and the diameter of the Si nanowire are equal to 500 and 400 nm, respectively. Furthermore, the major and minor axes of the Ag diamond shape are taken as x and y, respectively. In this investigation, x = y = 320 nm, while the diamond thickness h is equal to 80 nm.

Figure 9(a) shows the absorption spectra of the cylindrical SiNWs and cylindrical SiNWs decorated by Ag diamond. It is revealed from this figure that the cylindrical SiNWs with Ag diamond show superior absorption than cylindrical counterpart over the entire wavelength band. Additionally, **Figure 9(b)** shows the ultimate efficiency and short-circuit current density of the studied designs. The ultimate efficiency of the plasmonic design is equal to 21.1% which is greater than the conventional cylindrical design of ultimate efficiency = 16%. Therefore, the cylindrical-shaped design with Ag diamond offers an overall enhancement of 31.9% over the cylindrical SiNWs counterpart. Further, the plasmonic design has a short-circuit current density of 17.3 mA/cm^2 which is greater than that of the conventional cylindrical design of 13.1 mA/cm^2. The enhancement in the ultimate efficiency and hence short-circuit current density can be attributed to the generated plasmonic mode by the upper Ag diamond which is responsible for improving the absorption through the SiNWs.

Table 2 shows the calculated η, J_{sc}, V_{oc}, FF, and PCE of the cylindrical SiNWs and cylindrical SiNWs decorated by Ag diamond. It is found that the electrical parameters are also enhanced due to the existing plasmonic materials above the active layer. Additionally, the V_{oc} is increased from 640 to 647 mV, and the PCE is also improved from 7.9 to 10.6 with 34.1% enhancement over the cylindrical SiNW counterpart.

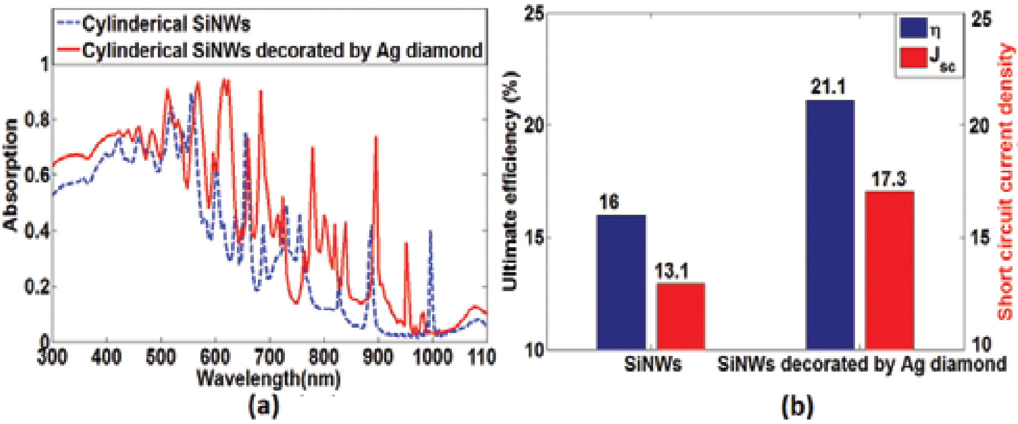

Figure 9. (a) Absorption spectra and (b) ultimate efficiency and short-circuit current density of cylindrical SiNWs and cylindrical SiNWs decorated by Ag diamond.

Structure	**η**	**J_{sc} (mA/cm^2)**	**V_{oc} (v)**	**FF**	**PCE**
Cylindrical SiNWs	16%	13.1	0.64	0.835	7.9
Cylindrical SiNWs decorated with Ag diamond	21.1%	17.3	0.647	0.8369	10.6

Table 2. The calculated values of η, J_{sc}, V_{oc}, FF, and PCE for cylindrical SiNWs and cylindrical SiNWs decorated by Ag diamond.

To further explore the underlying mechanism of the absorption enhancement in the proposed design, the field profiles in x-y and x-z planes at $\lambda = 616$ nm are shown in **Figure 10**. As shown from **Figure 10(b) and (d)**, the field penetration through the proposed design is greater than that of the conventional SiNWs. This is due to the plasmonic particles that have increased the light confinement around the plasmonic material and, thus, allowed more waveguide modes to couple into the SiNWs which is responsible for the absorption enhancement. Additionally, the figures show high field intensity penetration inside the reported SiNWs which is defined by the field hot spots in the figures.

In order to further enhance the absorption capabilities of the proposed SiNWs decorated by Ag diamond, the effects of the structure geometrical parameters are studied. **Figure 11(a)** shows the impact of the diamond minor axis (x) on the ultimate efficiency and short-circuit current density. In this investigation, the other parameters Λ, h_1, and y are kept constant at 500, 500, 400, and 320 nm, respectively. It is concluded that as the minor axis (x) increases to 280 nm, the absorption and hence the ultimate efficiency and short-circuit current density also increase. A maximum ultimate efficiency and short-circuit current density of 21.4% and 17.5 mA/cm^2, receptively, are obtained at x = 280 nm. If the minor axis is further increased, the ultimate efficiency and short-circuit current density will be decreased. Therefore, the tuned value of 280 nm for the minor axis will be used for the subsequent simulations. Next, the effect of the major axis y of the Ag diamond is also investigated and shown in **Figure 11(b)**. It may be seen from this figure that the ultimate efficiency and short-circuit current density have maximum values of 21.9% and 17.1% at y = 360 nm, respectively. If the major axis y is further increased, the reflection will be increased which decreases the absorption and ultimate efficiency as shown in **Figure 11(b)**.

Next, the effect of the diamond thickness (h) on the ultimate efficiency and short-circuit density is also investigated and shown in **Figure 12(a)**. It is revealed from this figure that the diamond height has a slight effect on the absorption and hence short-circuit current density and ultimate efficiency. A maximum ultimate and short-circuit current density of 22.5% and 18.4 mA/cm^2, respectively, occur at h = 120 nm. **Figure 12(b)** shows the variation of ultimate efficiency and short-circuit density with the periodicity of the NW, while the other parameters are kept constant at h = 120 nm, h_1 = 500 nm, x = 280 nm, and y = 360 nm. As the periodicity decreases, the ultimate efficiency and short-circuit current density increase. The maximum ultimate efficiency of 25.7% is obtained at periodicity of 400 nm which is higher than that of the conventional SiNWs without plasmonic material by 63% at the same periodicity. This enhancement is due to the change of the periodicity which leads to a change in the filling ratio (at fixed diamond size) which in turn influences the generated localized surface plasmon resonance.

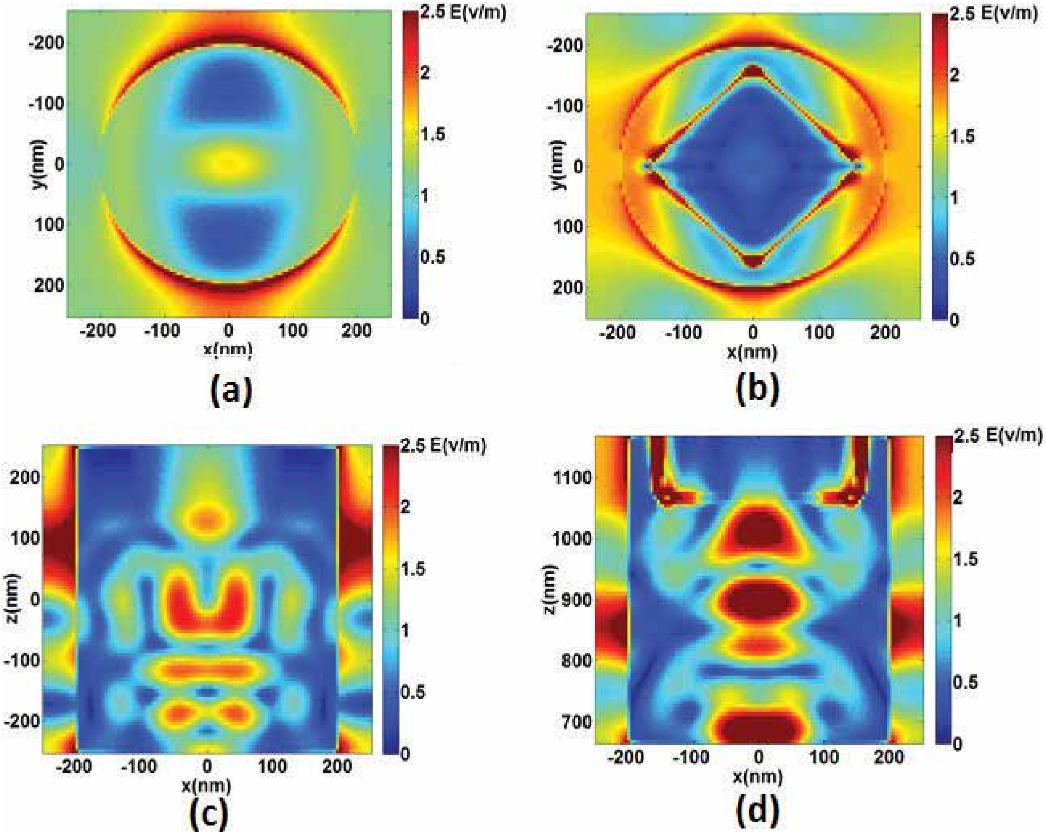

Figure 10. Absorbed field profiles for cylindrical SiNWs without and with Ag diamond particle in the (a, b) x-y plane and in the (c, d) x-z plane at $\lambda = 616$ nm.

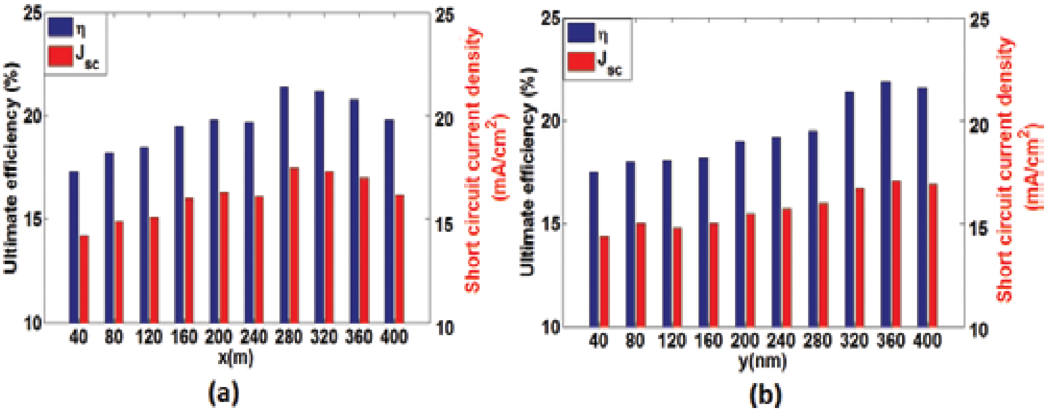

Figure 11. Variation of the short-circuit current density and ultimate efficiency of the conventional SiNWs and SiNWs decorated by Ag diamond with the (a) minor axis x and (b) major axis y.

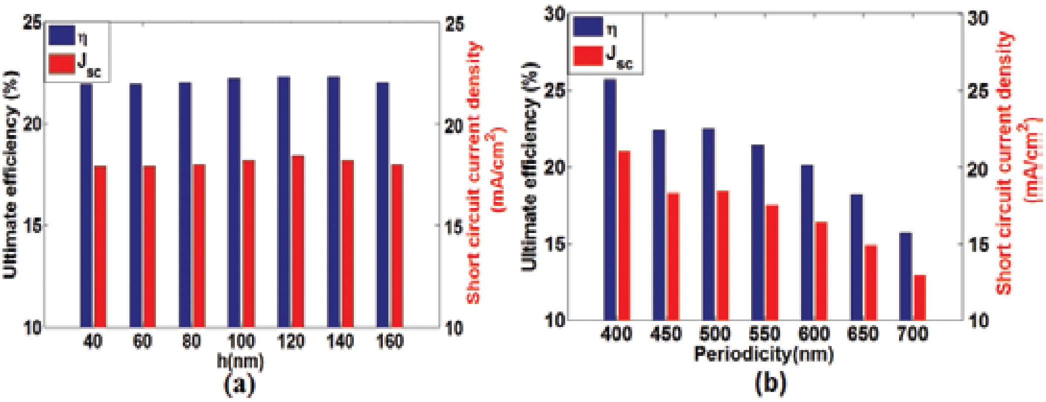

Figure 12. Variation of the short-circuit current density and ultimate efficiency for the conventional SiNWs and SiNWs decorated by Ag diamond with the (a) diamond height and (b) periodicity.

5. Conclusion

In this chapter, the possibility of improving the light trapping through the SiNWs by using plasmonic materials is discussed and studied. In this regard, the effects of using plasmonic materials inside or above the SiNWs are introduced. In these investigations, two novel designs of plasmonic SiNW solar cells are presented and analyzed using the 3D FDTD method. A full study for optical and analytical electrical efficiencies has been carried out. The ultimate efficiency and power conversion efficiency have been calculated to quantify the overall performance of the proposed designs. Further, the designed geometrical parameters are tuned to maximize the optical and electrical efficiencies. The obtained ultimate efficiency and power conversion efficiency of the plasmonic funnel design are equal to 44 and 18.9% with an enhancement of 43.3% over its cylindrical NW counterpart. Additionally, the cylindrical SiNWs decorated by Ag diamond offer an ultimate efficiency and short-circuit current density of 25.7% and 21.03 mA/cm^2, respectively, with an improvement of 63% over the conventional SiNWs. The proposed plasmonic solar cell designs could be very crucial to present low-cost, high-absorption efficiency, and shape-controlled nanopillars for energy-harvesting applications.

Author details

Mohamed Hussein[1,2,], Mohamed Farhat Othman Hameed[1,3,] and Salah S. A. Obayya[1,3,*]

*Address all correspondence to: sobayya@zewailcity.edu.eg

1 Centre of Photonics and Smart Materials, Zewail City of Science and Technology, Giza, Egypt

2 Faculty of Science, Ain Shams University, Cairo, Egypt

3 Faculty of Engineering, Mansoura University, Mansoura, Egypt

References

[1] G. Sadashivappa, and N. Sharvari, "Nanoantenna-a review," International Journal of Renewable Energy Technology Research, Vol. 4, pp. 1-9, 2015.

[2] M. A. Khan, P. Sichanugrist, S. Kato, and Y. Ishikawa, "Theoretical investigation about the optical characterization of cone-shaped pin-Si nanowire for top cell application," Energy Science & Engineering, Vol. 4, pp. 383-393, 2016.

[3] L. Mescia, and A. Massaro, "New trends in energy harvesting from earth long-wave infrared emission," Advances in Materials Science and Engineering, Vol. 2014, p. 10, 2014.

[4] F. Manzano-Agugliaro, A. Alcayde, F. G. Montoya, A. Zapata-Sierra, and C. Gil, "Scientific production of renewable energies worldwide: an overview," Renewable and Sustainable Energy Reviews, Vol. 18, pp. 134-143, 2//2013.

[5] A. Arigliano, P. Caricato, A. Grieco, and E. Guerriero, "Producing, storing, using and selling renewable energy: the best mix for the small medium industry," Computers in Industry, Vol. 65, pp. 408-418, 4//2014.

[6] O. D. Miller, "Photonic Design: From Fundamental Solar Cell Physics to Computational Inverse Design," ed, 2012 arXiv:1308.0212 [physics.optics].

[7] W. Wang, J. Zhang, X. Che, and G. Qin, "Large absorption enhancement in ultrathin solar cells patterned by metallic nanocavity arrays," Scientific Reports, Vol. 6, p. 34219, 10/05/online 2016.

[8] W. Raja, A. Bozzola, P. Zilio, E. Miele, S. Panaro, H. Wang ,A. Toma, A. Alabastri, F. Angelis and R. Zaccaria, et al., "Broadband absorption enhancement in plasmonic nanoshells-based ultrathin microcrystalline-Si solar cells," Scientific Reports, Vol. 6, p. 24539, 04/15 11/15/received 03/31/accepted 2016.

[9] S. Foster, and S. John, "Light-trapping design for thin-film silicon-perovskite tandem solar cells," Journal of Applied Physics, Vol. 120, p. 103103, 2016/09/14 2016.

[10] D. M. Powell, M. T. Winkler, H. J. Choi, C. B. Simmons, D. B. Needleman, and T. Buonassisi, "Crystalline silicon photovoltaics: a cost analysis framework for determining technology pathways to reach baseload electricity costs," Energy & Environmental Science, Vol. 5, pp. 5874-5883, 2012.

[11] O. El Daif, E. Drouard, G. Gomard, A. Kaminski, A. Fave, M. Lemiti, et al., "Absorbing one-dimensional planar photonic crystal for amorphous silicon solar cell," Optics Express, Vol. 18, pp. A293–A299, 2010/09/13 2010.

[12] J. Grandidier, D. M. Callahan, J. N. Munday, and H. A. Atwater, "Gallium arsenide solar cell absorption enhancement using whispering gallery modes of dielectric nanospheres," IEEE Journal of Photovoltaics, Vol. 2, pp. 123-128, 2012.

[13] B. Li, J. Liu, G. Xu, R. Lu, L. Feng, and J. Wu, "Development of pulsed laser deposition for CdS/CdTe thin film solar cells," Applied Physics Letters, Vol. 101, p. 153903, 2012/10/08 2012.

[14] P. J. Carrington, M. C. Wagener, J. R. Botha, A. M. Sanchez, and A. Krier, "Enhanced infrared photo-response from GaSb/GaAs quantum ring solar cells," Applied Physics Letters, Vol. 101, p. 231101, 2012/12/03 2012.

[15] J. Cao, Z. Zhan, L. Hou, Y. Long, P. Liu, and W. Mai, "Optical modeling of organic solar cells based on rubrene and C70," Applied Optics, Vol. 51, pp. 5718-5723, 2012/08/10 2012.

[16] D. Shahrjerdi, S. W. Bedell, C. Ebert, C. Bayram, B. Hekmatshoar, K. Fogel, et al., "High-efficiency thin-film InGaP/InGaAs/Ge tandem solar cells enabled by controlled spalling technology," Applied Physics Letters, Vol. 100, p. 053901, 2012/01/30 2012.

[17] A. G. Imenes, and D. R. Mills, "Spectral beam splitting technology for increased conversion efficiency in solar concentrating systems: a review," Solar Energy Materials and Solar Cells, Vol. 84, pp. 19-69, 10//2004.

[18] A. Polman, and H. A. Atwater, "Photonic design principles for ultrahigh-efficiency photovoltaics," Nature Materials, Vol. 11, pp. 174-177, 03//print 2012.

[19] J. A. Dobrowolski, D. Poitras, P. Ma, H. Vakil, and M. Acree, "Toward perfect antireflection coatings: numerical investigation," Applied Optics, Vol. 41, pp. 3075-3083, 2002/06/01 2002.

[20] P. Singh, S. N. Sharma, and N. M. Ravindra, "Applications of porous silicon thin films in solar cells and biosensors," JOM, Vol. 62, pp. 15-24, 2010.

[21] Z. Xi, D. Yang, and D. Que, "Texturization of monocrystalline silicon with tribasic sodium phosphate," Solar Energy Materials and Solar Cells, Vol. 77, pp. 255-263, 5/30/2003.

[22] D. Iencinella, E. Centurioni, R. Rizzoli, and F. Zignani, "An optimized texturing process for silicon solar cell substrates using TMAH," Solar Energy Materials and Solar Cells, Vol. 87, pp. 725-732, 5//2005.

[23] P. Papet, O. Nichiporuk, A. Kaminski, Y. Rozier, J. Kraiem, J. F. Lelievre, et al., "Pyramidal texturing of silicon solar cell with TMAH chemical anisotropic etching," Solar Energy Materials and Solar Cells, Vol. 90, pp. 2319-2328, 9/22/2006.

[24] S. Hayashi, T. Minemoto, H. Takakura, and Y. Hamakawa, "Influence of texture feature size on spherical silicon solar cells," Rare Metals, Vol. 25, pp. 115-120, 2006/10/01 2006.

[25] P. Campbell, and M. A. Green, "Light trapping properties of pyramidally textured surfaces," Journal of Applied Physics, Vol. 62, pp. 243-249, 1987/07/01 1987.

[26] S. C. Baker-Finch, and K. R. McIntosh, "Reflection of normally incident light from silicon solar cells with pyramidal texture," Progress in Photovoltaics: Research and Applications, Vol. 19, pp. 406-416, 2011.

[27] J. Zhao, A. Wang, M. A. Green, and F. Ferrazza, "19.8% efficient “honeycomb” textured multicrystalline and 24.4% monocrystalline silicon solar cells," Applied Physics Letters, Vol. 73, pp. 1991-1993, 1998/10/05 1998.

[28] M. Hussein, M. F. O. Hameed, N. F. F. Areed, and S. S. A. Obayya, "Ultra-high efficient solar cell based on decagonal arrays of silicon nanowires," Optical Engineering, Vol. 53, pp. 117105-117105, 2014.

[29] M. Hussein, M. F. O. Hameed, N. F. F. Areed, A. Yahia, and S. S. A. Obayya, "Funnel-shaped silicon nanowire for highly efficient light trapping," Optics Letters, Vol. 41, pp. 1010-1013, 2016/03/01 2016.

[30] Y.-C. Lee, C.-F. Huang, J.-Y. Chang, and M.-L. Wu, "Enhanced light trapping based on guided mode resonance effect for thin-film silicon solar cells with two filling-factor gratings," Optics Express, Vol. 16, pp. 7969-7975, 2008/05/26 2008.

[31] H. Nakaya, M. Nishida, Y. Takeda, S. Moriuchi, T. Tonegawa, T. Machida, et al., "Polycrystalline silicon solar cells with V-grooved surface," Solar Energy Materials and Solar Cells, Vol. 34, pp. 219-225, 1994/09/01 1994.

[32] X. D. Wang, E. Graugnard, J. S. King, Z. L. Wang, and C. J. Summers, "Large-scale fabrication of ordered nanobowl arrays," Nano Letters, Vol. 4, pp. 2223-2226, 2004/11/01 2004.

[33] J. W. Leem, D. H. Joo, and J. S. Yu, "Biomimetic parabola-shaped AZO subwavelength grating structures for efficient antireflection of Si-based solar cells," Solar Energy Materials and Solar Cells, Vol. 95, pp. 2221-2227, 8//2011.

[34] J. W. Leem, J. S. Yu, Y. M. Song, and Y. T. Lee, "Antireflective characteristics of disordered GaAs subwavelength structures by thermally dewetted Au nanoparticles," Solar Energy Materials and Solar Cells, Vol. 95, pp. 669-676, 2//2011.

[35] H. A. Atwater, and A. Polman, "Plasmonics for improved photovoltaic devices," Nature Materials, Vol. 9, pp. 205-213, 03//print 2010.

[36] S. Nie, and S. R. Emory, "Probing single molecules and single nanoparticles by surface-enhanced Raman scattering," Science, Vol. 275, p. 1102, 1997.

[37] S. A. Maier, M. L. Brongersma, P. G. Kik, S. Meltzer, A. A. G. Requicha, and H. A. Atwater, "Plasmonics—a route to nanoscale optical devices," Advanced Materials, Vol. 13, pp. 1501-1505, 2001.

[38] X. D. Hoa, A. G. Kirk, and M. Tabrizian, "Towards integrated and sensitive surface plasmon resonance biosensors: a review of recent progress," Biosensors and Bioelectronics, Vol. 23, pp. 151-160, 9/30/2007.

[39] M. Hussein, N. F. F. Areed, M. F. O. Hameed, and S. S. A. Obayya, "Design of flower-shaped dipole nano-antenna for energy harvesting," IET Optoelectronics, Vol. 8, pp. 167-173, 2014.

[40] O. Salah, A. Nihal Fayez Fahmy, O. H. Mohamed Farhat, and A. Mohamed Hussein, "Optical nano-antennas for energy harvesting," in Innovative Materials and Systems for Energy Harvesting Applications, M. Luciano, L. Onofrio, and P. Francesco, Eds., Hershey, PA, USA: IGI Global, 2015, pp. 26-62.

[41] Y. M. El-Toukhy, M. Hussein, M. F. O. Hameed, A. M. Heikal, M. M. Abd-Elrazzak, and S. S. A. Obayya, "Optimized tapered dipole nanoantenna as efficient energy harvester," Optics Express, Vol. 24, pp. A1107–A1122, 2016/07/11 2016.

[42] K. Nakayama, K. Tanabe, and H. A. Atwater, "Plasmonic nanoparticle enhanced light absorption in GaAs solar cells," Applied Physics Letters, Vol. 93, p. 121904, 2008.

[43] D. Derkacs, S. H. Lim, P. Matheu, W. Mar, and E. T. Yu, "Improved performance of amorphous silicon solar cells via scattering from surface plasmon polaritons in nearby metallic nanoparticles," Applied Physics Letters, Vol. 89, p. 093103, 2006.

[44] H. R. Stuart, and D. G. Hall, "Island size effects in nanoparticle-enhanced photodetectors," Applied Physics Letters, Vol. 73, pp. 3815-3817, 1998.

[45] D. M. Schaadt, B. Feng, and E. T. Yu, "Enhanced semiconductor optical absorption via surface plasmon excitation in metal nanoparticles," Applied Physics Letters, Vol. 86, p. 063106, 2005.

[46] S. Pillai, K. R. Catchpole, T. Trupke, and M. A. Green, "Surface plasmon enhanced silicon solar cells," Journal of Applied Physics, Vol. 101, p. 093105, 2007.

[47] Z. Ouyang, X. Zhao, S. Varlamov, Y. Tao, J. Wong, and S. Pillai, "Nanoparticle-enhanced light trapping in thin-film silicon solar cells," Progress in Photovoltaics: Research and Applications, Vol. 19, pp. 917-926, 2011.

[48] F. J. Beck, S. Mokkapati, and K. R. Catchpole, "Plasmonic light-trapping for Si solar cells using self-assembled, Ag nanoparticles," Progress in Photovoltaics: Research and Applications, Vol. 18, pp. 500-504, 2010.

[49] H. Tan, R. Santbergen, A. H. Smets, and M. Zeman, "Plasmonic light trapping in thin-film silicon solar cells with improved self-assembled silver nanoparticles," Nano Letters, Vol. 12, pp. 4070-4076, 2012.

[50] L. Lu, Z. Luo, T. Xu, and L. Yu, "Cooperative plasmonic effect of Ag and Au nanoparticles on enhancing performance of polymer solar cells," Nano Letters, Vol. 13, pp. 59-64, 2012.

[51] A. P. Kulkarni, K. M. Noone, K. Munechika, S. R. Guyer, and D. S. Ginger, "Plasmon-enhanced charge carrier generation in organic photovoltaic films using silver nanoprisms," Nano Letters, Vol. 10, pp. 1501-1505, 2010.

[52] I. Ding, J. Zhu, W. Cai, S. J. Moon, N. Cai, P. Wang, et al., "Plasmonic dye-sensitized solar cells," Advanced Energy Materials, Vol. 1, pp. 52-57, 2011.

[53] C. Hägglund, M. Zäch, and B. Kasemo, "Enhanced charge carrier generation in dye sensitized solar cells by nanoparticle plasmons," Applied Physics Letters, Vol. 92, p. 013113, 2008.

[54] B. P. Rand, P. Peumans, and S. R. Forrest, "Long-range absorption enhancement in organic tandem thin-film solar cells containing silver nanoclusters," Journal of Applied Physics, Vol. 96, pp. 7519-7526, 2004.

[55] A. J. Morfa, K. L. Rowlen, T. H. R. III, M. J. Romero, and J. V. D. Lagemaat, "Plasmon-enhanced solar energy conversion in organic bulk heterojunction photovoltaics," Applied Physics Letters, Vol. 92, p. 013504, 2008.

[56] F.-C. Chen, J.-L. Wu, C.-L. Lee, Y. Hong, C.-H. Kuo, and M. H. Huang, "Plasmonic-enhanced polymer photovoltaic devices incorporating solution-processable metal nanoparticles," Applied Physics Letters, Vol. 95, p. 013305, 2009.

[57] R. M. Ferdous, A. W. Reza, and M. F. Siddiqui, "Renewable energy harvesting for wireless sensors using passive RFID tag technology: a review," Renewable and Sustainable Energy Reviews, Vol. 58, pp. 1114-1128, 2016.

[58] J. Nelson, The Physics of Solar Cells. Vol. 1: World Scientific, Imperial College, UK, 2003.

[59] L. Hu, and G. Chen, "Analysis of optical absorption in silicon nanowire arrays for photovoltaic applications," Nano Letters, Vol. 7, pp. 3249-3252, 2007.

[60] L. Cao, P. Fan, A. P. Vasudev, J. S. White, Z. Yu, W. Cai, et al., "Semiconductor nanowire optical antenna solar absorbers," Nano Letters, Vol. 10, pp. 439-445, 2010.

[61] C. Lin, and M. L. Povinelli, "Optical absorption enhancement in silicon nanowire and nanohole arrays for photovoltaic applications," in Proc. SPIE 7772, Next Generation (Nano) Photonic and Cell Technologies for Solar Energy Conversion, 77721G (August 24, 2010); doi:10.1117/12.860254.

[62] C. Lin, and M. L. Povinelli, "Optical absorption enhancement in silicon nanowire arrays with a large lattice constant for photovoltaic applications," Optics Express, Vol. 17, pp. 19371-19381, 2009.

[63] C. Lin, and M. L. Povinelli, "Optimal design of aperiodic, vertical silicon nanowire structures for photovoltaics," Optics Express, Vol. 19, pp. A1148–A1154, 2011.

[64] J. Li, H. Yu, S. M. Wong, X. Li, G. Zhang, P. G.-Q. Lo, et al., "Design guidelines of periodic Si nanowire arrays for solar cell application," Applied Physics Letters, Vol. 95, p. 243113, 2009.

[65] O. L. Muskens, J. G. Rivas, R. E. Algra, E. P. Bakkers, and A. Lagendijk, "Design of light scattering in nanowire materials for photovoltaic applications," Nano Letters, Vol. 8, pp. 2638-2642, 2008.

[66] H. Bao, and X. Ruan, "Optical absorption enhancement in disordered vertical silicon nanowire arrays for photovoltaic applications," Optics Letters, Vol. 35, pp. 3378-3380, 2010.

[67] L. Hong, Rusli, X. Wang, H. Zheng, H. Wang, and H. Yu, "Design guidelines for slanting silicon nanowire arrays for solar cell application," Journal of Applied Physics, Vol. 114, p. 084303, 2013.

[68] R. Ren, Y.-X. Guo, and R.-H. Zhu, "Enhanced absorption in elliptical silicon nanowire arrays for solar energy harvesting," Optical Engineering, Vol. 53, pp. 027102-027102, 2014.

[69] B. Wang, E. Stevens, and P. W. Leu, "Strong broadband absorption in GaAs nanocone and nanowire arrays for solar cells," Optics Express, Vol. 22, pp. A386–A395, 2014.

[70] B. Wang, and P. W. Leu, "Enhanced absorption in silicon nanocone arrays for photovoltaics," Nanotechnology, Vol. 23, p. 194003, 2012.

[71] M.-D. Ko, C.-K. Baek, T. Rim, S. Park, and Y.-H. Jeong, "Optical and electrical characteristics of asymmetric nanowire solar cells," Journal of Applied Physics, Vol. 111, p. 073102, 2012.

[72] F. Lumerical, "Solution, FDTD Solutions 6.5," ed. http://www.lumerical.com/tcad-products/fdtd/

[73] E. D. Palik, Handbook of Optical Constants of Solids Vol. 3: Academic press, Elsevier Inc. 1998.

[74] NREL. Reference Solar Spectral Irradiance: ASTM G-173. Available: http://rredc.nrel.gov/solar/spectra/am1.5/astmg173/astmg173.html. 2016.

[75] Z. Jia, Q. Cheng, J. Song, M. Si, and Z. Luo, "Optical properties of a grating-nanorod assembly structure for solar cells," Optics Communications, Vol. 376, pp. 14-20, 2016.

[76] P. R. Pudasaini, and A. A. Ayon, "Nanostructured thin film silicon solar cells efficiency improvement using gold nanoparticles," Physica Status Solidi (a), Vol. 209, pp. 1475-1480, 2012.

A Comparative Study of Nanowire Arrays for Maximum Power Transmission

Hasan Aykut Şatana, Barışcan Karaosmanoğlu and
Özgür Ergül

Additional information is available at the end of the chapter

http://dx.doi.org/10.5772/67447

Abstract

In this chapter, we present a comparative study of nanowire arrays for the purpose of transmitting electromagnetic energy to long distances with minimum loss. Silver nanowires at an infrared frequency are considered as a case study, using an accurate simulation environment based on the surface-integral equations and the multilevel fast multipole algorithm (MLFMA). Reliable numerical results are obtained by considering arrays as three-dimensional structures with finite sizes in all dimensions. Nanowires with different cross sections are compared in alternative array configurations to assess and compare their transmission properties. While there are no significantly varying performances for the arrays of few elements, large discrepancies occur as the number of nanowires increases. We show that arrays involving nanowires with hexagonal cross sections in hexagonal arrangements can provide significantly better power transmissions in comparison to others. We also present the superiority of a particular case, where the nanowires and gaps between them, both with hexagonal cross sections, are equally distributed, leading to a honeycomb structure. This type of structures demonstrates high-quality transmissions that can be useful in diverse application areas, such as optical coupling, subwavelength imaging, and energy harvesting.

Keywords: nanowire arrays, optical power transmission, surface integral equations, multilevel fast multiple algorithm

1. Introduction

Nanowires are excellent tools for guiding electromagnetic waves with minimum loss at optical frequencies [1–4] particularly as an alternative to dielectric structures at nanometer scales. Plasmonic properties of metals, such as silver (Ag) and gold (Au), enable high-quality power transmissions along nanowires via surface plasmon polaritons [5]. In addition to their favorable characteristics that fully exploit the benefits of the surface plasmons to transfer electromagnetic energy to long distances [6, 7], nanowires are relatively easier to fabricate, making them popular in diverse optics applications, such as optical coupling [4], subwavelength imaging [8–10], microscopy and sensing [11–13], and energy harvesting [14, 15]. While the first samples of fabricated nanowires in the literature are often deformed with undesired defects on their surfaces, rapid advances in nanotechnology have enabled the fabrication of progressively improved structures with desired geometric features. Recent studies demonstrate not only isolated nanowires with smooth surfaces but also their periodic arrangements in regular and highly ordered forms [16, 17].

As in all subareas of nanotechnology, experimental studies on nanowires are supported by numerical and computational analysis [18, 19]. The plasmonic properties of metals at optical frequencies can be modeled using tabulated or formulated permittivity values [20] inserted into the conventional solvers for penetrable bodies [21]. Accurate simulation environments based on various methods and techniques can provide an ability to investigate the effects of the cross-sectional shapes [22–24] and the choice of the material [22] on the nanowire characteristics before their fabrications. For plasmonic problems, not only limited to nanowires, computational methods based on the differential equations are very popular in the literature due to their availability as commercial and noncommercial software. On the other hand, for nanowire simulations, these methods may not enable a rigorous analysis, as the nanowire arrays are typically long in terms of wavelength, while they must be modeled as finite to accurately quantify their electromagnetic responses in most cases. In addition, in array configurations, several nanowires must be modeled together by considering all interactions and coupling between them, without employing any periodicity and/or infinity. For this purpose, integral-equation formulations, particularly the surface-integral equations [25–31] that need discretizations only on the surfaces of the structures, are very suitable for the computational analysis of nanowires, as well as similar structures.

In parallel to the improved capabilities in nanotechnology, recent studies focus on geometric properties (e.g., cross section and length) of nanowires to maximize their performances in the related applications [32, 33]. On the other hand, the best geometric properties of the nanowires, especially their cross sections, and their arrangements in array configurations for maximizing the power output in transmission lines are not well known. In this chapter, we present a comparative study of nanowire arrays in terms of power transmission, that is, transfer of the electromagnetic energy with minimum loss. For numerical tests, we particularly consider transmission properties of Ag nanowires at an infrared frequency (250 THz) and compare various cross-sectional geometries in alternative arrangements. An accurate solver based on surface-integral equations and the multilevel fast multipole algorithm (MLFMA) [34, 35] is used to analyze nanowires as three-dimensional finite structures with full parametric modeling of metals using measured values of the electrical permittivity. Surface formulations lead to dense matrix solutions, whose solutions can be challenging due to the ill-conditioned nature of the problems, large negative permittivity values at optical frequencies, and large dimensions in terms of the operation wavelength. These challenges are solved by using MLFMA in an inner/outer iterative scheme. With the high efficiency and accuracy of the developed solver, we analyze realistic structures by including all mutual couplings between the interacting nanowires. The results demonstrate interesting properties of hexagonal arrangements of hexagonal cells, leading to honeycomb structures, which demonstrate much better transmission capabilities in comparison to others when the arrays are relatively large. In the literature, it is shown that such hexagonal arrangements of nanowires can indeed be fabricated [13, 17], while we also show that the periodicity and the size of the nanowires (that may bring additional challenges in the fabrication) are also critical on the transmission performances of the arrays.

This chapter is organized as follows. First, in Section 2, we briefly present the simulation environment used in this study with some details of the major components. Parameters and variables of the nanowire simulations are discussed in Section 3. Then, Section 4 includes numerical results and comparisons, followed by the discussion and concluding remarks in Sections 5 and 6.

2. Simulation environment

The developed simulation environment for the analysis of plasmonic problems, such as nanowires at optical frequencies, is extensively discussed in Ref. [36]. In this section, we consider the major components of the solver for accurate and efficient analysis of nanowires and their arrays.

2.1. Modified combined tangential formulation

Consider a homogeneous object (nanowire or nanowire array) located in free space (vacuum) and illuminated by time-harmonic sources described by incident electric and magnetic fields ($\boldsymbol{E}^{\mathrm{inc}}$ and $\boldsymbol{H}^{\mathrm{inc}}$). The object is assumed to be nonmagnetic with permeability $\mu_o = 4\pi \times 10^{-7}$ H/m and characterized by a permittivity $\varepsilon_p = (-\varepsilon_R + i\varepsilon_I)\varepsilon_o$, where $\varepsilon_o = 1/(c^2\mu_o)$ and $c = 299792458$ m/s. The equivalence theorem allows us to formulate the problem with equivalent currents $\boldsymbol{J} = \hat{n} \times \boldsymbol{H}$ and $\boldsymbol{M} = -\hat{n} \times \boldsymbol{E}$ defined on the surface of the object with outward normal $\hat{n}$. In phasor domain with the $\exp(-i\omega t)$ time convention, these currents radiate in homogeneous spaces using the impulse (Green's) functions $g_{o,p}(\boldsymbol{r},\boldsymbol{r}') = \exp(ik_{o,p}|\boldsymbol{r} - \boldsymbol{r}'|)/(4\pi|\boldsymbol{r} - \boldsymbol{r}'|)$, where $k_o = \omega\sqrt{\mu_o}\sqrt{\varepsilon_o}$ and $k_p = \omega\sqrt{\mu_o}\sqrt{\varepsilon_p}$ are the wavenumbers for the angular frequency $\omega = 2\pi f = 2\pi c/\lambda_o$ (hence, λ_o is the wavelength in free space). Outer and inner problems are superimposed using the boundary conditions, that is, continuity of the tangential electric and magnetic field intensities, leading to a set of equations that are discretized and converted into matrix equations for numerical solutions.

The method to enforce the boundary conditions leads to alternative ways to construct formulations. Among many, we prefer a recently developed modified combined tangential formulation (MCTF), which can be written as

$$\begin{bmatrix} \overline{\overline{\boldsymbol{Z}}}_{11}^{\mathrm{MCTF}} & \overline{\overline{\boldsymbol{Z}}}_{12}^{\mathrm{MCTF}} \\ \overline{\overline{\boldsymbol{Z}}}_{21}^{\mathrm{MCTF}} & \overline{\overline{\boldsymbol{Z}}}_{22}^{\mathrm{MCTF}} \end{bmatrix} \cdot \begin{bmatrix} \boldsymbol{a}_J \\ \boldsymbol{a}_M \end{bmatrix} = \begin{bmatrix} \boldsymbol{w}_1^{\mathrm{MCTF}} \\ \boldsymbol{w}_2^{\mathrm{MCTF}} \end{bmatrix}, \qquad (1)$$

where

$$\begin{aligned}\overline{\overline{\boldsymbol{Z}}}_{11}^{\mathrm{MCTF}}[m,n] &= i\omega\mu_o\int_{S_m} d\boldsymbol{r}\boldsymbol{t}_m(\boldsymbol{r})\cdot\int_{S_n} d\boldsymbol{r}'\boldsymbol{b}_n(\boldsymbol{r}')[g_o(\boldsymbol{r},\boldsymbol{r}')+g_p(\boldsymbol{r},\boldsymbol{r}')]\\ &\quad+\frac{i}{\omega}\int_{S_m} d\boldsymbol{r}\boldsymbol{t}_m(\boldsymbol{r})\cdot\int_{S_n} d\boldsymbol{r}'\nabla'\cdot\boldsymbol{b}_n(\boldsymbol{r}')\left[\frac{1}{\varepsilon_o}\nabla g_o(\boldsymbol{r},\boldsymbol{r}')+\frac{1}{\varepsilon_p}\nabla g_p(\boldsymbol{r},\boldsymbol{r}')\right]\end{aligned} \tag{2}$$

$$\overline{\overline{\boldsymbol{Z}}}_{12}^{\mathrm{MCTF}}[m,n] = -\int_{S_m} d\boldsymbol{r}\boldsymbol{t}_m(\boldsymbol{r})\cdot\int_{PV,S_n} d\boldsymbol{r}'\boldsymbol{b}_n(\boldsymbol{r}')\times[\nabla' g_o(\boldsymbol{r},\boldsymbol{r}')+\nabla' g_p(\boldsymbol{r},\boldsymbol{r}')] \tag{3}$$

$$\overline{\overline{\boldsymbol{Z}}}_{21}^{\mathrm{MCTF}}[m,n] = -\frac{\mu_o}{\sqrt{\varepsilon_o}\sqrt{\varepsilon_p}}\overline{\overline{\boldsymbol{Z}}}_{12}^{\mathrm{MCTF}}[m,n] \tag{4}$$

$$\begin{aligned}\overline{\overline{\boldsymbol{Z}}}_{22}^{\mathrm{MCTF}}[m,n] &= i\omega\mu_o\int_{S_m} d\boldsymbol{r}\boldsymbol{t}_m(\boldsymbol{r})\cdot\int_{S_n} d\boldsymbol{r}'\boldsymbol{b}_n(\boldsymbol{r}')\left[\frac{\sqrt{\varepsilon_o}}{\sqrt{\varepsilon_p}}g_o(\boldsymbol{r},\boldsymbol{r}')+\frac{\sqrt{\varepsilon_p}}{\sqrt{\varepsilon_o}}g_p(\boldsymbol{r},\boldsymbol{r}')\right]\\ &\quad+\frac{i}{\omega\sqrt{\varepsilon_o}\sqrt{\varepsilon_p}}\int_{S_m} d\boldsymbol{r}\boldsymbol{t}_m(\boldsymbol{r})\cdot\int_{S_n} d\boldsymbol{r}'\nabla'\cdot\boldsymbol{b}_n(\boldsymbol{r}')[\nabla g_o(\boldsymbol{r},\boldsymbol{r}')+\nabla g_p(\boldsymbol{r},\boldsymbol{r}')]\end{aligned} \tag{5}$$

and

$$\boldsymbol{w}_1^{\mathrm{MCTF}}[m] = -\int_{S_m} d\boldsymbol{r}\boldsymbol{t}_m(\boldsymbol{r})\cdot\boldsymbol{E}^{\mathrm{inc}}(\boldsymbol{r}) \tag{6}$$

$$\boldsymbol{w}_2^{\mathrm{MCTF}}[m] = -\frac{\mu_o}{\sqrt{\varepsilon_o}\sqrt{\varepsilon_p}}\int_{S_m} d\boldsymbol{r}\boldsymbol{t}_m(\boldsymbol{r})\cdot\boldsymbol{H}^{\mathrm{inc}}(\boldsymbol{r}). \tag{7}$$

In the above, $\boldsymbol{b}_n$ and $\boldsymbol{t}_m$ are the basis and testing functions for $\{n,m\} = \{1,2,\ldots,N\}$, and PV in Eq. (3) represents the principal value of the integral. In the numerical solutions in this chapter, we consider the Rao-Wilton-Glisson (RWG) functions defined on pairs of discretization triangles, that is, $\boldsymbol{b}_n(\boldsymbol{r}) = 0$ if $\boldsymbol{r} \notin S_n$ and $\boldsymbol{t}_m(\boldsymbol{r}) = 0$ if $\boldsymbol{r} \notin S_m$. Solution of the matrix equation in Eq. (1) provides the coefficients expanding the current densities, that is, $\boldsymbol{a}_J$ and $\boldsymbol{a}_M$ in $\boldsymbol{J}(\boldsymbol{r}) = \sum \boldsymbol{a}_J[n]\boldsymbol{b}_n(\boldsymbol{r})$ and $\boldsymbol{M}(\boldsymbol{r}) = \sum \boldsymbol{a}_M[n]\boldsymbol{b}_n(\boldsymbol{r})$.

It is remarkable that MCTF is stable for arbitrarily large values of ε_R (as opposed to the conventional formulations [37]). As $\varepsilon_R \rightarrow \infty$ and $\varepsilon_p \rightarrow -\infty$, we have $\boldsymbol{a}_M \rightarrow 0$, which is enforced by the second row that reduces into

$$\overline{\boldsymbol{G}}\cdot\boldsymbol{a}_M = 0. \tag{8}$$

In the above, $\overline{\boldsymbol{G}}$ is the Gram matrix, that is,

$$\overline{\boldsymbol{G}}[m,n] = \int_{S_m} d\boldsymbol{r}\boldsymbol{t}_m(\boldsymbol{r})\cdot\boldsymbol{b}_n(\boldsymbol{r}), \tag{9}$$

which contains only five nonzero elements (corresponding to the intersections of the RWG functions) per row or column. While the second row leads to vanishing magnetic currents, the first row of MCTF becomes

$$i\omega\mu_o\int_{S_m} d\boldsymbol{r}\boldsymbol{t}_m(\boldsymbol{r})\cdot\sum_{n=1}^{N}\boldsymbol{a}_J[n]\int_{S_n} d\boldsymbol{r}' g_o(\boldsymbol{r},\boldsymbol{r}')\boldsymbol{b}_n(\boldsymbol{r}') = -\int_{S_m} d\boldsymbol{r}\boldsymbol{t}_m(\boldsymbol{r})\cdot\boldsymbol{E}^{\mathrm{inc}}(\boldsymbol{r}) \tag{10}$$

for $m = 1, 2, \ldots, N$, which is the standard electric-field integral equation for perfectly conducting objects.

2.2. Accelerated matrix-vector multiplications with MLFMA

Matrix equations derived from MCTF can be solved iteratively, where the matrix-vector multiplications can be performed efficiently as

$$\begin{bmatrix} y_1 \\ y_2 \end{bmatrix} = \begin{bmatrix} \overline{\boldsymbol{Y}}_{11}^{\mathrm{MCTF}} & \overline{\boldsymbol{Y}}_{12}^{\mathrm{MCTF}} \\ \overline{\boldsymbol{Y}}_{21}^{\mathrm{MCTF}} & \overline{\boldsymbol{Y}}_{22}^{\mathrm{MCTF}} \end{bmatrix}\cdot\begin{bmatrix} \boldsymbol{x}_J \\ \boldsymbol{x}_M \end{bmatrix} + \begin{bmatrix} \overline{\boldsymbol{U}}_{11}^{\mathrm{MCTF}} & \overline{\boldsymbol{U}}_{12}^{\mathrm{MCTF}} \\ \overline{\boldsymbol{U}}_{21}^{\mathrm{MCTF}} & \overline{\boldsymbol{U}}_{22}^{\mathrm{MCTF}} \end{bmatrix}\cdot\begin{bmatrix} \boldsymbol{x}_J \\ \boldsymbol{x}_M \end{bmatrix}, \tag{11}$$

where $\overline{\boldsymbol{Y}}_{ab}^{\mathrm{MCTF}}$ for $\{a,b\} = \{1,2\}$ represents the near-field interactions that are between the basis and testing functions close to each other for a given distance threshold. There are only $\mathcal{O}(N)$ nonzero elements in each $\overline{\boldsymbol{Y}}_{ab}^{\mathrm{MCTF}}$ with an identical sparsity pattern. Most of the interactions (computations in matrix-vector multiplications) corresponding to the elements in the far-field matrices $\overline{\boldsymbol{U}}_{ab}^{\mathrm{MCTF}} \approx \overline{\boldsymbol{Z}}_{ab}^{\mathrm{MCTF}} - \overline{\boldsymbol{Y}}_{ab}^{\mathrm{MCTF}}$ are calculated on the fly using MLFMA. These matrix elements are never computed directly or stored in memory, while their multiplications with given input vectors $\boldsymbol{x}_J$ and $\boldsymbol{x}_M$ can still be performed with controllable accuracy, as described in [36]. Using MLFMA, a matrix equation can efficiently be solved via Krylov-subspace algorithms with $\mathcal{O}(N\log N)$ complexity per matrix-vector multiplication or iteration.

In the solutions of plasmonic problems, inner interactions are localized as the negative permittivity increases. Since MCTF involves the combinations of interactions from the inner and outer media, the contributions from the inner medium become very small for some long-distance interactions. This allows us to omit such contributions without deteriorating the accuracy [38]. As an example, consider the first term for $\overline{\boldsymbol{Z}}_{11}^{\mathrm{MCTF}}$ in Eq. (2). The integrand involves the combination of Green's functions as

$$g_o(\boldsymbol{r},\boldsymbol{r}') + g_p(\boldsymbol{r},\boldsymbol{r}') = \frac{\exp(ik_o|\boldsymbol{r}-\boldsymbol{r}'|)}{4\pi|\boldsymbol{r}-\boldsymbol{r}'|} - \frac{\exp(ik_p|\boldsymbol{r}-\boldsymbol{r}'|)}{4\pi|\boldsymbol{r}-\boldsymbol{r}'|} = \frac{\exp(ik_o|\boldsymbol{r}-\boldsymbol{r}'|) + \exp(ik_p|\boldsymbol{r}-\boldsymbol{r}'|)}{4\pi|\boldsymbol{r}-\boldsymbol{r}'|}. \tag{12}$$

In a normalized form, the contribution of the inner medium becomes more obvious as

$$\frac{g_o(\boldsymbol{r},\boldsymbol{r}') + g_p(\boldsymbol{r},\boldsymbol{r}')}{g_o(\boldsymbol{r},\boldsymbol{r}')} = 1 + \frac{\exp(ik_p|\boldsymbol{r}-\boldsymbol{r}'|)}{\exp(ik_o|\boldsymbol{r}-\boldsymbol{r}'|)}. \tag{13}$$

If the interactions in MLFMA are to be calculated with an error threshold of Δe, which is determined by the sampling and truncation used in the diagonalization of Green's function [34], it is possible to omit the contribution from the inner medium if

$$|\exp(ik_p|\mathbf{r}-\mathbf{r}'|)| \le \Delta e |\exp(ik_o|\mathbf{r}-\mathbf{r}'|)| = \Delta e. \tag{14}$$

For large values of ε_R, this inequality can be approximated as

$$|\mathbf{r}-\mathbf{r}'| \ge \frac{-\ln(\Delta e)}{k_o\sqrt{\varepsilon_R}} \tag{15}$$

as the condition for the distance to omit the related inner interaction. For example, for two digits of accuracy ($\Delta e = 0.01$) and $\varepsilon_R = 100$ at 250 THz, it is safe to omit the interaction if $|\mathbf{r}-\mathbf{r}'| \ge 88$ nm. This significantly accelerates the matrix-vector multiplications with MLFMA. We emphasize that omitting interactions as described above has no negative effect in the accuracy of the results. In fact, as the frequency drops and ε_R increases, we expect that inner interactions decay quickly such that the inner matrix becomes a Gram matrix and the formulation turns into a perfectly conducting version.

3. Nanowire simulations

In this section, we present the major parameters of the nanowire simulations considered in this chapter using the implementation described in Section 2.

3.1. Nanowire models

We consider Ag nanowires of length 5 μm at a fixed frequency of 250 THz, at which the nanowire length corresponds to approximately $4.17\lambda_o$. At this frequency, the permittivity of Ag can be found as approximately $-60.76 + 4.31i$ [20]. For the cross sections of the nanowires, we use square, circular (circular-like, more precisely, depending on the discretization size), and hexagonal shapes. For all shapes, the cross-sectional area of each nanowire is selected as 0.01 μm^2 (e.g., a square nanowire has 0.1×0.1 μm cross section) other than scaling trials for the hexagonal cases. For numerical solutions, nanowires are discretized with 0.05–0.075 μm triangles ($\lambda_o/24$–$\lambda_o/16$), on which the RWG functions are defined. As shown in the numerical results, we consider arrays of nanowires in 2×1, 2×2, 4×4, and 6×6 arrangements, while the main focus is the comparison of the 6×6 arrays. In the regular arrays, the distance between the centers of two nanowires is 0.2 μm. In the hexagonal arrangements involving hexagonal cells, the center-to-center distance between two nearby nanowires is approximately 0.186 μm. Discretization of each nanowire requires 2772–5376 unknowns. Then, for the 6×6 arrays, these discretizations lead to matrix equations involving 99,792–193,536 unknowns, which need a fast and efficient solver, such as MLFMA, to complete all simulations in hours.

3.2. Excitation

Each nanowire array is excited by a pair of Hertzian dipoles oriented in the opposite directions. The electric and magnetic field intensities created by a single dipole can be written as

$$\boldsymbol{E}^{\mathrm{inc}}(\boldsymbol{r}) = i\omega\mu_o \frac{\exp(ik_oR)}{4\pi R}\left\{\boldsymbol{I}_D\left(1+\frac{i}{k_oR}-\frac{1}{k_o^2R^2}\right) - \boldsymbol{I}_D\cdot\hat{\boldsymbol{R}}\hat{\boldsymbol{R}}\left(1+\frac{3i}{k_oR}-\frac{3}{k_o^2R^2}\right)\right\} \tag{16}$$

$$\boldsymbol{H}^{\mathrm{inc}}(\boldsymbol{r}) = \boldsymbol{I}_D\times\hat{\boldsymbol{R}}\frac{\exp(ik_oR)}{4\pi R}\left(\frac{1}{R}-ik_o\right), \tag{17}$$

where $\boldsymbol{R} = \boldsymbol{r} - \boldsymbol{r}' = \hat{\boldsymbol{R}}R$ and $\boldsymbol{I}_D$ is the dipole moment. The distance between the dipoles is 0.2 μm and they are located symmetrically with 0.2 μm distance from the nanowires. An example to the localization of the dipoles with respect to a 4×4 array of square nanowires is depicted in **Figure 1**. Except for the 2×1 arrays, the transverse locations of the dipoles correspond to gaps between the nanowires, leading to efficient dipole-to-array coupling. For the same reason, the power flow is mainly confined inside these arrays (on the interfaces between the nanowires and gaps), while for the 2×1 arrays (and somewhat for the 2×2 arrays), the transmission occurs mostly on the outer sides.

3.3. Field and power calculations

After the current coefficients are found through iterative solutions employing MLFMA, the near-zone electric and magnetic fields can be found anywhere using the discretized form of

$$\boldsymbol{E}^{\mathrm{sec}}(\boldsymbol{r}) = i\omega\mu_o\int d\boldsymbol{r}'\boldsymbol{J}(\boldsymbol{r}')g_u(\boldsymbol{r},\boldsymbol{r}') + \frac{i}{\omega\varepsilon_u}\int d\boldsymbol{r}'\nabla'\cdot\boldsymbol{J}(\boldsymbol{r}')\nabla g_u(\boldsymbol{r},\boldsymbol{r}') - \int d\boldsymbol{r}'\nabla g_u(\boldsymbol{r},\boldsymbol{r}')\times\boldsymbol{M}(\boldsymbol{r}') \tag{18}$$

$$\boldsymbol{H}^{\mathrm{sec}}(\boldsymbol{r}) = i\omega\varepsilon_u\int d\boldsymbol{r}'\boldsymbol{M}(\boldsymbol{r}')g_u(\boldsymbol{r},\boldsymbol{r}') + \frac{i}{\omega\mu_o}\int d\boldsymbol{r}'\nabla'\cdot\boldsymbol{M}(\boldsymbol{r}')\nabla g_u(\boldsymbol{r},\boldsymbol{r}') + \int d\boldsymbol{r}'\boldsymbol{J}(\boldsymbol{r}')\times\nabla' g_u(\boldsymbol{r},\boldsymbol{r}'), \tag{19}$$

where the integrals are over the surfaces of the structure. The calculations are carried out for the outer ($u = o$) and inner ($u = p$) problems, leading to vanishingly zero fields for the inner and outer regions, respectively. This also allows us to check the accuracy of solutions by testing the equivalence theorem. We note that, for the outer problem, incident fields $\boldsymbol{E}^{\mathrm{inc}}$ and $\boldsymbol{H}^{\mathrm{inc}}$ must be added to the secondary fields $\boldsymbol{E}^{\mathrm{sec}}$ and $\boldsymbol{H}^{\mathrm{sec}}$ to arrive at the total values. Then, by superimposing the results from inner and outer calculations, overall graphics demonstrating the electric and magnetic field intensities in the vicinity of the object are obtained. We

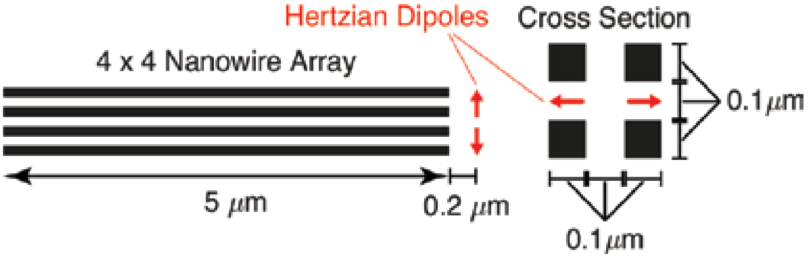

Figure 1. Positions of Hertzian dipoles with respect to a 4×4 nanowire array. The length of all arrays considered in this chapter is 5 μm, while the dipoles oriented in the opposite directions are located symmetrically with 0.2 μm distance from the nanowires.

particularly focus on the magnitudes of the electric field intensity and the magnetic field intensity with units V/m and A/m, respectively, in dB scales. In addition, as a major quantity in the analysis of nanowires, we calculate the Poynting vector (W/m^2), simply called the power density in this chapter, as

$$\boldsymbol{S}(\boldsymbol{r}) = \frac{1}{2}\boldsymbol{E}(\boldsymbol{r}) \times \boldsymbol{H}^{*}(\boldsymbol{r}), \tag{20}$$

where * is the conjugate operation. In this equation, $\boldsymbol{E}$ and $\boldsymbol{H}$ represent the field intensities, corresponding to only secondary fields inside the object and the sum of secondary and incident fields outside the object. We note that the time-average power density is the real part of the expression in Eq. (20). Similar to the field intensities, we present the magnitude of the power density in the results. Considering the continuity of the tangential fields on surfaces, the normal component of the power density is continuous across nanowire/air interfaces, while the main power flow is in the tangential directions (along nanowires). As an example to field intensity and power density distributions, **Figure 2** depicts the excitation of a pair of nanowires with square cross sections. Electric field intensity, magnetic fields intensity, and the real part of the power density are plotted in the vicinity of the dipoles and the tips of the nanowires, where the coupling of the electromagnetic energy to the nanowire system is clearly visible.

3.4. Iterative solutions and parameters

Nanowire problems are challenging in terms of iterative solutions, partially due to MCTF that provides accurate solutions of plasmonic problems at the cost of worse conditioning of matrix equations in comparison to those derived from the second-kind integral equations. Therefore, iterative solutions are performed using a flexible generalized minimal residual (FGMRES) algorithm, which allows for a nested strategy involving inner solutions through GMRES. Specifically, FGMRES employs MLFMA (with 1% maximum error in all solutions) for the matrix-vector multiplications, while it is preconditioned by inner solutions via GMRES. In the inner layer, GMRES employs an approximate form of MLFMA (AMLFMA) [39] that is derived from MLFMA by reducing the number of harmonics. GMRES is further preconditioned via

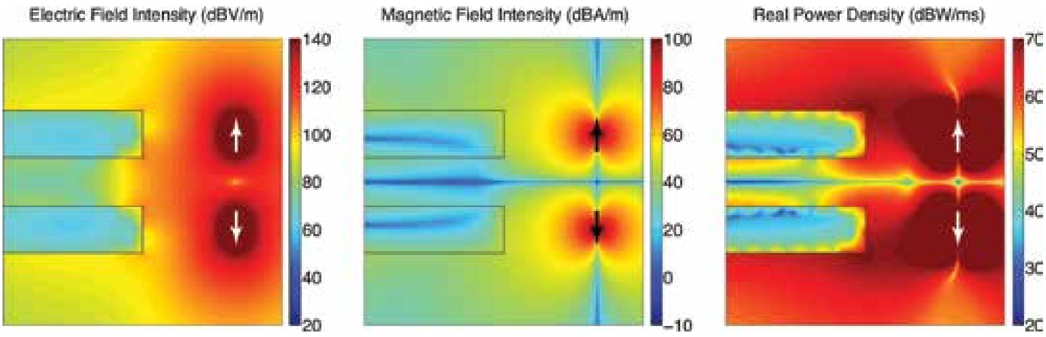

Figure 2. Excitation of a pair of nanowires with square cross sections through a pair of Hertzian dipoles. The electric field intensity, magnetic field intensity, and the real part of the power density are plotted in the vicinity of the dipoles (shown with arrows) and the tips of the nanowires.

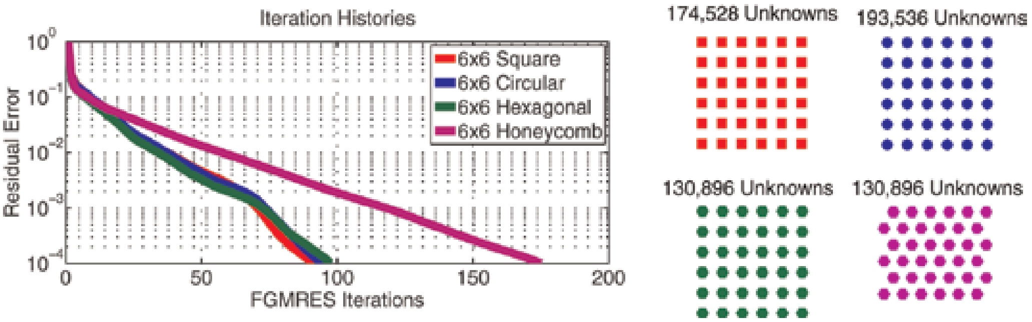

Figure 3. Iteration histories for the solutions of 6×6 nanowire arrays.

algebraic preconditioners based on the near-field interactions. As an example to iterative solutions, **Figure 3** depicts the iteration histories for the analysis of 6×6 nanowire arrays (with number of unknowns shown in **Figure 3**). The residual error is reduced to 10^{-4} (as in all solutions presented in this chapter), requiring nearly 100 iterations for the circular, square, and hexagonal cross sections. For the honeycomb structure, the number of iterations increases to more than 150 to achieve the desired residual error. The reason for larger number of iterations for the honeycomb structure seems to be related to very high transmission capabilities of the nanowires in this configuration, as shown in the simulation results.

4. Nanowire arrays for power transfer

Using the developed solver, we consider nanowires and their arrangements in alternative configurations. Near-zone field intensity and power density values, which are computed accurately with given error thresholds as described above, are used to precisely assess the efficiency of power transmission levels, leading to a rigorous study of nanowire arrays as transmission lines at optical frequencies.

4.1. Double nanowires

First, we consider transmission by pairs of nanowires with different cross sections. **Figure 4** presents the electric field intensity (dBV/m), magnetic field intensity (dBA/m), and power density (dBW/m^2) in the vicinity of the nanowires (on a plane containing dipoles). In each case, a total of 200×800 = 160,000 samples are used for high-quality plots. The excitation dipoles are located on the right-hand side, as clearly observed by large intensity and density values on this side. We observe that the power transmission is almost identical for different cross sections, that is, circular, hexagonal, and square. We note that the nanowires have the same cross-sectional area and the distance between them is the same for all cases. In general, there is a high-quality transmission of the electromagnetic energy along the nanowires, independent of the cross section. In each case, the variations in the electric field intensity, magnetic field intensity, and power density are related to the optical length of the nanowires, which is 5 μm corresponding to approximately 4.17λ_o. While not clearly visible in these plots,

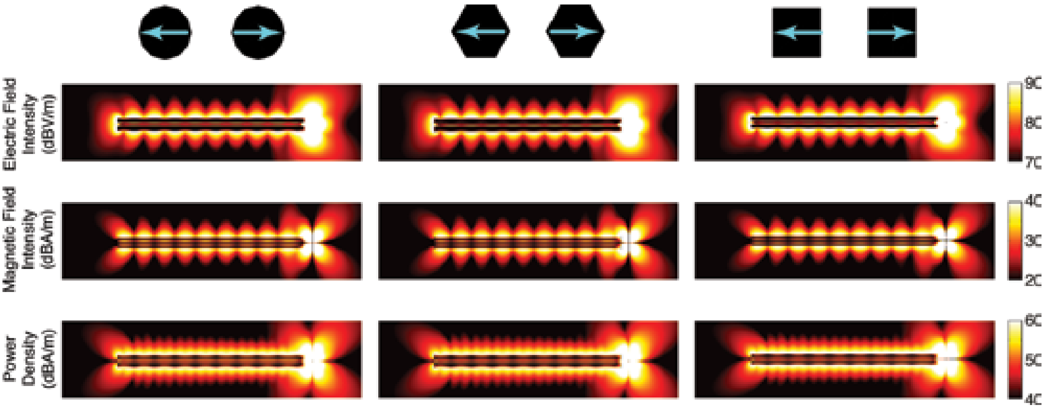

Figure 4. The electric field intensity, magnetic field intensity, and power density values in the vicinity of 2×1 nanowire arrays with different cross sections. The transverse locations of the dipoles (arrows) are also shown.

plasmonic oscillations with much higher rates in the power values exist on the air/metal interfaces, as depicted in **Figure 2** for the nanowires with square cross sections. **Figure 4** also shows that when the transmission line involves only two nanowires, the transmission occurs mostly along the outer surfaces.

4.2. Nanowires in array configurations

Next, we focus on 2×2 systems of nanowires, as depicted in **Figure 5**, again with different cross sections. In this case, the near-field samples (that are on the plane containing the dipoles) do not coincide with the nanowires. Comparing the results for different cross sections, we observe similar characteristics with high-quality transmissions. Specifically, none of the cross-sectional shapes seems to have an advantage over others. Considering the outputs of the

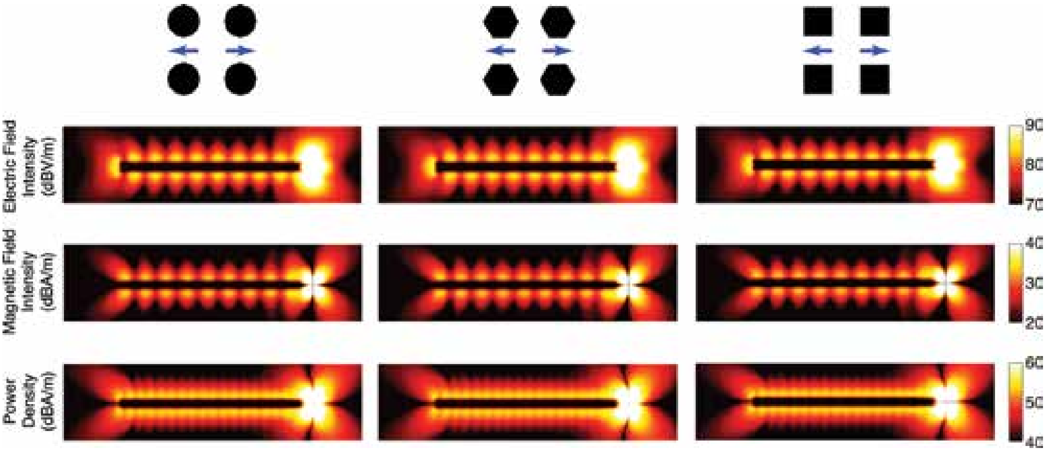

Figure 5. The electric field intensity, magnetic field intensity, and power density values in the vicinity of 2×2 nanowire arrays with different cross sections. The transverse locations of the dipoles (arrows) are also shown.

transmission lines, where the electromagnetic energy is coupled to air, 2×2 arrays seem to be slightly better than the nanowire pairs shown in **Figure 4**. For example, considering the power density distributions, larger beams occur on the left-hand sides of the plots, indicating better transmissions with the 2×2 arrays. Values along the nanowires seem to decrease in comparison to 2×1 systems, but this is (misleadingly) due to the sampling plane that is separated from the nanowires for the 2×2 arrangements. Therefore, for a fair comparison, we need to consider the outputs of the nanowires (on the left-hand sides of the plots).

Figure 6 presents similar results for 4×4 arrays. In this case, in addition to circular, square, and hexagonal nanowires that are regularly arranged, we consider a small-scale honeycomb structure involving hexagonal nanowires in a hexagonal arrangement. We note that the term honeycomb is used to describe the overall structure with hexagonal gaps between hexagonal nanowires with the same cross-sectional areas. In comparison to smaller arrays, the transmissions through 4×4 arrays, which occur in two parallel paths for the regular arrangements, are mostly confined inside the arrays. It is remarkable that the transmission properties are almost the same for the regular arrangements of the nanowires with circular, square, and hexagonal cross sections, while the transmission along the honeycomb structure occurs differently as distributed into more pathways. Nevertheless, considering again the outputs of the nanowires, there is not a clear advantage of this structure over others.

4.3. Comparisons of larger arrays

Dramatic changes occur when the nanowire arrays get larger. In **Figure 7**, we consider arrays of 6×6 nanowires that are arranged similar to the 4×4 arrays. For the regular arrays of nanowires with circular, square, and hexagonal cross sections, the electromagnetic energy is transmitted again in two main lines close to the transverse locations of the dipoles. The transmission performance of these arrays is very similar to each other. On the other hand, a significant improvement is observed when the arrangement is also made hexagonal, leading to a honeycomb structure. This structure clearly outperforms the others with higher quality field and power transmissions. This is further verified in **Figure 8**, where the intensity and density values are sampled at the outputs of the arrays. In these plots, the samples are selected on the transverse plane located at 0.2 μm distance from the nanowire tips (at the output side). In the power density values, more than 5 dB (more than three times) enhancement is observed when the honeycomb structure is used instead of the others.

4.4. Investigation of cross-sectional area

After demonstrating the significantly higher transmission capabilities of the honeycomb structure, it is questioned whether the cross-sectional areas of the nanowires are optimal or not. For this purpose, we consider hexagonal arrangements of 6×6 nanowires with only hexagonal cross sections. As depicted in **Figure 9**, we scale the cross-sectional dimensions by 0.5, 0.75, 1.25, and 1.375, when 1.0 corresponds to the original honeycomb structure. It can be observed that scaling cross-sectional dimensions both to smaller and to larger values leads to deteriorations in the transmission properties of the array. This is again verified by the output plots in **Figure 10**, where the results for a scaling with 1.125 ratio is included as well as for the original

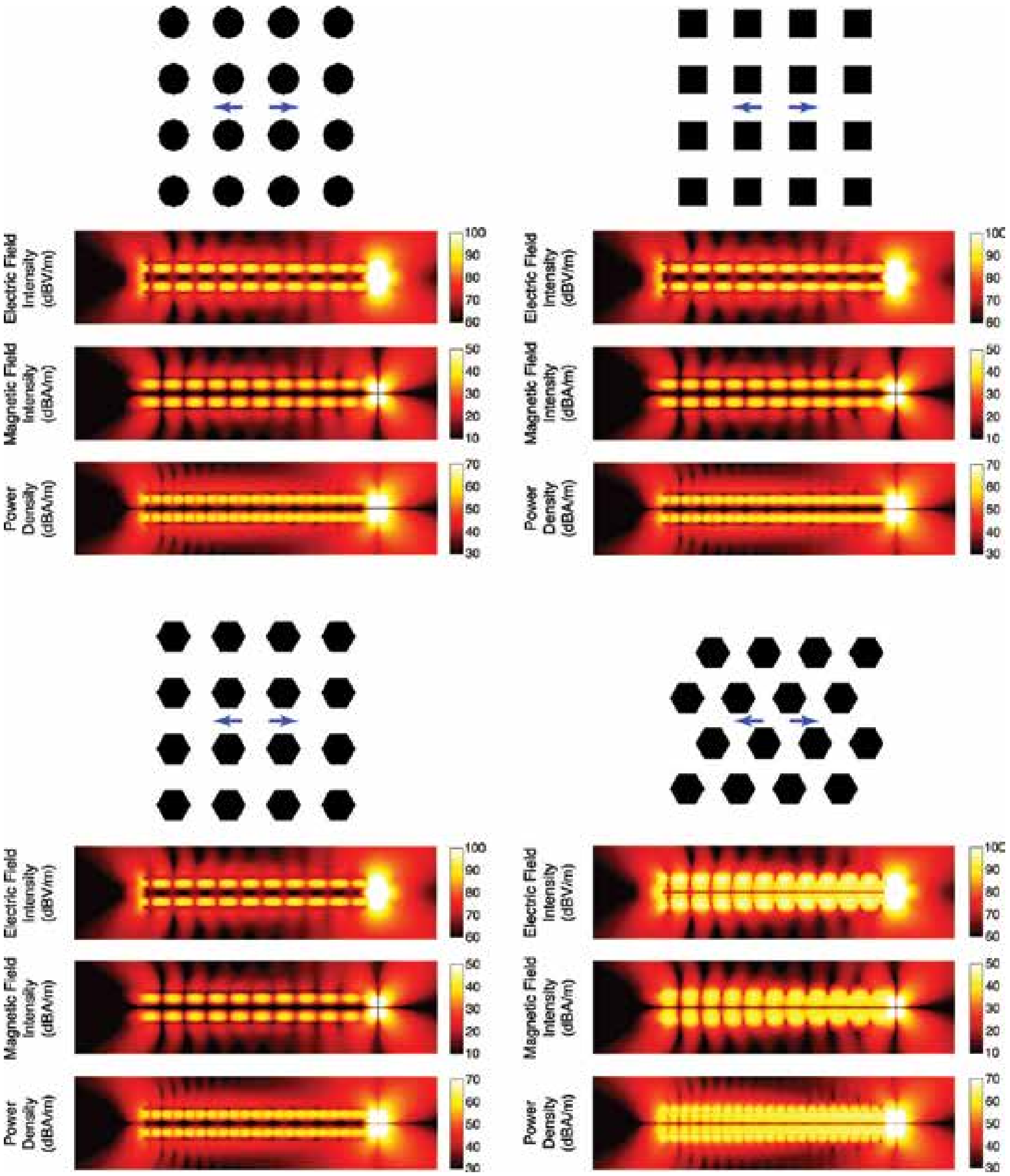

Figure 6. The electric field intensity, magnetic field intensity, and power density values in the vicinity of 4×4 nanowire arrays with different cross sections. The transverse locations of the dipoles (arrows) are also shown. We note that, in the longitudinal direction, the distance between the dipoles and the arrays is 0.2 μm in all cases.

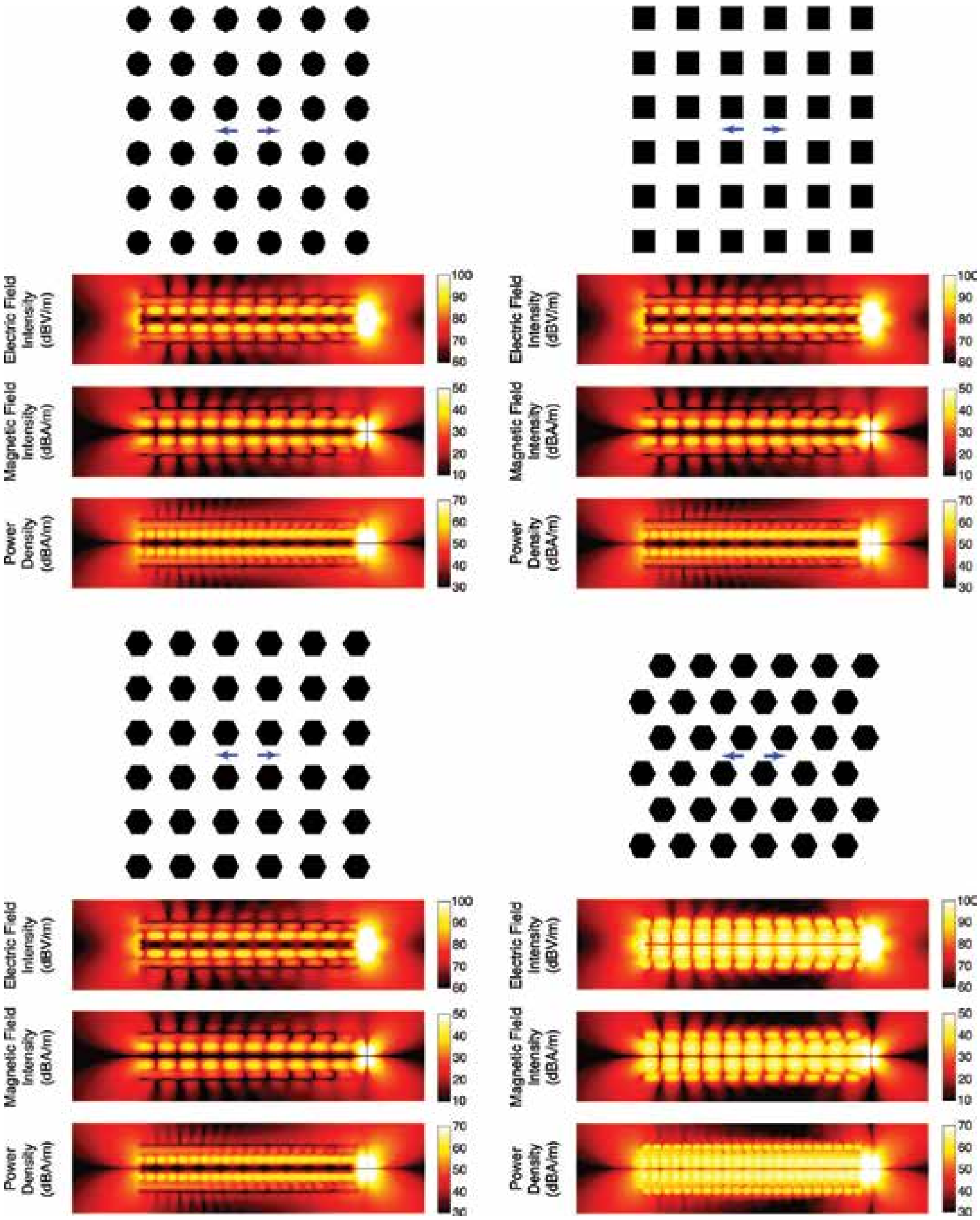

Figure 7. The electric field intensity, magnetic field intensity, and power density values in the vicinity of 6×6 nanowire arrays with different cross sections. The transverse locations of the dipoles (arrows) are also shown. We note that, in the longitudinal direction, the distance between the dipoles and the arrays is 0.2 μm in all cases.

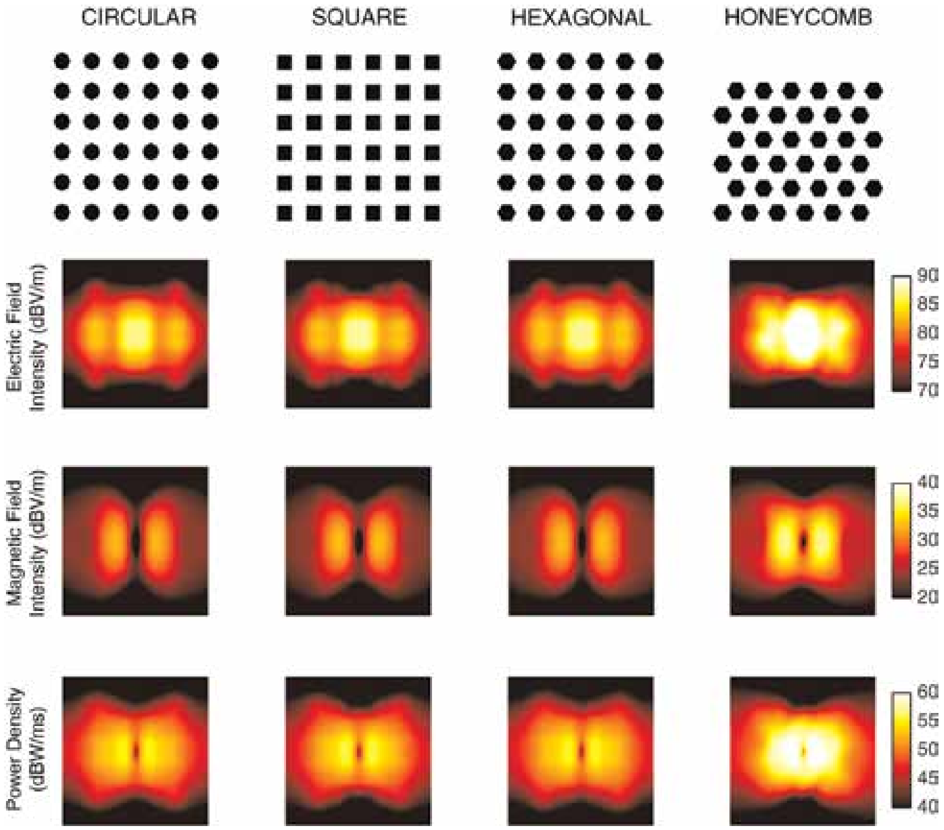

Figure 8. The electric field intensity, magnetic field intensity, and power density values at the outputs of 6×6 nanowire arrays with different cross sections.

structure. As demonstrated in these plots, even small changes in the cross-sectional areas of the nanowires deteriorate the performance of the array, showing the optimality of the honeycomb structure with equally filled and empty spaces.

5. Discussion

Based on the numerical results in Section 4, one may conclude that

- the 6×6 honeycomb structure demonstrates very good transmission properties, in comparison to other arrays with the same number of nanowires under the same conditions,
- closely packing the hexagonal nanowires (scaling up) deteriorates the transmission quality, and
- reducing the dimensions (scaling down) also has a negative effect.

In order to explain the results, we now consider the electric current density ($\boldsymbol{J} = \hat{\boldsymbol{n}} \times \boldsymbol{H}$) on the nanowire surfaces. **Figure 11** depicts the dominant electric current (in dB scale with 20 dB

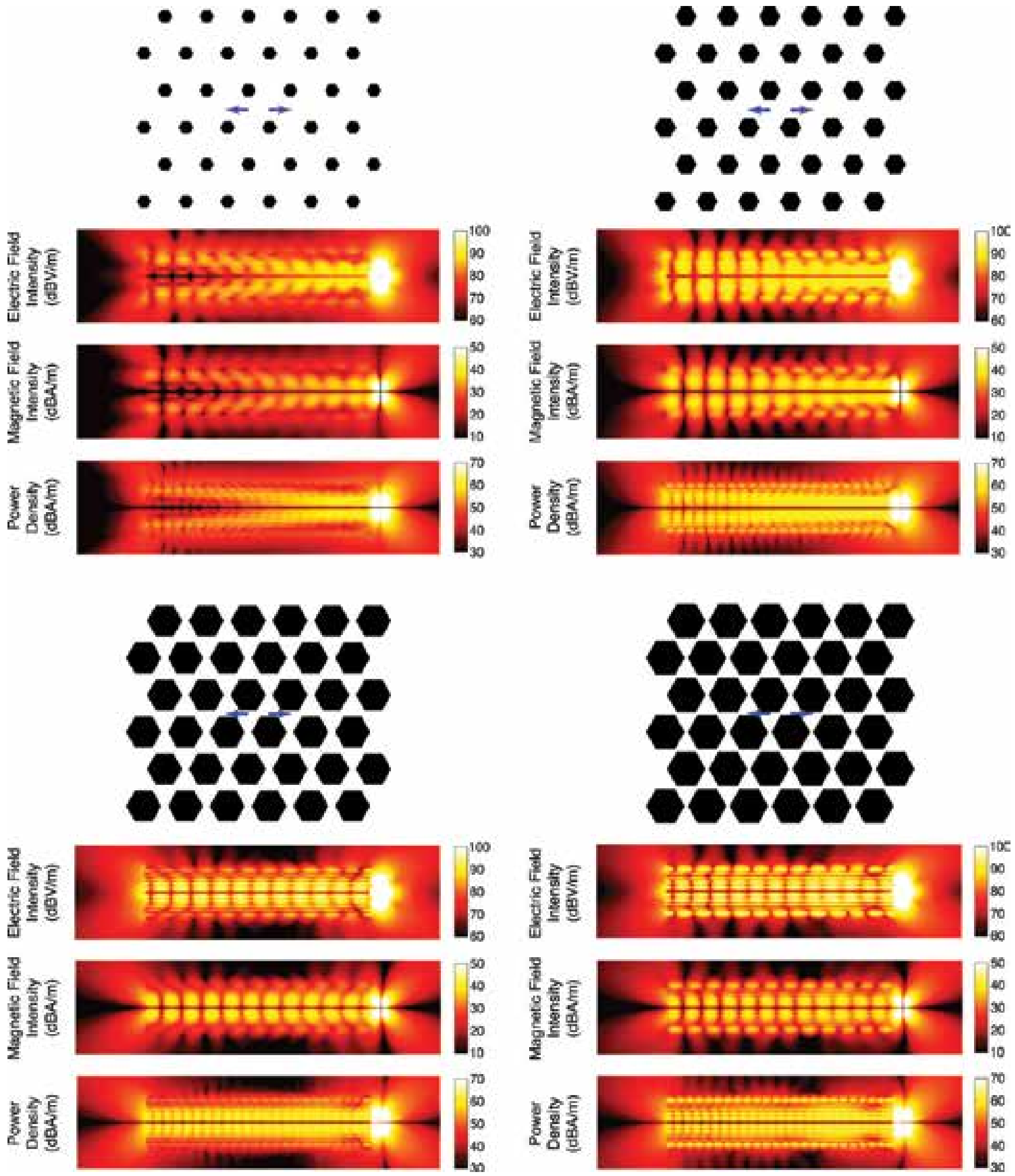

Figure 9. The electric field intensity, magnetic field intensity, and power density values in the vicinity of 6×6 nanowire arrays with hexagonal cross sections of different areas. We note that, in the longitudinal direction, the distance between the dipoles and the arrays is 0.2 μm in all cases.

dynamic range) along the 6×6 arrays of nanowires with circular, square, and hexagonal cross sections, as well as along the honeycomb structure. We also consider the hexagonal arrangement of hexagonal nanowires scaled by the factors of 0.5 and 1.4. It is evident that the current density is much higher for the honeycomb structure. In addition to three-dimensional views, we present a side view when the dipoles are oriented outward/inward. Comparison of current distributions reveals significant differences on the behaviors of the arrays. First, considering

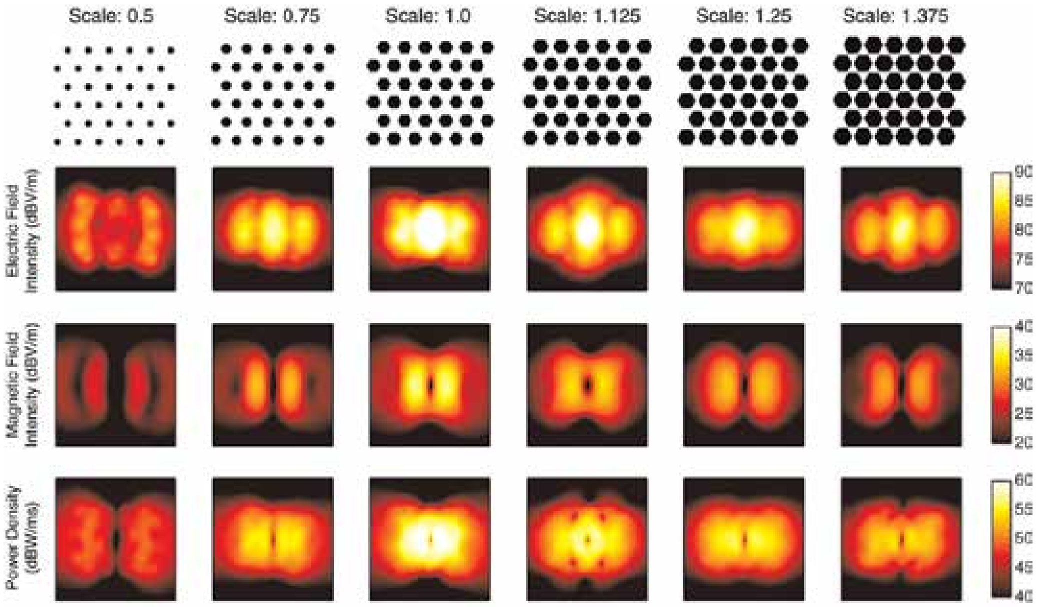

Figure 10. The electric field intensity, magnetic field intensity, and power density values at the outputs of 6×6 nanowire arrays with hexagonal cross sections of different areas. The scale of 1.0 corresponds to the original honeycomb structure.

the array with circular cross sections, it can be observed that the currents along the nanowires are out of phase. Specifically, the current density has maximum locations at different longitudinal positions for the inner two rows and the outer rows. The same situation is also observed for the arrays with square and hexagonal cross sections. All these observations are consistent with the near-zone plots depicted in **Figure 7**.

The out-of-phase currents along the regular arrays can be explained by the adverse effects of neighboring nanowires. Specifically, considering Ampere's circuital law, each nanowire creates a magnetic field that induces current in the opposite direction (to the main current flow) on the neighboring nanowires. Due to the cancellations of the main and secondary currents, the overall currents along the nanowires become out of phase, reducing the transmission capability of the arrays. From this perspective, nanowires in a honeycomb structure are located optimally such that the adverse interactions between nanowires are minimized. Considering how the nanowires are located, it can be observed that nearby surfaces of neighboring nanowires are not aligned and the magnetic coupling between the nanowires is weaker than those in the other arrangements. There are surfaces with identical alignments but these surfaces (on the same sides of the nanowires) are far away from each other. As a result, the currents along the nanowires are almost in phase, as depicted in **Figure 11**.

Scaling the nanowires in the honeycomb structures always has an adverse effect. Decreasing cross-sectional area reduces the overall area of the surfaces for the propagation of plasmonic waves. In addition, increasing distance between the surfaces of the neighboring nanowires adds extra phase in the magnetic coupling, deteriorating the synchronization of the currents. Obviously, increasing the cross-sectional area also has adverse effect as a result of increasing

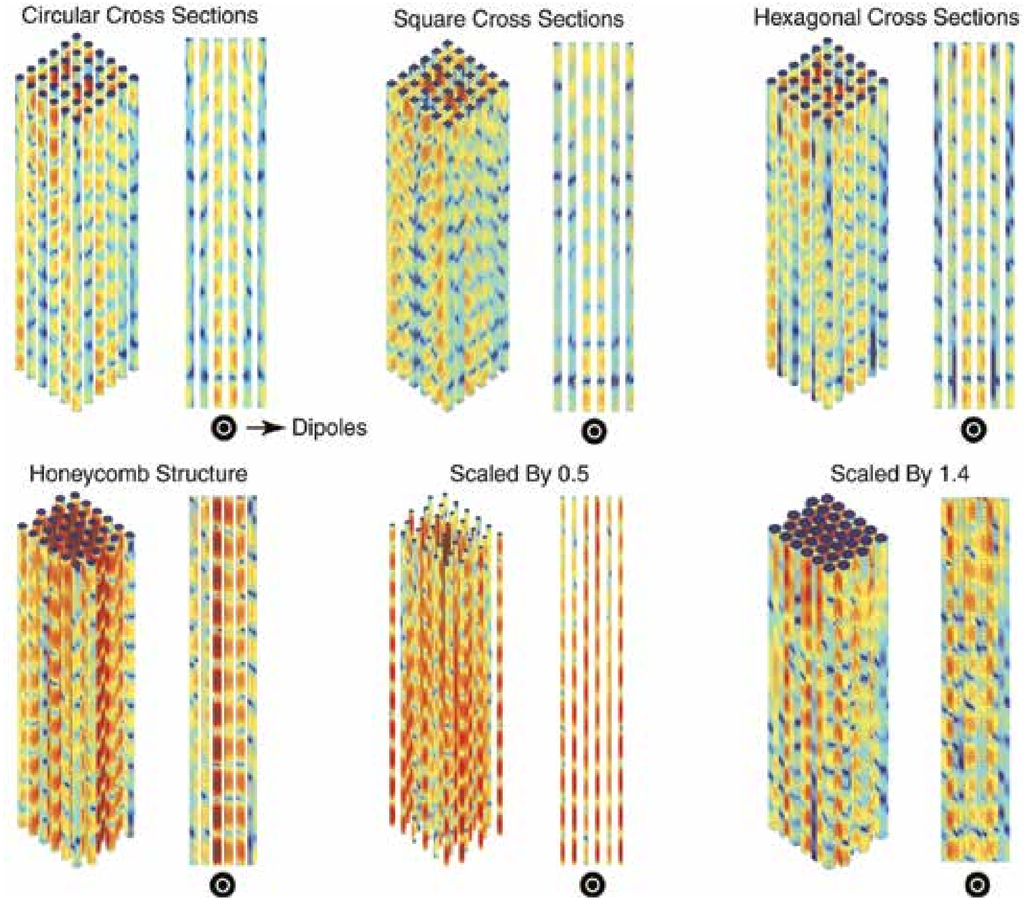

Figure 11. The magnitude of the electric current density induced on the nanowire surfaces for different array configurations. The location and orientation (outward and inward) of the dipole pair are shown in side views.

coupling between the nanowires. It appears that the honeycomb structure is a kind of optimal way to transmit power.

6. Concluding remarks

An investigation of nanowire transmission lines may lead to optimal structures that can be used in nano-optical devices. In this chapter, we present the effects of cross-sectional geometry and arrangement of array elements in different configurations. Using an accurate full-wave simulation environment, we obtain reliable results of three-dimensional finite arrays without resorting to approximation methods and asymptotic optical techniques that may have significant accuracy problems. Based on a comparative study of Ag nanowires at an infrared frequency, we show that power transmission becomes significantly higher for nanowires with hexagonal cross sections and their hexagonal arrangements, leading to honeycomb structures. We also explain the favorable electromagnetic characteristics of these structures, which may pave a way for improved nanowire systems for optimal power transmission.

Acknowledgements

This work was supported by the Scientific and Technical Research Council of Turkey (TUBITAK) under the Research Grant 113E129 and by the Turkish Academy of Sciences (TUBA) in the framework of the Young Scientist Award Program.

Authors contributions

Ö.E. developed the theory and formulations, B.K. and Ö.E. implemented the solvers, and H.A.Ş. conducted the numerical experiments.

Author details

Hasan Aykut Şatana, Barışcan Karaosmanoğlu and Özgür Ergül*

*Address all correspondence to: ozgur.ergul@eee.metu.edu.tr

Department of Electrical and Electronics Engineering, Middle East Technical University,
Ankara, Turkey

References

[1] Ditlbacher H, Hohenau A, Wagner D, Kreibig U, Rogers M, Hofer F, Aussenegg FR, Krenn JR. Silver nanowires as surface plasmon resonators. Phys. Rev. Lett. 2005;**95**: 257403.

[2] Sanders AW, Routenberg DA, Wiley BJ, Xia Y, Dufresne ER, Reed MA. Observation of plasmon propagation, redirection, and fan-out in silver nanowires. Nano Lett. 2006;**6**: 1822–1826.

[3] Akimov AV, Mukherjee A, Yu CL, Chang DE, Zibrov AS, Hemmer PR, Park H, Lukin MD. Generation of single optical plasmons in metallic nanowires coupled to quantum dots. Nature. 2007;**450**:402–406.

[4] Guo X, Qiu M, Bao J, Wiley BJ, Yang Q, Zhang X, Ma Y, Yu H, Tong L. Direct coupling of plasmonic and photonic nanowires for hybrid nanophotonic components and circuits. Nano Lett. 2009;**9**:4515–4519.

[5] Wang W, Yang Q, Fan F, Xu H, Wang ZL. Light propagation in curved silver nanowire plasmonic waveguides. Nano Lett. 2011;**11**:1603–1608.

[6] Li Z, Bao K, Fang Y, Guan Z, Halas NJ, Nordlander P, Xu H. Effects of a proximal substrate on plasmon propagation in silver nanowires. Phys. Rev. B. 2010;**82**:241402.

[7] Ma Y, Li X, Yu H, Tong L, Gu Y, Gong Q. Direct measurement of propagation losses in silver nanowires. Opt. Lett. 2010;**35**:1160–1162.

[8] Yao J, Liu Z, Liu Y, Wang Y, Sun C, Bartal G, Stacy AM, Zhang X. Optical negative refraction in bulk metamaterials of nanowires. Science. 2008;**321**:930.

[9] Liu Y, Bartal G, Zhang X. All-angle negative refraction and imaging in a bulk medium made of metallic nanowires in the visible region. Opt. Exp. 2008;**16**:15439–15448.

[10] Casse BDF, Lu WT, Huang YJ, Gultepe E, Menon L. Super-resolution imaging using a three-dimensional metamaterials nanolens. Appl. Phys. Lett. 2010;**96**:023114.

[11] Sun M, Zhang Z, Wang P, Li Q, Ma F, Xu H. Remotely excited Raman optical activity using chiral plasmon propagation in Ag nanowires. Light Sci Appl. 2013;**2**:112.

[12] Huang Y, Fang Y, Zhang Z, Zhu L, Sun M. Nanowire-supported plasmonic waveguide for remote excitation of surface-enhanced Raman scattering. Light Sci Appl. 2014;**3**:199.

[13] Wang X, Summers CJ, Wang ZL. Large-scale hexagonal-patterned growth of aligned ZnO nanorods for nano-optoelectronics and nano-sensor arrays. Nano Lett. 2004;**4**:423–426.

[14] Rockstuhl C, Fahr S, Lederer F. Absorption enhancement in solar cells by localized plasmon polaritons. J. Appl. Phys. 2008;**104**:123102.

[15] Bergin SM, Chen Y, Rathmell AR, Charbonneau P, Lib Z, Wiley BJ. The effect of nanowire length and diameter on the properties of transparent, conducting nanowire films. Nanoscale. 2012;**4**:1996–2004.

[16] Yin AJ, Li J, Jian W, Bennett AJ, Xu JM. Fabrication of highly ordered metallic nanowire arrays by electrodeposition. Appl. Phys. Lett. 2001;**79**:1039–1041.

[17] Wang RC, Liu CP, Huang JL. ZnO hexagonal arrays of nanowires grown on nanorods. Appl. Phys. Lett. 2005;**86**:251104.

[18] Kottmann JP, Martin OJF. Plasmon resonances of silver nanowires with a non-regular cross section. Phys. Rev. B. 2001;**64**:235402.

[19] Yılmaz A, Karaosmanoğlu B, Ergül Ö. Computational electromagnetic analysis of deformed nanowires using the multilevel fast multipole algorithm. Sci. Rep. 2015;**5**:8469.

[20] Johnson PB, Christy RW. Optical constants of the noble metals. Phys. Rev. B. 1972;**6**:4370–4379.

[21] Ergül Ö. Solutions of large-scale electromagnetics problems involving dielectric objects with the parallel multilevel fast multipole algorithm. J. Opt. Soc. Am. A. 2011;**28**:2261–2268.

[22] Kottmann JP, Martin OJF. Influence of the cross section and the permittivity on the plasmon-resonance spectrum of silver nanowires. Appl. Phys. B. 2001;**73**,299–304.

[23] Futamata M, Maruyama Y, Ishikawa M. Local electric field and scattering cross section of Ag nanoparticles under surface plasmon resonance by finite difference time domain method. J. Phys. Chem. B. 2003;**107**:7607–7617.

[24] Giannini V, Rodriguez-Oliveros R, Sanchez-Gil JA. Surface plasmon resonances of metallic nanostars/nanoflowers for surface-enhanced Raman scattering. Plasmonics. 2010;**5**:99–104.

[25] Hohenester U, Krenn J. Surface plasmon resonances of single and coupled metallic nanoparticles: a boundary integral method approach. Phys. Rev. B. 2005;**72**:195429.

[26] Sondergaard T. Modeling of plasmonic nanostructures: green's function integral equation methods. Phys. Stat. Sol. B. 2007;**244**:3448–3462.

[27] Kern AM, Martin OFJ. Surface integral formulation for 3D simulations of plasmonic and high permittivity nanostructures. J. Opt. Soc. Am. A. 2009;**26**:732–740.

[28] Gallinet B, Martin OFJ. Scattering on plasmonic nanostructures arrays modeled with a surface integral formulation. Photon. Nanostruct. Fund. Appl. 2010;**8**:278–284.

[29] Rodriguez-Oliveros R, Sanchez-Gil JA. Localized surface-plasmon resonances on single and coupled nanoparticles through surface integral equations for flexible surfaces. Opt. Exp. 2011;**16**:12208–12219.

[30] Solis DM, Taboada JM, Obelleiro F. Surface integral equation method of moments with multiregion basis functions applied to plasmonics. IEEE Trans. Antennas Propag. 2015;**63**:2141–2152.

[31] Karaosmanoğlu B, Gür UM, Ergül Ö. Investigation of nanoantennas using surface integral equations and the multilevel fast multipole algorithm. In Proceedings of the Progress in Electromagnetics Research Symposium (PIERS); Prague, 2015, pp. 2026–2030.

[32] Bora M, Fasenfest BJ, Behymer EM, Chang ASP, Nguyen HT, Britten JA, Larson CC, Chan JW, Miles RR, Bond TC. Plasmon resonant cavities in vertical nanowire arrays. Nano Lett. 2010;**10**:2832–2837.

[33] Nauert S, Paul A, Zhen Y, Solis D, Vigderman L, Chang WS, Zubarev ER, Nordlander P, Link S. Influence of cross sectional geometry on surface plasmon polariton propagation in gold nanowires. ACS Nano. 2014;**8**:572–580.

[34] Chew WC, Jin JM, Michielssen E, Song J. Fast and efficient algorithms in computational electromagnetics. Boston: Artech House; 2001.

[35] Ergül Ö, Gürel L. The multilevel fast multipole algorithm (MLFMA) for solving large-scale computational electromagnetics problems. Chichester, West Sussex, UK: Wiley-IEEE; 2014.

[36] Çekinmez A, Karaosmanoğlu B, Ergül Ö. Integral-equation formulations of plasmonic problems in the visible spectrum and beyond. In Reyhanoğlu M, editor. Dynamical systems—analytical and computational techniques. InTech; 2017.

[37] Karaosmanoğlu B, Yımaz A, Ergül Ö. On the accuracy and efficiency of surface formulations in fast analysis of plasmonic structures via MLFMA. In Proceedings of the Progress in Electromagnetics Research Symposium (PIERS); Shanghai, 2016, pp. 2629–2633.

[38] Karaosmanoğlu B, Yılmaz A, Gür UM, Ergül Ö. Solutions of plasmonic structures using the multilevel fast multipole algorithm. Int J RF Microw Comput. Aided Eng. 2016;**26**:335–341.

[39] Önol C, Karaosmanoğlu B, Ergül Ö. Efficient and accurate electromagnetic optimizations based on approximate forms of the multilevel fast multipole algorithm. IEEE Antennas Wirel Propag. Lett. 2016;**15**:1113–1115.

Edited by Khan Maaz

One-dimensional nanostructures, such as nanowires, have drawn extensive research interests in the recent years. The smaller size brings unique properties to the nanowires due to the finite size effect (quantum confinement effects). The unique geometrical features of the nanowires bring their utilization in many practical applications in the recent advanced technology. This book provides an updated review on fabrication, properties, and applications of various nanowires. This book is aimed to provide solid foundation of nanowires to the students, scientists, and engineers working in the field of material science and condensed matter physics.

ISBN 978-953-51-4762-6

Photo by eugenesergeev / iStock

IntechOpen